

The Detection of Gravitational Waves

Data Analysis and Interferometry



Von der Fakultät für Mathematik und Physik
der Gottfried Wilhelm Leibniz Universität Hannover
zur Erlangung des Grades

Doktor der Naturwissenschaften

Dr. rer. nat.

genehmigte Dissertation

von

Dipl. Phys. Jan Harms

geboren am 17.08.1976 in Lehrte

(2006)

Referent: Prof. K. Danzmann
Korreferent: Prof. B. Schutz
Tag der Promotion: 14.07.2006

Zusammenfassung

Zur Zeit entwickeln sich weltweit Projekte mit dem Ziel, die bisher lediglich indirekt nachgewiesenen Gravitationswellen zu messen. Das erfolgversprechendste Design stellen hierbei die interferometrischen Detektoren der jetzigen und vor allem zukünftiger Generationen dar. Dennoch hängt die Erfolgsaussicht einer Messung nicht nur von der Technologie der Detektoren ab. Insbesondere stellt sich die Aufgabe der Vorhersage der Form der Gravitationswellen, als auch die Optimierung der Datenanalyse unter den zur Verfügung stehenden Mitteln elektronischer Datenverarbeitung. Die genannten Teilaufgaben sollten dabei nicht voneinander getrennt betrachtet werden.

Der erste Teil dieser Arbeit beinhaltet eine theoretische Untersuchung der Datenanalyse des Big Bang Observers. Für den Erfolg dieser potenziellen Zukunftsmission – die Detektion des kosmischen Gravitationswellen Hintergrundes – muss gewährleistet sein, dass dominante Signale von anderen Quellen vom Datenstrom nach dessen Aufnahme subtrahiert werden können. Subtraktion eines Signals erfordert eine präzise Schätzung der Parameterwerte, welche eine ansonsten bekannte Wellenform des Signals bestimmen. Diese Aufgabe wird wesentlich durch das Konfusionsrauschen behindert, welches durch eine große Zahl anderer noch nicht subtrahierter Signale erzeugt wird. Allerdings deuten die Ergebnisse darauf hin, dass eine Subtraktion aller dominanten Signale, also aller Doppelsternsysteme des Universums, die sich mit einer bestimmten Frequenz umkreisen, zumindest basierend auf dem Standarddesign des Detektors durchführbar ist.

In den weiteren Kapiteln dieser Arbeit werden die theoretischen Mittel zur Untersuchung der optischen Eigenschaften interferometrischer Detektoren entwickelt und angewandt. Abgesehen von der Notwendigkeit einer quantenmechanischen Erklärung der Existenz optischer Minimalfluktuationen, liegt das Augenmerk auf den klassischen Eigenschaften und Transformationen der optischen Systeme. Es werden in erster Linie die linearen Relationen zwischen den Eingangs- und Ausgangsfeldern für die relevanten Michelson Topologien berechnet. Die entsprechenden Relationen des GEO 600 Detektors sind hierbei in aller Ausführlichkeit inklusive einer detaillierten Einbeziehung des wirksamen Strahlungsdruckes vorgestellt. Diese Arbeit setzt voraus, dass die abschließende Photodetektion des Ausgangsfeldes phasensensitiv erfolgt. Daher wird in den meisten Fällen eine bivariate Verteilung der Quadraturphasen des Feldes untersucht. Dieser Formalismus erlaubt zusätzlich auf einfache Weise den Einbezug von Korrelationen zwischen der Amplitude und der Phase eines Feldes. Minimal fluktuierende Felder nehmen dabei einen sogenannten gequetschten Zustand an, der zur Verbesserung der Sensitivität der Detektoren beitragen kann. Diese Zustände werden einerseits extern durch optische parametrische Verstärker präpariert, andererseits lassen sie sich auch in den Detektoren ponderomotiv oder durch Kerr Medien erzeugen. Die Untersuchungen werden zum Teil durch Vergleiche mit innovativeren Topologien wie zum Beispiel dem optischen Hebel oder dem optischen Tachometer in einen größeren Zusammenhang gestellt.

Stichworte: Gravitationswellendetektor, Datenanalyse, Interferometrie

Abstract

At this time, the world is witnessing the development of projects whose aim is to detect gravitational waves which so far have not been observed directly. The large-scale interferometric detector constitutes the most promising design especially in view of the vast choice of possible technological improvements which can be implemented in the next generation of detectors. Nevertheless, the prospect of success does not exclusively depend on the technology of the detectors. In particular, theorists have to provide accurate predictions of the form of gravitational waves for many different sources and they also have to optimize data analysis under the condition of limited computational power. The mentioned subtasks should not be considered separately.

The first part of this thesis comprises a theoretical investigation of a data analysis problem of the Big Bang Observer. For the success of this potential future mission – the detection of the cosmic gravitational-wave background – one has to guarantee that the dominant signals from other sources are subtractable from the data stream once it has been recorded. Subtraction of a signal requires an accurate estimation of its parameter values which determine an otherwise predictable form of the wave. The latter task is crucially hampered by confusion noise emerging from a very large number of other yet unsubtracted signals. However, the results indicate that a subtraction of all dominant signals – i.e. all binary stars of the universe with a certain orbital frequency – is feasible at least for the standard design of the detector.

In the following chapters of this thesis, the theoretical means to investigate the optical properties of interferometric detectors are developed and applied. Apart from the necessity of a quantum mechanical explanation of the existence of minimal optical fluctuations, the focus lies on the classical properties and transformations of the optical systems. Primarily, the linear relations between input and output fields are calculated for the relevant Michelson topologies. The respective relations of the GEO 600 detector are presented in all detail taking explicitly into account the active radiation pressure. In this thesis it is presumed that the final photo detection is sensitive to the phase of the light. Hence, in most cases the bivariate distribution of the field's quadrature phases is considered. In addition, this formalism allows in a simple way to include correlations between the amplitude and the phase of the field. Fields with minimal fluctuations which exhibit amplitude-phase correlations assume a so-called squeezed state which may contribute to an improvement of the sensitivity of the detectors. On the one hand, optical parametric amplifiers may provide squeezed states externally. On the other hand, they can be generated ponderomotively or by Kerr media inside the detector. In the end, the investigations are brought into a more general context comparing the performance of position meters with that of more innovative topologies like for example the optical lever or the optical speed meter.

Keywords: Gravitational wave detector, data analysis, interferometry

ex falso quodlibet sequitur

CONTENTS

1	Cosmological Distance Measures	1
1.1	Robertson-Walker Spacetimes	1
1.2	Distance Measures	4
1.2.1	Comoving Distance	5
1.2.2	Angular Diameter Distance	6
1.2.3	Luminosity Distance	7
1.3	Comoving Number of NS-NS Mergers	8
2	Gravitational Waves	11
2.1	Metric Perturbations	12
2.1.1	Linear Perturbations of a Background Metric	12
2.1.2	The Wave Equation for Radiative Perturbations	13
2.1.3	Metric Perturbations in TT gauge	15
2.2	Properties of Gravitational Waves	16
2.2.1	Polarization of Gravitational Waves	16
2.2.2	Propagation in Geometric Optics Approximation	18
2.2.3	Generation of Gravitational Waves	19
2.2.4	Energy of Gravitational Waves	20
2.3	Detection of Gravitational Waves	21
2.3.1	Geodesic Deviation	21
2.3.2	Doppler Spacecraft Tracking	22
2.3.3	Matter Wave Interferometry	24
3	NS/NS Binaries	27
3.1	Newtonian Waveforms	28
3.2	Corrections to the Newtonian Quadrupole Waveform	29
3.2.1	Orbital Eccentricity	30
3.2.2	Spin Effects	33
3.2.3	High-Order Post-Newtonian Effects, Neglecting Spin	35

4	BBO and Signal Analysis	37
4.1	Estimations in the Time Domain	39
4.2	Spectral Analysis	42
4.2.1	The Periodogram	43
4.2.2	Covariance Time-Lag and Spectral Windows	44
4.2.3	Power Spectral Density	47
4.3	Overview of BBO and the NS-Binary Background	49
4.3.1	The Big Bang Observer	49
4.3.2	NS-NS Merger Rates and the Associated Foreground Noise	50
4.4	Understanding Confusion Noise	53
4.4.1	Brief Review of Optimal Matched Filtering	54
4.4.2	Overlapping NS-NS Chirps as a Source of Self-Confusion	56
4.4.3	The Number of Overlapping Inspiral Tracks in the f - t Plane	58
4.5	Confusion Noise from Imperfectly Subtracted Waveforms	59
4.5.1	Subtraction Errors due to Noise	59
4.5.2	Projecting out Residual Subtraction Errors	62
4.6	The Detection Threshold	63
4.6.1	Lower Bound on the Detection Threshold	63
4.6.2	Limitations due to Finite Computing Power	65
4.7	Equations of Self-Consistent Subtraction Scheme	67
4.8	Evaluation of Self-Consistent Subtraction Scheme	68
4.8.1	Efficacy of Background Subtraction for BBO	69
4.8.2	Further Analyses of the Subtraction Scheme	70
4.8.3	Confusion Noise from a Very Strong NSm Foreground	72
5	Quantum Fluctuations of Light	75
5.1	Representations of the Electric Field	75
5.1.1	The Schrödinger Picture	76
5.1.2	The Interaction Picture	76
5.1.3	The Modulation Picture	77
5.2	Vacuum and Squeezed Vacuum Noise	78
5.3	Quantum Limits	81
5.4	Linear Quantum Measurements	84
5.5	Linearization of the Kerr Wigner Function	86
6	Optical Transferfunctions	89
6.1	The Propagation	89
6.2	The Mirror Coupling Equations	90
6.3	Characterization of Fabry-Pérot Cavities	92
6.4	Radiation Pressure Effects	99
6.5	The Suspended Fabry-Pérot Cavity	103
6.6	Third-Order Nonlinear Transformations	106

7	The Michelson Interferometer	113
7.1	Input-Output Relations without Radiation Pressure	113
7.2	Input-Output Relations with Radiation Pressure	118
7.2.1	The Coupling Equations	118
7.2.2	The Input-Output Relation	120
7.2.3	The Noise Spectral Density	122
7.3	Phase Sensitive Photo Detection	128
7.3.1	The Homodyne Detection	129
7.3.2	The Heterodyne Detection	131
8	Advanced Interferometer Topologies	135
8.1	Filtered Light for SR Interferometers	135
8.1.1	Signal Recycling	136
8.1.2	Squeezed Light Input	141
8.1.3	Squeezed-Variational Schemes	146
8.2	Dual Resonators	148
8.2.1	Optical Bars	149
8.2.2	Speed Meters	152
8.2.3	Symphotonic States	154
9	Space-Borne Interferometers	157
9.1	Time-Delay Interferometry	157
9.1.1	Unequal Arm Length Interferometric Combination	159
9.1.2	Fully Symmetric Sagnac Mode	160
9.1.3	Noise Curves	160
9.2	Doppler Signals from Gravitational Waves	162
9.3	Sensitivity Plots	165
10	Codes and Computations	167
10.1	MATLAB	167
10.1.1	The Michelson interferometer	167
10.1.2	The Signal-Recycled Interferometer	169
10.2	Mathematica	170
10.2.1	Signal Transfer Functions	170
10.2.2	Parametric Resonance	174
A	The Bivariate Normal Distribution	177
B	A Normal Ordering Theorem	179
C	Signal Combinatorics	181
D	Derivation of merger SNR	185
E	The Coupled Pendulum	187

LIST OF FIGURES

1.1	Comoving distance in Mpc	5
1.2	Observation of an object.	6
1.3	Angular diameter distance in Mpc	7
1.4	Luminosity distance in Mpc	8
1.5	Total number of merger events	9
2.1	Polarization of gravitational waves	17
2.2	Doppler spacecraft tracking	22
3.1	Gravitational waves from a NS/NS binary system.	27
4.1	Autocovariance of a stationary process.	41
4.2	Spectral estimates	45
4.3	Dirichlet kernel	47
4.4	The BBO configuration	50
4.5	BBO sensitivity curve	51
4.6	Fractional NS/NS foreground noise	54
4.7	Geometrical representation of the template space.	60
4.8	Binary subtraction (increased S_h^{inst})	70
4.9	SNR-redshift correspondence	72
4.10	Distance of resolvable NS-NS mergers	73
4.11	Binary subtraction (increased \dot{n}_0)	74
5.1	Complex amplitude diagram for squeezed light.	80
5.2	Measurement of a force	82
5.3	Scheme of a linear measurement.	85
6.1	Propagation of a field	90
6.2	Mirror coupling	91
6.3	The beam splitter coupling relations	92
6.4	Fabry-Pérot cavity	93

6.5	Power transmitted through a Fabry-Pérot cavity	94
6.6	PDH error signal	96
6.7	Fabry-Pérot cavity states	97
6.8	Power build-up inside Fabry-Pérot cavities	98
6.9	Phase shift of fields reflected from FP cavities	99
6.10	Two-stage mirror suspension	100
6.11	Mirror coupling relations with RP	102
6.12	Fabry-Pérot cavity	103
6.13	Detuned cavity: Reflected field with varying detuning	104
6.14	Detuned cavity: Transmitted field with varying detuning	105
6.15	Detuned cavity: Displacement noise	106
6.16	Nonlinear Kerr cavity	107
6.17	Bistability of a Kerr cavity	108
6.18	Transfer functions of a Kerr cavity	111
7.1	The linearized Michelson equations.	114
7.2	Bright-port dark-port transfer, part I.	117
7.3	Beam splitter coupling relations	119
7.4	Power-recycled interferometer	121
7.5	Topology of GEO 600	123
7.6	GEO 600 optical noise (300W)	126
7.7	GEO 600 optical noise (10kW)	127
7.8	The balanced homodyne detector.	130
7.9	Dark port field with heterodyning.	132
7.10	The heterodyne detector.	133
8.1	GEO 600 topology	137
8.2	Quantum noise in signal-recycled interferometers	140
8.3	Frequency-dependent squeezing	142
8.4	Variational output	146
8.5	Optimized homodyne angle	147
8.6	The dual resonator	148
8.7	Power inside a dual resonator	149
8.8	Optical bar	150
8.9	Optical lever	152
8.10	Speed meter performance	154
8.11	Symphotonic states	155
9.1	Doppler time series recorded by LISA	157
9.2	Simplified sketch of a LISA spacecraft.	158
9.3	Doppler noise spectral densities.	162
9.4	Coordinate frames of a source and the detector	163
9.5	Geometry of the LISA configuration	164
9.6	LISA sensitivity curve.	165
A.1	Noise ellipse	178

C.1	Distribution of signals among data bins	181
C.2	Estimation quality factor	183
E.1	The coupled pendulum	187
F.1	Solutions to perturbed oscillator	190
F.2	Parametric resonance	190

LIST OF TABLES

4.1	BBO parameters.	51
4.2	Fraction of subtractable NS binaries	69
4.3	Ratio of residual foreground to cosmic background	71
7.1	Interferometer with bright-port dark-port transfer.	116
7.2	GEO 600 parameters (2004)	125
8.1	GEO 600 design parameter values	137
8.2	Optomechanical coupling parameters	140
9.1	LISA parameters.	161
C.1	Multiple bin occupation	182

LIST OF NOTATIONS

Physical constants

$c = 299792458 \text{ m/s}$	speed of light
$G = 6.672 \cdot 10^{-11} \text{ N m}^2/\text{kg}^2$	gravitational constant
$\hbar = 1.054 \cdot 10^{-34} \text{ J s}$	reduced Planck constant
$M_{\odot} = 2 \cdot 10^{30} \text{ kg}$	solar mass

Glossary

$E(t), S(t), \dots$	electric field
$\bar{\mathbf{E}}(t), \bar{\mathbf{S}}(t), \dots$	quadrature phase vector
$a(\omega), b(\omega), \dots$	field amplitude
$a_1(\Omega), a_2(\Omega), a_{\zeta}(\Omega), \dots$	quadrature amplitude
$\bar{\mathbf{a}}, \bar{\mathbf{b}}, \dots$	quadrature amplitude vector
$\mathbf{R}(\Omega), \mathbf{T}(\Omega), \dots$	transfer function
$g_{\mu\nu}$	metric tensor
$h_{\mu\nu}$	metric perturbation
$\bar{h}_{\mu\nu}$	trace reversed metric perturbation
z	cosmological redshift
λ	reduced wavelength
\mathcal{V}	volume
\mathcal{A}	area
$\vec{e}_i, \vec{e}_1, \dots$	unit vectors
$\mathbb{Z}, \mathbb{R}, \mathbb{C}$	integer, real, complex numbers

CHAPTER 1

Cosmological Distance Measures

This chapter provides tools which are applied in [section 4.3](#) ff. There, we need to know the amplitude of a gravitational wave measured on Earth for a correctly modelled source. The amplitude is inversely proportional to the distance between the source and the gravitational wave detector. We expect that future gravitational wave detectors are going to locate sources at redshifts $z = 5$ and beyond. For these sources the problem arises that one has to consider cosmological distances which are travelled by the wave. As we show in [subsection 1.2.3](#), the cosmological distance measure which directly determines the amplitude of the wave is the luminosity distance. The outline of the following section is mainly designed along the lines of ([Hogg; 2000](#)). A more elaborate discussion of relativistic cosmological models can be found in ([Hartle; 2003](#)) and part VI of ([Misner et al.; 1973](#)). The distance measures in [section 1.2](#) are evaluated for (and probably in) a flat universe, i.e. the total energy density of the cosmological fluid equals the critical density. Furthermore, we assume a present-day Hubble constant $H_0 = 70 \text{ km/s Mpc}^{-1}$.

1.1 Robertson-Walker Spacetimes

On large scales the universe is homogeneous and isotropic. Therefore, a reasonable first approximation of our theoretical model is that the universe is homogeneous and isotropic at all scales. Technically this means that there exists a family of slices of simultaneity (3 dimensional spacelike hypersurfaces) which completely covers spacetime with the special property that on a given slice of simultaneity (i) no two points are distinguishable from each other ("homogeneity"), and (ii) at a given point no one spatial direction is distinguishable from each other ("isotropy"). These properties are inherited to the energy density inside the spatial hypersurfaces and its 3-dimensional Riemann curvature tensor. Thereby, the 3-dimensional Riemann curvature tensor must be expressible in terms of constants, the metric tensor and the Levi-Civita tensor. The only Riemann tensor of the hypersurface which can be constructed with the right symmetries is

$$R_{ijkl} = K(g_{ik}g_{jl} - g_{il}g_{jk}) \tag{1.1}$$

From the Riemann tensor it is possible to deduce a 3-metric of the hypersurface. That metric is fixed up to coordinate transformations. Now, we consider an observer who at any moment of proper time t observes an isotropic and homogeneous universe. For a specific choice of coordinates and substituting $1/a^2(t)$ for $|K|$, one may write the space-time metric in the concise form

$$ds^2 = -c^2 dt^2 + a^2(t) [d\chi^2 + \Sigma^2(\chi) \cdot (d\theta^2 + \sin^2(\theta)d\phi^2)] \quad (1.2)$$

where $\Sigma(\chi)$ is one of three different functions connected with the sign of spatial curvature

$$\Sigma(\chi) \equiv \begin{cases} \sin(\chi) & K > 0 \quad \text{positive spatial curvature} \\ \chi & K = 0 \quad \text{spatially flat} \\ \sinh(\chi) & K < 0 \quad \text{negative spatial curvature} \end{cases} \quad (1.3)$$

Eqs. (1.2)&(1.3) define a Robertson-Walker spacetime. The coordinate χ is dimensionless.

So far, we are unable to answer questions on how the universe evolves in time which means that we do not know the function $a(t)$. The dynamics are governed by the Einstein field equations and consequently we need the stress-energy tensor \mathbf{T} of the universe. Isotropy entails that the momentum density of the stress-energy tensor vanishes $T_{i0} = 0$, and its spatial part which describes the stress must be homogeneous and isotropic $T_{ij} = P g_{ij}$. It follows that the stress-energy tensor describes a perfect fluid whose frame independent stress-energy can be cast into the form

$$\mathbf{T} = (\rho + P)\vec{u} \otimes \vec{u} + P\mathbf{g} \quad (1.4)$$

The observer of a homogeneous and isotropic universe has 4-velocity $\vec{u} = (1, 0, 0, 0)$. Our first equation is derived from the law of energy conservation $u^\alpha T_{\alpha}{}^{\beta}{}_{;\beta} = 0$

$$\begin{aligned} 0 &= u^\alpha T_{\alpha}{}^{\beta}{}_{;\beta} \\ &= u^\alpha \left((\rho + P)u_\alpha u^\beta + P\delta_\alpha{}^\beta \right)_{;\beta} \\ &= -(\rho + P)u^\beta{}_{;\beta} - u^\beta \rho_{;\beta} \end{aligned}$$

$$\frac{d\rho}{d\tau} = -(\rho + P)\nabla \cdot \vec{u} \quad (1.5)$$

It turns out that isotropy automatically entails the local conservation of momentum and so the latter equation is the only information obtainable from the fact that the stress-energy tensor is divergence free $\nabla \cdot \mathbf{T} = \vec{0}$. In the coordinate system of Eq. (1.2), the law of energy conservation becomes

$$\frac{d(\rho a^3)}{dt} = -P \frac{da^3}{dt} \quad (1.6)$$

which we recognize as the first law of thermodynamics for a perfect fluid. This equation is easily calculated using $u^\beta{}_{;\beta} = 1/\sqrt{-g} \partial_\beta(u^\beta \sqrt{-g})$ with the 4-velocity as stated above. Another piece of information can be obtained from the time-time component of the Einstein field equations, i.e. the Friedmann equation

$$\left(\frac{\dot{a}}{a} \right)^2 + \frac{k}{a^2} = \frac{8\pi G}{3c^4} \rho \quad (1.7)$$

with $k \equiv \text{sgn}(K)$. Now, specifying an equation of state $P = P(\rho)$ and integrating the first law of thermodynamics which may be written as

$$\frac{d\rho}{da} = -3\frac{\rho + P}{a} \quad (1.8)$$

we obtain the pressure and energy density as functions of the scaling parameter a and one can integrate Eq. (1.7) and find the time evolution of our cosmological model. The equation of state depends on the constituents of the universe. Cold matter is pressureless ($P_M = 0$) and comprises dark matter and baryonic matter. Radiation comprises all high energy and zero rest mass particles and obeys the equation of state $P_R = \rho_R/3$. Dark energy has negative pressure (e.g. vacuum energy would contribute with $P_\Lambda = -\rho_\Lambda$). Since shortly after the Big Bang, energy transfer between these three forms has been negligible and so the energy conservation law holds for each type separately. The evolution of the respective energy densities is calculated from Eq. (1.8)

$$\rho_R = \rho_{R0} \cdot \left(\frac{a_0}{a}\right)^4, \quad \rho_M = \rho_{M0} \cdot \left(\frac{a_0}{a}\right)^3, \quad \rho_\Lambda = \text{const} \quad (1.9)$$

where a_0 denotes the present-day scale factor and ρ_{M0}, ρ_{R0} the present-day densities of cold matter and radiation. Expressed as fractions of the critical density $\rho_{\text{crit}} \equiv 3c^4/(8\pi G)(\dot{a}_0/a_0)^2$ (i.e. which marks the borderline between a closed and an open universe), current estimates for each type of matter are

$$\Omega_R \equiv \frac{\rho_{R0}}{\rho_{\text{crit}}} \sim 10^{-4}, \quad \Omega_\Lambda \equiv \frac{\rho_\Lambda}{\rho_{\text{crit}}} \sim 0.7 \quad \text{and} \quad \Omega_M \equiv \frac{\rho_{M0}}{\rho_{\text{crit}}} \sim 0.3 \quad (1.10)$$

If the scale factor $a(t)$ obeys the Einstein equations, then the metric Eq. (1.2) is called a Friedmann-Robertson-Walker (FRW) metric.

We conclude this section with an investigation of the propagation of light in flat ($k = 0$) FRW spacetimes. The center of our coordinate system coincides with the position of the observer. Note that inhabitants of the Earth do not observe an isotropic universe due to a relative motion of the Earth with respect to the cosmological fluid which gives rise to a dipole anisotropy. However, this detail should not bother us at this point. Light which propagates towards the center follows radial null curves which satisfy

$$c \frac{dt}{a(t)} = d\chi \quad (1.11)$$

Now we consider a series of light pulses emitted from the same point in space towards the center which are separated in time by small intervals δt . The pulses are detected at the center with separation δt_0 . All light pulses travel the same coordinate distance, so integrating the right-hand side of Eq. (1.11) yields the same value for each pulse. For small δt we have $a(t) = a(t + \delta t)$ and equating the integrals of the left-hand sides for two successive pulses one obtains

$$\frac{\delta t_0}{a_0} = \frac{\delta t}{a(t)} \quad (1.12)$$

The latter equation tells us that the frequency which characterizes a periodic process changes between emission and detection by

$$1 + z \equiv \frac{\omega_e}{\omega_0} = \frac{a_0}{a(t)} \quad (1.13)$$

which means that the observed frequency is smaller than the frequency during emission if the universe expanded in the meantime. The quantity z is the redshift which by definition is a measure of cosmological time intervals or distances.

1.2 Distance Measures

Cosmological events are usually observed by telescopes sensitive to light, X-ray, radio waves or in the near future by gravitational wave detectors. Therefore, the redshift of the observed wave is an experimentally accessible measure of the distance between the source and the detector provided that we possess reliable models which predict the frequency during emission. Other quantities like the apparent size of an object or its measured luminosity are related to different distance measures. However, all distance measures can be related to each other if we assume a certain cosmological model. Particularly, all distance measures are functions of the redshift z and these functions are parameterized by the Hubble constant $H_0 \equiv \dot{a}_0/a_0$ and $\Omega_M, \Omega_R, \Omega_\Lambda$ and the spatial curvature parameter k of a FRW model. It is helpful to include k in the density parameter of the Friedmann equation defining a spatial curvature density with

$$\Omega_k \equiv -\frac{k \cdot c^2}{(H_0 a_0)^2} \quad (1.14)$$

Evaluating the Friedmann equation at time $t = 0$, one obtains

$$\Omega_R + \Omega_M + \Omega_k + \Omega_\Lambda = 1 \quad (1.15)$$

and Eq. (1.7) can be cast into a form which is governed by the cosmological redshift

$$H(z) \equiv \frac{\dot{a}}{a} = H_0 \sqrt{\Omega_R(1+z)^4 + \Omega_M(1+z)^3 + \Omega_k(1+z)^2 + \Omega_\Lambda} \quad (1.16)$$

The simplest distance-redshift relation is derived from the Hubble law ([Harrison; 1993](#))

$$v = H_0 \cdot d \quad (1.17)$$

which says that all comoving objects (i.e. objects which do not change their spatial coordinates in the system which was introduced in Eq. (1.2)) at proper distance d recede with velocity v . In general, the relation between velocity and redshift is a little complicated with surprising effects ([Davis et al.; 2003](#)) depending on the interplay between peculiar and Hubble flow velocities. For redshifts $z \ll 1$ we have $z \approx v/c$ and our first (approximate) distance-redshift relation reads

$$d = D_H \cdot z, \quad D_H \equiv \frac{c}{H_0} \approx 1.3 \cdot 10^{26} \text{ m} \quad \text{or} \quad 4.3 \text{ Gpc} \quad (1.18)$$

In the following sections, we will present distance-redshift relations which also hold for large redshifts.

1.2.1 Comoving Distance

The distance-redshift relation for the comoving (line-of-sight) distance which holds for all redshifts z results from an integration of Eq. (1.11). Evaluating Eq. (1.2) at time $t = 0$, we find that $a_0 d\chi$ is the proper differential of the comoving distance (thereby ensuring that the differential of the comoving distance is $c dt$ for points very close to the origin). Neglecting the radiation energy density and considering a flat universe, the comoving distance travelled by light during time t is given by

$$\begin{aligned}
 D_C &= c a_0 \int_t^0 \frac{dt'}{a(t')} \\
 &= c a_0 \int_0^z \frac{dz'}{(\dot{a}/a) \cdot a_0} \\
 &= D_H \int_0^z \frac{dz'}{E(z')} \tag{1.19}
 \end{aligned}$$

$$\text{with } E(z) \equiv \sqrt{\Omega_M(1+z)^3 + \Omega_\Lambda} \tag{1.20}$$

Figure 1.1 shows a plot of the comoving distance as a function of the redshift for three different sets of density parameters which satisfy $\Omega_M + \Omega_\Lambda = 1$. The comoving distance

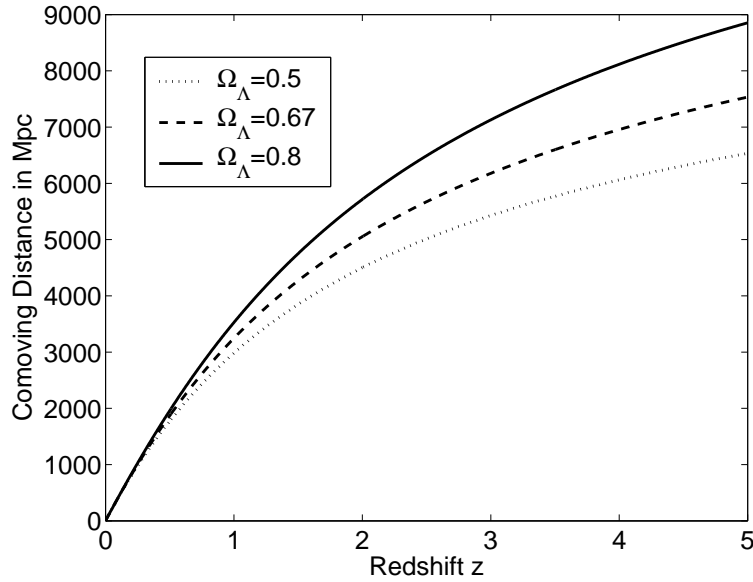


Figure 1.1: The plot shows the comoving distance redshift relation for a flat universe with negligible radiation energy density, i.e. the density parameters satisfy $\Omega_M + \Omega_\Lambda = 1$.

between two objects moving with the Hubble flow stays constant. The proper distance is obtained by multiplying the comoving distance with $a_0/a = 1 + z$.

1.2.2 Angular Diameter Distance

Consider an object at comoving distance D_C which has physical size L . The object subtends an angle $\Delta\theta$ on the sky as shown in Figure 1.2. The angular diameter distance is

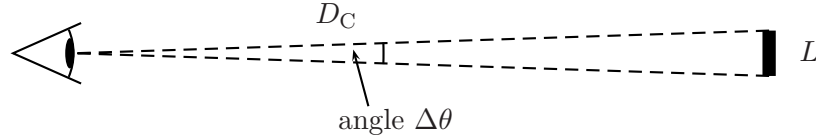


Figure 1.2: A transversally oriented rod-shaped object at comoving distance D_C subtends an angle $\Delta\theta$ on the sky. The ratio of the physical size L of the object and the angle $\Delta\theta$ defines its angular diameter distance.

defined by the ratio

$$D_A \equiv \frac{L}{\Delta\theta} \quad (1.21)$$

Given an angle $\Delta\theta$ and the comoving distance D_C between the object and the observer, we ask for the physical size of the object. Thereby, the angular diameter distance is found in terms of D_C . The relation is obtained from Eq. (1.2) where the object under observation is oriented such that $d\phi = d\chi = 0$

$$\begin{aligned} L &= a\Sigma(\chi) \cdot \Delta\theta \\ &= \frac{a_0\Sigma(\chi)}{1+z} \cdot \Delta\theta \end{aligned} \quad (1.22)$$

where χ is the coordinate distance of the source in a frame whose origin coincides with the position of the observer. Rewriting Eq. (1.2) in terms of a new coordinate $r \equiv \Sigma(\chi)$, it is easy to show that for $K \neq 0$

$$\chi = \frac{\sqrt{|\Omega_k|}D_C}{D_H} \quad \text{with} \quad a_0 = \frac{D_H}{\sqrt{|\Omega_k|}} \quad (1.23)$$

It follows that the angular diameter distance can be cast into the form

$$D_A = \frac{1}{1+z} \cdot \begin{cases} \frac{D_H}{\sqrt{|\Omega_k|}} \sin\left(\frac{\sqrt{|\Omega_k|}D_C}{D_H}\right) & K > 0 \\ D_C & K = 0 \\ \frac{D_H}{\sqrt{\Omega_k}} \sinh\left(\frac{\sqrt{\Omega_k}D_C}{D_H}\right) & K < 0 \end{cases} \quad (1.24)$$

Figure 1.3 shows a plot of the angular diameter distance for three different sets of density parameters which satisfy $\Omega_M + \Omega_\Lambda = 1$ ($K = 0$). The angular diameter distance decreases for higher redshifts (beyond $z \approx 1$). Objects subtend larger angles for greater redshifts!

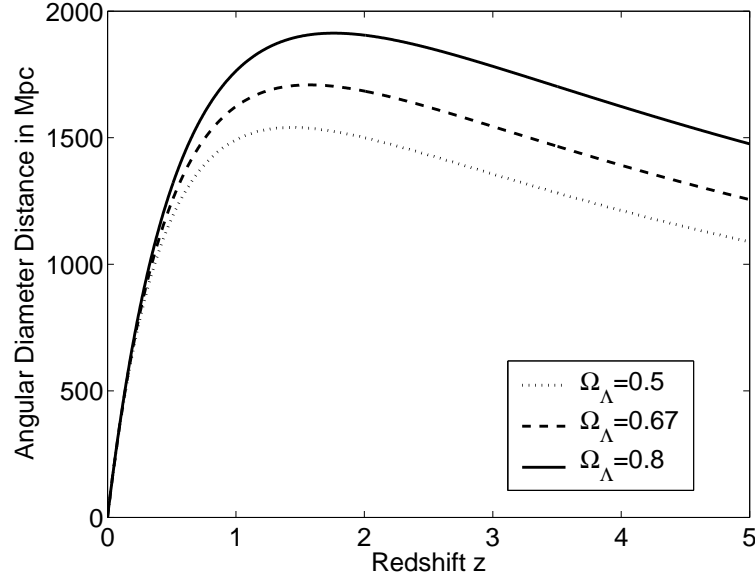


Figure 1.3: The plot shows the angular diameter distance redshift relation for a flat universe with negligible radiation energy density, i.e. the density parameters satisfy $\Omega_M + \Omega_\Lambda = 1$. The angular diameter distance has the peculiar property that it decreases for higher redshifts.

1.2.3 Luminosity Distance

Consider a binary system which loses energy by radiating gravitational waves. The total radiated power L (the luminosity) determines a gravitational wave flux S at some distance to the source. The luminosity distance D_L is defined through

$$S = \frac{L}{4\pi D_L^2} \quad (1.25)$$

The power P which flows through the surface of a sphere centered around the source measured by observers on the surface moving with the Hubble flow reads

$$P = \frac{L}{(1+z)^2} \quad (1.26)$$

One factor $(1+z)$ counts for the redshift of the 'gravitons', the second factor counts for the decrease of the 'graviton' number flux, i.e. 'gravitons' emitted each Δt are measured (absorbed) each $\Delta t' = \Delta t \cdot (1+z)$. The surface of the sphere encloses an area $\mathcal{A} = 4\pi D_A^2 \cdot (1+z)^2$ ($D_A \cdot (1+z)$ is the transverse comoving distance). Therefore, the flux in terms of the angular diameter distance is given by

$$S = \frac{L}{4\pi D_A^2 (1+z)^4} \quad (1.27)$$

and $D_L \equiv D_A(1+z)^2$. The amplitude of gravitational waves measured on Earth which were emitted from sources at large distances is also determined by the luminosity distance.

The distance-redshift relation is shown in [Figure 1.4](#) for a flat universe with $\Omega_M + \Omega_\Lambda = 1$.

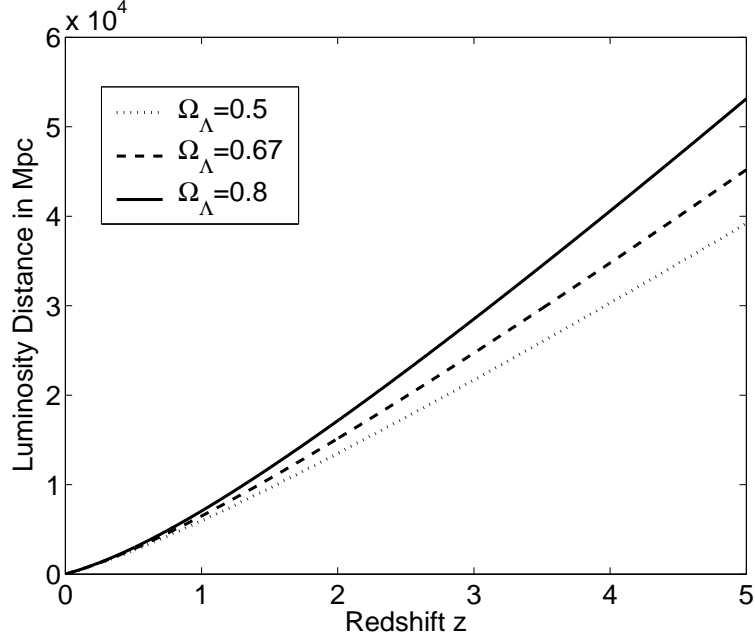


Figure 1.4: The plot shows the luminosity distance redshift relation for a flat universe with negligible radiation energy density, i.e. the density parameters satisfy $\Omega_M + \Omega_\Lambda = 1$.

1.3 Comoving Number of NS-NS Mergers

How many NS-NS merger events ΔN_m enter some detection band during some observation time $\Delta\tau_0$? Consider the number of merger events dN measured on Earth within a time interval $\Delta\tau_0$ which originate from a shell $d\mathcal{V}_C$ at a distance z

$$dN = \dot{n}(z) \frac{\Delta\tau_0}{1+z} d\mathcal{V}_C \quad (1.28)$$

where $\mathcal{V}_C = 4/3\pi D_C^3$ denotes the comoving volume. Summing the contributions from all redshifts, the rate $\dot{N} \equiv \Delta N_m / \Delta\tau_0$ is easily shown to be

$$\dot{N} = \int_0^\infty 4\pi [a_0 r_1(z)]^2 \dot{n}(z) \frac{d\tau_1}{dz} dz, \quad (1.29)$$

where (for our fiducial cosmology)

$$a_0 r_1(z) = \frac{1}{H_0} \int_0^z \frac{dz'}{\sqrt{(1-\Omega_\Lambda)(1+z')^3 + \Omega_\Lambda}} \quad (1.30)$$

$$\frac{d\tau_1}{dz} = \frac{1}{H_0} \frac{1}{1+z} \frac{1}{\sqrt{(1-\Omega_\Lambda)(1+z)^3 + \Omega_\Lambda}}. \quad (1.31)$$

Alternatively, the total number of observed merger events $\Delta N_m = \dot{N} \cdot \Delta\tau_0$ within a time $\Delta\tau_0$ is obtained by integrating Eq. (1.28)

$$\Delta N_m = 4\pi\dot{n}_0 c\Delta t \cdot \int_0^\infty dz \frac{r(z)D_G^2(z)}{H(z)} \quad (1.32)$$

which yields

$$\Delta N_m = 3.0 \cdot 10^5 \left(\frac{\Delta\tau_0}{3 \text{ yr}} \right) \left(\frac{\dot{n}_0}{10^{-7} \text{ Mpc}^{-3} \text{ yr}^{-1}} \right) \quad (1.33)$$

Figure 1.5 plots the number of observable mergers during 3 years that occur closer than (any given) redshift z . We see that only $\sim 15\%$ of mergers occur closer to us than $z = 1$.

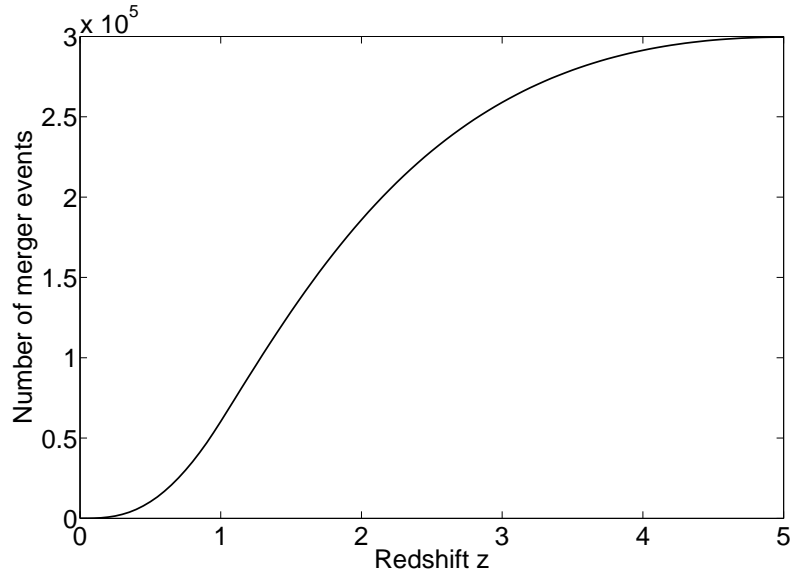


Figure 1.5: The total number of NS-NS mergers closer than redshift z . The results here are normalized to a 3-yr observation period and $\dot{n}_0 = 10^{-7} \text{ Mpc}^{-3} \text{ yr}^{-1}$.

CHAPTER 2

Gravitational Waves

The theory of general relativity predicts that periodic perturbations of the spacetime metric propagate with the speed of light through our universe. However, metric perturbation theory depends generically on the chosen coordinate system, i.e. it does not lead directly to a physical characterization of the involved processes. Therefore, inventing the concept of gravitational waves as a physical entity requires the definition of meaningful frame independent quantities which maintain some analogy to familiar wave phenomena in electromagnetism or mechanics. For instance, it is a nontrivial task to formulate an energy conservation law which includes the gravitational field ([Landau and Lifshitz; 1962](#)). Today we know that gravitational waves carry away energy from their source in agreement with the prediction of general relativity ([Taylor et al.; 1979](#)).

A formal theory of gravitational waves is usually erected on the assumption that an oscillating piece of an otherwise "static" background metric constitutes a weak metric perturbation. In fact, people tend to neglect the problem of defining a clear rule how to distinguish the background from the perturbation. In the following sections, we adopt the method developed in ([Isaacson; 1968a,b](#)) where it was proposed to solve the identification problem by means of a two-lengthscale expansion. Nevertheless, most equations are presented in their linearized form since higher order corrections are difficult to express explicitly. Then, concerning the propagation ([subsection 2.2.2](#)) and generation ([subsection 2.2.3](#)) of gravitational waves, we linearize the problem whereas second order effects determine the amount of energy released in the form of gravitational radiation ([subsection 2.2.4](#)). Finally, in [section 2.3](#), we outline why and how a gravitational wave may be measured by interferometric detectors on Earth or in space. Under certain circumstances, the detection process can be explained in terms of a force which acts on test masses. In other cases, it is more convenient to directly investigate – in a convenient coordinate system – the influence of an oscillating metric on the light propagating within a detector. Henceforth, we set $G = c = 1$, but frequently use their SI values whenever we want to obtain numerical values of interest.

2.1 Metric Perturbations

Similar to other perturbation problems, a metric perturbation expansion is carried out in terms of a small dimensionless expansion parameter. Accordingly, the first step we take is to identify the expansion parameter which is the oscillating piece of an otherwise slowly varying background metric $g_{\alpha\beta}^{\text{B}}$. More specifically, the background metric is defined as the full metric $g_{\alpha\beta}$ averaged over several (reduced) wavelengths λ of the oscillating part

$$g_{\alpha\beta}^{\text{B}} = \langle g_{\alpha\beta} \rangle \quad (2.1)$$

In other words, the wavelength λ of a metric perturbation has to be much shorter than the minimum of the two scales \mathcal{R}, \mathcal{L} which denote the background curvature radius and the typical scale for curvature changes respectively. Once the oscillating perturbation (i.e. gravitational wave) is identified, one may choose the order of perturbation which ought to be included. Except for the issue of calculating the energy loss of objects which irradiate gravitational waves, it is sufficient to focus on first order corrections to any of the tensor fields. Therefore, in [subsection 2.1.1](#), we revisit the theory of linear metric perturbations. The wave equation for radiative perturbations can be written in a frame independent way as shown in [subsection 2.1.2](#). We conclude this section with [subsection 2.1.3](#) providing a collection of equations in transversal traceless gauge which are useful for the remaining part of this chapter.

2.1.1 Linear Perturbations of a Background Metric

In this section, we focus on linear perturbations $h_{\alpha\beta}$ of the metric and derive the corresponding linear perturbation of the tensor fields which depend on the metric. Assume that the metric is decomposed into a background and a linear perturbation according to

$$g_{\alpha\beta} = g_{\alpha\beta}^{\text{B}} + h_{\alpha\beta} \quad (2.2)$$

Linearization entails a decomposition of all metric dependent quantities T into a background part T^{B} and a perturbation T^{h} which depends linearly on the metric perturbation $h_{\alpha\beta}$. In the following, we present the linear perturbation of the Riemann and Einstein tensor in a vacuum spacetime (i.e. the stress-energy tensor vanishes). The Riemann tensor is concisely defined in terms of the connection coefficient

$$\Gamma^{\alpha}{}_{\beta\gamma} \equiv \frac{1}{2} g^{\alpha\delta} (\partial_{\gamma} g_{\delta\beta} + \partial_{\beta} g_{\delta\gamma} - \partial_{\delta} g_{\beta\gamma}) \quad (2.3)$$

according to

$$R^{\alpha}{}_{\beta\gamma\delta} \equiv \partial_{\gamma} \Gamma^{\alpha}{}_{\beta\delta} - \partial_{\delta} \Gamma^{\alpha}{}_{\beta\gamma} + \Gamma^{\alpha}{}_{\gamma\mu} \Gamma^{\mu}{}_{\beta\delta} - \Gamma^{\alpha}{}_{\delta\mu} \Gamma^{\mu}{}_{\beta\gamma} \quad (2.4)$$

Inserting Eq. (2.2) into Eq. (2.3) and collecting terms linear in $h_{\mu\nu}$ yields the linear perturbation of the connection coefficients

$$\Gamma^{\text{h}\alpha}{}_{\beta\gamma} = \frac{1}{2} g^{\text{B}\alpha\mu} (h_{\mu\beta|\gamma} + h_{\mu\gamma|\beta} - h_{\beta\gamma|\mu}) \quad (2.5)$$

The slash ”|” denotes covariant derivatives with respect to the background metric $g_{\mu\nu}^B$. Indices of linear perturbations are raised and lowered with the background metric tensor. The corresponding perturbation of the Riemann tensor reads

$$\begin{aligned} R_{\alpha\beta\gamma\delta}^h &= \Gamma_{\alpha\beta\delta|\gamma}^h - \Gamma_{\alpha\beta\gamma|\delta}^h \\ &= \frac{1}{2} \left(h_{\alpha\delta|\beta\gamma} + h_{\alpha\beta|\delta\gamma} - h_{\beta\delta|\alpha\gamma} - h_{\alpha\gamma|\beta\delta} - h_{\alpha\beta|\gamma\delta} + h_{\beta\gamma|\alpha\delta} \right) \end{aligned} \quad (2.6)$$

The Ricci tensor perturbation is obtained by contracting the Riemann tensor perturbation $R_{\alpha\beta\gamma\delta}^h$ on its first and third indices

$$R_{\alpha\beta}^h = -\frac{1}{2} h_{\alpha\beta|\mu}{}^\mu - \frac{1}{2} h_{\mu}{}^\mu{}_{|\alpha\beta} + h^\mu{}_{(\beta|\alpha)\mu} \quad (2.7)$$

In vacuum, the Einstein field equations impose the condition

$$R_{\alpha\beta}^h = G_{\alpha\beta}^h = 0 \quad (2.8)$$

One often finds the Einstein field equations in terms of the trace-reversed metric perturbation

$$\bar{h}_{\alpha\beta} = h_{\alpha\beta} - \frac{1}{2} g_{\alpha\beta}^B h_{\mu}{}^\mu \quad (2.9)$$

In section 35.14 of (Misner et al.; 1973), one reads

$$\bar{h}_{\alpha\beta|\mu}{}^\mu + g_{\alpha\beta}^B \bar{h}_{\mu\nu}{}^{\mu\nu} - 2\bar{h}_{\mu(\alpha}{}^\mu{}_{\beta)} + 2R_{\mu\alpha\nu\beta}^B \bar{h}^{\mu\nu} - 2R_{\mu(\alpha}^B \bar{h}_{\beta)}{}^\mu = 0 \quad (2.10)$$

which also obtains for non-vacuum spacetimes (in vacuum, the background Ricci tensor vanishes) with unperturbed stress-energy, which means that the stress-energy tensor solely couples to the background metric. If the stress-energy is perturbed by $\delta T_{\alpha\beta}$ then the left-hand side of Eq. (2.10) equates to $-16\pi \cdot \delta T_{\alpha\beta}$. The Einstein field equations in terms of the trace-reversed metric are particularly useful when one investigates the generation of gravitational waves (see section 2.2).

2.1.2 The Wave Equation for Radiative Perturbations

In many textbooks, gravitational waves are introduced by deriving a wave equation for the metric perturbation $h_{\alpha\beta}$. Doing so, one has to work in a so-called transverse-traceless coordinate gauge. Nevertheless, the notion of a physical wave should be frame independent. The possibility of formulating a frame independent definition is most clearly exposed if one chooses to represent the wave in terms of its Riemann tensor as opposed to the metric perturbation itself (Thorne; 2005). Then it is sufficient to demand that a local Lorentz frame exists with respect to the background spacetime $g_{\alpha\beta}^B$ which is large enough to inclose a few wavelengths λ associated with the metric perturbation (measured in a local Lorentz frame of the background spacetime). As mentioned in the introduction to this chapter, the procedure goes under the name ”two-lengthscale expansion”. Accordingly, the Riemann curvature tensor is split into a background tensor and a wave tensor

$$R_{\alpha\beta\gamma\delta} = R_{\alpha\beta\gamma\delta}^B + R_{\alpha\beta\gamma\delta}^{\text{GW}} \quad (2.11)$$

The background Riemann tensor is an average of the Riemann tensor over a few wavelengths $R_{\alpha\beta\gamma\delta}^B \equiv \langle R_{\alpha\beta\gamma\delta} \rangle$. If the waves are weak then covariant derivatives are evaluated with respect to the background spacetime

$$R_{\alpha\beta\gamma\delta;\mu}^{\text{GW}} \simeq R_{\alpha\beta\gamma\delta|\mu}^{\text{GW}} \quad (2.12)$$

By virtue of Eq. (2.11), in a local Lorentz frame of the background spacetime the gravitational-wave part of the Riemann tensor acquires the same index symmetries as the Riemann tensor itself

$$R_{\alpha\beta\gamma\delta}^{\text{GW}} = -R_{\beta\alpha\gamma\delta}^{\text{GW}}, \quad R_{\alpha\beta\gamma\delta}^{\text{GW}} = -R_{\alpha\beta\delta\gamma}^{\text{GW}}, \quad R_{\alpha\beta\gamma\delta}^{\text{GW}} = R_{\gamma\delta\alpha\beta}^{\text{GW}} \quad (2.13)$$

This fact is crucial since it follows that the Bianchi identity also obtains for $R_{\alpha\beta\gamma\delta}^{\text{GW}}$

$$R_{\alpha\beta\gamma\delta|\epsilon}^{\text{GW}} + R_{\alpha\beta\delta\epsilon|\gamma}^{\text{GW}} + R_{\alpha\beta\epsilon\gamma|\delta}^{\text{GW}} = 0 \quad (2.14)$$

facilitating the derivation of a wave equation. Another important relation is found applying the two-lengthscale condition $\lambda/\mathcal{D} \ll 1$ to the double gradient of the wave's Riemann tensor

$$R_{\alpha\beta\gamma\delta|\epsilon\zeta}^{\text{GW}} \simeq \frac{R_{\alpha\beta\gamma\delta}^{\text{GW}}}{\lambda^2} \gg \frac{R_{\alpha\beta\gamma\delta}^{\text{GW}}}{\mathcal{D}^2} \simeq R_{\alpha\beta\gamma\delta}^{\text{GW}} R_{\epsilon\zeta\eta\theta}^B \quad (2.15)$$

where \mathcal{D} is the minimum of the two lengthscales \mathcal{R} , \mathcal{L} which have been introduced before as characteristic scales of the background metric. By consequence, gradients of the wave's Riemann tensor commute

$$\begin{aligned} R_{\alpha\beta\gamma\delta|\epsilon\zeta}^{\text{GW}} &= R_{\alpha\beta\gamma\delta|\zeta\epsilon}^{\text{GW}} - R_{\alpha\mu\epsilon\zeta}^B R^{\text{GW}\mu}{}_{\beta\gamma\delta} - \dots \\ &\simeq R_{\alpha\beta\gamma\delta|\zeta\epsilon}^{\text{GW}} \end{aligned} \quad (2.16)$$

Here, we are interested in waves which propagate in vacuum. From the Einstein field equation, we obtain

$$R^\mu{}_{\alpha\mu\beta} = 0. \quad (2.17)$$

Contracting the first and last index (i.e. α , ϵ) of Eq. (2.14), it follows that the Riemann tensor is divergence free and subsequently taking the divergence of the Bianchi identity and exploiting the commutation property of gradients, one obtains the wave equation for gravitational waves propagating in vacuum

$$R_{\alpha\beta\gamma\delta|\mu}^{\text{GW}}{}^\mu = 0 \quad (2.18)$$

The solution in a local Lorentz frame of the background spacetime far from the source describes a plane wave. Orienting the axes such that the wave propagates in the positive z -direction, the solution is given by an arbitrary function of $t - z$

$$R_{\alpha\beta\gamma\delta}^{\text{GW}} = R_{\alpha\beta\gamma\delta}^{\text{GW}}(t - z) \quad (2.19)$$

The latter equation states that, in vacuum, gravitational waves propagate with the speed of light.

2.1.3 Metric Perturbations in TT gauge

Consider a metric perturbation $\bar{h}_{\alpha\beta}$ governed by the Einstein field equations Eq. (2.10). Choose a local Lorentz frame with respect to a vacuum background metric and, in addition, impose the Lorenz gauge condition

$$\bar{h}_{\alpha\mu, \mu} = 0 \quad (2.20)$$

Then the Einstein field equations for the metric perturbation reduce to the wave equation

$$\square \bar{h}_{\alpha\beta} = 0 \quad (2.21)$$

One may prove that another gauge transformation can be applied which yields a transverse and traceless (TT) representation of the metric perturbation. Two degrees of freedom remain, which will later be identified as the polarizations of gravitational waves:

$$\begin{aligned} h_{\alpha 0}^{\text{TT}} &= 0 && \text{there are no time components} \\ h_{kj,j}^{\text{TT}} &= 0 && \text{spatial components are divergence free} \\ h_{kk}^{\text{TT}} &= 0 && \text{spatial components are trace free} \end{aligned} \quad (2.22)$$

One should keep in mind that only waves which are solutions to Eq. (2.21) can be reduced to TT-gauge. In general, this is not possible for solutions to $\square \bar{h}_{\alpha\beta} = -16\pi\delta T_{\alpha\beta}$. Far from the source where the wavefronts are planar, the components of the metric perturbation in TT-gauge are found by means of one projection \mathbf{P} which is valid throughout the entire local Lorentz frame of the background spacetime. At first, one projects out the longitudinal part $\mathbf{h}^{\text{L}} \equiv \mathbf{h} - \mathbf{P}\mathbf{h}\mathbf{P}$ of $h_{\alpha\beta}$ and subsequently subtracts the trace of the remaining transversal piece:

$$h_{jk}^{\text{TT}} = P_{jl}h_{lm}P_{mk} - \frac{1}{2}P_{jk}(P_{ml}h_{ml}) \quad (2.23)$$

or in matrix notation

$$\mathbf{h}^{\text{TT}} = \mathbf{P}\mathbf{h}\mathbf{P} - \frac{1}{2}\mathbf{P}\text{Tr}(\mathbf{P}\mathbf{h}). \quad (2.24)$$

The projection operator is determined by the wave vector \vec{k} according to $P_{ij} = \delta_{ij} - k_i k_j / k^2$. Integrating the Bianchi identity (Eq. (2.14)) in the local Lorentz frame, one finds that the components of the Riemann tensor (Eq. (2.6)) associated with the metric perturbation $h_{\alpha\beta}^{\text{TT}}$ are completely governed by

$$R_{j0k0}^{\text{h}} = -\frac{1}{2}\ddot{h}_{jk}^{\text{TT}} \quad (2.25)$$

All other components either vanish or can be recovered by application of the Riemann index symmetries. In fact, the latter equation holds in arbitrary coordinate systems (not necessarily TT). Therefore, Eq. (2.25) provides an alternative method to calculate the metric perturbation in TT gauge. Integrating the expression $-2R_{j0k0}$ twice with respect to time yields h_{jk}^{TT} on condition that the Riemann tensor is a planar wave solution of a wave equation in a local Lorentz frame of the background metric.

2.2 Properties of Gravitational Waves

Based on the formal description of gravitational waves which is presented in the previous section, one can derive their physical degrees of freedom and construct a phenomenological model of gravitational waves. In [subsection 2.2.1](#), we find that gravitational waves may have two different polarizations which constitute their internal degrees of freedom. Since gravitational waves in TT gauge are solutions of the same kind of wave equation as for electromagnetic waves, propagation laws and their simplifications which hold for electromagnetic waves must also have a correspondence in gravitational-wave physics. Accordingly, in [subsection 2.2.2](#) the geometric approximation known from optics is reformulated in terms of metric perturbations providing an accurate model of wave propagation far from the source. A summary of the basic equations which govern the generation of gravitational waves is given in [subsection 2.2.3](#). The theory is developed as much as necessary in order to be able to calculate the Newtonian waveform generated by a NS/NS binary system (see [Chapter 3](#)). Finally, in [subsection 2.2.4](#) we deduce a formula for the field energy deposited in gravitational waves and estimate the amount of energy released by a Newtonian binary star.

2.2.1 Polarization of Gravitational Waves

Consider a plane wave solution of Eq. (2.21) which travels along the direction of the coordinate z of a local Lorentz frame with respect to the background spacetime. The gravitational wave is then governed by a function $h_{\alpha\beta}^{\text{TT}}(t-z)$. The TT gauge conditions Eq. (2.23) state that the spatial components of the metric perturbation are determined by two functions

$$h_+ \equiv h_{xx}^{\text{TT}} = -h_{yy}^{\text{TT}}, \quad h_\times \equiv h_{xy}^{\text{TT}} = h_{yx}^{\text{TT}} \quad (2.26)$$

and that all other components vanish. These two (physical) degrees of freedom are the two polarizations of gravitational waves. In terms of the two polarization tensors

$$\mathbf{e}^+ \equiv (\vec{e}_x \otimes \vec{e}_x - \vec{e}_y \otimes \vec{e}_y), \quad \mathbf{e}^\times \equiv (\vec{e}_x \otimes \vec{e}_y + \vec{e}_y \otimes \vec{e}_x) \quad (2.27)$$

the gravitational-wave tensor in TT gauge is constructed according to

$$h_{\alpha\beta}^{\text{TT}} = h_+ e_{\alpha\beta}^+ + h_\times e_{\alpha\beta}^\times \quad (2.28)$$

The two functions h_+ , h_\times also determine all of the components of the associated Riemann tensor. By virtue of Eq. (2.25), only two of the 20 (ad-hoc) independent components of $R_{\alpha\beta\gamma\delta}^{\text{GW}}$ are independent functions of $t-z$:

$$R_{x0x0}^{\text{GW}} = -R_{y0y0}^{\text{GW}} \equiv -\frac{1}{2}\ddot{h}_+(t-z), \quad R_{x0y0}^{\text{GW}} = R_{y0x0}^{\text{GW}} \equiv -\frac{1}{2}\ddot{h}_\times(t-z) \quad (2.29)$$

The TT-gauge representation reveals the quadrupole nature of the gravitational wave field. Focussing on $+$ -polarized waves, the distance between free falling test masses in a local Lorentz frame of the background spacetime is determined by the spatial components of a perturbed Minkowski metric

$$ds^2 = (1 + h_{xx}^{\text{TT}})dx^2 + (1 - h_{yy}^{\text{TT}})dy^2 + dz^2 \quad (2.30)$$

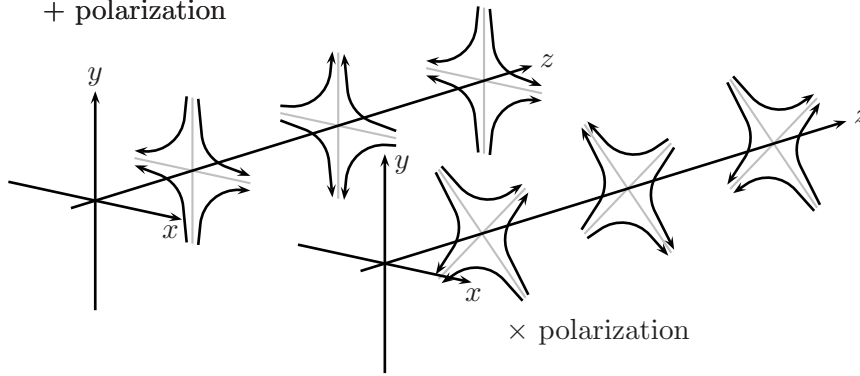


Figure 2.1: Polarization of gravitational waves

The problem of calculating the distance turns out to be remarkably simple, since test masses which initially are at rest with respect to each other (worldlines with constant spatial coordinates, i.e. unit tangent vector $\vec{u} = \partial_t$) preserve their TT coordinates even if a gravitational wave passes by. This property of a TT frame is analogous to claiming that the initial four velocity $\vec{u} = \partial_t$ of the free falling test masses fulfills the geodesic equation $u^\mu u^\alpha{}_{;\mu} = 0$ (where ";" denotes the covariant derivative with respect to the metric $g_{\alpha\beta} = \eta_{\alpha\beta} + h_{\alpha\beta}^{\text{TT}}$), which is readily verified:

$$\begin{aligned}
 u^\mu u^\alpha{}_{;\mu} &= u^\mu u^\alpha{}_{,\mu} + \Gamma^\alpha{}_{\nu\mu} u^\mu u^\nu \\
 &= \Gamma^\alpha{}_{00} \\
 &= \frac{1}{2} \eta^{\alpha\mu} (h_{0\mu,0}^{\text{TT}} + h_{\mu 0,0}^{\text{TT}} - h_{00,\mu}^{\text{TT}}) \\
 &= 0
 \end{aligned} \tag{2.31}$$

The time dependent distance $L(t)$ between two free falling bodies in the presence of a + - polarized gravitational wave is obtained by integrating the differential relation Eq. (2.30). In the simplest case, the amplitude h is spatially constant over the separation vector of the two masses which is assumed to be parallel to the x-axis. Then, for $h(t) \ll 1$ and initial separation L_0 , spatial integration yields

$$L(t) \approx L_0 + \frac{1}{2} L_0 h(t) \tag{2.32}$$

Measuring the distance $L(t)$ by means of a light wave travelling from the one to the other test mass and back again, a further temporal integration over the travelling time has to be carried out in order to obtain the impact of the gravitational wave on the light's phase. Especially, if the travelling time is identical to the period of the gravitational wave, then the result is independent of h and the gravitational wave becomes unmeasurable. In [subsection 2.3.2](#), we derive the phase shift as a function of the light's frequency.

2.2.2 Propagation in Geometric Optics Approximation

In addition to the conditions imposed by the two-lengthscale expansion, the geometric optics approximation of gravitational-wave propagation is erected on the assumption that the radius of curvature \mathcal{R}_{WF} of the wavefronts is much greater than the reduced wavelength λ . Therefore, the gravitational wave varies on scales λ with respect to retarded time ψ (e.g. $\psi = t - z$ in flat space) and varies on scales $\mathcal{D} \equiv \min(\mathcal{R}_{\text{WF}}, \mathcal{R}, \mathcal{L})$ (latter two are defined in [subsection 2.1.2](#)) with respect to all other spatial coordinates x^k

$$h_{\mu\nu}^{\text{TT}} = h_{\mu\nu}^{\text{TT}}(\psi, x^k) \quad (2.33)$$

Retarded time determines the propagation vector of the wave according to

$$k_\alpha \equiv -\psi_{|\alpha} \quad (2.34)$$

The geometric optics equations are obtained from the wave equation and the Lorenz gauge condition. Leading order in λ/\mathcal{D} of the Lorenz gauge condition tells us that $h_{\alpha\beta}^{\text{TT}}$ is orthogonal to \vec{k}

$$h_{\alpha\mu}^{\text{TT}} k^\mu = 0 \quad (2.35)$$

The leading order term of the wave equation imposes the condition that \vec{k} is a null vector, whereas the next order yields the propagation equation for $h_{\alpha\beta}^{\text{TT}}$

$$\vec{k} \cdot \vec{k} = 0, \quad h_{\alpha\beta|\mu}^{\text{TT}} k^\mu = -\frac{1}{2}(\nabla \cdot \vec{k}) h_{\alpha\beta}^{\text{TT}} \quad (2.36)$$

In addition, due to $k_{\alpha|\beta} = k_{\beta|\alpha}$ (since \vec{k} is a gradient of a scalar), the propagation vector satisfies the null geodesic equation

$$k_{\alpha|\mu} k^\mu = k_{\mu|\alpha} k^\mu = \frac{1}{2}(\vec{k} \cdot \vec{k})_{|\alpha} = 0 \quad (2.37)$$

Adopting a spherical coordinate system (r, θ, ϕ) in the local wave zone of the source (see [Chapter 3](#)), the gravitational-wave fields pertain the form

$$h_{\alpha\beta}^{\text{TT}} = \frac{Q_+(\psi, \theta, \phi)}{r} e_{\alpha\beta}^+ + \frac{Q_\times(\psi, \theta, \phi)}{r} e_{\alpha\beta}^\times \quad (2.38)$$

where the polarization tensors are set up by

$$\mathbf{e}^+ \equiv (\vec{e}_\theta \otimes \vec{e}_\theta - \vec{e}_\phi \otimes \vec{e}_\phi), \quad \mathbf{e}^\times \equiv (\vec{e}_\theta \otimes \vec{e}_\phi + \vec{e}_\phi \otimes \vec{e}_\theta) \quad (2.39)$$

The geometric optics equations imply that the polarization tensors obey a parallel-transport law along the null rays of the wave and we may write for arbitrary polarization $P \in \{+, \times\}$

$$k^\mu e_{\alpha\beta|\mu}^P = 0 \quad (2.40)$$

The $1/r$ falloff in Eq. (2.38) is ensured by requiring that for each ray (ψ, θ, ϕ) the coordinate r is propagated out to the universe (until the wave reaches the detectors on Earth) in accord with the law

$$r_{,\mu} k^\mu = \frac{1}{2}(\nabla \cdot \vec{k}) r \quad (2.41)$$

which – compared with the method adopted in [subsection 1.2.3](#) – offers an alternative starting point for calculating the luminosity distance. The latter equation is derived from the transport law Eq. (2.36) by inserting Eq. (2.38) and including the parallel-transport law Eq. (2.40) of the polarization tensors.

2.2.3 Generation of Gravitational Waves

In this section, we focus on the generation of gravitational waves by nearly Newtonian systems which are predominantly characterized by their time varying mass quadrupole moment \mathcal{I}_{ij} . The quadrupole approximation requires that characteristic speeds v of the source are significantly smaller than the speed of light, i.e. the reduced wavelength λ is much larger than the size L of the source. Neutron star binaries fall into this class except for the very last stage of their evolution right before the plunge. The mass quadrupole moment is a traceless representation of the second-order mass moment

$$\mathcal{I}_{ij} \equiv \int d^3x' \rho \left(x'_i x'_j - \frac{1}{3} r'^2 \delta_{ij} \right) \quad (2.42)$$

In the following, we derive an equation which relates the quadrupole moment with the solution of the wave equation for the metric perturbation. The wave generation is governed by the wave equation with stress-energy of the source

$$\square h_{ij}^{\text{TT}} = -16\pi [\delta T_{ij}]^{\text{TT}} \quad (2.43)$$

The TT projection of the stress-energy is calculated by means of the same operator \mathbf{P} introduced in [subsection 2.1.3](#) which yields h_{ij}^{TT} . In the local wave zone of the source, the solution reads

$$h_{ij}^{\text{TT}} = \frac{4}{r} \left[\int d^3x' \delta T_{ij}(t - r, x'^k) \right]^{\text{TT}} \quad (2.44)$$

The stress-energy tensor depends on the mass quadrupole moment according to

$$\left[\int d^3x' \delta T_{ij}(t - r, x'^k) \right]^{\text{TT}} = \frac{1}{2} \left[\ddot{\mathcal{I}}_{ij}(t - r) \right]^{\text{TT}} \quad (2.45)$$

And so we finally obtain the quadrupole formula for gravitational-wave generation

$$h_{ij}^{\text{TT}} = \frac{2G}{r c^4} \left[\ddot{\mathcal{I}}_{ij}(t - r) \right]^{\text{TT}} \quad (2.46)$$

We conclude this section with an order of magnitude estimation of the gravitational-wave amplitude from a neutron star binary at distance $r = 1$ Mpc. The two stars are assumed to have equal masses $1.4 M_\odot$ and to emit waves at frequency $f = 10$ Hz. By virtue of Kepler's third law, the distance between the two stars is $L = 730$ km (keep in mind that the GW frequency is twice the orbital frequency). The second time derivative of the mass quadrupole tensor is of order

$$\ddot{\mathcal{I}} \sim 2.8 M_\odot (2\pi f L)^2 \quad (2.47)$$

which yields $\ddot{\mathcal{I}} \approx 10^{46}$ J (see [Chapter 3](#) for details). The TT components of the metric perturbation are then of order $h_{ij}^{\text{TT}} \approx 5 \cdot 10^{-21}$.

2.2.4 Energy of Gravitational Waves

Gravitational waves, like any other curvature producing quantity, must possess a stress-energy representation $T_{\alpha\beta}^{\text{GW}}$. In (Isaacson; 1968b), it was proposed to obtain a simple expression by averaging the effective stress-energy (derived from the Einstein tensor) over a few wavelength. It has been shown that the stress-energy tensor for (trace-reversed) metric perturbations in Lorenz gauge assumes the form

$$T_{\alpha\beta}^{\text{GW}} = \frac{1}{32\pi} \langle \bar{h}_{\mu\nu|\alpha} \bar{h}^{\mu\nu}{}_{|\beta} \rangle \quad (2.48)$$

Considering a plane gravitational wave in TT gauge which propagates in the z direction (see Eq. (2.28)), one finds that the only non-vanishing components of $T_{\alpha\beta}^{\text{GW}}$ are

$$T_{00}^{\text{GW}} = T_{0z}^{\text{GW}} = T_{z0}^{\text{GW}} = T_{zz}^{\text{GW}} = \frac{1}{16\pi} \langle \dot{h}_+^2 + \dot{h}_\times^2 \rangle \quad (2.49)$$

This energy contributes to the total energy loss of a source which emits gravitational waves. Therefore, we ask for an equation which relates the wave producing mass quadrupole moment of the source to the radiated energy. In the local wave zone (distance to source much larger than λ), the TT amplitude of the wave is governed by Eq. (2.46) and the derivatives of $h_{\alpha\beta}^{\text{TT}}$ which appear in Eq. (2.48) are given by

$$h_{jk,r}^{\text{TT}} = -h_{jk,0}^{\text{TT}} = \left[\frac{2}{r} \ddot{\mathcal{I}}_{jk}^{\text{TT}}(t-r) \right]_{,r} \simeq -\frac{2}{r} \ddot{\mathcal{I}}_{jk}^{\text{TT}}(t-r) \quad (2.50)$$

Inserting the result into Eq. (2.48), we obtain the stress-energy tensor in the local wave zone

$$T_{00}^{\text{GW}} = T_{0r}^{\text{GW}} = T_{r0}^{\text{GW}} = T_{rr}^{\text{GW}} = \frac{1}{8\pi r^2} \langle \ddot{\mathcal{I}}_{jk}^{\text{TT}} \ddot{\mathcal{I}}_{jk}^{\text{TT}} \rangle \quad (2.51)$$

Before calculating the total integrated energy radiated into space, one has to care about the TT projection of the mass quadrupole moment. The last equation in terms of the unprojected moment reads

$$T_{0r}^{\text{GW}} = \frac{1}{8\pi r^2} \left\langle \ddot{\mathcal{I}}_{jk} \ddot{\mathcal{I}}_{jk} - 2n_i \ddot{\mathcal{I}}_{ij} \ddot{\mathcal{I}}_{jk} n_k + \frac{1}{2} [n_j \ddot{\mathcal{I}}_{jk} n_k]^2 \right\rangle \quad (2.52)$$

where \vec{n} is the unit radial vector. Now, the latter equation has to be integrated over a sphere centered around the source in order to obtain the total irradiated energy. Therefore, one has to solve the two integrals

$$\begin{aligned} \int d\Omega n_i n_j &= \frac{4\pi}{3} \delta_{ij} \\ \int d\Omega n_i n_j n_k n_l &= \frac{4\pi}{15} (\delta_{ij} \delta_{kl} + \delta_{ik} \delta_{jl} + \delta_{il} \delta_{jk}) \end{aligned} \quad (2.53)$$

which are easily derived by noticing that the left-hand sides are symmetric with respect to index shuffling and invariant under rotations. It follows that the integrated energy loss

due to gravitational wave emission is given by

$$\begin{aligned}\frac{dE}{dt} &= - \int d\Omega r^2 T_{\text{GW}}^{0r} \\ &= -\frac{1}{5} \frac{G}{c^5} \langle \ddot{I}_{jk} \ddot{I}_{jk} \rangle\end{aligned}\tag{2.54}$$

where we have converted the expression to SI units in the last step. Applying the result to our model binary system of [subsection 2.2.3](#), an order of magnitude estimation of the energy loss yields

$$\frac{dE}{dt} \sim -\frac{G}{c^5} (2.8M_{\odot}L^2(2\pi f)^3)^2 \approx -10^{41} \text{ W}\tag{2.55}$$

Again, a more detailed calculation is presented in [Chapter 3](#).

2.3 Detection of Gravitational Waves

2.3.1 Geodesic Deviation

Earth-bound interferometric gravitational-wave detectors typically seek for signals at frequencies around 100 Hz which corresponds to a wavelength $\lambda = 3000$ km. In contrast, the arms of those detectors have a length of a few kilometers. In that case, the interaction of the wave with the detector has a very simple description in terms of the wave-induced geodesic deviation between two optical elements (e.g. between a mirror and a beam splitter). Therefore, consider two freely falling particles A and B at constant distance $L \ll \lambda$ to each other before a gravitational wave comes by. Clinging to particle A, your mathematical investigation is carried out in A's proper reference frame with a flat spacetime metric

$$ds^2 = -c^2 dt^2 + dx^2 + dy^2 + dz^2\tag{2.56}$$

In the proper reference frame of A, a gravitational wave does not change the metric, but instead changes the coordinate position of particle B (be assured, it does change the metric, but these corrections are negligible here ([Misner et al.; 1973](#))). The equation of geodesic deviation determines the spatial position of particle B

$$\frac{d^2 x_{\text{B}}^j}{d\tau^2} = -R^j{}_{0k0} x_{\text{B}}^k\tag{2.57}$$

According to [Eq. \(2.25\)](#), the geodesic deviation in terms of the gravitational-wave amplitude reads

$$\frac{d^2 x_{\text{B}}^j}{dt^2} = \frac{1}{2} \ddot{h}_{jk}^{\text{TT}} x_{\text{B}}^k.\tag{2.58}$$

The change δx_{B}^j of particle B's coordinate due to the wave is much smaller than the initial separation L and we may cast the equation of motion into the form

$$\frac{d^2 \delta x_{\text{B}}^j}{dt^2} = \frac{1}{2} \ddot{h}_{jk}^{\text{TT}} L^k.\tag{2.59}$$

where \vec{L} is the spatial vector with $|\vec{L}| = L$ which points from A to B. In other words, particle B moves by virtue of a gravitational-wave force $1/2m_B\ddot{h}_{jk}^{\text{TT}}L^k$. Integrating the result twice with respect to time t , one obtains

$$\delta x_B^j = \frac{1}{2}h_{jk}^{\text{TT}}L^k. \quad (2.60)$$

Interferometric detectors measure this motion by sending light at frequency ω_0 from A to B and observing its phase shift $2\omega_0\delta x/c$ when it is reflected back to A where it interferes with a reference beam.

2.3.2 Doppler Spacecraft Tracking

The response of Doppler spacecraft tracking to gravitational waves was first described in (Estabrook and Wahlquist; 1975). A light beam is sent to the spacecraft and its Doppler frequency shift contains imprints of gravitational waves which interact with the light. The Doppler shift is observed on Earth where light which is reemitted from the spacecraft is detected. The interaction is described in a TT frame of a plane, +-polarized wave. Then,

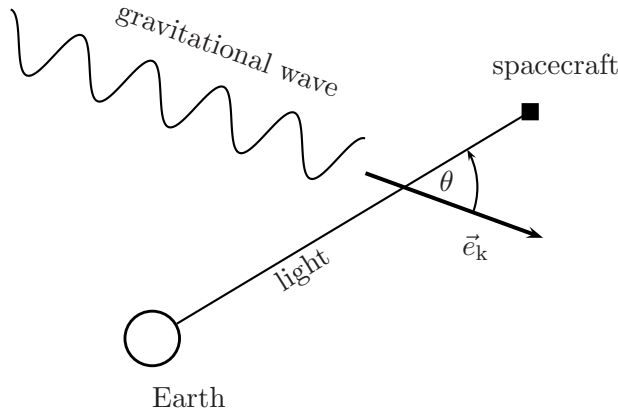


Figure 2.2: The spacecraft is controlled from Earth via Doppler spacecraft tracking. The gravitational wave propagates with an angle θ relative to the optical axis of the tracking system.

the amplitude of the gravitational wave $h \equiv h_+(t-z)$ travelling in z -direction is equivalent to a metric perturbation

$$ds^2 = -dt^2 + (1 + h_+(t-z))dx^2 + (1 - h_+(t-z))dy^2 + dz^2 \quad (2.61)$$

For later use we note that

$$k_1^\mu = (0, 1, 0, 0), \quad k_2^\mu = (0, 0, 1, 0), \quad k_3^\mu = (1, 0, 0, 1) \quad (2.62)$$

are Killing vectors ($k_{(\mu;\nu)} = 0$) of the spacetime in the coordinate basis of Eq. (2.61). The spacecraft and the detector on Earth are freely falling with constant coordinates in the

TT-frame (here, world lines with constant space coordinates are geodesics) and we find the imprints of gravitational waves by calculating a geodesic deviation between the world lines of the Earth and the spacecraft. Placing the optical axis inside the x, z -plane, light with frequency ω_0 leaves Earth along a null vector n_0^μ and is received with frequency ω_1 at the spacecraft coming from direction n_1^μ

$$n_0^\mu = \omega_0(1, (1 - \frac{1}{2}h_0) \sin \theta_0, 0, \cos \theta_0) \quad (2.63)$$

$$n_1^\mu = \omega_1(1, (1 - \frac{1}{2}h_1) \sin \theta_1, 0, \cos \theta_1) \quad (2.64)$$

The null vector n_1^μ at the spacecraft is obtained from a parallel transport of n_0^μ along the photon trajectory. Using the property of Killing vectors the parallel transport equation can be written

$$(n_\alpha k_i^\alpha)_{;\beta} n^\beta = 0 \quad (2.65)$$

which implies that scalar products $n_\alpha k_i^\alpha$ of the null vectors and the Killing vectors are constant. Therefrom, two constraint equations can be deduced which determine the light's frequency at the spacecraft. An analogue calculation leads to similar results for the light's return journey from the spacecraft to Earth

$$\frac{\omega_{\text{sc}}(t + \tau)}{\omega_0} = 1 + \frac{1}{2}(1 + \cos \theta)[h(t) - h(t + (1 - \cos \theta)\tau)] \quad (2.66)$$

$$\frac{\omega_\oplus(t + 2\tau)}{\omega_{\text{sc}}(t + \tau)} = 1 + \frac{1}{2}(1 - \cos \theta)[h(t + (1 - \cos \theta)\tau) - h(t + 2\tau)] \quad (2.67)$$

Multiplying these two equations and neglecting second order terms of the metric perturbation, we obtain the round trip Doppler shift

$$y(t + 2\tau) \equiv \frac{\Delta\omega}{\omega_0} = \frac{1 + \cos \theta}{2}h(t) - \cos \theta \cdot h(t + (1 - \cos \theta)\tau) - \frac{1 - \cos \theta}{2}h(t + 2\tau) \quad (2.68)$$

The one-way travelling time $\tau = L/c$ of the light is assumed to be constant during a measurement. We Fourier transform the Doppler time series and convert it into a phase shift of the detected light

$$\begin{aligned} \Delta\phi(\Omega) &= -\frac{\omega_0}{i\Omega} \cdot y(\Omega) \\ &= -\frac{\omega_0}{i\Omega} \left(\frac{1 + \cos \theta}{2} e^{2i\Omega L/c} - \cos \theta e^{i(1 + \cos \theta)\Omega L/c} - \frac{1 - \cos \theta}{2} \right) \cdot h(\Omega) \end{aligned} \quad (2.69)$$

The bracketed expression is the three-pulse transfer function (a gravitational wave pulse appears at three distinct times in your time series). The long wavelength limit $\Omega L/c \ll 1$ leads to an appropriate description of Earth bound interferometers where the light travels a few kilometers and the detection frequency band is centered around 100Hz. Expanding the exponentials up to first order in $\Omega L/c$, Eq. (2.69) becomes

$$\Delta\phi(\Omega) = -\frac{\omega_0 L}{c} (1 - \cos^2 \theta) [1 + \frac{1}{2} i(\cos \theta + 2)\Omega L/c] h(\Omega) \quad (2.70)$$

which tells you that the signal response increases linearly with the pathlength of the light. The model outlined in this section does not account for arbitrary polarizations of the wave. The necessary discussions are continued in [Chapter 9](#) where a model for a future space-borne gravitational wave detector is investigated in detail.

2.3.3 Matter Wave Interferometry

A first careful study of matter wave interferometry was published by ([Roura et al.; 2004](#)). The article is a corrective response to a previous erroneous investigation of nonrelativistic interferometry (as opposed to light interferometers), which claimed that matter interferometers may have better sensitivity to GW ([Speliotopoulos and Chiao; 2004](#)) and that a comparison of a quantum mechanical and classical approach leads to inconsistencies. We do not want to outline that discussion here. Instead, we briefly present the calculation of the phase shift according to ([Roura et al.; 2004](#)) in TT coordinates and summarize their main results.

The system being investigated constitutes a Michelson matter interferometer with rigid arms enforcing constant physical distance between the end mirrors and the central beam splitter ([Chiao and Speliotopoulos; 2004](#)) which has been called MIGO, the matter interferometer gravitational-wave observatory . The speed of the nonrelativistic particles is denoted by $v \ll c$. At first glance, the TT system is the natural choice of frame especially since the interferometer is supposed to operate at frequencies $f > v/(2L)$ where L denotes the length of one arm (compare with long-wavelength limit applicable to ground-based laser-interferometric GW detectors). However, the end mirrors are not free falling test masses and therefore, their TT coordinates are not preserved. It is easy to show that under the action of a GW the TT coordinates x^i are expressible in terms of constant, so-called rigid coordinates \tilde{x}^i and the time dependent TT-amplitude $h_{ij}(t)$ of the GW

$$x^i(t) = \tilde{x}^i - \frac{1}{2}h^i_j(t)\tilde{x}^j \quad (2.71)$$

Assume that the gravitational wave propagates in positive z direction, whereas the interferometer is confined to the $x - y$ plane. Then, the metric and the equation of motion of the test mass is given according to [subsection 2.1.3](#). The phase shift of a matter wave is deduced from the nonrelativistic action whose TT form is

$$\begin{aligned} S[x^i(t)] &= \int dt (x^i, \dot{x}^i) \\ &= \frac{m}{2} \int dt \left[\frac{dx^i}{dt} \frac{dx_i}{dt} + h_{ij}(t-z) \frac{dx^i}{dt} \frac{dx^j}{dt} - 2 \right] \end{aligned} \quad (2.72)$$

The derivation of the phase shift will be carried out in the geometric optics approximation where the length of the matter de Broglie waves is much shorter than the interferometer arms and the gravitational waves. Under these conditions, one has to solve

$$0 = \partial_t S + (\partial_i S, x^i, h_{ij}(t)) \quad (2.73)$$

with TT Hamiltonian

$$(x^i, p_i) = \frac{1}{2m} (\delta_{ij} - h_{ij}(t-z)) p^i p^j + mc^2 \quad (2.74)$$

and conjugate momenta

$$p_i = m (\delta_{ij} + h_{ij}(t - z)) \dot{x}^i \quad (2.75)$$

The action is expanded in powers of the metric perturbation

$$S(x^i, t) = S_0(x^i, t) + S_1(x^i, t; h_{ij}) + \mathcal{O}(h_{ij}^2) \quad (2.76)$$

furnishing two equations for the first two terms

$$0 = \partial_t S_0 + \frac{1}{2m} (\partial_i S_0) (\partial_j S_0) \delta^{ij} \quad (2.77)$$

$$0 = \partial_t S_1 + \frac{1}{m} (\partial_i S_0) (\partial_j S_1) \delta^{ij} + {}^{(1)}(\partial_i S_0, x^i, h_{ij}(t)) \quad (2.78)$$

The 0th-order solution for a matter wave with energy E whose direction of propagation points along the unit vector \vec{e}_k is given by

$$S_0(x^i, t) = -Et + \frac{\hbar}{\lambda} \vec{e}_k \cdot \vec{x} + \hbar\phi_0 \quad (2.79)$$

The (reduced) length $\lambda \equiv \lambda/(2\pi)$ of the de-Broglie wave depends on the energy E of the particle according to

$$\lambda = \frac{\hbar}{\sqrt{2mE}} \quad (2.80)$$

Defining the total derivative

$$\frac{dS_1}{dt} = \partial_t S_1 + \vec{v} \cdot \nabla S_1 \quad \text{with} \quad \vec{v} = \frac{\hbar}{m\lambda} \vec{e}_k \quad (2.81)$$

the first order solution – after insertion of Eq. (2.79) into Eq. (2.78) – obeys the equation

$$\begin{aligned} \frac{dS_1}{dt} &= - {}^{(1)}\left(\frac{\hbar}{\lambda} \vec{e}_k, x_{(0)}^i, h_{ij}(t)\right) \\ &= \frac{m}{2} h_{ij}(t) \dot{x}_{(0)}^i \dot{x}_{(0)}^j \\ &= \frac{mv^2}{2} h_{ij}(t) e_k^i e_k^j = \frac{\hbar v}{2\lambda} h_{ij}(t) e_k^i e_k^j \end{aligned} \quad (2.82)$$

where, in the last row, the 0th-order trajectory $x_{(0)}^i(t) = x^i + v e_k^i \cdot t$ has been substituted. Now, consider a matter wave propagating a distance L in the $x - y$ plane from position A (i.e. the beam splitter) to position B (i.e. one end mirror). Up to first order in h_{ij} , the wave accumulates a phase shift

$$\Delta\phi(t) = \frac{1}{\hbar} (\Delta S_0(t) + \Delta S_1(t)) \quad (2.83)$$

The lowest and 1st order changes of the action are readily calculated

$$\begin{aligned} \Delta S_0(t) &= S_0(x_B^i, t) - S_0(x_A^i, t - L/v) \\ &= \frac{\hbar L}{\lambda} - \frac{\hbar}{2\lambda} e_k^i [h_{ij}(t) \tilde{x}_B^i - h_{ij}(t - L/v) \tilde{x}_A^i] + E \frac{L}{v} \end{aligned} \quad (2.84)$$

$$\begin{aligned} \Delta S_1(t) &= S_1(x_B^i, t) - S_1(x_A^i, t - L/v) \\ &= \frac{\hbar v}{2\lambda} \int_{t-L/v}^t dt' h_{ij}(t') e_k^i e_k^j \end{aligned} \quad (2.85)$$

As mentioned before, the length of one arm $L = e_k^i(\tilde{x}_B^i - \tilde{x}_A^i)$ is constant. The GW amplitude appears in the lowest order phase shift because of a change of coordinates: We express the mirror positions with their time constant rigid coordinates \tilde{x}^i . The field measured at the output of an equal-arm Michelson interferometer is phase shifted by

$$\begin{aligned} \Delta\phi = & \frac{L}{\lambda}(e_{k_1}^i e_{k_1}^j - e_{k_2}^i e_{k_2}^j)h_{ij}(t - L/v) \\ & - \frac{v}{2\lambda} \int_{t-2L/v}^t dt'(e_{k_1}^i e_{k_1}^j - e_{k_2}^i e_{k_2}^j)h_{ij}(t') \end{aligned} \quad (2.86)$$

where \vec{k}_1, \vec{k}_2 denote the directions of the two arms. Assuming that the GW is monochromatic with frequency Ω , has constant amplitude h and that the wave's polarization tensor is given by $\mathbf{e}^+ = (\vec{e}_{k_1} \otimes \vec{e}_{k_1} - \vec{e}_{k_2} \otimes \vec{e}_{k_2})$ (the arms being perpendicular to each other), then the phase shift can be cast into the form

$$\Delta\phi = h \cdot \left[\frac{2L}{\lambda} - \frac{2v}{\lambda\Omega} \sin\left(\frac{\Omega L}{v}\right) \right] \sin\left(\Omega t + \phi - \frac{\Omega L}{v}\right) \quad (2.87)$$

and ϕ is the phase of the gravitational wave at time $t = 0$. Substituting ω_0 for v/λ we find that the second term inside the square brackets corresponds to the phase shift of light which senses free falling test masses (see Eq. (2.69)). Therefore, the first term arises due to the fact that the physical arm length of the MIGO interferometer is kept constant. In order to compare the sensitivity of laser interferometers to matter interferometers, we investigate the MIGO response to GW at high and low signal frequencies Ω . For frequencies $\Omega \ll v/L$, the phase shift of MIGO becomes $\Delta\phi \rightarrow 0$ and consequently, matter interferometers with rigid arms are inferior to laser interferometers at low frequencies (matter interferometers with suspended optics would have greatest response for $v = c$, as can be seen from Eq. (2.87)). At high frequencies, the first frequency-independent term dominates and one might speculate whether MIGO could have better sensitivity at higher frequencies. Although this may be possible in principle, one has to take into account the different forms of noise which limit the detectors' sensitivity. Presumably, shot noise which is the predominant noise form at high frequencies, is much lower in laser interferometers than in a matter interferometer. The reason is that advanced stages of the laser interferometers are expected to operate with a photon flux around $5 \cdot 10^{22} \text{ s}^{-1}$, which could hardly be furnished by atom sources! Thereby, we conclude that matter wave interferometry still has to overcome many obstacles to be considered as serious alternatives to present laser detectors.

CHAPTER 3

NS/NS Binaries

The amplitude of gravitational waves emitted by a neutron star binary can be calculated by comparatively simple means. The reason is that up to the very last stage before the merger, the stars orbit each other at low speed and that their gravitational fields are weak. Therefore, the orbits are Keplerian, but an energy loss due to gravitational-wave emission causes the orbital separation L to decrease slowly with time.

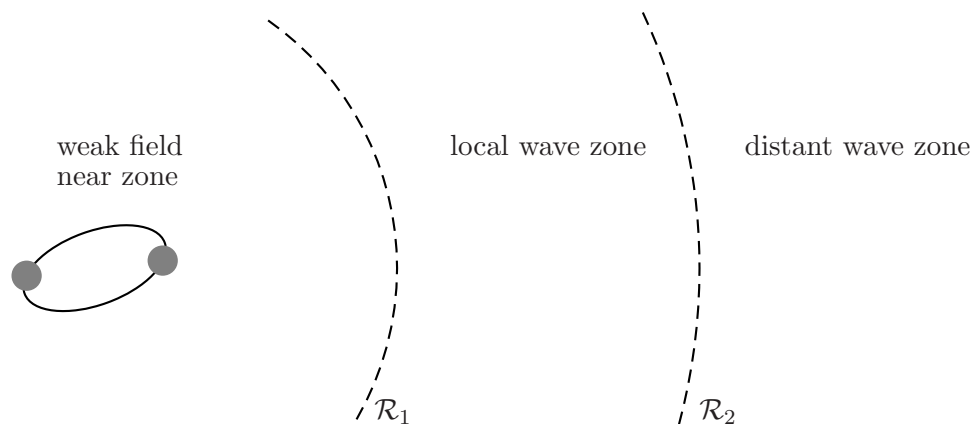


Figure 3.1: Beyond a distance \mathcal{R}_1 from the source, effects like backscattering or redshifting of the waves due to the spacetime curvature caused by the source are negligible. Furthermore, beyond \mathcal{R}_2 the radius of curvature of the wavefronts are much larger than the reduced wavelength λ . However, since the distant wave zone extends to infinity, the propagation of the gravitational waves is affected by the background spacetime (e.g. giving rise to a cosmological redshift).

Typically, the wave solution is calculated for the so-called local wave zone of the source. This region is sufficiently small to constitute a local Lorentz frame with respect to the back-

ground spacetime and sufficiently far away from the source such that dynamical changes of the spacetime curvature can be unambiguously assigned to gravitational waves (see [Figure 3.1](#)). In other words, radially propagating gravitational waves (i.e. being functions of retarded time $t - r$) are generated in the local wave zone and then propagated into the distant wave zone. There, the waves obey the laws of geometric optics (see [subsection 2.2.2](#)). In [section 3.1](#), we calculate the gravitational waves of a neutron star binary in the Newtonian limit.

In [subsection 4.4.1](#), we describe the detection of GW signals by means of matched filtering which requires a collection of waveform templates based on theoretical modelling. The yield of matched filtering crucially depends on an accurate prediction of the phase evolution of GW which are typically recorded over long time periods. The phase evolution is subject to more or less significant relativistic corrections like a spin-orbit coupling or a spin-spin coupling which are recovered by a post-Newtonian expansion of the binary's equation of motion. These effects are briefly discussed in [subsection 3.2.2](#). Post-Newtonian corrections to the amplitude of the GW are predominantly related to the orbit's eccentricity, see [subsection 3.2.1](#), which gives rise to energy being emitted into different modes than the dominant quadrupole GW frequency.

3.1 Newtonian Waveforms

Two stars which orbit each other with angular frequency Ω at distance L to each other are described by a mass quadrupole moment

$$(\mathcal{I}_{ij}) = \mu L^2 \cdot \begin{pmatrix} \cos^2(\Omega t) - \frac{1}{3} & \sin(\Omega t) \cos(\Omega t) & 0 \\ \sin(\Omega t) \cos(\Omega t) & \sin^2(\Omega t) - \frac{1}{3} & 0 \\ 0 & 0 & -\frac{1}{3} \end{pmatrix} \quad (3.1)$$

where μ is the reduced mass of the two stars with masses M_1, M_2

$$\mu = \frac{M_1 M_2}{M_1 + M_2} \quad (3.2)$$

According to [Eq. \(2.46\)](#), the gravitational wave amplitude in TT gauge is governed by the second time derivative of the mass quadrupole moment

$$(h_{ij}^{\text{TT}}) = \frac{G}{c^4} \frac{4}{r} \mu L^2 \Omega^2 \cdot \begin{pmatrix} -\cos(2\Omega t) & -\sin(2\Omega t) & 0 \\ -\sin(2\Omega t) & \cos(2\Omega t) & 0 \\ 0 & 0 & 0 \end{pmatrix} \quad (3.3)$$

The amplitudes h_+ and h_\times are calculated by projecting the TT amplitudes of the latter equation onto the axes $\{\vec{e}_\theta, \vec{e}_\phi\}$, i.e. the angular unit vectors of a spherical coordinate system

$$\begin{aligned} h_+ &= \frac{1}{2} (\vec{e}_\theta \cdot \mathbf{h}^{\text{TT}} \cdot \vec{e}_\theta - \vec{e}_\phi \cdot \mathbf{h}^{\text{TT}} \cdot \vec{e}_\phi) \\ &= \frac{G}{c^4} \frac{2}{r} \mu L^2 \Omega^2 (1 + \cos^2(\theta)) \cos(2\Omega t - 2\phi - \pi) \\ h_\times &= \vec{e}_\theta \cdot \mathbf{h}^{\text{TT}} \cdot \vec{e}_\phi \\ &= \frac{G}{c^4} \frac{4}{r} \mu L^2 \Omega^2 \cos(\theta) \sin(2\Omega t - 2\phi - \pi) \end{aligned} \quad (3.4)$$

where the unit vectors are defined as

$$\begin{aligned}\vec{e}_\theta &= \cos(\theta) \cos(\phi) \vec{e}_x + \cos(\theta) \sin(\phi) \vec{e}_y - \sin(\theta) \vec{e}_z \\ \vec{e}_\phi &= -\sin(\phi) \vec{e}_x + \cos(\phi) \vec{e}_y\end{aligned}\quad (3.5)$$

The Kepler law relates the orbital frequency Ω and the distance L between the two neutron stars

$$\Omega^2 = \frac{G(M_1 + M_2)}{L^3}\quad (3.6)$$

Furthermore, assuming that the binary is oriented perpendicular to the line of sight at $t = 0$, the amplitudes read

$$\begin{aligned}h_+ &= \frac{G}{c^4} \frac{2GM_1M_2}{Lr} (1 + \cos^2(\theta)) \cos(2\Omega t) \\ h_\times &= \frac{G}{c^4} \frac{4GM_1M_2}{Lr} \cos(\theta) \sin(2\Omega t)\end{aligned}\quad (3.7)$$

The binary system radiates energy into space and therefore, the separation L is a slowly decreasing function of time. The inspiral is determined by the radiated power

$$\frac{dL}{dt} = \frac{dE}{dt} \cdot \frac{dL}{dE} = -\frac{L}{E} \cdot \frac{dE}{dt}, \quad E = \frac{1}{2} \frac{GM_1M_2}{L}\quad (3.8)$$

Inserting the mass quadrupole moment into Eq. (2.54), the radiated power averaged over one orbital period is given by

$$\frac{dE}{dt} = -\frac{32}{5} \frac{c^5}{G} \left(\frac{G\mu}{c^2L} \right)^2 \left(\frac{G(M_1 + M_2)}{c^2L} \right)^3\quad (3.9)$$

Inserting Eq. (3.9) into Eq. (3.8) and subsequently applying the Kepler law, the Newtonian evolution of the gravitational-wave frequency $f = \Omega/\pi$ is governed by

$$\frac{df}{dt} = \frac{96}{5} \pi^{8/3} \left(\frac{G\mathcal{M}_c}{c^3} \right)^{5/3} f^{11/3}\quad (3.10)$$

Therefore, the Newtonian frequency evolution depends on a single parameter of the binary system, the so-called chirp mass

$$\mathcal{M}_c = \mu^{3/5} (M_1 + M_2)^{2/5}\quad (3.11)$$

In the following sections, relativistic corrections to the function $f(t)$ are investigated. These issues are of great importance. The accuracy of the predicted phase evolution (i.e. integrated frequency evolution) mainly determines the efficiency of the matched filtering supported detection of gravitational waves (see subsection 4.4.1).

3.2 Corrections to the Newtonian Quadrupole Waveform

In this section, the issue of deriving binary waveform templates by gradually taking into account post-Newtonian corrections, is oriented along the demands of a potential LISA

(Chapter 9) follow-on mission: the Big-Bang Observer (section 4.3). Post-Newtonian corrections are discussed inasmuch their negligence would lead to severe constrictions of the detector’s performance. For the BBO data analysis, a binary template is primarily used to identify and subtract a signal from the data stream. One potential source of subtraction error is inaccurate theoretical template waveforms. Provisionally, we will regard a physical parameter, effect, or post-Newtonian term as “relevant for BBO” if neglecting it would lead to relative errors in our theoretical inspiral waveforms of size $\delta h/h \gtrsim 10^{-3}$ (since errors of that magnitude could dominate over the sought-for inflationary background). Since each inspiral waveform contains $\sim 10^7$ cycles (3 yrs observation time of signals at ~ 0.1 Hz), knowing the waveforms to $\delta h/h \gtrsim 10^{-3}$ requires calculating the waveform phase to roughly one part in 10^{11} !

The post-Newtonian (PN) expansion is clearly the right tool for constructing the waveforms, since the PN expansion parameter $GM/(c^2 r)$ is small in the BBO band:

$$\frac{GM}{c^2 r} \approx 5.5 \times 10^{-4} \left(\frac{M[1+z]}{2.8M_\odot} \right)^{2/3} \left(\frac{f}{0.3 \text{ Hz}} \right)^{2/3}, \quad (3.12)$$

where f is the GW frequency. If one uses PN waveforms, the only reasons for theoretical error would be 1) failure to calculate post-Newtonian corrections to sufficiently high order in the PN expansion, or 2) failure to account for all relevant physical parameters (e.g., the spins of the NSs).

This section provides an initial “scoping out” of the questions of which physical parameters are relevant, and which post-Newtonian order is sufficient. For the sake of simplicity, we use units in which $G = c = 1$. Therefore, everything can be measured in the fundamental unit of seconds: $1 \text{ Mpc} = 1.029 \times 10^{14} \text{ s}$, and $1M_\odot = 4.926 \times 10^{-6} \text{ s}$.

3.2.1 Orbital Eccentricity

Typical eccentricities of binaries in the BBO band

Here we consider the implications of small (but non-zero) eccentricity for the subtraction problem. We begin by estimating typical eccentricities of NS binaries when they are emitting GWs in the BBO band.

It is well known that radiation reaction tends to circularize the orbits of nearly Newtonian binaries. For small eccentricity e , e^2 decreases with the orbital period P according to $e^2 \propto P^{19/9}$ (Peters; 1964). For arbitrary e , the mutual scaling is given by:

$$P^{2/3} \propto \frac{e^{12/19}}{(1-e^2)} \left[1 + \frac{121}{304} e^2 \right]. \quad (3.13)$$

The two known NS-NS binaries that dominate current merger rate estimates are PSR 1913+16 and PSR J0737-3039. Extrapolating from today’s values of e and P for these two binaries, using Eq. (3.13), we estimate that their eccentricities when they pass through the BBO band will be $e_{1913}^2 \approx 4.6 \times 10^{-8} \left(\frac{f}{0.3 \text{ Hz}} \right)^{-19/9}$ and $e_{0737}^2 \approx 2.0 \times 10^{-9} \left(\frac{f}{0.3 \text{ Hz}} \right)^{-19/9}$. Based on these two examples, we will provisionally assume that typical eccentricities are $e^2 \sim [10^{-9} - 10^{-7}] \left(\frac{f}{0.3 \text{ Hz}} \right)^{-19/9}$. However we will also consider the implications of a subpopulation of NS binaries with considerably larger eccentricity.

Effect of non-zero eccentricity on waveform phase

The effect of small, non-zero eccentricity is to slightly increase the inspiral rate; to lowest nontrivial PN order and to first order in e^2 , the increase (derivable from (Peters; 1964)) is given by:

$$\frac{df}{dt} = \left. \frac{df}{dt} \right|_{e=0} \left[1 + \frac{157}{24} e^2 \right] \quad (3.14)$$

In the stationary phase approximation, we can write the Fourier transform of the emitted waveform (omitting tensor indices) as (Cutler and Flanagan; 1994)

$$\tilde{h}(f) \propto (\mathcal{M}_c(1+z))^{5/6} f^{-7/6} [1 + \dots] e^{i\Psi(f)}, \quad (3.15)$$

where “...” stands for higher-order PN corrections, and where the phase $\Psi(f)$ can be written as

$$\Psi(f) = \Psi_0(f) + \Psi_e(f). \quad (3.16)$$

Here $\Psi_0(f)$ represents the zero-eccentricity phase evolution and has the following PN expansion:

$$\begin{aligned} \Psi_0(f) = & \text{const} + 2\pi f t_c + \frac{3}{4} (8\pi \mathcal{M}_c(1+z) f)^{-5/3} \\ & \times \left[1 + \frac{20}{9} \left(\frac{743}{336} + \frac{11\mu}{4M} \right) y - 16\pi y^{3/2} + \dots \right]. \end{aligned} \quad (3.17)$$

with $y \equiv (\pi M(1+z) f)^{2/3}$, while $\Psi_e(f)$ represents the phase correction due to non-zero e^2 , and is given (again, to lowest nontrivial PN order and to first order in e^2) by (Królak et al.; 1995):

$$\Psi_e(f) = -\frac{7065}{187136} [\pi \mathcal{M}_c(1+z)]^{-5/3} e_0^2 f_0^{19/9} f^{-34/9}. \quad (3.18)$$

Here e_0 is the binary’s eccentricity at the moment that the GW frequency (more specifically, the frequency of the dominant, $n = 2$ harmonic) sweeps through some fiducial frequency f_0 . (Note that, by Eq. (3.13), the combination $e_0^2 f_0^{19/9}$ is a constant, to lowest nontrivial order.)

Plugging in fiducial values, we can re-express Eq. (3.18) as

$$\begin{aligned} \Psi_e(f) = & -0.104 \\ & \times \left[\frac{e_{0.3\text{Hz}}^2}{5 \times 10^{-9}} \right] \left[\frac{(1+z)\mathcal{M}_c}{1.22M_\odot} \right]^{-5/3} \left[\frac{f}{0.3\text{Hz}} \right]^{-34/9}. \end{aligned} \quad (3.19)$$

Note the very steep fall-off of $\Psi_e(f)$ with increasing f . This $f^{-34/9}$ fall-off is much steeper than for the other PN correction terms in Eq. (3.17), so it seems quite unlikely that errors in fitting for e_0 could be “absorbed” into compensating errors in the other parameters. While $\Psi_e(f)$ is negligible for frequencies above a few Hz, it is typically of size $\sim 2\pi$ at $f = 0.1$ Hz. Clearly, then, orbital eccentricity is a relevant parameter that must be accounted for, both in subtracting out individual sources and in projecting out residual errors. From Eq. (3.19), we can also estimate roughly how accurately BBO can measure the eccentricity of each binary; it should be possible to determine $e_{0.3\text{Hz}}^2$ to within $\Delta(e_{0.3\text{Hz}}^2) \sim [10^{-8}/\text{SNR}] \sim 10^{-10}$.

Contribution of $n = 3$ radiation to $\Omega_{\text{GW}}^{\text{NSm}}$

Non-zero orbital eccentricity implies that even the quadrupole piece of the gravitational radiation is no longer purely sinusoidal, but exhibits harmonics at all multiples $n\nu$ of the orbital frequency ν (for integers $n \geq 1$). Let \dot{E}_n be the gravitational luminosity due to the n^{th} harmonic. For small e , $\dot{E}_n \propto e^{|2n-4|}$, so in the range of interest for e , only \dot{E}_3 and \dot{E}_1 could potentially be significant. While both \dot{E}_3 and \dot{E}_1 are $\propto e^2$, it is easy to show that the $n = 3$ contribution to $\Omega_{\text{GW}}^{\text{NSm}}$ dominates over the $n = 1$ contribution. Therefore we concentrate here on the $n = 3$ harmonic.

The ratio \dot{E}_3/\dot{E}_2 is (Peters and Mathews; 1963)

$$\dot{E}_3/\dot{E}_2 \approx (3/2)^6 e^2, \quad (3.20)$$

from which one easily derives

$$\begin{aligned} \Omega_{\text{GW}}^{n \geq 3}(f) &= \left(\frac{3}{2}\right)^6 \langle e_{2f/3}^2 \rangle \Omega_{\text{GW}}^{n=2}(2f/3) \\ &= \left(\frac{3}{2}\right)^6 \left(\frac{3}{2}\right)^{13/9} \langle e_f^2 \rangle \Omega_{\text{GW}}^{n=2}(f) \\ &\approx 1.6 \cdot 10^{-19} \left(\frac{n_0}{10^3 \text{ Mpc}^3}\right) \left(\frac{\langle e_{0.3\text{Hz}}^2 \rangle}{10^{-8}}\right) \left(\frac{f}{0.3\text{Hz}}\right)^{-13/9} \end{aligned} \quad (3.21)$$

where $\langle e_{0.3\text{Hz}}^2 \rangle$ is the average value (for all NS-NS mergers) of e^2 at $f = 0.3\text{Hz}$. For our fiducial estimate of $\langle e_{0.3\text{Hz}}^2 \rangle$, this is significantly below the sought-for level of inflation-generated GWs, and so the extra harmonics generated by non-zero e can be neglected.

However, our estimate that $\langle e_{0.3\text{Hz}}^2 \rangle \sim 10^{-8}$ was based on the few known examples of close NS-NS binaries; what if there is a subpopulation of NS-NS binaries that merge with substantially larger eccentricity (e.g., due to the Kozai mechanism (Wen; 2003))? The ratio of the $n = 3$ to the $n = 2$ piece of the waveform, $h^{n=3}/h^{n=2}$, is clearly of order e . Thus the $n = 3$ piece must be subtracted (or projected out) if $e \gtrsim 10^{-3}$. Fortunately, as the previous subsection makes clear, if $e_{0.3\text{Hz}} \gtrsim 10^{-5}$, then the waveform itself will inform us of this fact, via the phase evolution of the $n = 2$ piece.

Unfortunately, to subtract $h^{n=3}$, one needs to know *both* e and the perihelion angle ω (at some fiducial instant or frequency), since the latter clearly determines the relative phase of the $n = 3$ and $n = 2$ pieces. How accurately can $\omega_{0.3\text{Hz}}$ be extracted from the data? Since ω is encoded only in the $n \neq 2$ harmonics, we estimate that $\Delta\omega_{0.3\text{Hz}} \sim \min\{\pi, (e_{0.3\text{Hz}} \times \text{SNR})^{-1}\}$. Hence, while the $h^{n=3}$ piece is relevant for $e_{0.3\text{Hz}} \gtrsim 10^{-3}$, it will be impossible to subtract it when $e_{0.3\text{Hz}} \lesssim 10^{-2}$ (since $\omega_{0.3\text{Hz}}$ will be undetermined). Fortunately, even in this case, $h^{n=3}$ can simply be projected out of the data (in the manner described in Sec. IV.B) since all possible realizations of $h^{n=3}(t)$ lie in a two-dimensional vector space. To see this, note that if all parameters *except* $\omega_{0.3\text{Hz}}$ were known, then one could express $h^{n=3}(t)$ in the form $A_3(t)\cos[3(\Phi_3(t) + \omega_{0.3\text{Hz}})]$, where $A_3(t)$ and $\Phi_3(t)$ are both known functions, and this can be expanded as $\cos[3\omega_{0.3\text{Hz}}] \times A_3(t)\cos[3\Phi_3(t)] - \sin[3\omega_{0.3\text{Hz}}] \times A_3(t)\sin[3\Phi_3(t)]$. I.e., $h^{n=3}(t)$ is just some linear combination of two known waveforms, with (unknown) coefficients $\cos[3\omega_{0.3\text{Hz}}]$ and $\sin[3\omega_{0.3\text{Hz}}]$.

Summary of effects of orbital eccentricity

Extrapolating from the known NS-NS binaries, we have estimated that typical eccentricities for NS-NS binaries radiating in the BBO band will be $e \lesssim 10^{-4}$. At this level, they would have a significant impact on the phase evolution of the $n = 2$ harmonic, but the $n = 3$ and $n = 1$ pieces of the waveform would be negligibly small. In this case, when projecting out residual errors, one need not worry about the perihelion angle ω . On the other hand, if some subpopulation of NS-NS binaries has $e_{0.3\text{Hz}} \gtrsim 10^{-3}$, then this will be completely clear from the data itself. For these binaries, both $e_{0.3\text{Hz}}$ and $\omega_{0.3\text{Hz}}$ are relevant parameters, to be used both in subtraction and in projecting out residual errors. Finally, there are cases when $\omega_{0.3\text{Hz}}$ is relevant but impossible to determine. Fortunately, even in this case, $h^{n=3}$ can simply be projected out, at very modest additional cost in bandwidth.

3.2.2 Spin Effects

We turn now to the effects of the NS spins. Currently there are five known NS-NS binaries in our galaxy that will merge in a Hubble time (four binaries in the disk and one in globular cluster M15). In only one system—PSR J0737—are the spin periods of both NSs known. For PSR J0737, $P_A = 22.7\text{ms}$ and $P_B = 2.77\text{s}$. In the other four systems, the radio-emitting neutron star is also a fast rotator, with P ranging from 28.5 ms to 59.3 ms. The fast rotators all have low spindown rates and so appear to be recycled pulsars. From evolutionary considerations, one expects exactly one of the companions to be rapidly rotating (consistent with what we find for PSR J0737). We estimate the effect of the bodies’ spins on the gravitational waveform, for this presumed-typical case where one NS is rotating relatively rapidly ($P \sim 30\text{ms}$), while the other is slowly rotating ($P \gtrsim 1\text{s}$).

Precession of Orbital Plane

If the NSs are spinning, then the orbital angular momentum vector \vec{L} does not have fixed direction, but instead precesses around the binary’s total angular momentum vector \vec{J} , due to an effective $\vec{L} \times \vec{S}$ coupling. When either 1) the two masses are nearly equal, or 2) the spin of one NS is much greater than the other, then the lowest-order precessional dynamics take an especially simple form – so-called “simple precession” (Apostolatos et al.; 1994). In fact, we expect both these conditions to be satisfied in most NS-NS binaries, since (as mentioned above), we expect only one to be rapidly rotating, and since in those binaries where both NS masses are accurately known, the masses are indeed nearly equal. Therefore we shall use the simple-precession approximation to estimate the magnitude of precessional effects on the waveform.

Following (Apostolatos et al.; 1994), let λ_L be the precession amplitude; i.e., the angle between \vec{J} and \vec{L} . While λ_L depends on the magnitude and direction of the spins, the precession period depends on neither (to a very good approximation). The total number of precessions, from the moment the GW frequency sweeps through f until merger, is (for $M_1 \approx M_2$):

$$N_{\text{prec}} \approx 2.3 \times 10^3 \left(\frac{2.8M_\odot}{M(1+z)} \right) \left(\frac{0.3\text{Hz}}{f} \right). \quad (3.22)$$

It is useful to define dimensionless spin parameters χ_i by $\chi_i \equiv |\vec{S}_i|/M_i^2$. The χ_i are related to the spin periods P_i by

$$\chi_i = 0.036 \left(\frac{I_i}{10^{45} \text{ g cm}^2} \right) \left(\frac{1.4 M_\odot}{M_i} \right) \left(\frac{10 \text{ msec}}{P_i} \right). \quad (3.23)$$

where the I_i are the NS moments of inertia. Label the faster-rotating NS “1”. Assuming $\chi_1 \gg \chi_2$, the precession amplitude is simply

$$\lambda_L \approx 2.3 \times 10^{-4} (1 - \cos^2 \theta_{\text{LS}})^{1/2} \cdot \left(\frac{\chi_1}{0.01} \right) \left(\frac{M(1+z)}{2.8 M_\odot} \right) \left(\frac{f}{0.3 \text{ Hz}} \right)^{1/3}. \quad (3.24)$$

where θ_{LS} is the angle between \vec{L} and \vec{S}_1 . If we ignored spin-orbit precession when subtracting out the NS inspiral waveforms, we would make relative errors $\delta h/h \sim \lambda_L$. This is $\lesssim 10^{-3}$ for $P_1 \gtrsim 10$ ms, and so these errors would typically be benign. In any cases where P_1 is significantly less than 10 ms, this will generally be clear from the data (from its influence on the orbital phase evolution) and these very-high-spin systems would presumably be treated as a “special class”, requiring more parameters to fit them than typically necessary.

Effect of spin-orbit and spin-spin terms on waveform phase

We next consider the effect of the spin-orbit and spin-spin interactions on the waveform phase. Since we have considered the effects of orbital eccentricity and orbital-plane precession in previous subsections, we simplify the analysis here by assuming that the orbit is circular and that the orbital angular momentum vector \vec{L} and the two spin vectors, \vec{S}_1 and \vec{S}_2 , are all aligned. Then in a post-Newtonian expansion of the waveform phase $\Psi(f)$, the lowest order terms involving the spin-orbit and spin-spin interaction are (Vecchio; 2004)

$$\Psi_\beta(f) + \Psi_\sigma(f) = \frac{3}{4} (8\pi \mathcal{M}_c (1+z) f)^{-5/3} \times \left[4\beta y^{3/2} - 10\sigma y^2 \right]. \quad (3.25)$$

where the terms β and γ are explicitly given by

$$\beta \equiv \left(\frac{113}{12} + \frac{25}{4} \frac{M_2}{M_1} \right) (M_1/M)^2 (\hat{L} \cdot \hat{S}_1) \chi_1 + \left(\frac{113}{12} + \frac{25}{4} \frac{M_1}{M_2} \right) (M_2/M)^2 (\hat{L} \cdot \hat{S}_2) \chi_2 \quad (3.26)$$

and

$$\sigma \equiv \frac{\mu}{M} \chi_1 \chi_2 \left(\frac{247}{192} \hat{S}_1 \cdot \hat{S}_2 - \frac{721}{192} (\hat{L} \cdot \hat{S}_1) (\hat{L} \cdot \hat{S}_2) \right). \quad (3.27)$$

Assuming $P_1 \sim 30$ ms and $P_2 \sim 1$ s, this implies $\chi_1 \sim 0.01$ and $\chi_2 \sim 4 \times 10^{-4}$, and then $\beta \sim 0.04$, while $|\sigma| \sim 2.5 \times 10^{-6}$. So plugging in fiducial values (with $M_1 = M_2 = 1.4 M_\odot$),

the spin-related phase terms are

$$\begin{aligned}\Psi_\beta(f) &\sim 6.8 \times 10^1 \left(\frac{\beta}{0.1}\right) \left(\frac{f}{0.3\text{Hz}}\right)^{-2/3} (1+z)^{-2/3} \\ \Psi_\sigma(f) &\sim -4 \times 10^{-4} \left(\frac{\sigma}{10^{-5}}\right) \left(\frac{f}{0.3\text{Hz}}\right)^{-1/3} (1+z)^{-1/3}\end{aligned}\tag{3.28}$$

In summary, the spin-orbit term β is clearly relevant, while spin-spin term σ is negligible for typical cases. Thus, while it takes 6 parameters to describe (initial conditions for) the two spin vectors \vec{S}_1 and \vec{S}_2 , for typical cases the spins' influence on the waveform can be adequately subsumed into a single parameter, β .

3.2.3 High-Order Post-Newtonian Effects, Neglecting Spin

To-date, the post-Newtonian equations governing the inspiral of (quasi-)circular-orbit binaries have been derived through P^{3.5}N order beyond the lowest-order, quadrupole-formula level (Nissanke and Blanchet; 2005). Is that good enough for accurately subtracting out the merger waveforms from the BBO data, or are even higher-order treatments called for? In this subsection, we do a rough estimate that suggests that the P^{3.5}N equations are sufficiently accurate for this purpose (or are at least very close). Since we have considered the effects of spin and orbital eccentricity in previous subsections, for this subsection we will specialize to the case of nonspinning NSs in (quasi-)circular orbits.

We return again to the stationary-phase approximation of the waveform

$$\tilde{h}(f) \propto (\mathcal{M}_c(1+z))^{5/6} f^{-7/6} [1 + \dots] e^{i\Psi(f)}\tag{3.29}$$

and to the PN expansion of the phase $\Psi(f)$:

$$\begin{aligned}\Psi(f) &= \text{const} + 2\pi f t_c + \frac{3}{4} (8\pi \mathcal{M}_c(1+z)f)^{-5/3} \\ &\times \left[1 + \frac{20}{9} \left(\frac{743}{336} + \frac{11\mu}{4M} \right) y - 16\pi y^{3/2} + \dots \right].\end{aligned}\tag{3.30}$$

Terms up through P^{3.5}N have already been calculated. We want to estimate the size of the P⁴N term in the series, which corresponds to a term of the form $\frac{3}{4} (8\pi \mathcal{M}_c(1+z)f)^{-5/3} \times [(C + D(\mu/M) + E(\mu/M)^2 + \dots)y^4]$, for some coefficients C, D, E, \dots . The coefficient C could be derived from the results in (Sasaki and Tagoshi; 2003); we have not done that calculation, but it is clear from (Sasaki and Tagoshi; 2003) that C is of order 10^2 . It seems reasonable to assume that the sum $C + D(\mu/M) + E(\mu/M)^2 + \dots$ is also $\sim 10^2$. The *rest* of the P⁴N term, $\frac{3}{4} (8\pi \mathcal{M}_c(1+z)f)^{-5/3} y^4$, has magnitude

$$4.06 \times 10^{-6} \left(\frac{M(1+z)}{2.8M_\odot} \right) \left(\frac{f}{1\text{Hz}} \right)\tag{3.31}$$

and so the full term is of order 10^{-3} at $f = 1\text{Hz}$.

Thus the P⁴N contribution is just at the border of being relevant. We suspect the full P⁴N term will have been calculated long before BBO flies, but even today one could

generate a “poor man’s” P⁴N waveform by simply omitting the terms involving $D(\mu/M)$, $E(\mu/M)^2$, etc., but including the term $\propto C$, which we repeat is easily derivable from published results. Because $\mu/M \approx 1/4$, the omitted terms could easily be an order of magnitude smaller than the C-term, and so would be truly negligible.

Therefore we believe that already, today, one could produce PN waveforms that are sufficiently accurate for BBO, or that are at least quite close. However we add that if this view turned out to be too optimistic – if it *did* prove difficult to generate sufficiently accurate waveforms, corresponding to realistic solutions of Einstein’s equation—then there is also an obvious fall-back strategy: use an enlarged space of “phenomenological waveforms,” such as those developed by (Buonanno et al.; 2004), to identify and subtract out the inspirals. The family of phenomenological waveforms would depend on a few more parameters than the physical waveforms, so projecting out subtraction errors would cost somewhat more bandwidth, but the estimates in Sec. IV.B show that this cost would still likely be minimal. Therefore as long as *some* member of the phenomenological family lies quite close to each true waveform, meaning $\delta h/h \lesssim 10^{-3}$, the phenomenological family would suffice for the purposes of inspiral-waveform subtraction.

CHAPTER 4

BBO and Signal Analysis

The Big Bang Observer (BBO) is a proposed space-based gravitational wave (GW) mission designed to search for stochastic gravitational-wave background generated in the very early universe (Phinney et al.; 2003; Ungarelli et al.; 2005). The design goal is to be able to detect primordial GWs with energy density $\Omega_{\text{GW}}(f) \gtrsim 10^{-17}$ in the frequency band $10^{-1} \text{ Hz} < f < 1 \text{ Hz}$. Standard, slow-roll inflation predicts $\Omega_{\text{GW}}(f) \lesssim 10^{-16} - 10^{-15}$ (Turner; 1997).

To achieve this sensitivity to a primordial GW background, it will *first* be necessary to subtract from the BBO data stream the GW foreground generated by $\sim 10^5 - 10^6$ neutron star-neutron star (NS-NS), neutron star-black hole (NS-BH), and black hole-black hole (BH-BH) binary mergers, out to $z \sim 5$. This foreground "noise" has an amplitude substantially greater than BBO's instrumental noise, which in turn is probably substantially greater than the amplitude of the sought-for primordial GWs. To achieve BBO's goal, the GWs from the merger foreground must be subtracted to a level well *below* that of the primordial background. This means that the amplitude of the *residual*, post-subtraction foreground must be $\lesssim 10^{-2.5}$ of the pre-subtraction level.

Will it be possible for BBO data analysts to subtract out the binary merger foreground to this accuracy? This question is non-trivial to answer precisely because confusion noise from unresolved mergers can in principle dominate the BBO noise spectrum. To decide which mergers are unresolvable, one needs to know the full BBO noise curve, *including* the level of confusion noise from the unresolvable mergers. But to determine the level of confusion noise, of course one needs to know which mergers are unresolvable. Clearly, one needs somehow to solve both these problems simultaneously.

The focus of our investigations will be on NS-NS mergers, since these are the most problematic for BBO. The less numerous BH-BH and BH-NS merger events will have higher signal-to-noise ratios and therefore should be easier to subtract. If we find the NS-NS mergers can be almost fully subtracted from the BBO data stream, then the same should be true for the BH-BH and BH-NS mergers.

How, in practice, will almost all the NS-NS mergers be subtracted out? We imagine that something like the following iterative scheme could be used: begin by resolving and

subtracting out the brightest merging binaries (i.e., those with highest signal-to-noise-ratio), then resolve and subtract the next brightest ones, etc - regularly updating *all* the parameters of the subtracted binaries, as one goes along, to give the best global fit. Each subtraction decreases the foreground confusion noise and so increases the distance out to which NS binaries can be resolved. Will such a scheme suffice for BBO? The aim of this paper is to answer that question *without actually having to carry out the whole procedure*. We develop a method for determining the likely efficacy of foreground subtraction in a self-consistent manner. Our method is (very roughly) as follows. Imagine that BBO is surrounded by a huge sphere out to some redshift \bar{z} , such that NS-NS mergers inside the sphere (i.e., at redshifts less than \bar{z}) can all be individually resolved and subtracted (using realistic computational power), while none of the sources outside the sphere is resolvable. This redshift \bar{z} marking the boundary of the resolvable sources is not known initially, so we start with a reasonable guess. We then calculate the confusion noise due to all NS-NS mergers (NSm) at redshifts greater than \bar{z} , $S_h^{\text{NSm}, > \bar{z}}(f)$, which we add to the instrumental noise $S_h^{\text{inst}}(f)$ to obtain the total noise:

$$S_h^{\text{tot}}(f) = S_h^{\text{inst}}(f) + S_h^{\text{NSm}, > \bar{z}}(f). \quad (4.1)$$

One can use this total noise level, $S_h^{\text{tot}}(f)$, to improve one's estimate of \bar{z} , and iterate this procedure until \bar{z} converges.

Actually, of course, the detectability of any particular NS-NS binary depends not just on its distance (or redshift), but also on $\mu \equiv \hat{L} \cdot \hat{N}$, where \hat{L} is the normal to the binary's orbital plane and \hat{N} points along our line-of-sight. (The binary's detectability also depends, of course, on the other three angles describing the binary's orientation and position on the sky, but to a much lesser extent.) Our calculation *does* properly account for the μ -dependence of the binary's detectability; i.e, we take \bar{z} to be a function of μ , not a single number.

We stress that there are actually two different sorts of confusion noise associated with merging binaries: the full signals from unresolved binaries (mentioned above), and the small *errors* that inevitably occur when waveforms from resolved mergers are subtracted out of the data. In Sec. IV we propose a method for dealing with these *residual* errors, by projecting out the subspace in which these errors can lie, at the cost of some bandwidth. We also estimate that this fractional decrease in BBO's bandwidth is small enough that for our purpose (deciding whether an iterative subtraction scheme is feasible) it can be neglected.

We remark that our calculation is quite similar in spirit to a recent analysis of WD-binary subtraction in LISA data analysis, by (Cornish and Crowder; 2005). In both cases, the idea is to use the requirement of *self-consistency* to arrive at a unique estimate of the efficacy of foreground subtraction, without actually coding up the whole analysis pipeline and testing it on simulated data.

We also remark that a recent paper (Buonanno et al.; 2005) estimates that supernova explosions *could* provide another important BBO foreground, via the GW memory effect, but only if the anisotropy of neutrino emission is quite high, on average. For the rest of this paper we will neglect the possibility of a large foreground from supernovae.

A gravitational wave signal may be embedded in a much greater instrumental noise spectrum. This means that when analyzing the measured (estimated) spectrum, one is

most probably not able to discern traces from gravitational wave within the noisy data. Therefore, one has to apply clever data analysis schemes which discriminate signal from noise. One finds that the optimal data analysis scheme for signals with known waveform is to let the data stream pass a Wiener filter which correlates the detector output with a so-called template of the expected signal. In [Chapter 3](#), we saw how such templates look like for NS/NS binaries.

The main results of this chapter were published in ([Cutler and Harms; 2006](#)). At first, we are going to introduce the fundamental quantities of data analysis in the time domain ([section 4.1](#)) and in the frequency domain ([section 4.2](#)) and how to estimate them from a data record which consists of N samples.

In [section 4.3](#) we give a brief overview of the BBO mission, its design sensitivity, and the foreground produced by merging NS binaries. In [section 4.4](#) we briefly explain *why* the most distant NS-NS binaries are effectively a noise source when it comes to resolving more nearby ones. In [section 4.5](#) we summarize our proposed strategy of dealing with any residual subtraction errors by projecting them out.

In [section 4.6](#) we take a first cut at estimating ρ_{th} , which we assume will be set by the then-available computational power. This task requires estimates regarding the importance of eccentricity, NS spin, and high-order post-Newtonian (PN) effects in correctly subtracting out the resolved mergers which have already been provided in [section 3.2](#). Our equations for self-consistently determining the efficacy of foreground subtraction are developed in [section 4.7](#). We solve these equations for a variety of assumptions regarding the NS merger rate, the detection threshold ρ_{th} , and BBO's instrumental noise level, and display the solutions in [section 4.8](#).

For concreteness, we assume the universe corresponds to a flat Friedmann-Robertson-Walker model, with the universe's matter and vacuum energy densities being given by $\Omega_{\text{m}} = 0.33$ and $\Omega_{\Lambda} = 0.67$, respectively. Our fiducial value for the Hubble constant is $H_0 = 70 \text{ km s}^{-1} \text{ Mpc}^{-1}$.

4.1 Estimations in the Time Domain

Noisy observational data is a realization of a stochastic process with a (time dependent) probability distribution. In general, one seeks for certain components of the data stream which belong to a signal. Due to noise we can never be 100% sure that a signal is observed, but if we know the probability distribution of the noise then it is possible to claim with a certain confidence whether a signal is present or not. Let us consider the simple case of stationary noise. Stationary random processes do not change their statistical properties over time. We say that a random process $\{X(t)\}$ is stationary if the joint probability distribution of $\{X(t_1 + \tau), X(t_2 + \tau), \dots, X(t_N + \tau)\}$ is identical to the distribution of $\{X(t_1), X(t_2), \dots, X(t_N)\}$. Sometimes people say that a system with stationary noise is in statistical equilibrium. Now, we would like to infer the parameters of those distributions based on observational data with N samples ([Figure 4.1](#)). If the process were stationary Gaussian, then we would like to estimate its mean μ and its variance σ^2 (the probability distribution of a stationary Gaussian process is determined by two time independent parameters). In other words, based on a certain realization $\vec{x} = (x_1, x_2, \dots, x_N)$ of a random

process $\{X(t)\}$, one writes down the joint probability density function (pdf) $p(\vec{x}, \theta_i)$ which has a known form, but which depends on unknown parameters θ_i and then tries to find the most plausible values for these parameters. For this purpose, one estimates fundamental quantities like the mean, variance and autocovariance or higher order noise moments of the pdf. At this point we should emphasize that we consider purely stationary processes, which implies that the data stream does not contain any (time dependent) signal. The estimation of signal parameters is discussed in [section 4.5](#). Let us begin with the estimation $\hat{\mu}$ of the mean μ of a probability distribution. By intuition, one would propose the sample mean to be an appropriate estimate

$$\hat{\mu} = \frac{1}{N} \sum_{n=1}^N X(t_n) \quad (4.2)$$

Since $\hat{\mu}$ is defined in terms of random variables, it is a random variable by itself with its own expectation value and variance. There are several very natural demands which we impose on estimates of a parameter θ ([Priestley; 2001](#))

- (Asymptotically) unbiased: $\lim_{N \rightarrow \infty} \langle \hat{\theta} \rangle = \theta$.
- Mean square error criterion: The mean square error $M^2(\hat{\theta}) = \langle (\hat{\theta} - \theta)^2 \rangle = \text{var}(\hat{\theta}) + \langle (\hat{\theta}) - \theta \rangle^2$ should be as small as possible.
- Consistency: The larger the sample size N , the better the estimator. In mathematical terms: given $\epsilon, \eta > 0$, $\exists N_0$ such that probability $p(|\hat{\theta} - \theta| < \epsilon) > 1 - \eta$, $\forall N \geq N_0$.
- Sufficiency: Apart from the estimator, there exists no other function of the samples which improves our knowledge of the parameter. The conditional probability $p(X_1, \dots, X_N | \hat{\theta})$ is independent of θ .

If one unbiased estimate has a lower mean square error than another unbiased estimator, then we say that the former one is more efficient than the latter. In that case, the estimator's variance is the distinguishing property. There exists a lower bound for the variance of estimates. If that boundary is assumed, then we call the estimator fully efficient. Also notice that an asymptotically ($N \rightarrow \infty$) vanishing variance of an (asymptotically) unbiased estimator implies consistency. We return to the estimator $\hat{\mu}$ of the mean. It is easy to show that it is unbiased

$$\langle \hat{\mu} \rangle = \frac{1}{N} \sum_{n=1}^N \langle X(t_n) \rangle = \frac{1}{N} \cdot N\mu = \mu \quad (4.3)$$

Furthermore, it can be proved that the sample mean $\hat{\mu}$ is a consistent estimator. However, this requires the introduction of the spectral density $S(\omega)$ which we will not meet before the next section:

$$\lim_{N \rightarrow \infty} \text{var}(\hat{\mu}) = \lim_{N \rightarrow \infty} \frac{2\pi}{N} S(0) = 0. \quad (4.4)$$

At next, we present estimators for the autocovariance $R(\tau) \equiv \text{cov}(X(t), X(t+\tau))$ between two random variables with the same probability distribution. The estimators may be

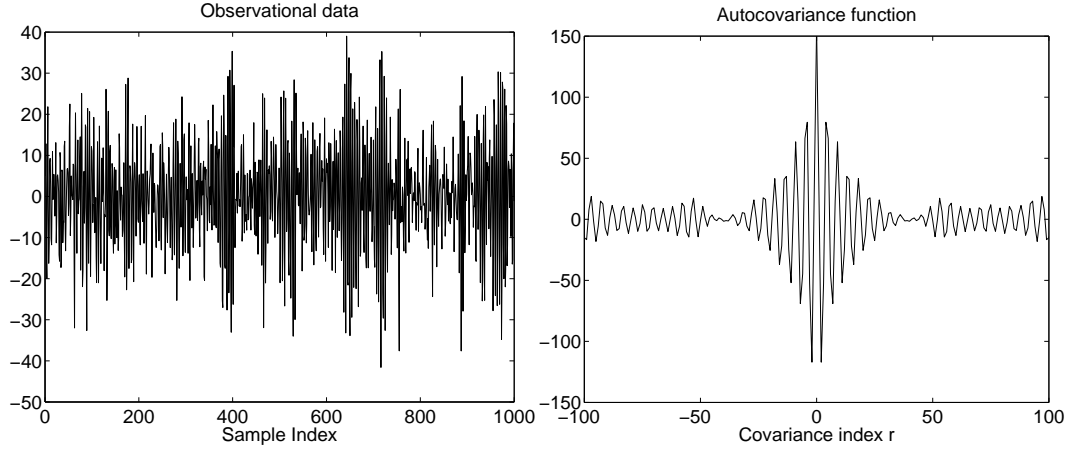


Figure 4.1: The left graph shows observational data from a second order autoregressive process. The record consists of $N = 1000$ samples. Such noise can be found in LC-circuits in statistical equilibrium subject to purely random (white noise) excitations. Its autocovariance was estimated using Eq. (4.7). It is nonzero for relatively high values of $|r|$ and it oscillates around zero. Both features indicate periodicity of the system.

written in terms of the mean μ or its estimator $\hat{\mu}$. Here, the latter case is considered and a short investigation of its biasedness succeeds. The first estimator is

$$\hat{R}^a(r) = \frac{1}{N - |r|} \sum_{n=1}^{N-|r|} (X(t_n) - \hat{\mu})(X(t_{n+|r|}) - \hat{\mu}) \quad (4.5)$$

Each value $\hat{R}^a(r)$ is obtained by averaging upon $N - |r|$ pairs of variables. Consequently, the estimate is worse for larger $|r|$. The estimator is constructed such that the known property $R(r) = R(-r)$ for real valued processes is preserved. The estimator is biased due to the variance of the estimator $\hat{\mu}$

$$\begin{aligned} \langle \hat{R}^a(r) \rangle &= \frac{1}{N - |r|} \sum_{n=1}^{N-|r|} \langle (X(t_n) - \hat{\mu})(X(t_{n+|r|}) - \hat{\mu}) \rangle \\ &= \frac{1}{N - |r|} \sum_{n=1}^{N-|r|} R(r) - \text{var}(\hat{\mu}) \\ &= R(r) - \text{var}(\hat{\mu}) \end{aligned} \quad (4.6)$$

If we had prior knowledge of the mean, then the estimator $\hat{R}^a(r)$ would be unbiased. From Eq. (4.4) we know that in any case the estimator is asymptotically unbiased. Another asymptotically unbiased estimate is found to be

$$\hat{R}^b(r) = \frac{1}{N} \sum_{n=1}^{N-|r|} (X(t_n) - \hat{\mu})(X(t_{n+|r|}) - \hat{\mu}) \quad (4.7)$$

whose bias for each N is larger than the bias of $\hat{R}^a(r)$ which depends on the number $|r|$

$$\langle \hat{R}^b(r) \rangle = R(r) - \left[\frac{|r|}{N} \cdot R(r) + \left(1 - \frac{|r|}{N} \right) \text{var}(\hat{\mu}) \right] \quad (4.8)$$

Interestingly though, people prefer to choose the second estimator. The reason is that its variance $\text{var}(\hat{R}^b(r))$ is smaller. In addition, it has been shown that for a particular random process, the mean square error $M(\hat{R}^b(r))$ is smaller than $M(\hat{R}^a(r))$ for $|r| > 0$ (reference given in (Priestley; 2001)).

Imagine that the N samples $X(t_n)$ are recorded within a time T , e.g. $0 \leq t_n \leq T$. Assume further that the sampling frequency is constant

$$f_s \equiv \frac{1}{\Delta t} = \frac{N-1}{T} \quad (4.9)$$

Then increasing the total number of samples while keeping the observation time T constant, the covariance estimation $\hat{R}^b(r)$ possesses an integral approximation

$$\hat{R}(\tau) = \frac{1}{T} \int_0^{T-|\tau|} dt X(t)X(t+|\tau|) \quad (4.10)$$

where $X(t)$ has zero mean. For infinitely large observation time T the integral estimator yields the autocovariance of the random process $X(t)$

$$R(\tau) = \lim_{T \rightarrow \infty} \frac{1}{T} \int_{-T/2}^{T/2} dt X(t)X(t+|\tau|) \quad (4.11)$$

4.2 Spectral Analysis

The investigation of harmonic processes or the spectral analysis of a random process requires the estimation of quantities which are related to the measured energy or power at a specific frequency. Most of the theoretical work is spent on stationary random processes which do not possess a Fourier transform (i.e. stationary noise never dies out). However, there exists a well-defined spectral representation for stationary noise: the power spectral density $S(\omega)$. The estimate $\hat{S}(\omega)$ of the spectral density is called the periodogram whose most important features are governed by the observation time T and the sampling frequency $f_s = 1/\Delta t$ (assuming constant sampling frequency). In subsection 4.2.1, we introduce the double-sided periodogram (i.e. defined for positive and negative frequencies). Its expectation value is given for a data record which contains white noise and harmonic signals. In subsection 4.2.2, we briefly discuss the application of windows which reduce the mean-square error of spectral estimates derived from the covariance estimate of the respective process. Finally, in subsection 4.2.3, the continuous parameter limit ($\Delta t \rightarrow 0$) of the periodogram is derived and we also find a suitable definition of the spectral density for infinite observation time ($T \rightarrow \infty$) in terms of the δ -distribution.

4.2.1 The Periodogram

This section closely follows (Priestley; 2001). However, here the periodogram is explicitly defined in terms of the sampling interval Δt and the observation time T and normalized in order to furnish an estimate of the power spectrum. The meaningfulness of the normalization factor becomes obvious as soon as the continuous parameter, infinite observation time limit is carried out (see subsection 4.2.3).

At first, we define the discrete Fourier transform of a continuous random process $X(t)$ based on N data points measured with fixed period $t_{n+1} - t_n = \Delta t$

$$\tilde{X}_N(\omega) = \sum_{n=1}^N X(t_n) e^{i\omega t_n} \Delta t, \quad \text{with} \quad -\frac{\pi}{\Delta t} \leq \omega \leq \frac{\pi}{\Delta t} \quad (4.12)$$

Discrete sampling of a continuous parameter process $X(t)$ gives rise to the so-called alias effect. It can be shown that the discrete Fourier transform $\tilde{X}_N(\omega)$ depends on all amplitudes $\tilde{X}(\omega + 2\pi f_s \cdot k)$ with $k \in \mathbb{Z}$, $f_s \equiv 1/\Delta t$ which – under general conditions – forces data analysts to give up their interpretation of the periodogram as a simple representation of a physical frequency space. We say that any frequency $\omega + 2\pi f_s \cdot k$, $k \neq 0$ has the alias ω inside the interval $[-\pi/\Delta t; \pi/\Delta t]$. In this context, one often calls $\omega_s = 2\pi f_s$ the Nyquist frequency. Since we cannot distinguish between the two functions $\exp(i\omega t)$ and $\exp(i(\omega + \omega_s \cdot k)t)$, there is no way to define periodograms beyond the frequency interval $[-\omega_s/2; \omega_s/2]$ and therefore, we impose the condition $|\omega| < \pi/\Delta t$ on the frequencies in Eq. (4.12). Since the aliasing effect at first place occurs for constant sampling frequencies f_s (periodic sampling), one may find an alias free sampling by varying the sampling step size in a certain manner (Shapiro and Silverman; 1960). Alternatively, contributions $\tilde{X}(\omega + 2\pi f_s \cdot k)$ from higher frequencies may be suppressed by applying the windowing technic which is briefly described in the next section. Nonetheless, many physical processes are characterized by decreasing amplitudes $\tilde{X}(\omega)$ for increasing frequency. Provided with such prior knowledge, a well-chosen sampling frequency may allow us to neglect the alias effect.

Now, the double-sided periodogram – i.e. defined for positive and negative frequencies – is given by

$$\hat{S}(\omega) = \frac{1}{T} |\tilde{X}_N(\omega)|^2 \quad (4.13)$$

or in terms of the (biased) covariance estimate $\hat{R}(s)$ of stationary random processes as defined in Eq. (4.7), one obtains

$$\hat{S}(\omega) = \sum_{s=-(N-1)}^{N-1} \hat{R}(s) \cos(\omega \Delta t \cdot s) \Delta t \quad (4.14)$$

which reflects the Wiener-Khintchine theorem for discrete monitoring.

Now, consider a specific noisy process $X(t)$ containing K harmonic components with amplitudes A_i , angular frequencies $|\omega_i| < \pi/\Delta t$ and phases ϕ_i

$$X(t_n) = \sum_{i=1}^K A_i \cos(\omega_i t_n + \phi_i) + \epsilon(t_n) \quad (4.15)$$

where $\epsilon(t_n)$ is a purely random process (a Gaussian, Markovian process with zero relaxation time, see [subsection 4.2.3](#))

$$\begin{aligned}\langle \epsilon(t) \rangle &= 0 \\ \text{cov}(\epsilon(t), \epsilon(t + \tau)) &= \sigma_\epsilon^2 \delta_{\tau,0}\end{aligned}\tag{4.16}$$

Taking the expectation value of the periodogram and averaging over the phases ϕ_i ($p(\phi_i) = 1/(2\pi)$) of the harmonic components, we find

$$\langle \hat{S}(\omega) \rangle = \sigma_\epsilon^2 \Delta t + \frac{\Delta t^2}{4T} \sum_{i=1}^K A_i^2 \left\{ \frac{\sin^2(\frac{1}{2}T(\omega + \omega_i))}{\sin^2(\frac{1}{2}(\omega + \omega_i)\Delta t)} + \frac{\sin^2(\frac{1}{2}T(\omega - \omega_i))}{\sin^2(\frac{1}{2}(\omega - \omega_i)\Delta t)} \right\}\tag{4.17}$$

If the frequency ω_i of a harmonic component lies midway between two adjacent frequencies $\omega_p = (2\pi/T) \cdot p$ with $p \in \mathbb{Z}$, then the maximum value of the periodogram ordinate is less by a factor $4/\pi^2$ compared to its maximum value when $\omega_i = \omega_p$.

An important property of the periodogram is revealed when we examine its covariance in frequency space. Consider a purely random process $X(t) = \epsilon(t)$ (see Eq. (4.16)). The covariance of its periodogram ordinates reads

$$\text{cov}\{\hat{S}(\omega_1), \hat{S}(\omega_2)\} = \frac{\kappa_4}{T} \Delta t^3 + \frac{\sigma_X^4}{T^2} \Delta t^4 \left[\frac{\sin^2(\frac{1}{2}T(\omega_1 + \omega_2))}{\sin^2(\frac{1}{2}(\omega_1 + \omega_2)\Delta t)} + \frac{\sin^2(\frac{1}{2}T(\omega_1 - \omega_2))}{\sin^2(\frac{1}{2}(\omega_1 - \omega_2)\Delta t)} \right]\tag{4.18}$$

The fourth cumulant $\kappa_4 = \langle X^4 \rangle - 3\sigma_X^4$ vanishes if $X(t)$ is Gaussian. The variance can be readily deduced

$$\text{var}\{\hat{S}(\omega)\} = \Delta t^2 \cdot \begin{cases} \sigma_X^4 + \frac{\kappa_4}{T} \Delta t + \mathcal{O}(\Delta t^2/T^2) & \text{if } \omega \neq 0, \pm\pi/\Delta t, \\ 2\sigma_X^4 + \frac{\kappa_4}{T} \Delta t & \text{if } \omega = 0, \pm\pi/\Delta t \end{cases}\tag{4.19}$$

The covariance and variance can be made arbitrarily small by increasing the sampling frequency $f_s = 1/\Delta t$ which is a highly appreciated property of the periodogram for purely random processes. Especially in the continuous sampling limit $\Delta t \rightarrow 0$, the fact that spectral ordinates are uncorrelated lays the foundation of powerful concepts like distinguishing between linear and non-linear physical evolutions (see [Chapter 5](#) and [Chapter 6](#)). The influence of the observation time T and the sampling interval Δt on the periodogram is shown in [Figure 4.2](#).

4.2.2 Covariance Time-Lag and Spectral Windows

As pointed out by ([Priestley; 2001](#)), the periodogram is an inconsistent estimate of the power spectral density which, here, means that the variance of the estimate does not tend to zero when the number N of samples is increased. By virtue of Wiener-Khinchine, the variance of \hat{S} is determined by the variance of \hat{R} . Without proof we claim that the variance of the biased covariance estimate decreases with sample size $N = \Delta t/T + 1$ according to

$$\text{var}(\hat{R}(s)) \sim \mathcal{O}(1/N)\tag{4.20}$$

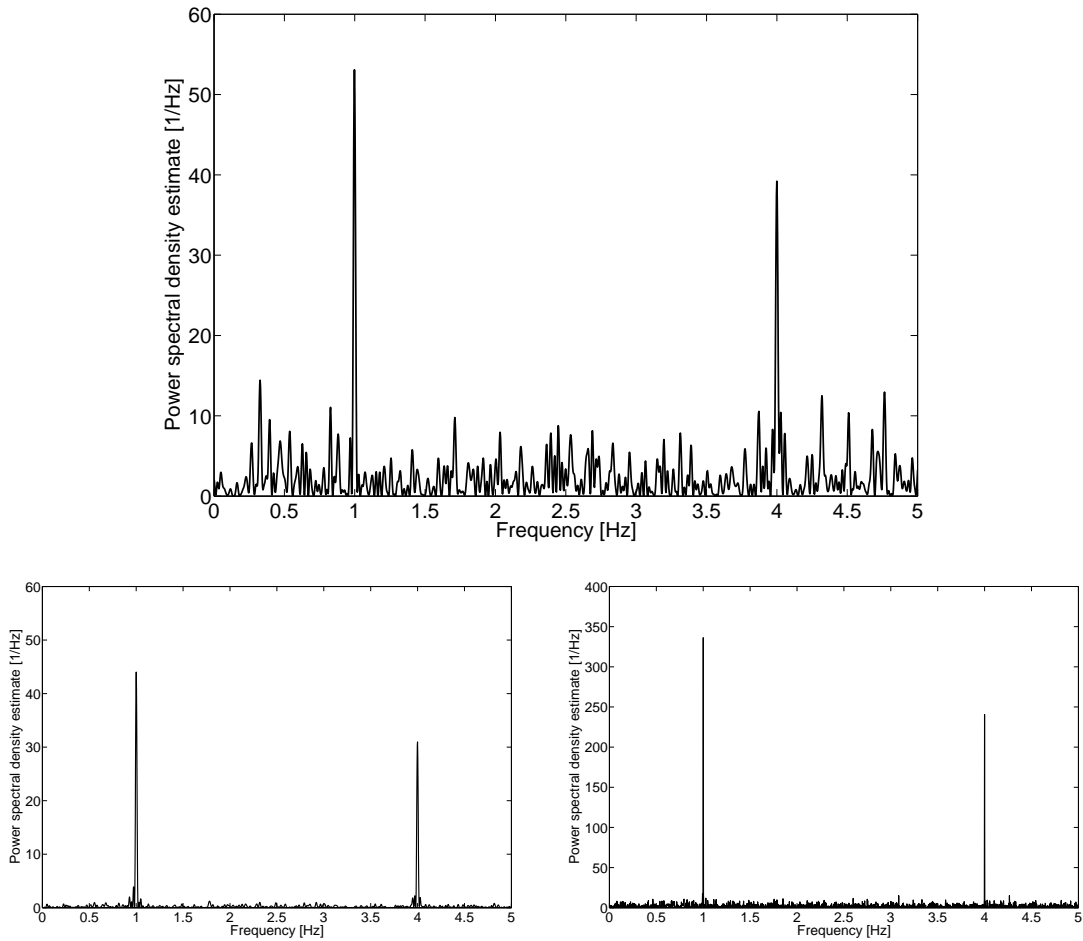


Figure 4.2: The **upper** figure displays the periodogram of a (dimensionless) purely random process $\sigma_\epsilon^2 = 20$ with harmonic components at $f_1 = 1$ Hz and $f_2 = 4$ Hz and amplitudes $A_1 = 1.3$ and $A_2 = 1.1$. The process is observed for $T = 50$ s and sampled with $f_s = 20$ Hz. The noise contributes the spiky ground equally at all frequencies (white noise). The **lower left** figure shows the periodogram of the same random process (another realization though), sampled with $f_s = 200$ Hz. The maximum peak height of the harmonic components is slightly decreased. However, the important difference is that the noise ground is weakened considerably. The **lower right** figure shows the periodogram for a third realization of the random process observed for $T = 500$ s and sampled with $f_s = 20$ Hz. The noise floor appears to be smaller which is merely a consequence of the change of scale of the ordinates. In fact, the variance of the periodogram is the same than in the upper figure. It is the maximum peak height of the harmonic components which is increased. All those phenomenological observations are in agreement with Eq. (4.17) and Eq. (4.19).

which holds for all s . In contrast, the variance of the unbiased covariance estimate crucially depends on s , i.e. the variance increases with increasing s . Clearly, investigating the consistency of \hat{S} , one has to take into account the correlation between the covariance estimates summed up in Eq. (4.14). Nevertheless, it turns out that the Wiener-Khinchine theorem which sums N autocovariance estimates with the property Eq. (4.20) yields a quantity which has variance of order $\mathcal{O}(1)$. Consequently, the periodogram is an inconsistent estimate of the power spectral density S .

One obvious way out of this dilemma is to reduce the number of summed covariance estimates in Eq. (4.14). A weight function λ governs the relative contribution of each covariance estimate:

$$\hat{S}_\lambda(\omega) = \sum_{s=-(N-1)}^{N-1} \lambda(s) \hat{R}(s) \cos(\omega \Delta t \cdot s) \Delta t \quad (4.21)$$

Processes with continuous spectrum (i.e. no harmonic components), share the property $R(s) \rightarrow 0$ for $|s| \rightarrow \infty$. It follows that the weight function, also known as the covariance time-lag window, should be chosen such that it reduces the weight of large s contributions in order to maintain an acceptable bias which is usually increased through the application of windows. The simplest time-lag window assumes the form

$$\lambda(s) = \begin{cases} 1, & |s| \leq M \\ 0, & |s| > M \end{cases} \quad (4.22)$$

where M denotes a cutoff index (e.g. $M = \sqrt{N}$). In that way, the spectral estimate $\hat{S}_\lambda(\omega)$ becomes a consistent estimate of the power spectral density. To any lag window λ we may associate its spectral counterpart, or spectral window $W(\omega)$

$$W(\omega) = \sum_{s=-(N-1)}^{N-1} \lambda(s) \cos(\omega \Delta t \cdot s) \Delta t \quad (4.23)$$

which is then applied as kernel to the inconsistent spectral estimate

$$\hat{S}_W(\omega) = \frac{1}{2\pi} \int_{-\pi/\Delta t}^{\pi/\Delta t} d\omega' \hat{S}(\omega') W(\omega - \omega') \quad (4.24)$$

The spectral window yields the same estimate than the lag window: $\hat{S}_\lambda = \hat{S}_W$. The spectral definition of windows provides a useful tool towards a deeper understanding of the action of windows. The spectrum D_M of the truncating window Eq. (4.22) is known as the Dirichlet kernel

$$D_M(\omega) = \frac{\sin((T_M + \Delta t/2)\omega)}{\sin(\omega \Delta t/2)} \Delta t, \quad \text{with } T_M \equiv M \Delta t \quad (4.25)$$

As shown in Figure 4.3, the spectral window D_M describes a function which, when applied according to Eq. (4.24), effectively averages the inconsistent estimate \hat{S} over the linewidth

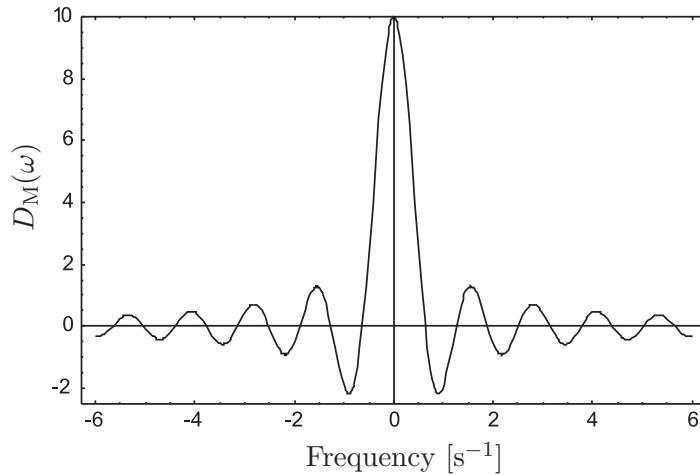


Figure 4.3: The graph shows the Dirichlet kernel in the continuous sampling limit $\Delta t \rightarrow 0$ for a truncation time $T_M = 5$ s. Focussing on the zeroth order maximum, the window effectively averages the estimate \hat{S} over the linewidth $\sim \pi/T_M$ of the kernel.

$\sim \pi/T_M$ of the zeroth order maximum.

The truncating window yields a spectral estimate which assumes negative values for certain frequency intervals. This odd feature can be eliminated by choosing another window function which drops smoothly in contrast to the truncating lag window. The Bartlett window

$$\lambda(s) = \begin{cases} 1 - |s|/M, & |s| \leq M \\ 0, & |s| > M \end{cases} \quad (4.26)$$

is described by the Fejer kernel in the frequency domain and leads to strictly nonnegative estimates of the power spectral density

$$F_M(\omega) = \frac{1}{T_M} \frac{\sin^2(T_M\omega/2)}{\sin^2(\omega\Delta t/2)} \Delta t^2 \quad (4.27)$$

Literature names many more windows (e.g. Daniell, Parzen, Tukey, ...) which are all optimized in the one or the other way, especially with regard to the mean error criterion of the spectral estimate \hat{S}_λ (see [section 4.1](#)).

4.2.3 Power Spectral Density

In this section, we are going to investigate the continuous monitoring $\Delta t \rightarrow 0$, infinite observation time $T \rightarrow \infty$ limits of the formulas presented in [subsection 4.2.1](#). Although a clean definition of the $T \rightarrow \infty$ limit of the discrete Fourier transform cannot be provided for stationary random processes since its very existence requires the time-domain function to "die out" at infinity, we claim that the sufficient condition of absolute integrability of

$X(t)$ is satisfied in all conceivable physical measurements. In that sense, the problem of deriving the mentioned limits of the power spectral density is a mere problem of satisfying purely mathematical needs which can be resolved by the introduction of the δ -distribution. Alternatively, a frequency-space representation of stationary processes exists in terms of its Fourier-Stieltjes integral which is defined and applied in (Priestley; 2001).

If the observation period spans the interval $[-T/2; T/2]$, then it should be obvious that carrying out the limits $T = (N - 1)\Delta t \rightarrow \infty$ together with $\Delta t \rightarrow 0$ in Eq. (4.12) yields the familiar continuous parameter Fourier transform $\tilde{X}(\omega)$ (provided the limit exists). Even if it is the case that the Fourier transform cannot be calculated, then the power spectral density may still be well defined. At first, we write down the continuous time limit $\Delta t \rightarrow 0$ of Eq. (4.17):

$$S_T(\omega) = \frac{T}{4} \sum_{i=1}^K A_i^2 \left\{ \frac{\sin^2(\frac{1}{2}T(\omega + \omega_i))}{(\frac{1}{2}T(\omega + \omega_i))^2} + \frac{\sin^2(\frac{1}{2}T(\omega - \omega_i))}{(\frac{1}{2}T(\omega - \omega_i))^2} \right\} \quad (4.28)$$

Contributions from the purely random process have vanished. The remaining function describes groups of peaks flanked by lower-amplitude side peaks which are centered around the frequencies $\pm\omega_i$. A subsequent infinite measurement time limit $T \rightarrow \infty$ is a little harder to obtain. Obviously, the peak height increases with increasing T . Simultaneously, the peak width is decreasing. In other words, the function turns into a δ -distribution. In order to find the right normalization factor of the limit, one exploits the well-known property of the δ -distribution that its integral has value one. Together with

$$\int dx \frac{\sin^2 x}{x^2} = \pi, \quad (4.29)$$

it follows that the infinite observation time limit $T \rightarrow \infty$ of Eq. (4.28) can be cast into the form (Schulz; 1993)

$$\lim_{T \rightarrow \infty} S_T(\omega) = 2\pi \sum_{i=1}^K \frac{A_i^2}{4} \{ \delta(\omega + \omega_i) + \delta(\omega - \omega_i) \} \quad (4.30)$$

which corresponds to the double-sided power spectral density of a purely random process with harmonic components. The single-sided spectral density (i.e. restricted to positive frequencies ω) acquires an additional factor 2 on the right-hand side. We emphasize again that the limits were evaluated for the expectation value of the periodogram and not for the periodogram itself. In fact, since the periodogram is not a consistent estimate of the power spectral density (see subsection 4.2.2), the usefulness of the corresponding limits of the periodogram is doubtful.

It is not a generic feature of the limits Eq. (4.28) and Eq. (4.30) to be devoid of contributions from noise. For instance, the purely random (Gaussian) process is one member of the family of Gaussian, Markov random processes whose covariance function is commonly written

$$R(\tau) = \sigma_\epsilon^2 e^{-|\tau|/\tau_\tau} \quad (4.31)$$

where τ_r is called the relaxation time of the process. By means of the Wiener-Khintchine theorem, one obtains the corresponding (double-sided) noise power spectral density

$$S(\omega) = 2 \int_0^{\infty} d\tau R(\tau) \cos\left(\frac{\omega\tau}{c}\right) = \frac{2\sigma_\epsilon^2 \tau_r}{1 + \omega^2 \tau_r^2} \quad (4.32)$$

Comparing Eq. (4.31) with Eq. (4.16), we see that the purely random process has relaxation time $\tau_r = 0$ and consequently, its power spectral density Eq. (4.32) vanishes in agreement with the continuous monitoring (and infinite observation time) limit of Eq. (4.17).

4.3 Overview of BBO and the NS-Binary Background

4.3.1 The Big Bang Observer

BBO is essentially a follow-on mission to LISA, the planned Laser Interferometer Space Antenna (LISA study teams; 2000), but optimized to detect GWs generated by parametric amplification during inflation. (For a review of inflation-generated GWs, see (Allen; 1996) and references therein.) In the LISA band, 10^{-5} Hz – 10^{-1} Hz, an inflation-generated signal with $\Omega_{\text{GW}} \lesssim 10^{-15}$ would be completely covered up by the foreground produced by galactic and extra-galactic white-dwarf binaries. By contrast, BBO will have its best sensitivity in the range ~ 0.1 Hz – 1 Hz. This band avoids the GW foreground produced by all the white dwarf binaries in the universe, which cuts off at $f \lesssim 0.2$ Hz (where the most massive of the WD binaries merge). In the BBO band, the dominant foreground GW sources are inspiralling NS-NS, NS-BH, and BH-BH binaries. BBO’s baseline design, and corresponding instrumental noise curve, have been set in large part by the requirement that one must be able to individually identify practically *all* such inspiral signals and subtract them out of the data. An initial rough estimate suggested that the baseline ”specs” in Table I are adequate for this purpose (Phinney et al.; 2003); our primary task in this paper is to examine that issue much more carefully.

The current BBO design calls for four constellations of three satellites each, all following heliocentric orbits at a distance of 1 AU from the Sun (see Figure 4.4). Each 3-satellite constellation can be thought of as a “short-armed LISA”. Two of the constellations overlap to form a “Jewish star”; the other two are ahead and behind by $2\pi/3$ radians, respectively. Briefly, the idea behind this orbital geometry is that $\Omega_{\text{GW}}(f)$ will be measured by cross-correlating the outputs of the two overlapping constellations in the Jewish star (much as LIGO attempts to measure $\Omega_{\text{GW}}(f)$ by cross-correlating the outputs of the Livingston and Hanford interferometers (Allen and Romano; 1999)). The other two constellations give BBO its angular resolution: $\Delta\theta \sim 10^{-2}(\text{SNR})^{-1}$ radians. It is not clear whether this angular resolution is strictly necessary for the purpose of measuring $\Omega_{\text{GW}}(f)$, but it will be immensely useful for BBO’s secondary goal – to identify, map, and accurately determine the physical parameters of practically all merging compact binaries in the observable universe.

From the output of each 3-satellite constellation (i.e., each ”mini-LISA”), using time-delay interferometry (TDI) one can synthesize data streams that are free of laser phase noise and optical bench noise (Estabrook et al.; 2000; Prince et al.; 2002; Królak et al.;

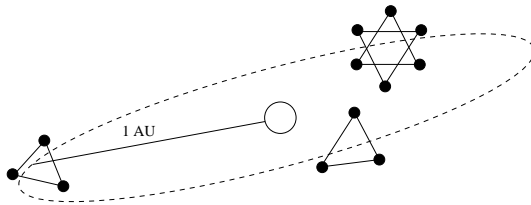


Figure 4.4: The Big-Bang Observer (BBO) consists of four LISA-like triangular constellations orbiting the Sun at 1 AU. The GW background is measured by cross-correlating the outputs of the two overlapping constellations.

2004). A particularly convenient set of TDI variables to work with is $\{A, E, T\}$; all the GW information registered by each mini-LISA is encoded in these variables, plus the noises in these 3 channels are uncorrelated with each other (i.e., they are statistically independent). Then, for instance, it is straightforward to find, for any source, the particular combination of $\{A, E, T\}$ that yields the optimum detection statistic, and so to determine LISA’s optimum sensitivity to that source (Prince et al.; 2002).

For our purposes, however, the following simplified treatment is adequate. As is clear from Fig. 4 of Prince et al. (Prince et al.; 2002), for NS-NS inspirals, each mini-LISA’s sensitivity (using the optimum combination of the A, E and T channels) is practically equivalent to the sensitivity of two synthetic Michelson detectors, represented by the TDI variables X and Y . For our purposes, then, we can regard BBO, which is made up of 4 mini-LISAs, as formally equivalent to 8 synthetic Michelson interferometers.

To construct the instrumental noise curve, $S_h^{\text{inst}}(f)$, of *each* of these synthetic Michelson’s, we used Larson’s on-line “Sensitivity curve generator” (Larson; 2005), plugging in the parameters appropriate to BBO, which are listed here in Table 4.1. The parameters we adopt as reference values here are taken from the BBO proposal (Phinney et al.; 2003); these parameters do not necessarily represent the latest thoughts on the mission’s design (which is a moving target), but do provide a convenient baseline for comparison. (Reference (Phinney et al.; 2003) also lists parameters for less and more ambitious versions of the BBO mission, referred to as “BBO-lite” and “BBO-grand”, respectively, but in this paper we concentrate on the intermediate version, or “standard BBO”.) In using the on-line generator, we have specified that the high-frequency part of S_h^{inst} is 4 times larger than the contribution from photon shot noise alone. This is the same choice made in Fig. 1 of the BBO proposal (Phinney et al.; 2003), and is consistent with assumptions typically made in drawing the LISA noise curve. As is conventional in the LISA literature, we take $S_h(f)$ to be the *single-sided, sky-averaged* noise spectrum for each synthetic Michelson. This BBO instrumental noise curve is shown in Figure 4.5.

4.3.2 NS-NS Merger Rates and the Associated Foreground Noise

In this section we estimate the magnitude of the GW foreground from all NS-NS mergers. We denote the NS-NS merger rate (per unit proper time, per unit co-moving volume) at redshift z by $\dot{n}(z)$. The present-day density n_0 of merger remnants is related to $\dot{n}(z)$

	Symbol	Value
Laser power	P	300 W
Mirror diameter	D	3.5 m
Optical efficiency	ϵ	0.3
Arm length	L	$5 \cdot 10^7$ m
Wavelength of laser light	λ	$5.0 \mu\text{m}$
Acceleration noise	$\sqrt{S_{\text{acc}}}$	$3 \cdot 10^{-17} \text{ m}/(\text{s}^2\sqrt{\text{Hz}})$

Table 4.1: BBO parameters.

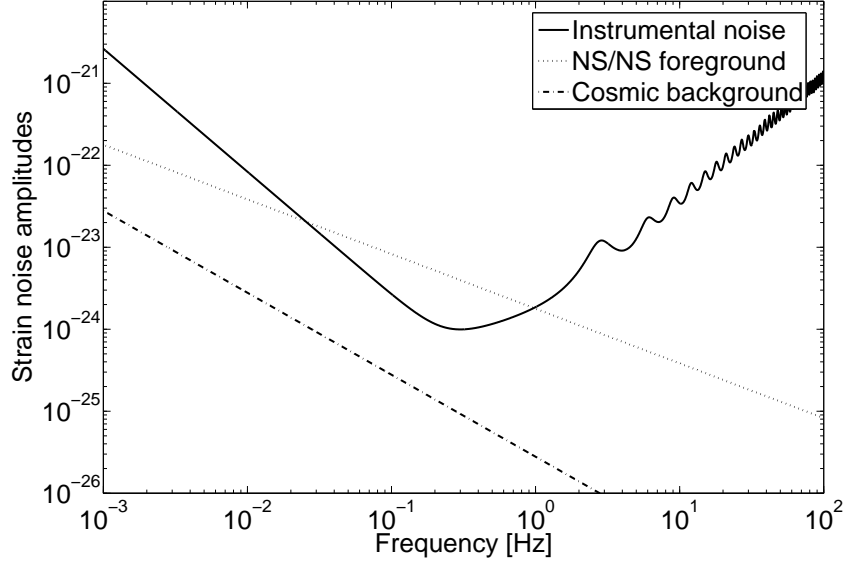


Figure 4.5: Shows the amplitude of the instrumental noise, $(fS_{\text{h}}^{\text{inst}}(f))^{1/2}$, compared to the amplitude of the (pre-subtraction) NS binary foreground (plotted for $\dot{n}_0 = 10^{-7} \text{ Mpc}^{-3} \text{ yr}^{-1}$) and the sought-for cosmic GW background (plotted for $\Omega_{\text{GW}}(f) = 10^{-15}$). Clearly, to reveal a cosmic GW background at this level, the NS foreground must be subtracted off, with fractional residual of $\lesssim 10^{-2.5}$.

by (Phinney; 2001)

$$n_0 = \int_0^{\infty} dz \frac{\dot{n}(z)}{(1+z)H(z)}, \quad (4.33)$$

where – in the following – $H(z)$ specifies a flat FRW model

$$H(z) \equiv H_0 \sqrt{\Omega_{\text{M}}(1+z)^3 + \Omega_{\Lambda}}. \quad (4.34)$$

As is conventional, we define $\Omega_{\text{GW}}(f)$ to be the universe's fractional energy in GWs, per logarithmic frequency interval:

$$\Omega_{\text{GW}}(f) \equiv \frac{1}{\rho_c} \frac{d\rho_{\text{GW}}(f)}{d(\ln f)}, \quad (4.35)$$

where $\rho_c = 3(cH_0)^2/(8\pi G)$ is the universe's current energy density. Then the GW energy density (in the BBO band) due to (the inspiral phase of) all NS-NS mergers is given by (Phinney; 2001)

$$\begin{aligned} \Omega_{\text{GW}}^{\text{NSm}}(f) &= \frac{8\pi^{5/3}}{9} \frac{c^3}{H_0^2} \left(\frac{GM}{c^3} \right)^{5/3} f^{2/3} n_0 \langle (1+z)^{-1/3} \rangle \\ &= 1.7 \times 10^{-12} h_{70}^{-2} \left(\frac{\mathcal{M}}{1.22 M_\odot} \right)^{5/3} \left(\frac{f}{1 \text{ Hz}} \right)^{2/3} \\ &\quad \cdot \left(\frac{n_0}{10^3 \text{ Mpc}^{-3}} \right) \left(\frac{\langle (1+z)^{-1/3} \rangle}{0.80} \right) \end{aligned} \quad (4.36)$$

The term $\langle (1+z)^{-1/3} \rangle$ in Eq. (4.36) is the merger-rate-weighted average of $(1+z)^{-1/3}$, given by

$$\langle (1+z)^{-1/3} \rangle \equiv \frac{1}{n_0} \int_0^\infty dz \frac{\dot{n}(z)}{(1+z)^{4/3} H(z)}. \quad (4.37)$$

What is the universe's NS-NS merger rate history, $\dot{n}(z)$? It is convenient to regard $\dot{n}(z)$ as the product of two factors:

$$\dot{n}(z) = \dot{n}_0 \cdot r(z), \quad (4.38)$$

where \dot{n}_0 is the merger rate today and $r(z)$ encapsulates the rate's time-evolution.

For $r(z)$, we adopt the following piece-wise linear fit to the rate evolution derived in (Schneider et al.; 2001):

$$r(z) = \begin{cases} 1 + 2z & z \leq 1 \\ \frac{3}{4}(5 - z) & 1 \leq z \leq 5 \\ 0 & z \geq 5 \end{cases} \quad (4.39)$$

For this $r(z)$ and our fiducial cosmological model, one has

$$n_0 = \dot{n}_0 \cdot (2.3 \cdot 10^{10} \text{ yr}), \quad (4.40)$$

and $\langle (1+z)^{-1/3} \rangle = 0.82$. (We note that, as stressed in (Phinney; 2001), the value of $\langle (1+z)^{-1/3} \rangle$ is actually quite insensitive to one's choice of the function $r(z)$, generally being in the range $\sim 0.7 - 0.9$.)

The current NS-NS merger rate, \dot{n}_0 , is also usefully regarded as the product of two factors: the current merger rate in the Milky Way and a factor that extrapolates from the Milky Way rate to the average rate in the universe. The NS-NS merger rate in the Milky Way has been estimated by several authors; it is still highly uncertain, but most estimates are in the range $10^{-6} - 10^{-4} \text{ yr}^{-1}$ (Belczynski et al.; 2002; Kalogera et al.; 2001; Voss and Tauris; 2003). To extrapolate to the rest of the universe, Kalogera et

al. (Kalogera et al.; 2001) estimate that one should multiply the Milky Way rate by $1.1 - 1.6 \times 10^{-2} \cdot h_{70}^{-1} \text{Mpc}^{-3}$. That factor is obtained by extrapolating from the B-band luminosity density of the universe, and it is only a little larger than the extrapolation factor derived by Phinney in (Phinney; 1991). Given the large overall uncertainty, in this paper we will consider 3 possible rates: $\dot{n}_0 = 10^{-8}, 10^{-7},$ and $10^{-6} \text{Mpc}^{-3} \text{yr}^{-1}$.

The (single-sided, sky-averaged) noise spectral density associated with any given GW background is (Allen; 1996):

$$S_h^{\text{GW}} = \frac{3}{2} \frac{H_0^2}{\pi^2} \frac{1}{f^3} \Omega_{\text{GW}}(f) \quad (4.41)$$

or

$$[f S_h^{\text{GW}}(f)]^{1/2} = 8.8 \times 10^{-25} \cdot h_{70} \left(\frac{\Omega_{\text{GW}}(f)}{10^{-12}} \right)^{1/2} \left(\frac{1 \text{Hz}}{f} \right). \quad (4.42)$$

The effective noise from all NS-NS inspirals (before subtraction) is plotted in Figure 4.5, alongside the noise level from the sought-for inflationary background and BBO’s instrumental noise curve. Clearly, the NS-binary foreground has amplitude $\sim 10^2$ times higher than the (hypothetical) inflationary background’s, in the BBO band, and so it must be possible to reduce (by subtraction) the foreground amplitude by more than $\sim 10^{2.5}$ to reveal an underlying primordial background.

Given our $r(z)$ and fiducial cosmological model, it is also straightforward to determine what fraction of $S_h^{\text{NSm}}(f)$ is due to sources farther out than some given redshift z . The result is plotted in Figure 4.6. For example, 64% of the foreground spectral density is due to sources at $z < 1$, and 99% is due to sources merging at $z < 3.6$. Thus, very roughly speaking, one must subtract out all NS-NS mergers up to $z \approx 3.6$ to reduce the foreground noise *amplitude* by one order of magnitude. Of course, that conclusion is too simplistic, since the redshift out to which any particular NS binary can be observed depends on that binary’s orientation as well as its redshift; see Section VI below for a proper accounting of this dependence. The time required for a NS-NS inspiral signal to sweep through the BBO band will typically be comparable to BBO’s lifetime. More specifically, the time remaining until merger, from the moment the GW frequency sweeps through f , is given (to lowest post-Newtonian order) by

$$t(f) = 4.64 \times 10^5 \text{s} \left(\frac{\mathcal{M}(1+z)}{1.22 M_\odot} \right)^{-5/3} \left(\frac{f}{1 \text{Hz}} \right)^{-8/3} \quad (4.43)$$

where $\mathcal{M} \equiv \mu^{3/5} M^{2/5}$ is the so-called “chirp mass” of the binary. (Here M is the binary’s total mass and μ is its reduced mass.) Therefore, for two $1.4 M_\odot$ NSs, $f \approx 0.205 \text{Hz}$, 0.136Hz , and 0.112Hz at one year, three years, and five years before merger, respectively.

4.4 Understanding Confusion Noise

So far, we have computed a spectrum for the NS-NS inspiral foreground, but we have not yet explained in what sense this foreground represents a noise source for BBO. We do so in this section, showing how GW signals from different mergers “interfere with” and so obscure each other. In this section we simply sketch the main results.

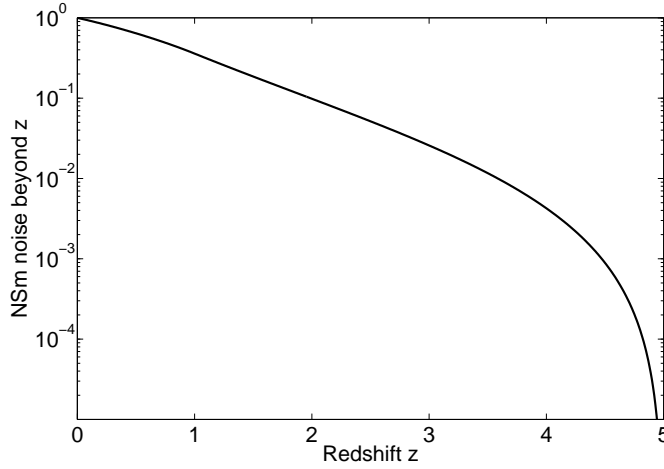


Figure 4.6: Figure plots $S_h^{\text{NSm},>z}/S_h^{\text{NSm}}$ vs. z , i.e., it plots the fractional contribution of NS-NS binaries beyond redshift z to the total NS-NS foreground noise.

4.4.1 Brief Review of Optimal Matched Filtering

Ultimately, matched filters fulfill two purposes. At first, we may compare the SNR of a filtered signal with predictions from our physical models. Therefore, all parameters of the source which determine the signal template have to be known from independent observations. If the comparison shows a deviation then we know that the physical models are inaccurate. Secondly, provided that the template models are accurate, a signal which fits a template can be subtracted from the data revealing weaker signals or allowing a more precise analysis of other signals.

Typical NS-NS merger signals will have amplitudes roughly two orders of magnitude smaller than the amplitude of BBO’s instrumental noise. In practice, therefore, (some version of) matched filtering will be required to dig these buried signals out of the noise. Hence we will begin by briefly reviewing optimal matched filtering, partly to fix notation. For a more complete discussion, see (Cutler and Flanagan; 1994) or (Wainstein and Zubakov; 1962).

The output of N detectors can be represented by the vector $s_A(t)$, $A = 1, 2, \dots, N$. It is often convenient to work with the Fourier transform of the signal; the convention we use is

$$\tilde{s}_A(f) \equiv \int_{-\infty}^{\infty} e^{2\pi i f t} s_A(t) dt, \quad (4.44)$$

The output $s_A(t)$ is the sum of gravitational wave signal $h_A(t)$ plus instrumental noise $n_A(t)$. In this section we will assume that the instrumental noise is both stationary and Gaussian. ‘Stationarity’ essentially means that the different Fourier components $\tilde{n}_A(f)$ of the noise are uncorrelated; thus we have

$$\overline{\tilde{n}_A(f) \tilde{n}_B(f')^*} = \frac{1}{2} \delta(f - f') S_{h,AB}(f), \quad (4.45)$$

where an overline ‘ $\overline{\quad}$ ’ denotes the ‘expectation value’ and $S_{h,AB}(f)$ is referred to as the

spectral density of the noise. [When $N=1$ (i.e., when there is just a single detector), we will dispense with detector indices and just write $\tilde{s}(f)$ and $S_h(f)$.] For our problem, we can restrict attention to the case where noises in different detectors are uncorrelated; then we have

$$\overline{\tilde{n}_A(f) \tilde{n}_B(f')^*} = \frac{1}{2} \delta(f - f') S_{h,A}(f) \delta_{AB}. \quad (4.46)$$

Given stationarity, ‘Gaussianity’ implies that each Fourier component has Gaussian probability distribution. Under the assumptions of stationarity and Gaussianity, we obtain a natural inner product on the vector space of signals. Given two signals $g_A(t)$ and $k_A(t)$, we define $\langle \mathbf{g} | \mathbf{k} \rangle$ by

$$\langle \mathbf{g} | \mathbf{k} \rangle = 2 \sum_A \int_{-\infty}^{\infty} \frac{\tilde{g}_A^*(f) \tilde{k}_A(f) df}{S_{h,A}(f)}. \quad (4.47)$$

It also follows from Eqs. (4.46) and (4.47) that for any functions $g_A(t)$ and $k_A(t)$, the expectation value of $\langle \mathbf{g} | \mathbf{n} \rangle \langle \mathbf{k} | \mathbf{n} \rangle$, for an ensemble of realizations of the detector noise $n_A(t)$, is just $\langle \mathbf{g} | \mathbf{k} \rangle$.

In terms of this inner product, the probability for the noise to have some realization \mathbf{n}_0 is just

$$p(\mathbf{n} = \mathbf{n}_0) \propto e^{-\langle \mathbf{n}_0 | \mathbf{n}_0 \rangle / 2}. \quad (4.48)$$

Thus, if the actual incident waveform is \mathbf{h} , the probability of measuring a signal \mathbf{s} in the detector output is proportional to $e^{-\langle \mathbf{s} - \mathbf{h} | \mathbf{s} - \mathbf{h} \rangle / 2}$. Correspondingly, given a measured signal \mathbf{s} , the gravitational waveform \mathbf{h} that “best fits” the data is the one that minimizes the quantity $\langle \mathbf{s} - \mathbf{h} | \mathbf{s} - \mathbf{h} \rangle$.

For a given incident gravitational wave, different realizations of the noise will give rise to somewhat different best-fit parameters. However, for large SNR, the best-fit parameters will have a Gaussian distribution centered on the correct values. Specifically, let $\tilde{\lambda}^\alpha$ be the “true” values of the physical parameters, and let $\tilde{\lambda}^\alpha + \Delta\lambda^\alpha$ be the best fit parameters in the presence of some realization of the noise. Then for large SNR, the parameter-estimation errors $\Delta\lambda^\alpha$ have the Gaussian probability distribution

$$p(\Delta\lambda^\alpha) = \mathcal{N} e^{-\frac{1}{2} \Gamma_{\alpha\beta} \Delta\lambda^\alpha \Delta\lambda^\beta}. \quad (4.49)$$

Here $\Gamma_{\alpha\beta}$ is the so-called Fisher information matrix defined by

$$\Gamma_{\alpha\beta} \equiv \left\langle \frac{\partial \mathbf{h}}{\partial \lambda^\alpha} \middle| \frac{\partial \mathbf{h}}{\partial \lambda^\beta} \right\rangle \quad (4.50)$$

and $\mathcal{N} = \sqrt{\det(\mathbf{\Gamma}/2\pi)}$ is the appropriate normalization factor. For large SNR, the variance-covariance matrix is given by

$$\overline{\Delta\lambda^\alpha \Delta\lambda^\beta} = (\mathbf{\Gamma}^{-1})^{\alpha\beta} + \mathcal{O}(\text{SNR})^{-1}. \quad (4.51)$$

In the above notation, optimal filtering for some gravitational-waveform $h(t)$ simply amounts to taking the inner product of $h(t)$ with the data stream $s(t)$. Assuming $\mathbf{s} = \mathbf{n} + \mathbf{h}$, then

$$\langle \mathbf{s} | \mathbf{h} \rangle = \langle \mathbf{n} | \mathbf{h} \rangle + \langle \mathbf{h} | \mathbf{h} \rangle \quad (4.52)$$

The first term on the rhs of Eq. (4.52) has rms value $\langle \mathbf{h} | \mathbf{h} \rangle^{1/2}$, so the signal-to-noise of the detection will be approximately given by

$$\text{SNR}[\mathbf{h}] = \frac{\langle \mathbf{h} | \mathbf{h} \rangle}{\text{rms} \langle \mathbf{h} | \mathbf{n} \rangle} = \langle \mathbf{h} | \mathbf{h} \rangle^{1/2}. \quad (4.53)$$

All physically realizable filters must be complex and thus produce a phase shift, since the transfer function is real only if the impulse response function is even which means that the output depends on future values of the input.

4.4.2 Overlapping NS-NS Chirps as a Source of Self-Confusion

Now imagine that the detector output $s(t)$ consists of instrumental noise $n(t)$ plus the sum of some large number of merger signals (labelled by “i”):

$$s(t) = n(t) + \sum_i h_i(t). \quad (4.54)$$

(For simplicity, here we will consider the case of a single detector, and so eliminate the index A ; the generalization to multiple detectors is trivial.)

As explained above, optimally filtering the data for any particular merger waveform $h_j(t)$ is equivalent to taking the inner product $\langle \mathbf{s} | \mathbf{h}_j \rangle$, which we can write as the sum of three pieces:

$$\langle \mathbf{s} | \mathbf{h}_j \rangle = \langle \mathbf{n} | \mathbf{h}_j \rangle + \sum_{i \neq j} \langle \mathbf{h}_i | \mathbf{h}_j \rangle + \langle \mathbf{h}_j | \mathbf{h}_j \rangle. \quad (4.55)$$

For the signal to be detectable, the third term should be significantly larger than the rms values of the first and second terms. We now explain *why* the second term can be sizeable; i.e., why different chirp signals can have substantial overlaps. To simplify this discussion, let us use a slightly simpler version of the inner product; define

$$(\mathbf{g} | \mathbf{k}) \equiv \int_{-\infty}^{\infty} \tilde{g}^*(f) \tilde{k}(f) df = \int_{-\infty}^{\infty} g(t) k(t) dt, \quad (4.56)$$

where the second equality in Eq. (4.56) is just Parseval’s theorem. (Clearly, this is just our usual inner product, but without the “re-weighting by $1/S_h$ ” in the frequency domain. For white noise, where $S_h(f) = \text{constant}$, $(|)$ and $\langle | \rangle$ are equivalent, except for an overall constant.)

We now want to estimate the values of $\langle \mathbf{n} | \mathbf{h}_i \rangle$ and $\langle \mathbf{h}_i | \mathbf{h}_j \rangle$ for any two binary inspiral waveforms $h_i(t)$ and $h_j(t)$. In the nearly-Newtonian regime of interest to BBO, these are simple chirp waveforms:

$$h_i(t) = A_i(t) \cos \Phi_i(t), \quad (4.57)$$

$$h_j(t) = A_j(t) \cos \Phi_j(t), \quad (4.58)$$

where

$$\Phi_i(t) = \cos \int^t 2\pi f_i(t') dt', \quad (4.59)$$

$$\Phi_j(t) = \cos \int^t 2\pi f_j(t') dt', \quad (4.60)$$

and where $A_i(t)$, $A_j(t)$, $f_i(t)$ and $f_j(t)$ are all slowly varying (meaning their fractional change during one cycle is $\ll 1$), and $f_i(t)$ and $f_j(t)$ are monotonically increasing. Then, since the integrand is highly oscillatory, it is clear that the integral $\int h_i(t)h_j(t) dt$ will show substantial waveform overlap only if there is some instant t_0 when the two signals have the same frequency:

$$f_i(t_0) = f_j(t_0). \quad (4.61)$$

I.e., if one considers the "track" of each signal in the f-t plane, then t_0 is the instant of time when the two tracks cross. Using the stationary phase approximation, it is straightforward to show that:

$$(\mathbf{h}_i | \mathbf{h}_j) \approx \frac{1}{2} A_i(t_0) A_j(t_0) |\delta \dot{f}|^{-1/2} \cos[\Delta \Phi_0 \pm \pi/4], \quad (4.62)$$

where $\Delta \Phi_0 \equiv [\Phi_i(t_0) - \Phi_j(t_0)]$, $\delta \dot{f} \equiv [\dot{f}_i(t_0) - \dot{f}_j(t_0)]$, and where the sign in front of the $\pi/4$ in Eq. (4.62) is positive when $\delta \dot{f} > 0$ and negative when $\delta \dot{f} < 0$.

We want to use this result to estimate

$$\left(\mathbf{h}_j \left| \sum_{i \neq j} \mathbf{h}_i \right. \right), \quad (4.63)$$

ie., to sum the contributions from all binaries whose f-t tracks overlap the j^{th} track. Since the phase differences $\Delta \Phi_0$ at different intersections will clearly be uncorrelated, the contributions accumulate in a random-walk fashion; i.e., the square of the sum is approximately the sum of the squares of the individual terms. Also, as we show in the next subsection, a typical NS-NS "track" will intersect a very large number of tracks from other merging binaries, so we are in the realm of large-number statistics. Finally, while the magnitude of each squared-contribution scales like $|\delta \dot{f}|^{-1}$, the number of terms in the sum scales like the average value of $|\delta \dot{f}|$, since the larger the "relative velocities" of the tracks, the more crossings. The dependence of the sum on the typical size of $|\delta \dot{f}|$ therefore ends up cancelling out, and one can show the following. Let $H(t) = \sum_i h_i(t)$ be the entire foreground generated by NS-NS chirps, and let H 's spectral density be $S_H(f)$, normalized so that

$$\overline{H^2(t)} = \int_0^\infty S_H(f) df. \quad (4.64)$$

Then the expectation value of $(\mathbf{h}_j | \sum_{i \neq j} \mathbf{h}_i)^2$ is given by

$$\overline{\left(\mathbf{h}_j \left| \sum_{i \neq j} \mathbf{h}_i \right. \right)^2} = \frac{1}{2} \int h_j^2(t) S_H(f_j(t)) dt. \quad (4.65)$$

But the same result holds for the mean-square overlap of $h_j(t)$ with stationary, Gaussian noise $n(t)$:

$$\overline{(\mathbf{h}_j | \mathbf{n})^2} = \frac{1}{2} \int h_j^2(t) S_h(f_j(t)) dt \quad (4.66)$$

with $\overline{n^2(t)} = \int_0^\infty S_h(f) df$. I.e., the mean-square overlap of a single chirp $h_j(t)$ with the chirp foreground $H(t)$ (excluding h_j itself) is the same as the mean-square overlap of $h_j(t)$ with stationary, Gaussian noise having the same spectral density as H . (It is straightforward to generalize this result to inner products with non-trivial frequency-weighting. It is for this reason that in Eq. (4.1) we simply add together the spectral densities of the instrumental noise and the "confusion noise" from unresolved chirps.

4.4.3 The Number of Overlapping Inspiral Tracks in the f - t Plane

We saw in the previous subsection that two chirp signals have substantial overlap only if their tracks in the f - t plane intersect. Here we consider the track from a typical NS-NS inspiral and estimate how many *other* inspiral tracks it crosses.

Let $\rho(f)$ be the probability density of merger signals in frequency space; i.e., at any instant, $\rho(f)\Delta f$ is the average number of NS-NS GW signals received near the Earth that are in the frequency range $[f - \Delta f/2, f + \Delta f/2]$. Since the BBO mission lifetime is vastly shorter than the age of the universe, we can assume $\rho(f)$ is time-independent, implying

$$\rho(f)\frac{df}{dt} = \text{const} = \dot{N}, \quad (4.67)$$

where, again, $\dot{N} \equiv \Delta N_m / \Delta \tau_0$ is the total rate of mergers in the observable universe (from all z). The GW frequency derivative \dot{f} is given by

$$df/dt = \frac{96}{5}\pi^{8/3} \left[\frac{\mathcal{M}(1+z)}{c^3} \right]^{5/3} f^{11/3}. \quad (4.68)$$

so clearly $\rho(f) \propto f^{-11/3}$.

Now consider any one track in the $f-t$ plane, and examine it in the neighborhood of some frequency f . It is easy to see that the rms rate r_c at which it intersects neighboring tracks is

$$r_c = 0.5 \rho(f) \Delta \dot{f} \quad (4.69)$$

where $\Delta \dot{f}$ is the rms variation in frequency derivatives for sources with GW frequency f . The 0.5 factor in Eq. (4.69) arises because, for any two neighboring tracks at any instant, there is a 50% chance that they are approaching each other and a 50% chance that they are separating.

Using Eq. (4.68), we see that the rms relative “velocity” of nearby tracks is

$$\frac{\Delta \dot{f}}{\dot{f}} = 5/3 \frac{\Delta \mathcal{M}_{\text{eff}}}{\mathcal{M}_{\text{eff}}}, \quad (4.70)$$

where we define $\mathcal{M}_{\text{eff}} \equiv \mathcal{M}(1+z)$, and where $\Delta \mathcal{M}_{\text{eff}}$ is the rms variation in this quantity. Now the fractional variation in \mathcal{M} itself, $\Delta \mathcal{M}/\mathcal{M}$, is probably at least of order 0.1. However, from Figure 1.5 we see that this is small compared to the variation $\Delta(1+z)/(1+z)$, which is ~ 0.4 .

Thus r_c is roughly given by

$$r_c = 0.5(5/3)\rho\dot{f}\frac{\Delta\mathcal{M}_{\text{eff}}}{\mathcal{M}_{\text{eff}}} \sim \frac{1}{3}\dot{N} \quad (4.71)$$

independent of the particular frequency f . That is, the rate at which any particular track crosses all other tracks is about one-third the total merger rate from all observable sources, independent of where one is on the track. Thus, for any one track over the last 3 years of inspiral, one expects of order 10^5 crossings. This amply justifies our use of large-number statistics in the previous subsection.

4.5 Confusion Noise from Imperfectly Subtracted Waveforms

NS binaries limit BBO’s sensitivity to a primordial background in two ways. First, there will be some binaries that are too weak (because of their distance and/or orientation) to be individually identified and subtracted, and these “unidentified binaries” clearly represent a source of “confusion noise.” Second, even identified NS binaries will not be removed perfectly from the data stream; inevitably (due to the finite signal-to-noise of the observations) there are subtraction errors, which represent a second source of confusion noise. This section addresses the confusion noise that results from subtraction errors. First we will prove a simple theorem regarding the magnitude of subtraction errors. Then we will sketch a simple strategy for largely eliminating their impact on other analyses by projecting them out, at the cost of some bandwidth. We estimate that lost bandwidth for BBO, and conclude that the loss is small enough that in the rest of this paper we can safely neglect it.

We believe the analysis and strategy we outline here will also be useful in similar contexts, especially in dealing with problems of confusion noise in LISA data. Here we provide only a sketch of the main ideas; more details will be provided in a forthcoming publication by Curt Cutler.

4.5.1 Subtraction Errors due to Noise

We have argued that, before searching for a primordial GW background, one will want to first subtract from the data the best fit to each identified inspiralling compact binary. However, because of detector noise, the best-fit values of the binary parameters will differ from their true values, and so the best-fit waveforms will be somewhat in error. A geometrical representation of the problem can be seen in [Figure 4.7](#).

What is the typical size of the error? That is easy to calculate: Let $h(t)$ be some gravitational waveform immersed in noisy data, and assume the waveform depends on N_p physical parameters λ^α ($\alpha = 1, \dots, N_p$). Because of the noise, the best-fit parameter values $\hat{\lambda}^\alpha$ will differ from the true parameter values by ([Cutler and Flanagan; 1994](#))

$$\delta\lambda^\alpha \equiv \hat{\lambda}^\alpha - \lambda^\alpha \approx (\Gamma^{-1})^{\alpha\beta} \langle \mathbf{n} | \partial_\beta \mathbf{h} \rangle, \quad (4.72)$$

and, correspondingly, the best-fit waveform $\hat{h}(t)$ will differ from the true one by

$$\begin{aligned} \delta\mathbf{h} &\equiv \hat{\mathbf{h}} - \mathbf{h} \\ &= \partial_\alpha \mathbf{h} \delta\lambda^\alpha + \mathcal{O}(\delta\lambda)^2. \end{aligned} \quad (4.73)$$

Using Eqs.([4.50](#)), ([4.51](#)), and ([4.73](#)), we can immediately estimate the norm-squared of this residual error. To lowest order in $\delta\lambda^\alpha$, we have

$$\begin{aligned} \overline{\langle \delta\mathbf{h} | \delta\mathbf{h} \rangle} &= \langle \partial_\alpha \mathbf{h} | \partial_\beta \mathbf{h} \rangle \overline{\delta\lambda^\alpha \delta\lambda^\beta} \\ &= \Gamma_{\alpha\beta} (\Gamma^{-1})^{\alpha\beta} = N_p. \end{aligned} \quad (4.74)$$

Thus the size of $\langle \delta\mathbf{h} | \delta\mathbf{h} \rangle$ is independent of the signal strength, but increases linearly with the number of parameters that need to be fit for.

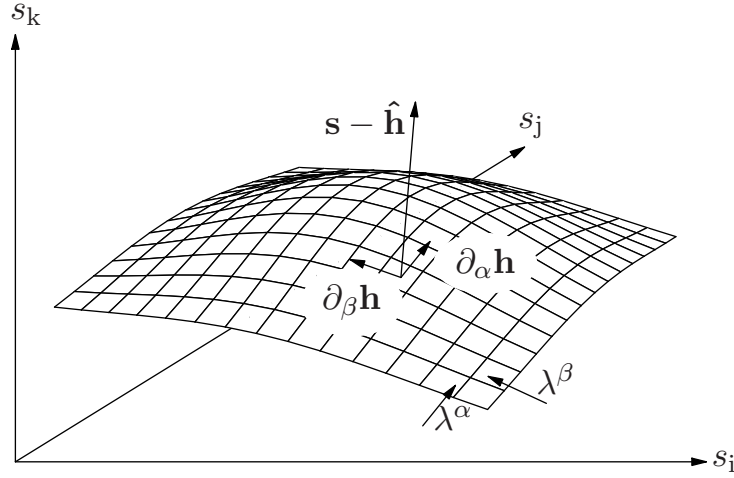


Figure 4.7: The template space which is parameterized by λ^α (e.g. spin parameters, masses, etc for each NS binary) is shown as a submanifold of the data space. The collection of all samples form a vector \mathbf{s} which is then projected onto the template submanifold yielding the best fit $\hat{\mathbf{h}}$.

Eq. (4.74) estimates the weighted integral of $|\delta\tilde{h}(f)|^2$; it says nothing about rms size of $|\delta\tilde{h}(f)|^2$ at any *particular* frequency f . Now, one can always calculate $|\delta\tilde{h}(f)|^2$ using (to lowest order)

$$|\delta\tilde{h}(f)|^2 = \partial_\alpha \tilde{h}(f) \partial_\beta \tilde{h}^*(f) (\Gamma^{-1})^{\alpha\beta}, \quad (4.75)$$

but for back-of-the-envelope calculations, it is reasonable to simply turn Eq. (4.74) into a point estimate for the relative error:

$$\frac{|\delta\tilde{h}(f)|}{|\tilde{h}(f)|} \sim \left[\frac{\langle \delta\mathbf{h} | \delta\mathbf{h} \rangle}{\langle \mathbf{h} | \mathbf{h} \rangle} \right]^{1/2} \sim \frac{N_p^{1/2}}{\text{SNR}}. \quad (4.76)$$

For BBO measurements of NS-NS binaries, $N_p \approx 11$ (cf. Section VI), and for a typical source (i.e. for a source at $z \approx 1.5$, with $\mu = 0.5$, where μ is the cosine of the angle between the line-of-sight and the normal to the binary's orbital plane), $\text{SNR} \approx 140$, so $\delta h/h \sim 2.4 \times 10^{-2}$.

Given the extreme accuracy with which foreground sources must be subtracted, at first glance this level of error seems unacceptable. However it would be a mistake to regard δh as a completely random, additive noise source in the data. For one thing, after the best-fit signal $\hat{h}(t)$ has been removed from the data stream, the amplitude of noise plus residual is *smaller* (on average) than that of the noise alone. To see this, consider again the case of data $s(t) \equiv n(t) + h(t)$, and assume that the observation time is T , and that the data has been band-limited to $[-f_{\max}, f_{\max}]$. Then it is easy to show that the noise alone has squared-magnitude:

$$\overline{\langle \mathbf{n} | \mathbf{n} \rangle} = 2f_{\max}T, \quad (4.77)$$

which is just the number of data points, for data sampled at the Nyquist rate $2f_{\max}$. Next consider the magnitude-squared of the post-subtraction data set, $\mathbf{s} - \hat{\mathbf{h}}$, where again $\hat{\mathbf{h}}$ is

the waveform that best fits the data. A straightforward calculation shows that

$$\overline{\langle \mathbf{s} - \hat{\mathbf{h}} \mid \mathbf{s} - \hat{\mathbf{h}} \rangle} = \overline{\langle \mathbf{n} - \delta\mathbf{h} \mid \mathbf{n} - \delta\mathbf{h} \rangle} \quad (4.78)$$

$$= 2f_{\max}T - N_p. \quad (4.79)$$

I.e., fitting out waveform \hat{h} causes the norm-squared of the data to decrease below what is expected from noise alone. This is easy to understand: the fitting procedure takes out not only the signal \mathbf{h} , but also that part of the noise that "looks like" the difference between \mathbf{h} and some other waveform, $\hat{\mathbf{h}}$, having slightly different physical parameters. Stated geometrically, if one considers the manifold of physical gravitational waveforms, embedded in the vector space of possible measured signals, one sees that any piece of the noise that is tangent to the waveform manifold (at the location of the true signal) gets fitted out. Indeed, one sees from Eq. (4.72) that it is just this piece of the noise, lying in the tangent space to the waveform manifold, that is "responsible" for the parameter estimation errors $\delta\lambda^\alpha$ in the first place. In the next subsection we outline a strategy projecting out this error *before* one searches for an inflation-generated background.

Note that nothing in the above arguments required the signal to emanate from a single physical source. E.g., if $H(t)$ is the entire foreground signal coming from N_s sources,

$$H(t) = \sum_{i=1}^{N_s} h_i(t), \quad (4.80)$$

and if each $h_i(t)$ is described by p parameters, then the full parameter space is described by $N_p = p \times N_s$ parameters, and

$$\overline{\langle \delta\mathbf{H} \mid \delta\mathbf{H} \rangle} = p \times N_s \quad (4.81)$$

to lowest order in $1/\text{SNR}$. The total SNR^2 of the foreground H is just N_s times the average SNR^2 of the individual sources, and N_p is of course directly proportional to N_s , so the fractional error in subtracting the whole foreground is just the fractional error in subtracting a typical source:

$$\delta H/H \sim \delta h/h. \quad (4.82)$$

For BBO measurements of the NS-NS foreground, we thus estimate $\delta H/H \sim 2.4 \times 10^{-2}$.

As a digression, we remark that because our foreground consists of a large number of overlapping sources, it should not be surprising if there are some near-degeneracies that make it practically impossible to determine some of the physical parameters of some of the sources. (These are cases where the affect on $H(t)$ of adjusting the parameters of one source can be almost perfectly cancelled by adjusting the parameters of another source.) We bring this up to make the point that such near-degeneracies do *not* necessarily imply any degradation in one's ability to subtract out the foreground. Indeed, in the case of very high SNR (per source), it implies the opposite: near degeneracies would imply that the residual $\delta\mathbf{H}$ is somewhat smaller than estimated above. The reason is simple: a near degeneracy means that the effective dimensionality of the signal space (near the actual signal) is smaller than the number of parameters being used to describe it. I.e., one could find a new parametrization using a fewer number of variables, N'_p . Then a repetition of

the above arguments would yield $\overline{\langle \delta \mathbf{H} | \delta \mathbf{H} \rangle} = N_p' < N_p$. For the BBO case, where SNR per source is ≈ 140 , it probably will require detailed simulations to determine whether subtraction errors are larger or smaller than indicated by the high-SNR result, Eq. (4.81). We leave this question to future work.

4.5.2 Projecting out Residual Subtraction Errors

In this subsection we propose one strategy for effectively cleaning the BBO data of subtraction errors, after the NS-NS binaries have been subtracted out. Using this strategy, we argue that the impact of subtraction residuals (arising from instrumental noise) becomes sufficiently small that they can be ignored in the rest of this paper. We do not argue that our strategy is the best one possible, but rather offer it as an “existence argument” that some such strategy is possible. The use of any alternative strategy that leads to the same conclusion would not affect the main results of this paper.

The basic observation behind our strategy is that the residual $\delta H(t)$ is mostly confined to a surface within the vector space of all signals: the tangent space to the waveform manifold at the best-fit point. The corresponding errors in the subtracted waveform can be expanded in a Taylor series:

$$\delta H(t) = \partial_\alpha H(t) \delta \lambda^\alpha + \frac{1}{2} \partial_\alpha \partial_\beta H(t) \delta \lambda^\alpha \delta \lambda^\beta + \dots \quad (4.83)$$

where $\alpha, \beta = 1, \dots, p \times N_s$. The first-order piece on the rhs is the linear combination of $N_p = p \times N_s$ wavefunctions (the $\partial_\alpha H(t)$), with unknown coefficients (determined by the noise). We propose projecting these directions out of the data stream. This is simple in principle. Consider the operator

$$P \equiv I - (\Gamma^{-1})^{\alpha\beta} |\partial_\alpha \mathbf{H}\rangle \langle \partial_\beta \mathbf{H}|. \quad (4.84)$$

where for simplicity we use here standard bra-ket notation of quantum mechanics. It is trivial to verify that $P^2 = P$ and that P destroys any wavefunction of the form $\partial_\alpha H(t) \delta \lambda^\alpha$. We propose acting on the data streams with P before searching them for an inflation-generated background.

What fraction of the data have we thrown away, by using P ? For a fiducial 3-yr BBO lifetime, with, say, $\sim 3 \times 10^5$ subtracted sources, each determined by ~ 11 parameters, $N_p \sim 3 \times 10^6$. Assuming a 2-Hz sampling rate (sufficient for capturing most of the signal), with $\sim 10^8$ s of data and 8 independent channels, the dimension S of the full data space is $S \sim 1.5 \times 10^9$. Thus the fraction of the data that is discarded is only $N_p/S \sim 2 \times 10^{-3}$, which is a negligible loss.

So far we have discussed projecting out the first-order piece of the subtraction error; i.e., the piece linear in the parameter estimation errors $\delta \lambda^\alpha$. What is the magnitude of the second-order subtraction errors (i.e., the ones quadratic in $\delta \lambda^\alpha$)? This is clearly given by

$$\overline{\langle \delta^2 \mathbf{H} | \delta^2 \mathbf{H} \rangle} = \frac{1}{4} \langle \partial_\alpha \partial_\beta \mathbf{H} | \partial_\gamma \partial_\epsilon \mathbf{H} \rangle \overline{\delta \lambda^\alpha \delta \lambda^\beta \lambda^\gamma \delta \lambda^\epsilon}. \quad (4.85)$$

but evaluating the rhs of Eq. (4.85) is beyond the scope of this paper, and so we content ourselves with a cruder estimate. The second-order errors clearly scale like the square

of the first-order errors, so a very crude estimate is $\delta^2 H/H \sim (\delta H/H)^2 \sim 6 \times 10^{-4}$. Of course, this estimate is properly multiplied by some pre-factor (which can only be obtained by calculating of the rhs of Eq. (4.85)). Depending on this pre-factor and the actual level of the NS-NS foreground, these second-order subtraction errors could be comparable in size to the sought-for inflationary background. If this is the case, we would advocate projecting out the second-order errors as well. The second-order errors are linear combinations of second derivatives $\partial_\alpha \partial_\beta H(t)$. It is important to notice that such second derivatives vanish identically *unless α and β are parameters describing the same binary*. Thus the vast majority of such second derivatives vanish. For each binary, there are $(11 \times 12)/2 = 66$ non-vanishing second derivatives, so projecting out the second-order piece of the subtraction errors would cost only $\sim 1\%$ of BBO's bandwidth. A crude estimate of the size of third-order subtraction errors is $\delta^3 H/H \sim (\delta H/H)^3 \sim 10^{-5}$. Clearly, unless the missing pre-factor here is quite large (of order 100 or more), it should not be necessary to project these third-order errors out of the data.

4.6 The Detection Threshold

The GW strength (at the Earth) of any NS-NS binary is characterized by its signal-to-noise-squared, ρ^2 . By ρ^2 , we mean the matched-filtering SNR² for the entire 4-constellation BBO network (whose output is 12 independent GW data streams, 8 of which have good sensitivity to NS binaries). We want to estimate the threshold value ρ_{th}^2 required for the signal to be detectable. There are basically two sorts of considerations here. If one possessed infinite computing power, then this threshold value would be set just by the requirement that one has sufficient confidence in the detection (i.e., that the false alarm rate be sufficiently low). However in practice we expect the search sensitivity to be (severely) computationally limited, which implies a somewhat higher detection threshold.

4.6.1 Lower Bound on the Detection Threshold

Let N_t be the number of independent templates required to cover the parameter space of NS-NS inspiral waveforms ('independent' in the sense that they have only modest overlap with each other). Then for a given threshold value ρ_{th} , the number of false alarms generated by this entire set is $\sim N_t \text{erfc}(\rho_{\text{th}}/\sqrt{2}) \approx N_t (2\pi)^{-1/2} (\rho_{\text{th}})^{-1} e^{-\rho_{\text{th}}^2/2}$. In practice, one would probably want this false alarm rate to be no greater than ~ 0.01 . How large is N_t for our problem? This has not yet been calculated, but because ρ_{th} depends only logarithmically on N_t , a very rough estimate will suffice for our purposes.

Consider the parameter space of 'typical' inspiral waveforms, normalized by $\langle \mathbf{h} | \mathbf{h} \rangle = 1$. These are effectively described by 10 parameters:

$$\begin{aligned} \lambda^\alpha &\equiv (\lambda^1, \dots, \lambda^N) \\ &= [t_0, \ln \mathcal{M}_{\text{eff}}, \ln \mu_{\text{eff}}, \beta, e_0^2, \Phi_0, \theta, \phi, \theta_L, \phi_L]. \end{aligned} \quad (4.86)$$

Here, t_0 is the instant of time when the ($n = 2$ piece of the) GW frequency sweeps through some fiducial value f_0 (e.g., $f_0 = 0.3$ Hz); $\mathcal{M}_{\text{eff}} \equiv \mathcal{M}(1+z)$; $\mu_{\text{eff}} \equiv \mu(1+z)$; β is the spin parameter defined in Eq. (3.26) (and approximated here as a constant); e_0^2 is the square of

the orbital eccentricity at t_0 ; Φ_0 describes the orbital phase (the angle between the orbital separation vector \hat{r} and some fixed vector in the orbital plane) at t_0 ; (θ, ϕ) give the position of the source on the sky; and (θ_L, ϕ_L) give the orientation of the binary's total angular momentum vector \vec{L} (which precesses slightly, but which we can typically approximate as constant). We have omitted from this list the perihelion angle ω_0 and 5 of the 6 parameters characterizing the two NS spin vectors, since we estimated in [subsection 3.2.2](#) that they typically have a negligible impact on the waveform. The luminosity-distance to the source, D_L , has been omitted since it affects only the waveform's overall normalization.

Now imagine covering our N -dimensional manifold of waveforms with a hypercubic grid, such that the overlap of any waveform on the manifold with the nearest gridpoint is $\geq (1-x)$, where x is a number that characterizes the fineness of our grid. The number of gridpoints N_t is then ([Owen; 1996](#))

$$N_t \approx (N/8x)^{N/2} \int \sqrt{\Gamma} d\lambda^1 \dots d\lambda^N \quad (4.87)$$

where Γ is the determinant of the Fisher matrix $\Gamma_{\alpha\beta} \equiv \langle \partial_\alpha \mathbf{h} | \partial_\beta \mathbf{h} \rangle$ (again, subject to the constraint $\langle \mathbf{h} | \mathbf{h} \rangle = 1$). In our case $N = 10$, and we adopt $x = 0.5$ as our fiducial grid spacing, so $(N/8x)^{N/2} \approx 100$. We can obtain a rough estimate of the integral $\int \sqrt{\Gamma} d\lambda^1 \dots d\lambda^N$ from estimates of the sizes of the diagonal elements of Γ , as follows. For each parameter λ_α , let $n_{\lambda_\alpha} = \delta_{\lambda_\alpha} |h^{-1} \partial h / \partial \lambda_\alpha|$, where δ_{λ_α} is the range of integration for the α^{th} parameter and $|h^{-1} \partial h / \partial \lambda_\alpha|$ is supposed to represent some 'typical' or 'rms' value of this quantity. Then

$$\int \sqrt{\Gamma} d\lambda^1 d\lambda^2 \dots d\lambda^N \lesssim n_{\lambda_1} n_{\lambda_2} \dots n_{\lambda_N}. \quad (4.88)$$

The rhs represents a rough upper limit to the integral because it ignores possible cancellations in the determinant coming from the off-diagonal terms. Based on a post-Newtonian expansion of the waveform, of the form shown in [subsection 3.2.3](#), we derive the following order-of-magnitude estimates for the different factors:

$$\begin{aligned} n_{t_0} &\sim 10^8, \quad n_{\ln \mathcal{M}} \sim 10^8, \quad n_{\ln \mu} \sim 10^5, \\ n_\beta &\sim 10^2, \quad n_{e_0^2} \sim 10^2, \quad n_{\Phi_0} \sim 10^1, \quad n_\Omega \sim 10^7, \\ n_{\Omega_J} &\sim 10^1 \end{aligned} \quad (4.89)$$

where $n_\Omega \equiv n_\theta n_\phi$, $n_{\Omega_J} \equiv n_{\theta_J} n_{\phi_J}$, and where we have used $\delta\beta \sim 0.5$ and $\delta e_0^2 \sim 10^{-7}$. Using the above estimates, we find $N_t \lesssim 10^{36}$. Allowing for cancellations from off-diagonal terms, it seems reasonable to assume N_t is in the range $N_t \sim 10^{30} - 10^{36}$, implying $\rho_{\text{th}} \geq 12.5 - 13.5$. That is, if matched filtering reveals a NS-NS inspiral with total SNR $\gtrsim 13$, then one can be confident it is not simply a randomly generated peak.

Now, one could complain that we have undercounted N_t by restricting to the parameter space of 'typical' signals, whereas among the $10^5 - 10^6$ NS binaries that BBO will observe, there are probably *some* atypical ones; e.g., binaries in which *both* NSs are rapidly rotating. And these must also be identified and subtracted, for BBO to do its main job. This complaint has some merit, but we do not dwell on it here, since in any case we expect that in practice ρ_{th} will be set not by the false alarm rate, but by computational limitations. We turn to these next.

4.6.2 Limitations due to Finite Computing Power

From the estimates in the previous section, one readily concludes that straightforward matched filtering for all templates in the template bank will *not* be possible. The simplest implementation would require of order $\sim 10^9 N_t$ floating point operations (since each year-long template has $\sim 3 \times 10^8$ data points, if sampled at ~ 10 Hz). A well known, FFT-based trick to efficiently search over all t_0 (Schutz; 1991) reduces this cost by a factor $\sim n_{t_0}/[3\ln(10^9)] \sim 10^6$, but would still require computation speeds of $\sim 10^{28\pm 3}$ flops (operations per second). Extrapolation of Moore’s law to the year 2025 suggests that perhaps $\sim 10^{17}$ flops will be readily available, which is 11 orders of magnitude too small for the job.

Therefore one will need to devise a suboptimal (but computationally practical) search algorithm, and live with the attendant loss in sensitivity. It is beyond the scope of this paper to design such an algorithm and evaluate its efficiency. Fortunately, though, the problem of searching for NS-NS binary signals in BBO data is closely analogous to the problem of searching for unknown GW pulsars in LIGO data, and the problem of devising efficient search algorithms for the latter has been studied in some detail (Brady and Creighton; 2000; Cutler et al.; 2005). We will estimate the threshold sensitivity of BBO NS-binary searches based on this analogy, so we digress to describe optimized LIGO searches for unknown GW pulsars.

By unknown GW pulsars, we mean rapidly rotating NSs whose sky location, amplitude and polarization, and gravitational-wave frequency (at any instant) and frequency derivatives are all unknown, and so must be searched over. I.e., the unknown parameters are the sky location (θ, ϕ) , four parameters describing the amplitude, polarization, and overall phase of the waves (these can be usefully thought of as two complex amplitudes—one for each GW polarization), and the gravitational wave frequency and frequency derivatives at any instant: $f, \dot{f}, \ddot{f}, \overset{\cdot\cdot\cdot}{f}$, etc. The typical magnitude of frequency derivatives is assumed to be $d^n f/dt^n \sim f/\tau^n$, where τ is some characteristic timescale (basically the NS’s spindown-age), but these derivatives are otherwise considered independent.

For GW pulsars, we briefly describe the most efficient schemes that have been considered to-date, which are semi-coherent and hierarchical (i.e., multi-stage) searches; we refer to (Cutler et al.; 2005) for more details. A “semi-coherent” search is one where short data stretches (say, a few days long) are all coherently searched, using some technique akin to matched filtering, and then the resulting powers from the different stretches are summed. The method is only “semi-coherent” because powers are added instead of complex amplitudes; i.e., information regarding the overall phase of the signal in different stretches is discarded. This allows one to use a much coarser grid on parameter space than would be required in a fully coherent search of the same data. The basic idea of multi-stage searches is as follows. In the first stage one searches, semi-coherently, through some fraction of the data (say, a month’s worth), and identifies promising “candidates” in parameter space. One then follows up these candidates in the second stage, using a higher resolution on parameter space (a finer grid) and more data. This generates a second, sublist of candidates, which one then investigates with even higher resolution and yet more data, and so on. The idea is to reject unpromising regions in parameter space as quickly as possible, so as not to waste valuable computer resources on them. After N_s semi-coherent stages like

this, any remaining candidates are verified using a final, fully coherent follow-up search in a very tiny region of parameter space. A priori, the best value for N_s is unclear; it was shown in (Cutler et al.; 2005) that for realistic GW pulsar searches, the gains from increasing N_s saturate at $N_s = 3$ semi-coherent stages.

The GW signal from a NS binary is practically the same as the signal from a low-frequency GW pulsar (except the binary's orbital frequency changes on a much shorter timescale than the spin-period of slowly rotating NSs). In both cases, the signal is essentially monochromatic at any instant, with a frequency that is slowly time-varying. In both cases there is an unknown sky position, two unknown complex amplitudes (equivalent to D , θ_L , ϕ_L , and Φ_0 in the NS-binary case). The optimal statistic for searching over the two complex (four real) amplitudes, in both the GW-pulsar and NS-binary cases, is the F-statistic, which follows a chi-squared distribution with 4 degrees of freedom (Bose et al.; 2000; Cutler and Schutz; 2005). (The distribution is the same no matter how many detectors are combined in the analysis; the 4 d.o.f. correspond to the 2 complex – or 4 real – unknown amplitude parameters. The fact that BBO is composed of 4 LISA-like constellations outputting 12 independent data streams does not affect this counting.) The biggest difference between the two sources is that for actual GW pulsars, the signal's intrinsic amplitude can be approximated as constant over the observation time, while in the NS-binary case, the GW amplitude grows significantly during the observation time. However we do not consider this difference as very important when comparing detection thresholds, especially because the search sensitivity is really set by the early stages, where the coherent integration times will be significantly shorter than one year.

The sensitivity of the GW-pulsar search is limited by the size of the parameter space one wishes to search; e.g., for an all-sky search, the size of the parameter space is set by the maximum frequency f_{\max} and the shortest spin-down age τ_{\min} that one wishes to search over. We now try to choose a search-space that makes the LIGO GW pulsar search comparable in difficulty to the BBO NS-binary search. The pulsar parameters (\dot{f} , \ddot{f} , $\ddot{\dot{f}}$) are closely analogous to the NS-binary parameters (\mathcal{M} , μ , β), which control the inspiral rate. Assuming a search up to frequency $f_{\max} = 1000$ Hz, and an observation time of $T_0 = 1$ yr, we estimate $n_{\dot{f}} n_{\ddot{f}} n_{\ddot{\dot{f}}} \sim (f_{\max} T_0)^3 (T_0 / \tau_{\min})^6 \sim 3 \times 10^{31} (1 \text{ yr} / \tau_{\min})^6$. Using the estimates from Eq. (4.89), we find that $n_{\dot{f}} n_{\ddot{f}} n_{\ddot{\dot{f}}} \sim n_{\ln \mathcal{M}} n_{\ln \mu} n_{\beta}$ for $\tau_{\min} \sim 300$ yr.

Continuing our comparison of the LIGO/pulsar and BBO/binary searches, we note that because three of BBO's four constellations have separations of order 1 AU (≈ 500 s), the number of distinct patches on the sky that must be searched over is $\sim (4\pi)(2\pi \times 0.3 \text{ Hz} \times 500 \text{ s})^2 \sim 10^7$. In comparison, for GW pulsar searches, the number of distinct sky patches is set by the Earth's rotation about its axis, and is $\sim 3 \times 10^4$, or roughly 300 times fewer. (This counting assumes that the larger, but more slowly varying, Doppler shift due to Earth's motion around the Sun can be absorbed into the unknown pulsar spin-down parameters, which should be true for integration times shorter than a few months. This is good enough for our purposes, since the sensitivity of the search is really set at early stages, where only a month or two of data is examined.) On the other hand, assuming sampling at ~ 10 Hz for BBO and sampling at ~ 3 kHz for the LIGO network, a year-long GW pulsar template contains ~ 300 times as many points as a year-long BBO NS-binary template, so each coherent integration requires about 300 times more floating point operations in the LIGO/pulsar case than in the BBO/binary case.

Therefore we conclude that a LIGO/pulsar search for unknown NSs, over a parameter range set by ($f_{\max} = 1000$ Hz, $\tau_{\min} = 300$ yr), is comparable in difficulty, computationally, to the BBO/binary search. The code used by (Cutler et al.; 2005) to calculate the efficiencies of multi-stage GW pulsar searches was re-run for this parameter range, assuming an available computational power of 10^{17} flops (and computation time of one year). For this parameter range and computational power, LIGO/pulsar search with 3 semi-coherent stages (plus a final, coherent follow-up) should be able to detect GW pulsars with ρ as small as 20 (with false-dismissal rate = 10% and false-alarm rate = 1%). Therefore we estimate that BBO will *also* be able to detect and remove NS binaries with $\rho > \rho_{\text{th}} = 20$ (or roughly 50% higher than the minimum $\rho_{\text{th}} \sim 13$ required for detection confidence).

However: as in the last subsection, one could complain that we have counted only the cost of searching for 'typical' binaries, whereas in practice most of the computational budget may be spent on searching for the few atypical ones. Also, we have assumed (reasonably, we think, but without justification) that the computational cost of identifying all the individual sources is greater than (or at least comparable to) the cost of finding the combined best fit. Also, the comparison was made for a single false-dismissal rate (10%), whereas we imagine that, in actual practice for the BBO analysis, one would want to do the BBO analysis in stages, with an ever-decreasing FD rate. Also, actual BBO searches may be plagued by many more outliers than would be present for the purely Gaussian noise that our sensitivity estimates were based on, and this would increase the threshold. For all these reasons, and because our method of estimating $\rho_{\text{th}} \approx 20$ "by analogy" was so crude in the first place, we will investigate the efficacy of NS-binary subtraction for a range of detection thresholds: $\rho_{\text{th}} = 20, 30, \text{ or } 40$.

4.7 Equations of Self-Consistent Subtraction Scheme

Fix the values of the merger rate \dot{n}_0 (which sets the overall magnitude of $S_{\text{h}}^{\text{NSm}}$) and the detection threshold ρ_{th}^2 . We want to calculate what fraction F^2 of the spectral density of the NS-binary foreground *cannot* be subtracted. For simplicity, we will assume that all NSs have mass $1.4M_{\odot}$. Then our method for self-consistently determining F^2 proceeds by the following steps. Step 1: Adopt some initial "guess" value F_{G}^2 . Based on this guess, we obtain a corresponding guess for the total noise level:

$$S_{\text{h}}^{\text{tot}}(F_{\text{G}}, f) = S_{\text{h}}^{\text{inst}}(f) + F_{\text{G}}^2 \cdot S_{\text{h}}^{\text{NSm}}(f) \quad (4.90)$$

Step 2: Based on this total noise level, we determine the redshift $\bar{z}(\mu)$, out to which a NS-binary with orientation $\mu \equiv \hat{L} \cdot \hat{N}$ can be detected. This boundary $\bar{z}(\mu)$ (separating detectable and undetectable sources) is determined by the equation (derived in Appendix D):

$$\rho_{\text{th}}^2 = 8 \cdot \frac{2f(\mu)}{3\pi^{4/3}} \frac{(\mathcal{M}(1 + \bar{z}))^{5/3}}{D_L^2(\bar{z})} \int_0^{\infty} df \frac{f^{-7/3}}{S_{\text{h}}^{\text{tot}}(F_{\text{G}}, f)}. \quad (4.91)$$

where the function $f(\mu)$ gives the dependence of the squared waveform amplitude on μ :

$$f(\mu) \equiv \frac{(1 + \mu^2)^2 + 4\mu^2}{\int_0^1 d\mu [(1 + \mu^2)^2 + 4\mu^2]} = \frac{5}{16}(\mu^4 + 6\mu^2 + 1). \quad (4.92)$$

Note we have normalized $f(\mu)$ so that $\int_0^1 f(\mu)d\mu = 1$.

Step 3: We compute the fraction F^2 of the NS-binary foreground that is due to sources more distant than $\bar{z}(\mu)$. Based on Eqs. (10) and (12) in (Phinney et al.; 2003), this fraction is easily seen to be

$$F^2 = \frac{S_h^{\text{NSm}, > \bar{z}}(f)}{S_h^{\text{NSm}}} = \frac{1}{C(0)} \int_0^1 d\mu f(\mu)C(\bar{z}(\mu)), \quad (4.93)$$

in terms of the integral

$$C(\bar{z}) \equiv \int_{\bar{z}}^{\infty} dz \frac{r(z)}{(1+z)^{4/3}H(z)}. \quad (4.94)$$

where $H(z)$ and $r(z) \equiv \dot{n}(z)/\dot{n}_0$ are given explicitly in Eqs. (4.34) and (4.39), respectively.

So far, we have given an algorithm for computing $F(F_G)$, i.e., for iteratively improving our initial guess F_G . An initial guess F_G leads to a self-consistent solution if $F(F_G) = F_G$. Clearly, we can short-cut the iterative procedure simply by looking for fixed points of this function. I.e., our last step is

Step 4: Plot $F(F_G)$, and look for fixed points, i.e., values F_G such that $F(F_G) - F_G = 0$.

Our results are displayed in the next section.

4.8 Evaluation of Self-Consistent Subtraction Scheme

As motivated in previous sections, we calculate the efficacy of foreground subtraction for 3 different values of the present-day merger rate density, $\dot{n}_0 = \{10^{-8}, 10^{-7}, 10^{-6}\} \text{yr}^{-1} \text{Mpc}^{-3}$, and 3 values of the detection threshold, $\rho_{\text{th}} = \{20, 30, 40\}$. This yields 9 different results for the self-consistent F representing the fraction of the foreground noise amplitude due to undetectable (and hence unsubtractable) NS binaries. We calculate these results both for the ‘‘standard BBO’’ design sensitivity, $S_h^{\text{st.inst}}(f)$, shown in Figure 4.5, and for a less sensitive version having $S_h^{\text{inst}} = 4 \times S_h^{\text{st.inst}}(f)$, i.e., with $2 \times$ higher instrumental noise amplitude. As a shorthand, we will refer to the latter as ‘‘standard/2’’ sensitivity. Our main results are presented in subsection 4.8.1. In subsection 4.8.2 we gain insight into our results by exploring *which* binaries (i.e., which z and μ) are undetectable, for different \dot{n}_0 and ρ_{th} . Finally, in subsection 4.8.3, we consider the case of a larger foreground, $\dot{n}_0 = 10^{-5} \text{yr}^{-1} \text{Mpc}^{-3}$; although this merger rate is unrealistically high, this case provides a rather interesting illustration of our general method.

4.8.1 Efficacy of Background Subtraction for BBO

In [subsection 4.6.2](#) we showed that self-consistent F values are fixed points of the function $F(F_G)$, where F_G denotes a "guessed" value for this fraction. For standard BBO sensitivity, we find that the solution F is practically independent of \dot{n}_0 , for realistic merger rates. Specifically, we find

$$\begin{aligned} F_{20} = F_{30} &= 0, \\ F_{40} &= 0.0015, \end{aligned} \tag{4.95}$$

where our notation is that F_{20} is the solution F for $\rho_{\text{th}} = 20$, assuming the standard BBO instrumental noise level, and similarly for F_{30} and F_{40} . Therefore standard BBO is sensitive enough that the NS-NS foreground can be entirely (or almost entirely) subtracted, independent of the merger rate or detection threshold (for realistic values of those quantities).

Next we consider BBO with "standard/2" sensitivity. We denote by F'_{20} the self-consistent solution for $\rho_{\text{th}} = 20$ and standard/2 sensitivity, and similarly for F'_{30} and F'_{40} . For this case, the results do generally depend on \dot{n}_0 (unlike for standard BBO). Our nine results for F' , corresponding to the nine combinations of $(\dot{n}_0, \rho_{\text{th}})$, are given in [Table 4.2](#). To illustrate how these results are derived, in [Figure 4.8](#) we show the function $F(F_G) - F_G$ for each \dot{n}_0 , and for fixed $\rho_{\text{th}} = 30$. The entries in the second row of [Table 4.2](#) are just the the F_G values where the three curves in [Figure 4.8](#) pass through zero.

		$S_{\text{h}}^{\text{inst}} = 4 \cdot S_{\text{h}}^{\text{st.inst}}$		
		10^{-8}	10^{-7}	10^{-6}
ρ_{th}	\dot{n}_0			
20		0.0015	0.0015	0.0015
30		0.071	0.077	0.11
40		0.15	0.17	0.55

Table 4.2: Results for "standard/2" sensitivity. Table lists $F' = (S_{\text{h}}^{\text{NSm}, > \bar{z}} / S_{\text{h}}^{\text{NSm}})^{1/2}$ for different combinations $(\dot{n}_0, \rho_{\text{th}})$. F' is the amplitude of confusion noise from unsubtractable NS binaries, divided by the total foreground amplitude.

None of the F' values in [Table 4.2](#) is zero; which ones are sufficiently small that unsubtracted binaries would not significantly interfere with BBO's main goal? To answer this, in [Table 4.3](#) we give the ratio $[S_{\text{h}}^{\text{NSm}, > \bar{z}}(f) / S_{\text{h}}^{\text{GW}}(f)]^{1/2}$, evaluated at $f = 1$ Hz, for each combination $(\dot{n}_0, \rho_{\text{th}})$. Again, $S_{\text{h}}^{\text{NSm}, > \bar{z}}(f) \equiv (F')^2 S_{\text{h}}^{\text{NSm}}(f)$, while in [Table 4.3](#) $[S_{\text{h}}^{\text{GW}}(f)]^{1/2}$ is the noise spectrum for a primordial background with $\Omega_{\text{GW}}(f) = 10^{-15}$. Thus, ratios smaller than one indicate that the unsubtracted piece of the foreground is smaller than a primordial background with this energy density. We see that if $\rho_{\text{th}} = 20$ (i.e., if the detection pipeline can uncover almost all NS binaries with total SNR = 20), then even

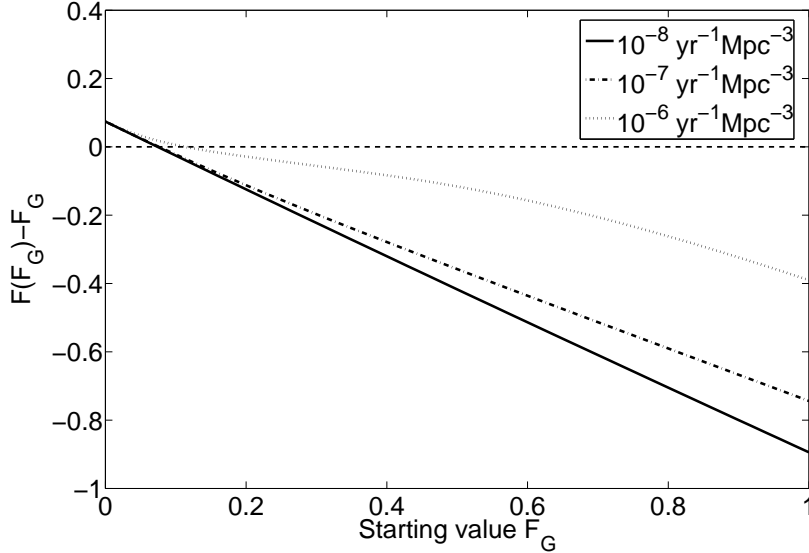


Figure 4.8: Shows the function $F(F_G) - F_G$ for three merger rates: $\dot{n}_0 = \{10^{-8}, 10^{-7}, 10^{-6}\} \text{ yr}^{-1} \text{ Mpc}^{-3}$. All curves are for “standard/2” sensitivity and detection threshold $\rho_{\text{th}} = 30$.

with standard/2 sensitivity, BBO would still be able to detect a primordial background having $\Omega_{\text{GW}}(f) \geq 10^{-15}$.

However [Table 4.3](#) also shows that if $\rho_{\text{th}} = 30$ or 40, and instrumental sensitivity is standard/2, then BBO would be unable to detect primordial background of $\Omega_{\text{GW}}(f) \sim 10^{-15}$ (since it would be “covered up” by the unsubtractable part of the foreground).

We point out that entries for the case ($\dot{n}_0 = 10^{-8}, \rho_{\text{th}} = 20$) in [Tables 4.2](#) and [4.3](#) should not be taken too literally, since in that case our solution F' corresponds to less than one unsubtracted binary. (A single merging NS binary at $z = 5$, even with $\mu = 0$, contributes $\sim 10^{-18}$ to our local $\Omega_{\text{GW}}(f)$, in the BBO band.) What this means, of course, is that our solution F' lies outside the range of validity of our equations, whose derivation implicitly assumed that at least one source was undetectable. Just as clearly, our main conclusions are unaffected. The proper interpretation of the ($\dot{n}_0 = 10^{-8}, \rho_{\text{th}} = 20$) entries is that, for these values, BBO with standard/2 sensitivity would likely detect every single NS-NS merger occurring on its past light cone.

We also repeated the above analysis for BBO with only standard/4 sensitivity, i.e, with $S_{\text{h}}^{\text{inst}}(f) = 16 \cdot S_{\text{h}}^{\text{st.inst}}(f)$. This noise level is clearly inadequate, since even for $\rho_{\text{th}} = 20$ and a low merger rate, $\dot{n}_0 = 10^{-8} \text{ yr}^{-1} \text{ Mpc}^{-3}$, we find $[S_{\text{h}}^{\text{NSm}, > \bar{z}}(f) / S_{\text{h}}^{\text{GW}}(f)]^{1/2} \approx 3.0$ at $f = 1 \text{ Hz}$, for $\Omega_{\text{GW}}(f) = 10^{-15}$.

4.8.2 Further Analyses of the Subtraction Scheme

Here we expand on the results of the previous subsection, to improve understanding. In [Figure 4.9](#) we plot the SNR of NS binaries having $\mu = 0$ (i.e, those seen edge-on:

ρ_{th}	\dot{n}_0	$S_{\text{h}}^{\text{inst}} = 4 \cdot S_{\text{h}}^{\text{st.inst}}$		
		10^{-8}	10^{-7}	10^{-6}
20		0.030	0.10	0.30
30		1.4	4.9	22
40		3.0	11	110

Table 4.3: Table of ratios $[S_{\text{h}}^{\text{NSm}, > \bar{z}}(f)/S_{\text{h}}^{\text{GW}}(f)]^{1/2}$ evaluated at $f = 1$ Hz, for BBO with standard/2 sensitivity. Here $S_{\text{h}}^{\text{GW}}(f)$ is from a primordial background with $\Omega_{\text{GW}}(f) = 10^{-15}$. Ratios smaller than one indicate that the unsubtractable part of the NSm foreground noise is smaller than this primordial background level. The results here are equivalent to those in [Table 4.2](#).

the least detectable case) as a function of z , under three different assumptions. The lowest curve (solid line) assumes standard BBO instrumental noise and assumes that the foreground confusion noise is the full $S_{\text{h}}^{\text{NSm}}(f)$ (i.e., the level before any subtraction), with $\dot{n}_0 = 10^{-7} \text{ yr}^{-1} \text{ Mpc}^{-3}$. In this case, assuming $\rho_{\text{th}} = 30$, all binaries out to $z \approx 1.5$ could be detected, even without first subtracting out the brightest sources. (And of course, the binaries with more favorable orientations could be detected even farther out.) In an iterative subtraction scheme, one would begin by subtracting out all the high-SNR sources, which would lower the total noise and allow one to “look deeper” in succeeding iterations. For standard BBO, this iterative scheme reaches the point where there are *zero*, or almost zero, unsubtracted sources, and then the total noise is just the instrumental noise.

The SNR for this “instrumental noise only” case is shown in the upper (dot-dashed) curve in [Figure 4.9](#). From this curve one sees immediately that $F = 0$ is indeed a self-consistent solution: even the sources with $\mu = 0$ at $z = 5$ are detectable. What [Figure 4.9](#) *cannot* show is whether $F = 0$ is the *only* self-consistent solution, but the rest of our analysis shows that this is true (again, for standard BBO sensitivity and $\rho_{\text{th}} \leq 30$). This has the practical implication that our envisioned iterative subtraction procedure should not get “stuck” at some higher F value: it can keep going until all binaries have been removed. The situation for standard/2 sensitivity is different, as illustrated by the middle (dotted) curve, which corresponds to the case $\rho_{\text{th}} = 30$ and $\dot{n}_0 = 10^{-7} \text{ yr}^{-1} \text{ Mpc}^{-3}$. For this case $F' = 0.077$, so the unsubtractable foreground noise is small compared to the instrumental noise, and the SNRs are roughly half the standard-BBO values. But then the $\mu = 0$ binaries can only be detected to $z \approx 2.2$.

The distribution of unsubtractable binaries, for BBO with standard/2 sensitivity, is explored further in [Figure 4.10](#), which shows the maximal redshift to which NS binaries can be detected, as a function of μ . The three curves are for our three detection thresholds: $\rho_{\text{th}} = 20, 30, 40$; all assume $\dot{n}_0 = 10^{-7} \text{ yr}^{-1} \text{ Mpc}^{-3}$. For $\rho_{\text{th}} = 20$ (solid curve), only a tiny corner of the (z, μ) -space contains sources too weak to be detected, and the number of sources occupying that corner would be of order one (for $\dot{n}_0 = 10^{-7}$). For $\rho_{\text{th}} = 30$ or 40,

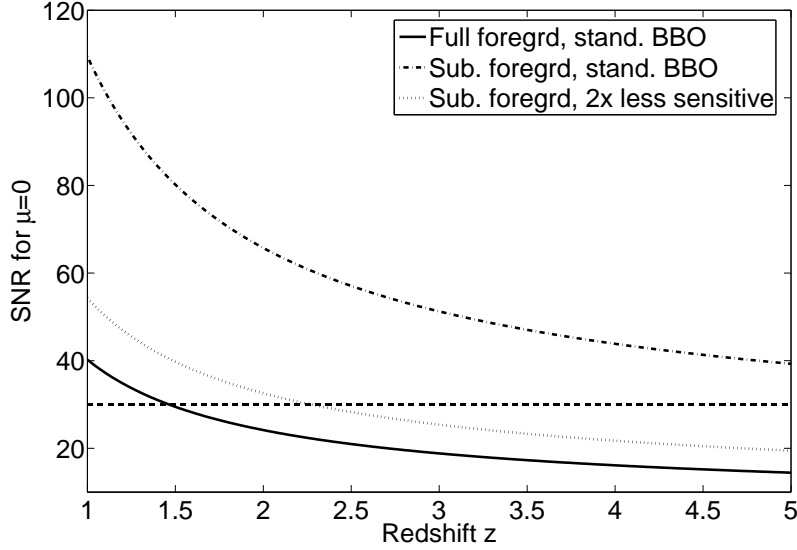


Figure 4.9: Shows the SNR ratio of NS-NS mergers with $\mu = 0$ in Eq. (4.91). The total noise level is different for each curve. The solid curve is for standard BBO instrumental noise plus confusion noise from *all* NS binaries. The dotted curve is for “standard/2” instrumental noise plus foreground corresponding to $\dot{n}_0 = 10^{-7} \text{ yr}^{-1} \text{ Mpc}^{-3}$, with $F'_{30} = 0.077$. The highest curve is for standard-BBO instrumental noise and zero foreground noise. The horizontal line just highlights $\text{SNR} = 30$.

the “undetectable regions” are clearly much larger, and contain several percent (or more) of all sources.

4.8.3 Confusion Noise from a Very Strong NSm Foreground

The results for F in Eq. (4.95) had basically no dependence on the merger rate \dot{n}_0 , and the F' results Table 4.2 showed only weak dependence on \dot{n}_0 , except at the highest values of \dot{n}_0 and ρ_{th} . The reason for this is simple: for BBO to succeed, the unsubtracted foreground noise must be smaller than the primordial background. Therefore, for BBO even to be “in the right ballpark”, the unsubtracted foreground must be well below the instrumental noise level. In this regime, the SNR of any source is set almost entirely by $S_{\text{h}}^{\text{inst}}$, and so is insensitive to \dot{n}_0 . Our results are consistent with the fact that, even with sensitivity degraded by a factor 2, BBO would still be “in the ballpark” (albeit insufficient for high ρ_{th}).

However the dependence of F on \dot{n}_0 becomes greater as one increases the merger rate, i.e., as unsubtractable binaries come to represent a significant fraction of the total noise. Because such cases display the full utility of our self-consistent method, we here show results for an unrealistically high merger rate: $\dot{n}_0 = 10^{-5} \text{ yr}^{-1} \text{ Mpc}^{-3}$. Figure 4.11 shows the function $F(F_{\text{G}}) - F_{\text{G}}$ for this \dot{n}_0 , for standard BBO instrumental noise, and for our 3 values of ρ_{th} . Interestingly, each curve now has two zeroes; i.e., each case has two self-

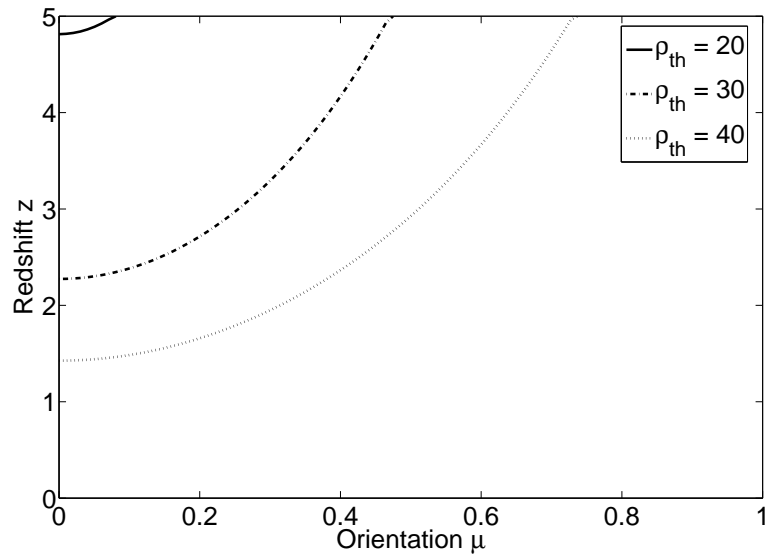


Figure 4.10: Graph displays the maximum distance to which NS binaries can be detected, as function of their orientation angle $\mu \equiv \hat{L} \cdot \hat{N}$, for three different detection thresholds ρ_{th} . Here the instrumental sensitivity is “standard/2” and the merger rate density is $\dot{n}_0 = 10^{-7} \text{ yr}^{-1} \text{ Mpc}^{-3}$ for all three curves.

consistent solutions. A moment’s thought, however, convinces one that the *larger* of the two solutions is the only one that is accessible by an iterative subtraction scheme. Such a scheme essentially starts at the right-most end of the curve and proceeds along it, moving to the left as sources are subtracted, until it reaches the first zero of $F(F_G) - F_G$. At that point, any undetected source is too deeply buried in the noise of the other undetected ones (plus the instrumental noise) to be identified. Otherwise stated: while you can self-consistently “be at” the lower- F_G solution, the class of schemes we are considering cannot “bring you there” (and we suspect that no scheme can). Thus, we see that in a universe with $\dot{n}_0 = 10^{-5} \text{ yr}^{-1} \text{ Mpc}^{-3}$, more than half the foreground noise would be unresolvable by standard BBO.

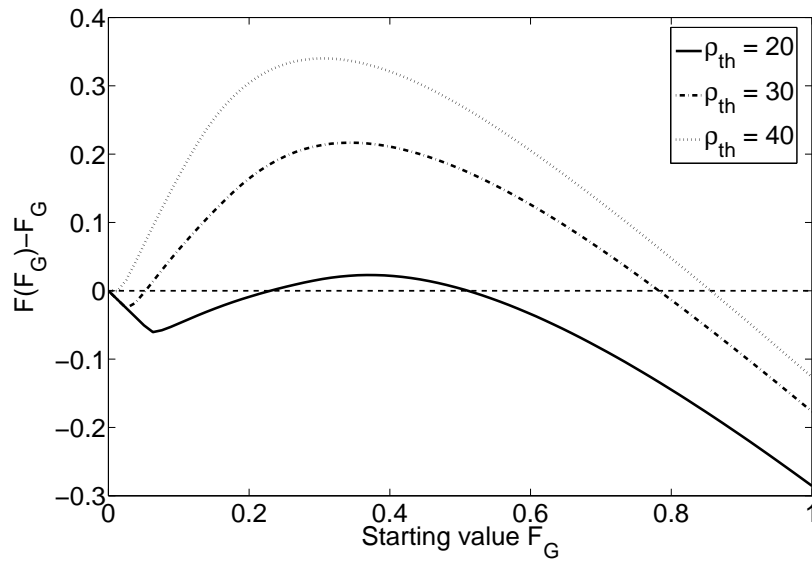


Figure 4.11: Plots $F(F_G) - F_G$ for an unrealistically high merger rate density, $\dot{n}_0 = 10^{-5} \text{ yr}^{-1} \text{ Mpc}^{-3}$. In contrast to cases with lower \dot{n}_0 , each curve now has two zeroes. However only the higher zero (larger F value) can be reached by an iterative subtraction scheme.

CHAPTER 5

Quantum Fluctuations of Light

The quantum nature of light inevitably leads to noise which cannot be reduced in the usual sense (i.e. by idealizing the set-up). Measuring the power of light means to count the number N of photons. Most counting processes follow a Poisson statistic with variance N . The photon counting error is also known as the shot noise of a power measurement. However, it is possible to apply certain transformations to the light before detection which change the counting statistics and thereby allow to decrease the counting error. The formal description of these transformations is outlined in the following.

The first section defines the quadrature-phase amplitudes and two-mode squeezed states which were first introduced in (Caves and Schumaker; 1985). These two quantities are the building blocks to describe light interferometers and to predict the quantum noise spectral density of phase sensitive photo detections. The spectral densities are evaluated as vacuum expectation values of transformed field operators. All relevant field transformations and notational conventions are introduced in section 5.2 focussing on the measurement of observables with two-photon coherent noise. In section 5.3, the notion of a quantum limit is introduced and we will try to understand by generic means how these limits arise and how they are surmounted. In section 5.4, we present relevant concepts of linear quantum measurement theory. The tools will help to characterize and understand complex dynamical behavior of advanced topologies (see Chapter 8). We conclude this chapter with section 5.5 where we introduce the phase space representation of light in a Kerr medium and then carry out explicitly a linearization of the interaction between light and medium.

5.1 Representations of the Electric Field

The electromagnetic field may be represented in many different ways. All representations are related by unitary transformations and one says that the field is represented in a certain quantum mechanical picture. We will make use of three different pictures: the Schrödinger picture, the modulation picture and the interaction picture. In fact, the

modulation picture is already a special interaction picture, but we use the terminology in a way that operators in the interaction picture are time independent as long as the field does not interact with other systems (e.g. a Kerr medium). We do not want to delve too deep into intricacies of the theory. We just introduce conventions which obtain throughout the thesis. Henceforth, all calculations are carried out for the electric field. Transformations of the magnetic field are derivable from the transformations of the electric field.

5.1.1 The Schrödinger Picture

In the Schrödinger picture the dynamical time evolution of a system is completely transferred onto the states. The free (scalar) field depends on the coordinate along the direction of propagation. The operator of the free electric field is usually decomposed into a positive (+) and a negative (-) frequency part

$$\hat{E}(x) = \hat{E}^{(+)}(x) + \hat{E}^{(-)}(x) \quad (5.1)$$

where the two frequency parts are related by $\hat{E}^{(+)}(x) = [\hat{E}^{(-)}(x)]^\dagger$. The electric field can be decomposed into annihilation and creation operators which act at certain frequencies ω

$$\hat{E}(x) = \sqrt{\frac{2\pi}{\mathcal{A}c}} \int_0^\infty \frac{d\omega}{2\pi} \sqrt{\hbar\omega} \left(\hat{a}(\omega) e^{i\omega x/c} + \hat{a}(\omega)^\dagger e^{-i\omega x/c} \right) \quad (5.2)$$

The amplitudes satisfy the well-known continuous parameter commutation relation

$$[\hat{a}(\omega), \hat{a}^\dagger(\omega')] = 2\pi\delta(\omega - \omega') \quad (5.3)$$

The quantization area \mathcal{A} usually corresponds to an effective cross section of the beam (i.e. a circle if the beam is Gaussian). The Schrödinger operators will serve as a basis to derive the operators of the modulation and interaction pictures. Whereas its amplitudes $\hat{a}(\omega)$ are frequently used quantities, the Schrödinger field $\hat{E}(x)$ is less important. In fact, later on the coordinate x will be set to zero in most cases since transformations on the field are derived in the modulation or interaction picture.

5.1.2 The Interaction Picture

The electric field operator in the interaction picture bears the free time evolution. The Hamilton operator of a free electric field is

$$\hat{H}_0 \equiv \int_0^\infty \frac{d\omega}{2\pi} \hbar\omega \hat{a}^\dagger(\omega) \hat{a}(\omega) \quad (5.4)$$

The Hamilton operator \hat{H}_0 is time independent. Therefore, transforming into the interaction picture is accomplished by

$$\begin{aligned} \hat{E}(x, t) &\equiv e^{i\hat{H}_0 t} \hat{E}(x) e^{-i\hat{H}_0 t} \\ &= \sqrt{\frac{2\pi}{\mathcal{A}c}} \int_0^\infty \frac{d\omega}{2\pi} \sqrt{\hbar\omega} \left(\hat{a}(\omega) e^{-i\omega(t-x/c)} + \hat{a}(\omega)^\dagger e^{i\omega(t-x/c)} \right) \end{aligned} \quad (5.5)$$

In this thesis, we consider weak interactions between light and optical elements in the sense that in a stationary state of the optical system the set of all transfer functions provide a complete description (i.e. interactions can be linearized with respect to the variables and the results are still accurate). Therefore, a transformation due to an interaction will be directly applied to the Schrödinger amplitudes of the field which then acquire an index τ corresponding to an interaction time. In some cases, the interaction time may equally well be substituted by a spatial interaction interval (Imoto et al.; 1985). Then, a thorough distinction between interaction times and the time parameter of the free evolution is not necessary.

5.1.3 The Modulation Picture

Photo detectors cannot produce current oscillations as fast as light oscillations (e.g. 10^{17} Hz). The observables derived from the electric field which determine the photo current must therefore oscillate at a much lower frequency. It turns out that the quadrature phases \hat{E}_1, \hat{E}_2 which describe modulations of a so-called carrier field at frequency ω_0 are measurable observables of the electric field. In terms of the quadrature phases the electric field in the interaction picture assumes the form

$$\hat{E}(x, t) = \hat{E}_1(x, t) \cos(\omega_0(t - x/c)) + \hat{E}_2(x, t) \sin(\omega_0(t - x/c)) \quad (5.6)$$

The detector which measures these quadrature phases is known as a phase sensitive (i.e. homodyne or heterodyne) detector. The coefficients which appear in Eq. (5.6) are time dependent. If one wanted to define the quadrature phase amplitudes \hat{a}_1, \hat{a}_2 , then these amplitudes would be time dependent in the Schrödinger picture. The interaction picture which works with time independent quadrature phase amplitudes is the modulation picture. Based on the Schrödinger amplitudes one obtains the modulation picture amplitudes via

$$\hat{a}_{1,2} = e^{i\hat{H}_R t} \hat{a}_{1,2}(t) e^{-i\hat{H}_R t} \quad (5.7)$$

which is a unitary transformation generated by the Hamilton operator

$$\hat{H}_R(\omega_0) \equiv \hbar\omega_0 \int_{\mathcal{M}} \frac{d\Omega}{2\pi} \left(\hat{a}^\dagger(\omega_0 + \Omega) \hat{a}(\omega_0 + \Omega) + \hat{a}^\dagger(\omega_0 - \Omega) \hat{a}(\omega_0 - \Omega) \right) \quad (5.8)$$

where we integrated over all modulation frequencies. Then, the expansion of the quadrature phases into its modulation picture amplitudes reads

$$\hat{E}_{1,2}(x, t) = \sqrt{\frac{4\pi\hbar\omega_0}{\mathcal{A}c}} \int_{\mathcal{M}} \frac{d\Omega}{2\pi} \left(\hat{a}_{1,2}(\Omega) e^{-i\Omega(t-x/c)} + \hat{a}_{1,2}^\dagger(\Omega) e^{i\Omega(t-x/c)} \right) \quad (5.9)$$

and the quadrature phase amplitudes in the modulation picture are related to the field amplitudes in the Schrödinger picture by

$$\hat{a}_1(\Omega) \equiv \sqrt{\frac{\omega_0 + \Omega}{2\omega_0}} \hat{a}(\omega_0 + \Omega) + \sqrt{\frac{\omega_0 - \Omega}{2\omega_0}} \hat{a}^\dagger(\omega_0 - \Omega) \quad (5.10)$$

$$\hat{a}_2(\Omega) \equiv -i \sqrt{\frac{\omega_0 + \Omega}{2\omega_0}} \hat{a}(\omega_0 + \Omega) + i \sqrt{\frac{\omega_0 - \Omega}{2\omega_0}} \hat{a}^\dagger(\omega_0 - \Omega) \quad (5.11)$$

Sections 5.2 and 7.3 will add physical meaning to quadrature phases and which kind of noise one expects to encounter in phase sensitive measurements. The energy normalization factors in front of the amplitudes are usually very close to one. Typical modulation frequencies do not exceed the MHz scale. Especially, the frequencies of gravitational waves measured by light interferometers lie at most in the acoustic range. In the literature, one often finds Eqs. (5.10)&(5.11) without energy normalization. Nevertheless, the low frequency limit ($\Omega \rightarrow 0$) does not yield the degenerate limit ($\Omega = 0$). Again, this is due to normalization issues (Caves and Schumaker; 1985). From Eq. (5.6) we conclude that the quadrature phases are the components of a two dimensional vector in a vector space with basis vectors \cos and \sin . We denote these vectors by

$$\bar{\mathbf{E}}(x, t) \equiv \begin{pmatrix} \hat{E}_1(x, t) \\ \hat{E}_2(x, t) \end{pmatrix} \quad (5.12)$$

The convention extends to amplitudes and fields in any of the quantum mechanical pictures. In this notation, linear transformations of the quadrature phases are represented by 2×2 -matrices. Most of the fundamental transformations possess a simple geometric interpretation in the quadrature vector space (see Chapter 6).

5.2 Vacuum and Squeezed Vacuum Noise

In this section, we investigate transformations due to ideal one-photon and two-photon processes. An interaction is considered as ideal if it is characterized by a c-number, i.e. if the field couples to a classical source. Although it is common usage to talk of coherent states and squeezed states, we actually restrict to work with one and only one state, the ground state (or vacuum state) $|0\rangle$ of the field. Consequently, expectation values of operators are obtained from the ground state which allows us to introduce the following convention

$$\langle \hat{O} \rangle \equiv \langle 0 | \hat{O} | 0 \rangle \quad (5.13)$$

We prefer to say squeezed vacuum or squeezed noise. Following this convention, we will see that it is the joint probability density function of the two quadrature phases which is squeezed and not the associated quantum state. Transformations are applied to operators. The unitary transformation of the ideal one-photon process is

$$D(\alpha) \equiv \exp(\alpha \hat{a}^\dagger - \alpha^* \hat{a}) \quad (5.14)$$

The operator $D(\alpha)$ is also known as the displacement operator. When acting on field amplitudes, it adds a c-number to the amplitude

$$D^\dagger(\alpha) \hat{a} D(\alpha) = \hat{a} + \alpha \quad (5.15)$$

which means that the expectation value of the amplitude is exactly changing by that number, but it does not change the spectral density of the field, i.e. it does not change

the mean square uncertainty of the amplitude (see below). Introducing the notation $\hat{a}_\pm \equiv \hat{a}(\omega_0 \pm \Omega)$, the ideal two-photon process is defined as

$$S(r, \phi) \equiv \exp \left(r(\hat{a}_+ \hat{a}_- e^{-2i\phi} - \hat{a}_+^\dagger \hat{a}_-^\dagger e^{2i\phi}) \right) \quad (5.16)$$

The two-mode squeezing operator $S(r, \phi)$ is parameterized by two real numbers: the squeezing factor r and the squeezing phase ϕ . It transforms field amplitudes according to

$$S^\dagger(r, \phi) \hat{a}_\pm S(r, \phi) = \hat{a}_\pm \cosh(r) - \hat{a}_\mp^\dagger e^{2i\phi} \sinh(r) \quad (5.17)$$

An alternative representation of the transformation Eq. (5.17) is found when we look at the transformation of a quadrature amplitude vector

$$S^\dagger(r, \phi) \bar{\mathbf{a}} S(r, \phi) = \underbrace{\begin{pmatrix} \cosh(r) - \frac{1}{2} \sinh(r) m_+ & -\frac{i}{2} \sinh(r) m_- \\ -\frac{i}{2} \sinh(r) m_- & \cosh(r) + \frac{1}{2} \sinh(r) m_+ \end{pmatrix}}_{\bar{\mathbf{S}}(r, \phi)} \cdot \bar{\mathbf{a}} \quad (5.18)$$

$$m_\pm = e^{-2i\phi} \sqrt{\frac{\omega_0 - \Omega}{\omega_0 + \Omega}} \pm e^{2i\phi} \sqrt{\frac{\omega_0 + \Omega}{\omega_0 - \Omega}}$$

The matrix has unit determinant and eigenvalues $\lambda_{1,2} = \exp(\pm r)$. The trace of the matrix provides a simple tool to extract the squeezing factor from the transformation

$$\text{Tr} [\bar{\mathbf{S}}(r, \phi)] = 2 \cosh(r) \quad (5.19)$$

A squeezed field has stationary quadrature phase noise, but due to Eq. (5.6) it has non-stationary amplitude noise. The fluctuations of the two phases are correlated unless one measures along the principle axes of the squeezing ellipse (the fluctuations of the quadrature phases of a coherent field are uncorrelated). A schematic representation of these properties is given in Figure 5.1. It shows the decomposition of the squeezed noise in the principle system of the squeezing ellipse. Each of the two principle quadratures is represented in a phase space spanned by the real and imaginary part of its amplitude. The quadrature noise amplitudes differ by an amount which depends on the squeezing factor r .

In general, a transformation \mathbf{T} acting on the field amplitudes embodies mirror coupling relations, propagations, optomechanical coupling matrices, ... which are introduced in Chapter 6. As mentioned before, the noise spectral densities (analogously, variance-covariance matrices) are evaluated as vacuum expectation values of transformed field observables. Focussing on the spectral density matrix of a quadrature vector, the spectral density of the transformed field $S(\mathbf{T} \cdot \bar{\mathbf{v}})$ expressed in terms of the initial vacuum density $S(\bar{\mathbf{v}}) = \mathbb{I}$ reads

$$\begin{aligned} S(\mathbf{T} \cdot \bar{\mathbf{v}}) &= \frac{1}{2} \left(\mathbf{T} \cdot S(\bar{\mathbf{v}}) \cdot \mathbf{T}^\dagger + \mathbf{T}^* \cdot S(\bar{\mathbf{v}}) \cdot \mathbf{T}^\text{T} \right) \\ &= \frac{1}{2} \left(\mathbf{T} \cdot \mathbf{T}^\dagger + \mathbf{T}^* \cdot \mathbf{T}^\text{T} \right) \end{aligned} \quad (5.20)$$

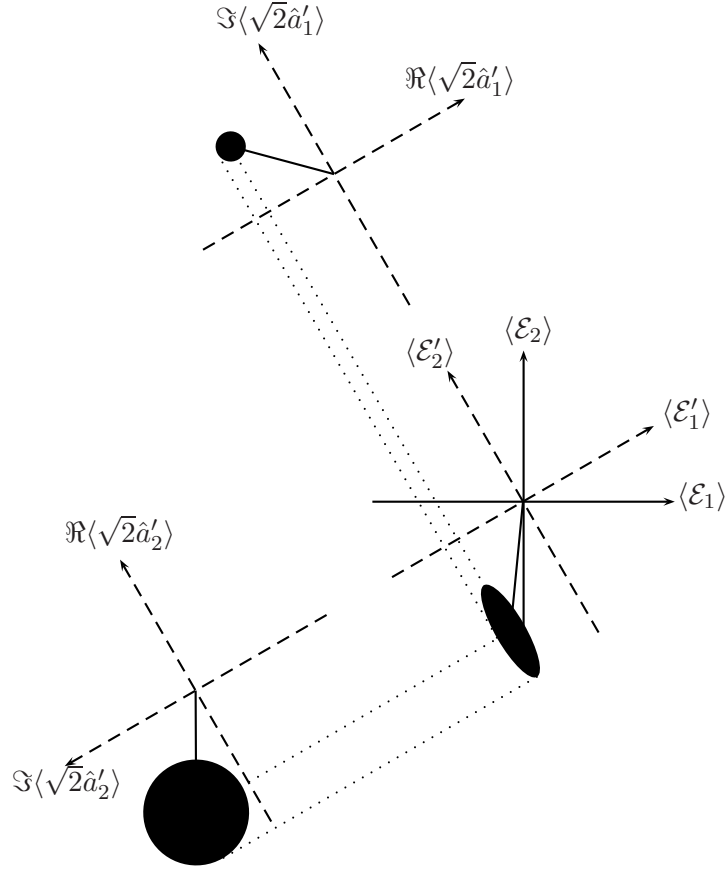


Figure 5.1: The figure shows the quadrature space representation of a squeezed field with classical excitation. The (normalized) quadrature phases $\mathcal{E}'_1, \mathcal{E}'_2$ of the principle system are oriented along the principle axes of the squeezing ellipse. Each quadrature phase is characterized by stationary noise whose noise amplitudes depend on the squeezing factor (i.e. the deformation of the squeezing ellipse).

The diagonal components of 2×2 -matrix $S(\mathbf{T} \cdot \bar{\mathbf{v}})$ correspond to the spectral densities of the field's amplitude and phase quadrature. Off-diagonal components are due to correlations between the two quadratures. Certainly, a matrix $S(\bar{\mathbf{a}})$ also governs the spectral density of any measured linear combination $\hat{a}_\zeta = \cos(\zeta)\hat{a}_1 + \sin(\zeta)\hat{a}_2$ of the field where ζ denotes the homodyning angle (see [Chapter 7](#)):

$$S(\hat{a}_\zeta) = (\cos(\zeta) \ \sin(\zeta)) \cdot S(\bar{\mathbf{a}}) \cdot \begin{pmatrix} \cos(\zeta) \\ \sin(\zeta) \end{pmatrix} \quad (5.21)$$

In some cases, it may even be advantageous to choose the angle ζ in a frequency dependent way. By intuition one might expect that an optimized choice for ζ always corresponds to

a projection into the principle system and then measuring the quadrature with minimal noise. However, since we really want to measure a signal which is distributed among the two quadratures, one has to take into account that the signal might be weaker in a quadrature with less noise and that a calculation of the optimized homodyning angle is a little more complicated. This proposition due to (Kimble et al.; 2001) is further investigated in subsection 8.1.3.

5.3 Quantum Limits

The notion of quantum limits has changed considerably over the years. Today, quantum limits are useful benchmarks to rate the performance of real measurement devices, but nobody expects that quantum mechanics ultimately limits the sensitivity of GW detectors – limits just exist for specific optical configurations. The most generic answer to the question how quantum mechanics enforces a limit on the sensitivity of a certain measurement device is given by means of linear quantum measurement theory (see section 5.4).

One defines standard quantum limits for coordinate measurements of free masses or harmonic oscillators (Braginsky and Khalili; 1999b), or evaluates limits based on detailed analyzes of more complex objects (Buonanno and Chen; 2002). In general, a quantum limit is imposed through a generalized Heisenberg inequality relating the second order noise moments of a pair of canonically conjugate variables \hat{p} , \hat{q}

$$S_{pp}(\Omega)S_{qq}(\Omega) - S_{pq}^2(\Omega) \geq 1 \quad (5.22)$$

where the second order noise moments of stationary quadrature noise is characterized by the spectral density matrix which – according to the Wiener-Khintchine theorem – can be written as the Fourier transform of the correlation between two quantities

$$S_{xy}(\Omega) = \int d\tau \langle \Delta \hat{x}(t + \tau) \Delta \hat{y}(t) \rangle_{\text{sym}} e^{-i\Omega\tau} \quad (5.23)$$

The derivation of the so-called standard quantum limit (SQL) is erected on two assumptions:

1. The canonically conjugate variables are uncorrelated $\rightarrow S_{pq} = 0$
2. The QM state has minimum uncertainty $\rightarrow S_{pp}(\Omega)S_{qq}(\Omega) = 1$

The two most important examples are the quantum limits for the coordinate measurement of a free test mass and of a harmonic oscillator. Measuring the position of a free test mass over a time τ or the coordinate of a harmonic oscillator whose eigenfrequency is ω_M , one obtains the following minimum uncertainty values for the respective coordinate measurement

$$\begin{aligned} \Delta \hat{X}_{\text{SQL}}^{\text{free}} &= \sqrt{\frac{\hbar\tau}{2m}} \\ \Delta \hat{X}_{\text{SQL}}^{\text{osc}} &= \sqrt{\frac{\hbar}{2m\omega_M}} \end{aligned} \quad (5.24)$$

Other variables – e.g. energies or momenta – can be measured with arbitrary precision by means of a quantum non-demolition (QND) device (Caves et al.; 1980). A QND measurement device does not act on the time evolution of the observed variable. A theoretical analysis has to furnish the QND variables of a detector-probe system and how the system has to be prepared initially. Despite of being poorly investigated in most of the proposed configurations for future generation gravitational-wave detectors, the quantum limit has important and well understood implications for current or next generation topologies (Jaekel and Reynaud; 1990).

We are going to investigate the measurement of an external classical force derived from the record of the oscillator's coordinate. The results were first presented in (Vyatchanin and Matsko; 1993). According to Figure 5.2, the oscillator is a mirror coupled to a spring (alternatively, it may be a suspended mirror) and the coordinate is sensed with a light beam reflected from the mirror. A displacement Δx of the mirror gives rise to a phase change

$$\Delta\phi = 2\frac{\omega\Delta x}{c} \quad (5.25)$$

of the reflected light which has frequency ω . The classical amplitude $A(t)$ at frequency ω_0

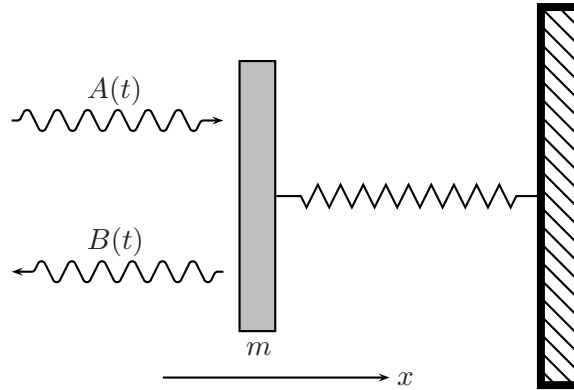


Figure 5.2: The light exerts a force onto the mirror when it is reflected. The apparatus measures the coordinate x of the mirror. The mirror is coupled to a spring and to a heat bath. The phase of the reflected light bears information about changes of the position of the mirror.

and the QM amplitudes $\hat{a}(\omega)$ of the incident field which is reflected from a perfect mirror are related to the respective outgoing quantities $B(t)$, $\hat{b}(\omega)$ by

$$\begin{aligned} A(t) e^{i\omega_0 x/c} + \int_0^\infty \frac{d\omega}{2\pi} \sqrt{\frac{2\pi\hbar\omega}{\mathcal{A}c}} \hat{a}(\omega) e^{-i(\omega-\omega_0)t+i\omega x/c} \\ = B(t) e^{-i\omega_0 x/c} + \int_0^\infty \frac{d\omega}{2\pi} \sqrt{\frac{2\pi\hbar\omega}{\mathcal{A}c}} \hat{b}(\omega) e^{-i(\omega-\omega_0)t-i\omega x/c} \end{aligned} \quad (5.26)$$

Assuming that $\omega_0 x/c \ll 1$, one obtains in the Fourier domain at sideband frequency $\omega_0 + \Omega$ an expression which relates the noise amplitudes $\hat{a}(\omega)$, $\hat{b}(\omega)$ including the amplitude $x(\Omega)$

of mirror displacements

$$\hat{b}(\omega_0 + \Omega) = \hat{a}(\omega_0 + \Omega) + 2i \frac{\omega_0 x(\Omega)}{c} \sqrt{\frac{P}{\hbar\omega_0}} \quad (5.27)$$

where P is the average power of the incident wave. The mirror forms part of a mechanical oscillator. The total force which acts on the mirror consists of the radiation-pressure force F_{rp} , a fluctuating force F_{th} which originates from the oscillator's coupling to a heat bath and finally the signal force F_{s} which is the aim of the measurement. The radiation-pressure force is given by

$$F_{\text{rp}} = \frac{2}{c} \left[P + \sqrt{P\hbar\omega_0} \int_{-\omega_0}^{\infty} \frac{d\Omega}{2\pi} \sqrt{1 + \frac{\Omega}{\omega_0}} \left(\hat{a} e^{-i\Omega t} + \hat{a}^\dagger e^{i\Omega t} \right) \right] \quad (5.28)$$

By virtue of the fluctuation-dissipation theorem, (Callen and Welton; 1951) or (Callen and Greene; 1952), the heat bath exerts a force which depends on the damping δ of the oscillator

$$F_{\text{th}} = 2 \int_0^{\infty} \frac{d\Omega}{2\pi} \sqrt{m\delta\hbar\Omega} \left(\hat{d} e^{-i\Omega t} + \hat{d}^\dagger e^{i\Omega t} \right) \quad (5.29)$$

The expectation values of the bosonic amplitudes is governed by the Bose-Einstein statistics

$$\langle \hat{d}^\dagger(\Omega) \hat{d}(\Omega') \rangle_{\text{sym}} = 2\pi \cdot \delta(\Omega - \Omega') \frac{1}{e^{\frac{\hbar\Omega}{k_{\text{B}}T}} - 1} \quad (5.30)$$

Solving the equation of motion of the mirror and substituting the result into Eq. (5.27), the reflected field in terms of the oscillator's susceptibility $\mathcal{Z}(\Omega) = \omega_{\text{M}}^2 - \Omega^2 - 2i\delta\Omega$ reads

$$\begin{aligned} \hat{b}(\omega_0 + \Omega) &= \hat{a}(\omega_0 + \Omega) \left(\frac{4i\omega_0 P}{mc^2 \mathcal{Z}(\Omega)} + 1 \right) + \hat{a}^\dagger(\omega_0 - \Omega) \frac{4i\omega_0 P}{mc^2 \mathcal{Z}(\Omega)} \\ &+ i \hat{d}(\Omega) \sqrt{2\Re \left(\frac{-4i\omega_0 P}{mc^2 \mathcal{Z}(\Omega)} \right)} \frac{|\mathcal{Z}(\Omega)|}{\mathcal{Z}(\Omega)} + i \sqrt{\frac{4P\omega_0}{\hbar}} \frac{F_{\text{s}}(\Omega)}{mc\mathcal{Z}(\Omega)} \end{aligned} \quad (5.31)$$

Henceforth, we consider the strong coupling regime $\mathcal{K} \equiv \left| \frac{4i\omega_0 P}{mc^2 \mathcal{Z}(\Omega)} \right| \gg 1$. Then, we have for the signal part $\hat{s}_\zeta(\Omega)$ of the reflected field in its ζ -quadrature

$$\hat{s}_\zeta(\Omega) = \sqrt{\frac{P\omega_0}{\hbar}} \frac{4F_{\text{s}}(\Omega)}{mc\mathcal{Z}(\Omega)} \sin \zeta \quad (5.32)$$

It is straightforward to write down the noise spectral density of the respective output quadrature \hat{b}_ζ and then normalize the expression with respect to the classical force F_{s} . Then, for signal frequencies $\omega_{\text{F}} \gg \omega_{\text{M}}$, we end up with the minimum noise of the squared force amplitude

$$F_{\text{min}}^2 = 4 \frac{\hbar\omega_{\text{F}} m \delta}{\tau} \left[(2n_{\text{T}} + 1) + \frac{1}{2} \left(\frac{1}{2\mathcal{K}} + 2\mathcal{K} \right) \right] \quad (5.33)$$

where τ is the observation time and n_T denotes the number of photons in the thermal bath. The pumping power can still be optimized yielding

$$\mathcal{K} \equiv \frac{8\omega_0 P}{mc^2} \frac{\delta \Omega}{|\mathcal{Z}|^2} = \frac{1}{2} \quad (5.34)$$

which entails a maximum sensitivity

$$F_{\min}^2 = 8 \frac{\hbar \omega_F m \delta}{\tau} (n_T + 1) \quad (5.35)$$

The optimum sensitivity for a lossless oscillator ($\delta = 0$) is found to be inversely proportional to the square-root of the pumping power P . In other words, there exist no sensitivity limit for force measurements when the oscillator has no dissipation.

5.4 Linear Quantum Measurements

In previous sections of this chapter, the measurement error or measurement noise is characterized by Heisenberg uncertainty relations of a generalized coordinate and momentum of the light field. However, this approach has to be established on more secure grounds. Especially, the link between measurement errors and inherent uncertainties of an object's quantum state has to be formulated. In the following, we are going to investigate linear quantum measurements where the measurement error and the perturbation of the object's momentum by the detector do not depend on the object's initial state (Braginsky and Khalili; 1999b). In some sense, a linear quantum measurement (LQM) corresponds to a classical transform (i.e. a transform determined by numbers) of object observables to the data storage device. All of the intriguing quantum phenomena (Misra and Sudarshan; 1977) which characterize more general detector – object interactions disappear. The first step is to distinguish the components of a measurement apparatus and then to derive equations of motion of the entire system assuming that the system behaves like a LQM apparatus. In order to solve the latter task, one has to procure a formal condition satisfied by LQM devices based on the definition given above. Our analysis is closely oriented along the lines of (Buonanno and Chen; 2002) who solved the equations of motion in the frequency domain and specified the results to interferometric gravitational-wave detectors.

Consider the following experiment (Figure 5.3). A classical force G (e.g. gravitational wave) acts on a probe (test mass) and leaves its mark in the probe's coordinate \hat{x} . A detector unit (interferometer) is designed to measure \hat{x} . In general, the detector exerts a back-action force \hat{F} (radiation-pressure force) on the probe. The coordinate \hat{Z} (output-light amplitude or photo-current amplitude) of the detector constitutes the output observable of the system.

In linear measurement theory, the coupling between the probe and the detector is linear and we also assume that the force G acts linearly on the coordinate \hat{x} . Linearity implies that the commutators among any of the operators \hat{Z} , \hat{x} and \hat{F} is a number (and therefore does not depend on the state of the system)

$$C_{AB}(t, t') \equiv [\hat{A}(t), \hat{B}(t')], \quad \hat{A}, \hat{B} \in \{\hat{Z}, \hat{x}, \hat{F}\} \quad (5.36)$$

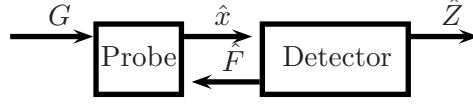


Figure 5.3: The picture shows a linear measurement scheme.

These commutators are also known as the susceptibilities of the system. The output observable is monitored continuously and stored classically which means that one has to impose the simultaneous measurability condition

$$C_{ZZ}(t, t') = 0 \quad (5.37)$$

By virtue of the linear coupling between the detector \mathcal{D} and the probe \mathcal{P} , the total Hilbert space can be factorized $\mathcal{H} = \mathcal{H}_{\mathcal{P}} \otimes \mathcal{H}_{\mathcal{D}}$ such that \hat{x} acts in a different Hilbert space than \hat{Z} , \hat{F} and their commutators vanish: $C_{xF} = C_{xZ} = 0$.

Finally, if the free Hamiltonian of the probe and the detector are time independent, then the remaining commutators are functions of $(t - t')$ only. Thereby, it is possible to switch to a linearized frequency-domain version of the equations of motion (Buonanno and Chen; 2002)

$$\begin{aligned} \hat{Z}^{(1)}(\Omega) &= \hat{Z}^{(0)}(\Omega) + R_{ZF}(\Omega) \cdot \hat{x}^{(1)}(\Omega) \\ \hat{F}^{(1)}(\Omega) &= \hat{F}^{(0)}(\Omega) + R_{FF}(\Omega) \cdot \hat{x}^{(1)}(\Omega) \\ \hat{x}^{(1)}(\Omega) &= \hat{x}^{(0)}(\Omega) + R_{xx}(\Omega) \cdot [G(\Omega) + \hat{F}^{(1)}(\Omega)] \end{aligned} \quad (5.38)$$

which are governed by the frequency-domain susceptibilities

$$R_{AB}(\Omega) = \frac{i}{\hbar} \int_0^{\infty} d\tau e^{i\Omega\tau} C_{AB}(0, -\tau) \quad (5.39)$$

The quantities $\hat{Z}^{(1)}$, $\hat{F}^{(1)}$, $\hat{x}^{(1)}$ on the left-hand side of Eq. (5.38) are subject to the full linearized time evolution, whereas the quantities $\hat{Z}^{(0)}$, $\hat{F}^{(0)}$, $\hat{x}^{(0)}$ correspond to a free evolution of the respective subsystem. The susceptibilities in Eq. (5.38) are evaluated on the operators subject to the free evolution.

Now, consider a detector which measures the coordinate of a free probe with reduced mass μ ($R_{xx} = -1/(\mu\Omega^2)$). Solving Eq. (5.38) for the coordinate $x^{(1)}$, one obtains

$$-\mu\Omega^2 \hat{x}^{(1)} - R_{FF} \hat{x}^{(1)} = -\mu\Omega^2 \hat{x}^{(0)} + G + \hat{F}^{(0)} \quad (5.40)$$

The perturbed probe behaves like an oscillator with a frequency dependent ponderomotive rigidity $-R_{FF}(\Omega)$ under the action of a quantization force $-\mu\Omega^2 \hat{x}^{(0)}$, a signal force G and a back-action force $\hat{F}^{(0)}$. The conventional Michelson interferometer is a detector with vanishing rigidity (Kimble et al.; 2001) whereas the detuned signal-recycled/signal-extracted

Michelson interferometer has a nonvanishing rigidity (Buonanno and Chen; 2001). Hence, a signal-recycled interferometer exhibits further resonances which arise due to the interaction of the probe and the detector. A detailed analysis of the detector is needed in order to specify R_{FF} – usually a complicated multi-parameter expression. In Chapter 6 and Chapter 7, a straightforward method is presented which yields an explicit solution of $\hat{Z}^{(1)}$ for various interferometric detectors.

5.5 Linearization of the Kerr Wigner Function

The Wigner function $W(q, p)$ is a phase-space representation of a quantum-mechanical system. Given a pure state $|\psi\rangle$, it is defined in terms of the Schrödinger wave function (Mandel and Wolf; 1995)

$$W(q, p) \equiv \frac{1}{2\pi\hbar} \int dx \psi^*(q - \frac{1}{2}x) \psi(q + \frac{1}{2}x) e^{ixp/\hbar} \quad (5.41)$$

In general, the Wigner function assumes positive and negative values. Therefore, it is called a quasi-probability density. However, its marginal integrals yield true probability densities, e.g.

$$\int dp W(q, p) = |\psi(q)|^2 \quad (5.42)$$

In the case of optical fields, the generalized coordinate and momentum are given by the real and imaginary part of the complex field amplitude α which is the eigenvalue of the field's annihilation operator \hat{a} (the eigenstates are the coherent states $|\alpha\rangle$). In contrast, Gaussian Wigner functions can be interpreted as a true joint probability density of coordinate and momentum. The width of a Gaussian Wigner function is associated with the standard deviation of a measurement. In many cases, Gaussian Wigner functions are excellent approximations to the true Wigner function of a system.

Let us consider the Wigner function of a field state inside a Fabry-Pérot cavity with Kerr medium. The theoretical model of the Kerr cavity is that of the anharmonic oscillator. For weak interactions between the light and the Kerr medium, one may try to find an approximate Wigner function. In section 6.6, we calculate the width of the Wigner function starting with a linearized treatment of the interaction. In this section, we are going to derive the linearized (therefore Gaussian) Wigner function from the full quantum-mechanical Wigner function which was first presented in (Kheruntsyan; 1999):

$$W(\alpha) \propto e^{-2|\alpha|^2} \cdot \left| \frac{J_{\lambda-1}(\sqrt{-8\epsilon\alpha^*})}{(\alpha^*)^{(\lambda-1)/2}} \right|^2 \quad (5.43)$$

The complex parameters λ and ϵ are defined in terms of the cavity detuning Δ , its linewidth γ , the amplitude E of the classical pump and the Kerr nonlinearity parameter χ'' (see Eq. (6.42): $\chi = 2\chi''$)

$$\begin{aligned} \lambda &\equiv \frac{\Delta}{\chi''} - i \frac{\gamma}{\chi''} \\ \epsilon &\equiv -i \frac{E}{\chi''} \end{aligned} \quad (5.44)$$

where we have neglected two-photon losses. Obviously, the Wigner function is a complicated expression which involves Bessel functions of the first kind. However, for our purpose, Bessel functions possess a very useful representation in terms of the confluent hypergeometric function of the first kind

$$J_\nu(z) = \frac{1}{\Gamma(\nu+1)} \left(\frac{z}{2}\right)^\nu {}_0F_1(\nu+1; -\frac{z^2}{4}), \quad -\nu \notin \mathbb{N}^+ \quad (5.45)$$

It follows that the Wigner function can be cast into the form

$$W(\alpha) \propto e^{-2|\alpha|^2} |{}_0F_1(\lambda; 2\epsilon\alpha^*)|^2 \quad (5.46)$$

Weak interaction means $\chi'' \ll 1$. Later, we are going to introduce further restrictions in order to guarantee that the approximation converges. Now, the function ${}_0F_1(\lambda; 2\epsilon\alpha^*)$ expands according to

$${}_0F_1(\lambda; 2\epsilon\alpha^*) = 1 + \frac{2\epsilon\alpha^*}{\lambda} + \frac{1}{2!} \frac{(2\epsilon\alpha^*)^2}{\lambda(\lambda+1)} + \frac{1}{3!} \frac{(2\epsilon\alpha^*)^3}{\lambda(\lambda+1)(\lambda+2)} + \dots \quad (5.47)$$

Together with Eq. (5.44), we transform the latter expansion into a power series for χ'' . Most suitably, one recollects the orders understanding the expansion as perturbation of the generating function. The zeroth order expression reads

$${}_0F_1(\lambda; 2\epsilon\alpha^*) = e^{2\epsilon\alpha^*/\lambda} + \mathcal{O}(\chi'') \quad (5.48)$$

Similarly, we find the following expression for the generating function up to first order of χ''

$${}_0F_1(\lambda; 2\epsilon\alpha^*) = e^{2\epsilon\alpha^*/\lambda - 2(\epsilon\alpha^*)^2/\lambda^3} + \mathcal{O}(\chi'')^2 \quad (5.49)$$

Inserting the zero order term into Eq. (5.46), we obtain the unperturbed Wigner function

$$W_0(\alpha) \propto \exp \left[-2 \left(\left(\Re\alpha - \frac{E\gamma}{\Delta^2 + \gamma^2} \right)^2 + \left(\Im\alpha + \frac{E\Delta}{\Delta^2 + \gamma^2} \right)^2 \right) \right] \quad (5.50)$$

which is a rotationally symmetric Gaussian function centered around a point whose coordinates are proportional to the power of the light inside the resonator. The first order term generates squeezing and rotation of the Wigner function. We are going to illustrate the squeezing for a Kerr resonator with $\Delta = 0$. Its Wigner function simplifies to

$$W_1(\alpha) \propto \exp \left[-2 \left(\left(\Re\alpha - \frac{E}{\gamma} \right)^2 + (\Im\alpha)^2 + \frac{4\chi'' E^2}{\gamma^3} \Re\alpha \Im\alpha \right) \right] \quad (5.51)$$

Now, the last term describes a correlation between the real and imaginary part of α . This correlation could be due to a simple rotation, but here it describes a squeezing which alters the width w of the Gaussian by $w \rightarrow w(1 \pm 2\chi'' E^2/\gamma^3)$ along two orthogonal directions of the coordinate system (in one direction the width increases, in the other the width decreases). Thereby, we managed to recover the linearized action of a Kerr medium – rotation and squeezing – from its full quantum-mechanical phase-space description.

CHAPTER 6

Optical Transferfunctions

In this chapter, we are going to derive a class of transfer functions which allows us to obtain a linearized description of light interferometers ([Chapter 7](#) & [Chapter 8](#)). Our intention is to focus on the two-photon (2P) formalism, but to compare the results with familiar equations of the one-photon (1P) formalism whenever it seems to be helpful. The reader who is not familiar with the two-photon formalism will recognize that the algebraic structure of the coupling equations is identical in both cases. The difference is that transfer functions in the 1P formalism map numbers whereas in the 2P formalism they map vectors. In fact, it should be obvious from [Chapter 5](#) that the only linear transformation which makes all the difference is the free propagation of the field. The first three sections aim towards a description of linear cavities wherefrom input-output relations like Eq. (3) in ([Meers; 1988](#)) can be calculated. Then, we are going to add radiation pressure effects and investigate the new coupling relations for mirrors. Finally, we consider third-order non-linearities in a more general context based on a rigorous linearization of the quantum-mechanical equations of motion. Throughout this chapter (and this line is followed throughout the entire thesis), we restrict to derive the transfer functions for scalar fields and decide to ignore the transversal mode structure of the beam. We believe that such details would not improve the applicability of results given here, but instead may lead to ignorance with respect to more important statements in this context.

6.1 The Propagation

As mentioned before, the substantial difference between the one- and two-photon formalism lies in the treatment of the propagation. It is suitable in any formalism to decompose the propagation into two parts. The idea stems from practical convenience to describe the properties of Fabry-Pérot cavities. The one part is the (microscopic) detuning δ of the path and the second part is directly related to the macroscopic length L of the path, see [Figure 6.1](#). The detuning as a parameter of the propagation denotes the phase shift

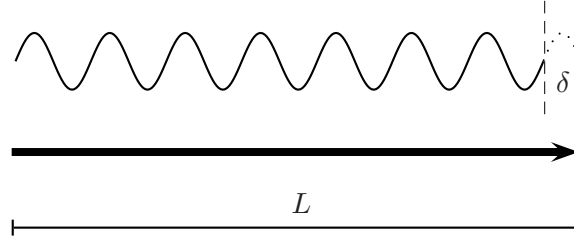


Figure 6.1: Introducing a reference frequency ω_0 (i.e. the carrier frequency of a field), the propagation is composed of a phaseshift $\exp(i\Omega L/c)$ depending on the sideband frequency relative to ω_0 and a microscopic phaseshift $\exp(i\delta)$ acting on all frequencies.

of amplitudes at a reference frequency ω_0 :

$$\hat{a}(\omega_0) \rightarrow e^{i\delta} \hat{a}(\omega_0), \quad \text{with } \delta = \omega_0 L/c \pmod{2\pi} \quad (6.1)$$

Now, the macroscopic length becomes important if one considers *relative* phase shifts between nearby frequencies. Consider amplitudes at $\omega = \omega_0 + \Omega$. Then, we obtain the following propagation

$$\hat{a}(\omega_0 + \Omega) \rightarrow e^{i(\delta + \Omega L/c)} \hat{a}(\omega_0 + \Omega) \quad (6.2)$$

Usually, Ω denotes a modulation frequency with $\Omega \ll \omega_0$. In [Chapter 5](#) we saw that if amplitudes at sideband frequencies $\omega_0 \pm \Omega$ are due to a modulation, then the 2P formalism provides a better description of the field. The propagation of the quadrature amplitudes can be deduced from [Eq. \(5.6\)](#) and [Eq. \(5.9\)](#)

$$\bar{\mathbf{a}}(\Omega) \rightarrow e^{i\Omega L/c} \begin{pmatrix} \cos(\delta) & -\sin(\delta) \\ \sin(\delta) & \cos(\delta) \end{pmatrix} \cdot \bar{\mathbf{a}}(\Omega) \quad (6.3)$$

Comparing the last two equations, we see that the phase shift at ω_0 of the field amplitudes is converted into a real rotation in the quadrature space. Remember that although the phase $\Omega L/c$ appears with both signs in the propagation of field amplitudes depending on whether one transfers the upper or lower sideband, the phase is always positive in the 2P formalism.

6.2 The Mirror Coupling Equations

Next, we deal with the coupling of fields at mirrors. Mirrors are thoroughly designed elements. A sequence of layers on each surface of the mirror ensures that these surfaces either obtain the property of being anti-reflective or a highly reflective ([Figure 6.2](#)). Henceforth, the reflective surface of the mirror is assumed to be flat and lossless. Therefore, our effective description of mirrors is that of a flat, lossless, reflecting surface. Losses may occur

when light transmits through the mirror substrate. In that case, one has to take account of them independently which means that losses are not embodied in the coupling relations. There exist different possibilities to couple the fields which are denoted by A, B, C, D in

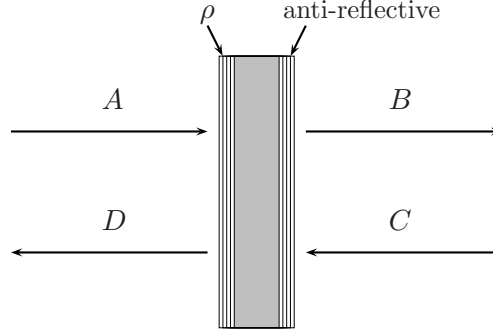


Figure 6.2: Mirror coupling. Mirrors are coated on both surfaces. A coating is a multi layer structure which extends a few micrometers in the direction of beam propagation. One coating is designed to minimize reflection. The other coating defines the reflectivity ρ of the mirror. Effectively, the mirror can be treated as a flat reflecting surface.

Figure 6.2. One choice of coupling relations has the following form

$$\begin{aligned} B &= \tau A - \rho C \\ D &= \tau C + \rho A \end{aligned} \tag{6.4}$$

These relations are favorable upon others since the coupling parameters are real. This property is quite important in view of the fact that the symbols A, \dots may either stand for fields or for the fields' quadrature vectors. In the latter case, a complex coupling parameter in the 1P formalism (e.g. $i\tau$) has to be substituted by a matrix

$$i\tau \rightarrow \begin{pmatrix} 0 & -\tau \\ \tau & 0 \end{pmatrix}. \tag{6.5}$$

A mirror with complex coupling parameters in the 1P formalism flips transmitted quadrature vectors such that amplitude quadratures become phase quadratures and vice versa.

The beam splitter coupling relations are derivable from the mirror coupling relations Eq. (6.4). The only difference is that the angle of incidence of the fields is different from $\pi/2$. Consequently, the number of fields which couple with each other is doubled. In other chapters, we exclusively consider 50/50 beam splitters, which reflect and transmit fields with the same coefficient $\rho = \tau = 1/\sqrt{2}$. In that case, the coupling relations read (see

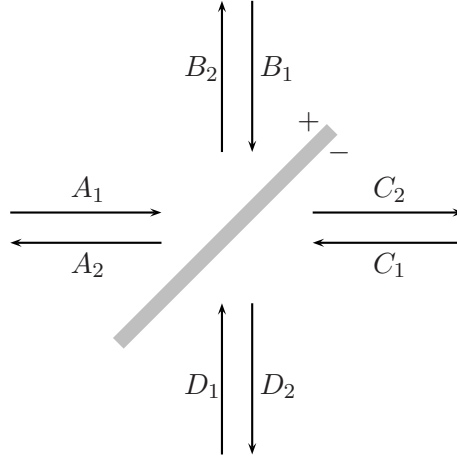


Figure 6.3: The beam splitter is an optical element with four ports A , B , C , D . In accordance with the mirror coupling relations, the reflection coefficient has opposite signs when fields are reflected on the one or the other side.

Figure 6.3)

$$\begin{aligned}
 A_2 &= \frac{1}{\sqrt{2}} (B_1 + C_1) \\
 B_2 &= \frac{1}{\sqrt{2}} (A_1 + D_1) \\
 C_2 &= \frac{1}{\sqrt{2}} (A_1 - D_1) \\
 D_2 &= \frac{1}{\sqrt{2}} (B_1 - C_1)
 \end{aligned} \tag{6.6}$$

We conclude this section with a remark on lossy substrates. There are two aspects which have to be taken into account. At first, losses mean that the amplitude of light is diminished by a fraction $\sqrt{\alpha}$ (field energy flows into inaccessible channels or is converted into heat). At second, losses mix the quantum mechanical part of the field with another coherent vacuum field \hat{v} which for example could lead to a degradation of squeezed states

$$\hat{a}_{\text{out}} = \sqrt{\alpha} \cdot \hat{a}_{\text{in}} + \sqrt{1 - \alpha} \cdot \hat{v} \tag{6.7}$$

where \hat{a}_{in} may contain a classical excitation. Now, we are prepared to combine the transfer functions which have been presented to calculate the transformations of cavities and interferometers without radiation pressure.

6.3 Characterization of Fabry-Pérot Cavities

This section is devoted to introducing the terminology which is used when characterizing Fabry-Pérot cavities. Most of the content is reviewed with more detail in (Black; 2000)

and also (Meers; 1989). Primarily, the properties of a cavity are governed by the properties of the mirrors and the distance between them (see Figure 6.4). Nevertheless, people working with cavities derive more phenomenological quantities from these parameters like the finesse \mathcal{F} or the free spectral range $\Delta\nu_{\text{fsr}}$ which can be directly read off from the measured data. So our first goal is to define these quantities and to discuss their physical meaning. Imagine a simple measurement where the power transmitted through a Fabry-Pérot cavity

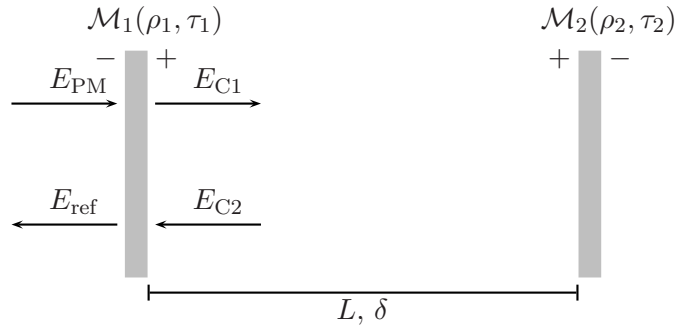


Figure 6.4: The properties of a lossless Fabry-Pérot cavity are determined by the amplitude transmissivities τ_1 , τ_2 and reflectivities ρ_1 , ρ_2 of the two mirrors and the distance between them. If the input field E_{PM} is decomposed into a carrier field at frequency ω_0 and sidebands at $\omega_0 \pm \Omega$, then one usually makes use of two parameters to describe the distance between \mathcal{M}_1 and \mathcal{M}_2 : The detuning δ which corresponds to the phase shift of the carrier and the macroscopic distance L which determines relative phase shifts $\Phi = \Omega L/c$ between adjacent frequencies of the field. The macroscopic distance does not have to be known with great precision.

is measured. The frequency of the input field is varied slowly in order to ascertain that the cavity always reaches its stationary state. The time τ_s needed to reach that state is called the storage or relaxation time (see below). As shown in Figure 6.5, the transmission peaks every free spectral range $\Delta\nu_{\text{fsr}}$. The peaks themselves are characterized by their linewidth γ . The finesse of a cavity is defined as the ratio of the free spectral range $\Delta\nu_{\text{fsr}}$ to the linewidth γ of the cavity

$$\mathcal{F} \equiv \frac{\Delta\nu_{\text{fsr}}}{\gamma} = \pi \frac{\sqrt{\rho_1 \rho_2}}{1 - \rho_1 \rho_2} \quad (6.8)$$

It is a scale invariant property in the sense that the finesse does not depend on the size L of the cavity. The greater the finesse, the sharper are the peaks. The finesse may also be understood as the quality factor of the (Fabry-Pérot) resonator. The free spectral range measures the distance between two peaks of the transmitted power:

$$\Delta\nu_{\text{fsr}} = \frac{c}{2L} \quad (6.9)$$

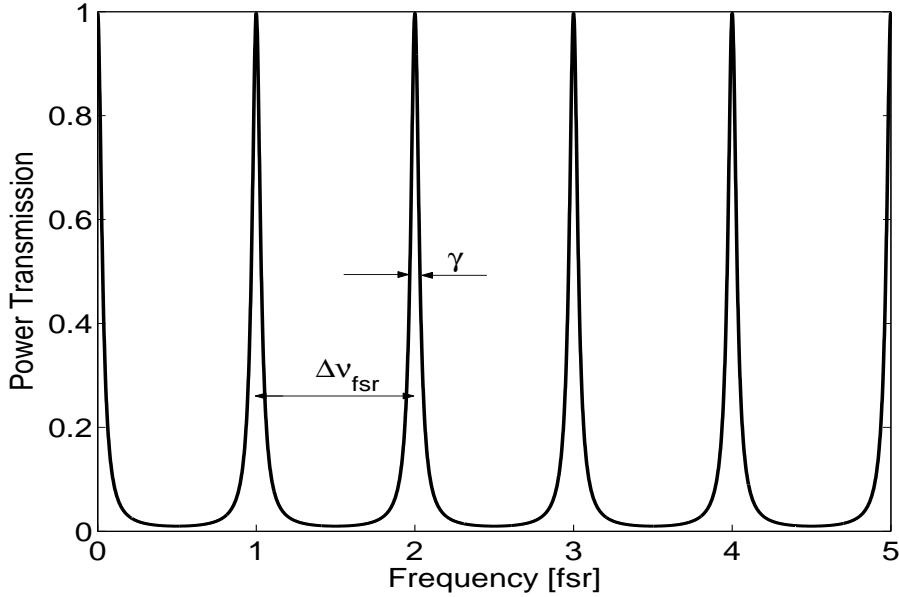


Figure 6.5: The power transmissivity of a Fabry-Pérot cavity peaks every $\Delta\nu_{\text{fsr}} = c/2L$. Here, the linewidth γ of the cavity is significantly smaller than its free spectral range. The cavity is lossless and impedance matched (see below).

According to Eqs. (6.8)&(6.9), the linewidth (i.e. full width at half maximum) of the cavity assumes the form

$$\gamma = \frac{1}{\pi} \frac{c}{2L} \frac{1 - \rho_1 \rho_2}{\sqrt{\rho_1 \rho_2}} \quad (6.10)$$

Alternatively, the latter equation can be calculated using the formula which governs the transmitted power or the intracavity power (see Eq. (6.38)). Then, one recognizes that the linewidth formula Eq. (6.10) is valid only if $\gamma \ll \Delta\nu_{\text{fsr}}$. The storage time τ_s is related in a simple way to the linewidth of the cavity

$$\tau_s \equiv \frac{1}{\pi\gamma} = \frac{\mathcal{F}}{\pi\Delta\nu_{\text{fsr}}} \quad (6.11)$$

In average, light on resonance spends a time τ_s inside the cavity. If the state of a cavity is changed, then the same time is needed to return to its stationary state. In that context τ_s is referred to as the relaxation time.

Another important property of Fabry-Pérot cavities concerns their response to phase modulated light, i.e. predicting the amount of the reflected and transmitted power and the corresponding phase shifts. These issues have to be investigated when one tries to lock a cavity in a certain state or stabilize the frequency of a laser with a so-called Pound-Drever-Hall (PDH) locking or stabilization scheme. There, phase-modulated light reflected from a cavity is measured with a photodetector obtaining an error signal which indicates deviations from the desired cavity state or laser frequency (Black; 2000). The response leads to a further categorization of Fabry-Pérot cavities: undercoupled, overcoupled and

impedance matched cavities. In the following, we investigate phase-modulated fields reflected from a cavity and introduce the above mentioned categorization guided in part by a discussion of the PDH locking scheme.

Phase modulation means that the phase of a field oscillates periodically with time. The amplitude m of the phase oscillations is called the modulation index or modulation depth. In most cases, one deals with small indices. The spectrum of a phase-modulated carrier at frequency ω_0 shows peaks at sideband frequencies $\omega_0 \pm l \cdot \Omega$ with $l = 1, 2, 3, \dots$ whose amplitude is given by

$$\begin{aligned} E_{\text{PM}} &= E_0 e^{i(\omega_0 t + m \cos(\Omega t))} \\ &= E_0 \cdot \left[J_0(m) + \sum_{l=1}^{\infty} i^l J_l(m) \left(e^{i l \Omega t} + e^{-i l \Omega t} \right) \right] e^{i \omega_0 t} \\ &\simeq E_0 \cdot \left[J_0(m) + i J_1(m) \left(e^{i \Omega t} + e^{-i \Omega t} \right) \right] e^{i \omega_0 t} \end{aligned} \quad (6.12)$$

The last equation shows that for small modulation depth m two modulation sidebands appear which in frequency space are separated from the carrier by Ω . The Bessel functions $J_l(m)$ expand according to

$$\begin{aligned} J_l(m) &= \frac{1}{l!} \left(\frac{m}{2} \right)^l + \dots \\ J_0(m) &= 1 - \frac{m^2}{4} + \frac{m^4}{64} - \dots \\ J_1(m) &= \frac{m}{2} \left(1 - \frac{m^2}{8} + \dots \right) \end{aligned} \quad (6.13)$$

Therefore, the last step in Eq. (6.12) neglects terms of order $\mathcal{O}(m^2)$. Henceforth, we assume that the approximation can be applied. Consequently, fields reflected from a cavity are calculated by specifying a transfer function \mathbf{F} for three different frequencies ω_0 , $\omega_0 \pm \Omega$:

$$E_{\text{ref}} = E_0 e^{i \omega_0 t} \cdot \left[\mathbf{F}(\omega_0) J_0(m) + i J_1(m) \left(\mathbf{F}(\omega_0 + \Omega) e^{i \Omega t} + \mathbf{F}(\omega_0 - \Omega) e^{-i \Omega t} \right) \right] \quad (6.14)$$

where the transfer function \mathbf{F} for a lossless cavity is given by

$$\mathbf{F}(\omega_0 + \Omega) = \frac{\rho_2 e^{2i(\delta + \Omega L/c)} - \rho_1}{1 - \rho_1 \rho_2 e^{2i(\delta + \Omega L/c)}} \quad (6.15)$$

In a PDH locking scheme, one measures the power of the reflected field E_{ref} , which for $m \ll 2$ yields

$$\begin{aligned} P_{\text{ref}} &= P_0 J_0^2 |\mathbf{F}(\omega_0)|^2 + P_0 J_1^2 \left(|\mathbf{F}(\omega_0 + \Omega)|^2 + |\mathbf{F}(\omega_0 - \Omega)|^2 \right) \dots \\ &\quad + 2P_0 J_0 J_1 \Re \left[\mathbf{F}(\omega_0) \mathbf{F}^*(\omega_0 - \Omega) - \mathbf{F}^*(\omega_0) \mathbf{F}(\omega_0 + \Omega) \right] \sin(\Omega t) \dots \\ &\quad + 2P_0 J_0 J_1 \Im \left[\mathbf{F}(\omega_0) \mathbf{F}^*(\omega_0 - \Omega) - \mathbf{F}^*(\omega_0) \mathbf{F}(\omega_0 + \Omega) \right] \cos(\Omega t) \end{aligned} \quad (6.16)$$

The absolute square of \mathbf{F} is also known as the Airy function. The term in front of the cosine function vanishes for low modulation frequencies $\Omega \ll \gamma$, which is revealed by a first order Taylor expansion of the transfer functions $\mathbf{F}(\omega_0 \pm \Omega)$. In PDH schemes, the

modulation frequency obeys $\Omega \gg \gamma$. Assuming further that the carrier frequency lies close to the cavity resonance (i.e. one intends to lock the laser frequency on the cavity resonance), the term in front of the sine function vanishes since modulation sidebands beyond the cavity linewidth are totally reflected from the cavity: $\mathbf{F}(\omega_0 \pm \Omega) \approx -1$. For fast modulations (i.e. $\Omega \gg \gamma$), the leakage beam $\tau_1 E_{C2}$ acts as stable frequency reference (its frequency corresponds to the input beam frequency averaged over the storage time). So, the laser is locked to a time average of itself. The error signal of PDH schemes is obtained by mixing the power with a $\cos(\Omega t)$ and subsequently filtering the output with a low pass

$$P_{\text{err}} = 2P_0 J_0 J_1 \Im [\mathbf{F}(\omega_0) \mathbf{F}^*(\omega_0 - \Omega) - \mathbf{F}^*(\omega_0) \mathbf{F}(\omega_0 + \Omega)] \quad (6.17)$$

Provided that the resonance of the cavity is more steady than the laser frequency ω_0

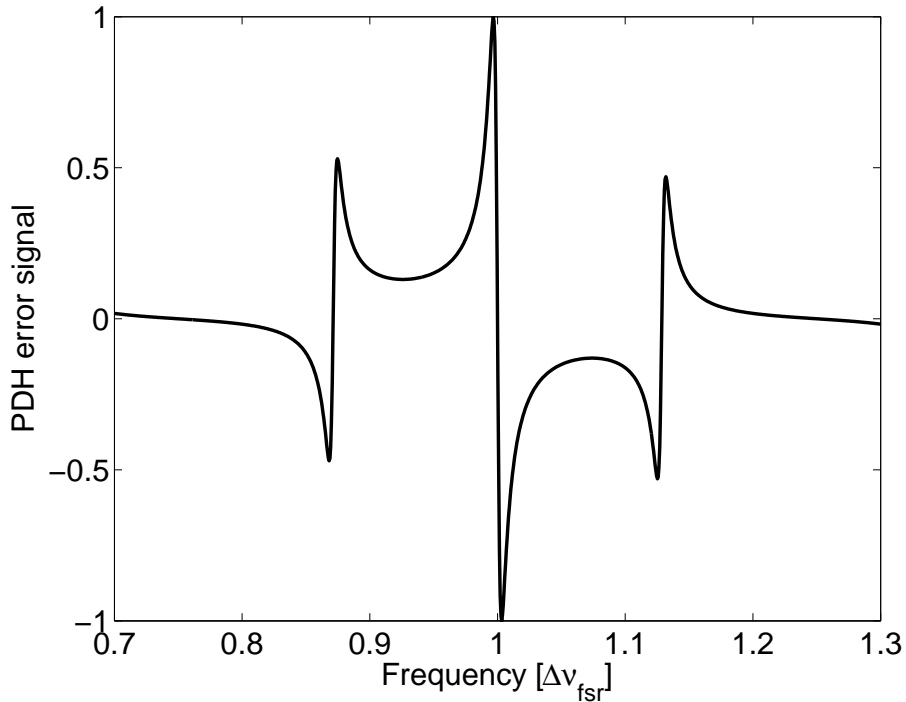


Figure 6.6: The curve shows the PDH error signal according to Eq. (6.17). The free spectral range is roughly a factor 78 greater than the linewidth of the cavity. The abscissa corresponds to the carrier frequency ω_0 which is phase modulated with $\Omega = 10 \cdot \gamma$. The two mirrors possess the same reflectivity.

(i.e. the linewidth γ of the cavity is smaller than the linewidth of the laser), the error signal constitutes a frequency measurement of the laser: If the frequency ω_0 is close to the symmetry point of the error signal, then small fluctuations of the frequency lead to large fluctuations of the error signal. The sign of the error signal tells you whether the frequency is smaller or greater than the cavity resonance. A feed-back loop which acts on the laser will try to correct its frequency according to the error signal.

Considering \mathbf{F} as a function of $\exp(i\omega/\Delta\nu_{\text{fsr}})$, the transfer function becomes a Möbius

map of the unity circle in the complex plane. Möbius functions have the property that they map circles in the complex plane onto circles and therefore the picture of \mathbf{F} must be a circle again. As shown in [Figure 6.7](#), that feature can be used to furnish a pictorial definition of critical coupling (impedance match), undercoupling and overcoupling. If $\Re(\mathbf{F}) < 0$ for all frequencies, then one says that the cavity is undercoupled. Respectively, the condition for overcoupling is that the circle \mathbf{F} intersects the line $\Re(z) = 0$ and impedance matched cavities exhibit a circle which is tangent to that line. If the light is on resonance with an

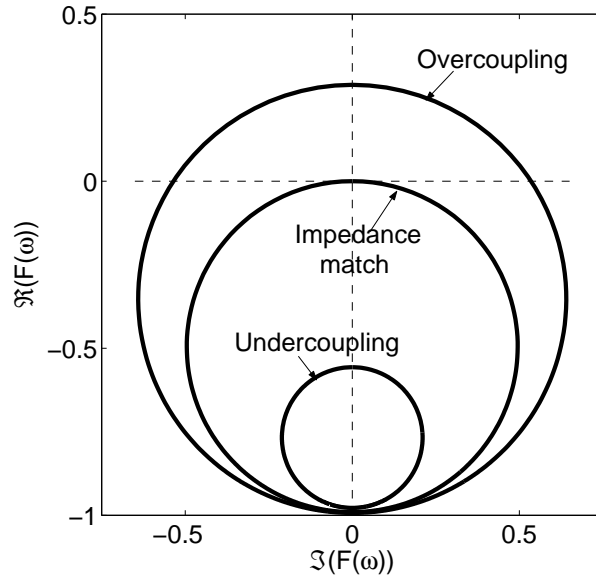


Figure 6.7: Varying the frequency ω from 0 to $2\pi\Delta\nu_{\text{fsr}}$, the transfer function $F(\omega)$ traces a circle in the complex plane. The reflected intensity vanishes on resonance when the cavity is impedance matched. The three circles correspond to three different amplitude reflectivities of the second mirror.

impedance matched cavity, then the reflected power is equal to zero. In all other cases, the Airy function $|\mathbf{F}|^2$ is nonzero. A straight-forward calculation shows that for lossless cavities the circles' centers are shifted from the origin towards negative real values by ([Black; 2000](#))

$$F_c = -\frac{\rho_1\tau_2^2}{1 - \rho_1^2\rho_2^2} \quad (6.18)$$

and that the radius of a circle is given by

$$R = \frac{\tau_1^2\rho_2}{1 - \rho_1^2\rho_2^2} \quad (6.19)$$

Next, we investigate the properties for each of the three categories with respect to the resonant power build-up and the phase shift experienced by the reflected light for lossless cavities. The pumping beam is denoted by E_{in} (substituting E_{PM} in Eq. (6.4)). At first, consider an impedance matched cavity: $\rho \equiv \rho_1 = \rho_2$. We know that the cavity is totally transmissive on resonance. Therefore, the promptly reflected light ρE_{in} must interfere

destructively with the leakage beam τE_{C2} . On resonance, the leakage beam is 180° out of phase with the promptly reflected beam and we obtain

$$\tau E_{C2} - \rho E_{in} = 0 \quad (6.20)$$

We define the power build-up of the cavity by $(E_{C1}/E_{in})^2$. Together with $E_{C2} = \rho E_{C1}$, we deduce that the power build-up has to be $1/\tau^2$. As a second example, we apply the same reasoning to derive the power build-up for an overcoupled cavity with $\rho_2 = 1$. In that case, all of the ingoing field is reflected

$$\tau E_{C2} - \rho E_{in} = E_{in} \quad (6.21)$$

Since $E_{C2} = E_{C1}$, the power build-up has to be $(1+\rho_1)/(1-\rho_1)$ which for high reflectivities can be approximated by $4/\tau_1^2$. That means, given a reflectivity $\rho_1 \approx 1$ and input power P_{in} , the power inside the cavity is 4 times as high for the overcoupled cavity with $\rho_2 = 1$ than for the impedance matched cavity. [Figure 6.8](#) shows the build-up for a continuous variation of the reflectivities. Keeping ρ_2 constant, the build-up is maximal for the impedance matched cavity. If ρ_1 is kept constant, the overcoupled cavity exhibits the largest build-up.

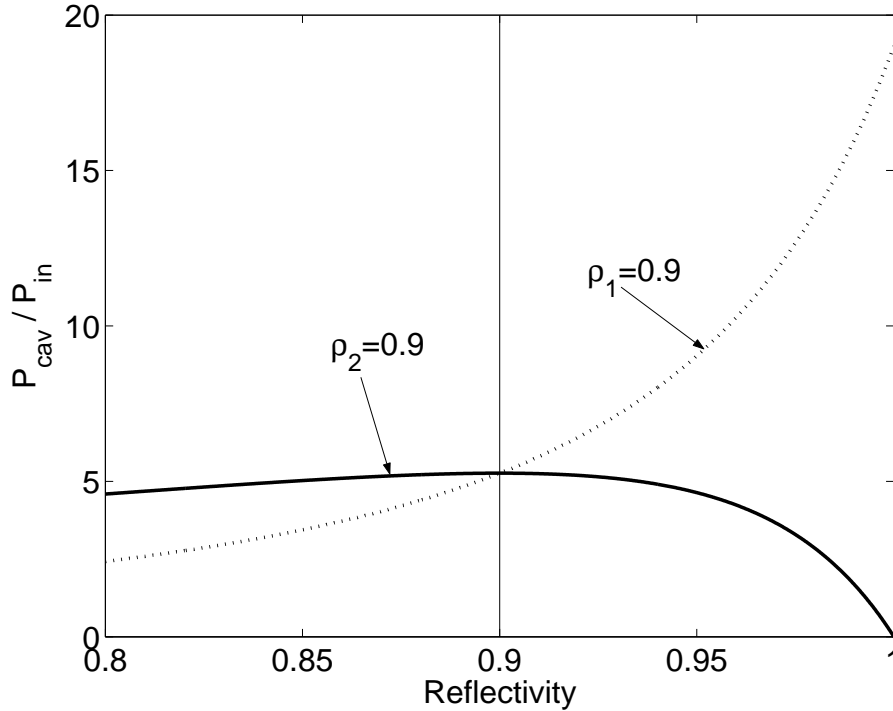


Figure 6.8: The figure shows the ratio of the intracavity power to the input power. One curve is evaluated with fixed reflectivity ρ_1 , the other with fixed ρ_2 . The vertical line marks the reflectivity which yields the impedance matched cavity.

The transfer function \mathbf{F} also determines the phase shift $\Delta\phi_{ref}$ of the reflected light. Again, undercoupled, overcoupled and impedance matched cavities show qualitatively different dependencies of the phase shift on the frequency of the incident field. In [Figure 6.9](#),

$\Delta\phi_{\text{ref}}$ is shown as a function of the frequency. The cavity linewidth is identical for each curve. The phase shift of an impedance matched cavity features a discontinuity at resonance caused by the vanishing of the reflected power. In contrast, the apparent discontinu-

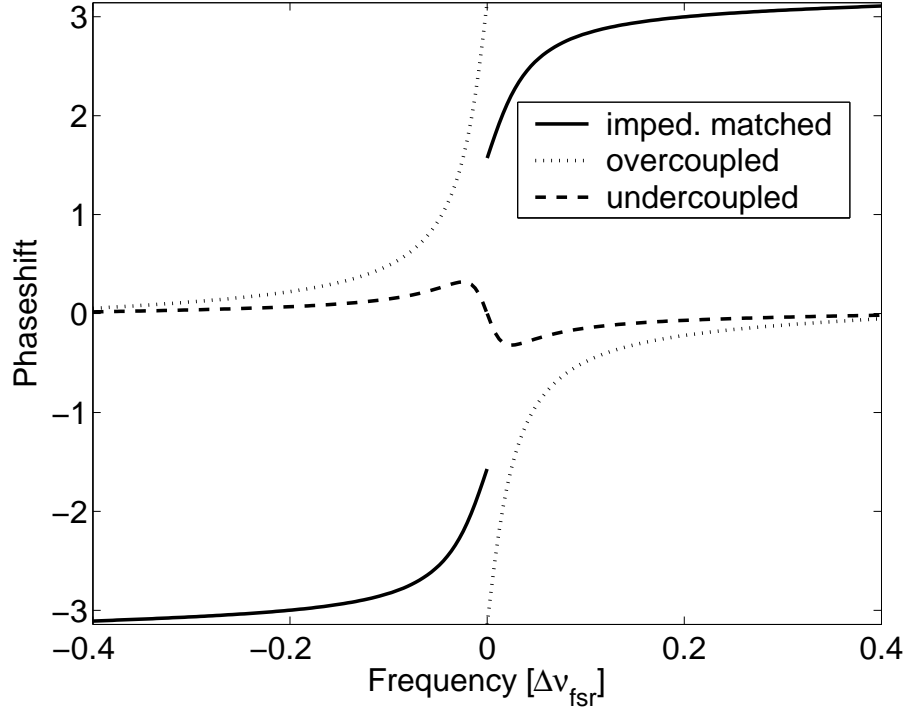


Figure 6.9: Phase shift of fields reflected from FP cavities.

ity of the phaseshift for the overcoupled cavity is not fundamental. The axis of phaseshifts is cyclic with period 2π and obviously, the phaseshift modulo 2π is continuous (i.e. the function is continuous on a cylinder with circumference 2π).

6.4 Radiation Pressure Effects

Radiation pressure has to be taken into account when the displacement of suspended mirrors due to a radiation-pressure force leads to measurable phase shifts of reflected fields. The force is governed by the power of the light. Power fluctuations give rise to a fluctuating displacement of the suspended mirror. In that case, the phase shift of reflected fields is characterized by a variance (in the time domain) or a noise spectral density (in the frequency domain), i.e. power fluctuations lead to additional phase noise of the light. For reasons which will become clear soon, we choose to represent the fields by their quadrature amplitudes. At first, we introduce the (frequency domain) susceptibility $\chi(\Omega)$ of suspended mirrors with respect to a radiation-pressure force $F(\Omega)$. Consider a two-stage system with an intermediate mass as shown in [Figure 6.10](#). The system exhibits two resonance frequencies which are determined by the lengths L_1 , L_2 of the two pendulums and the mass m of the suspended objects. In the frequency domain, the equation of motion

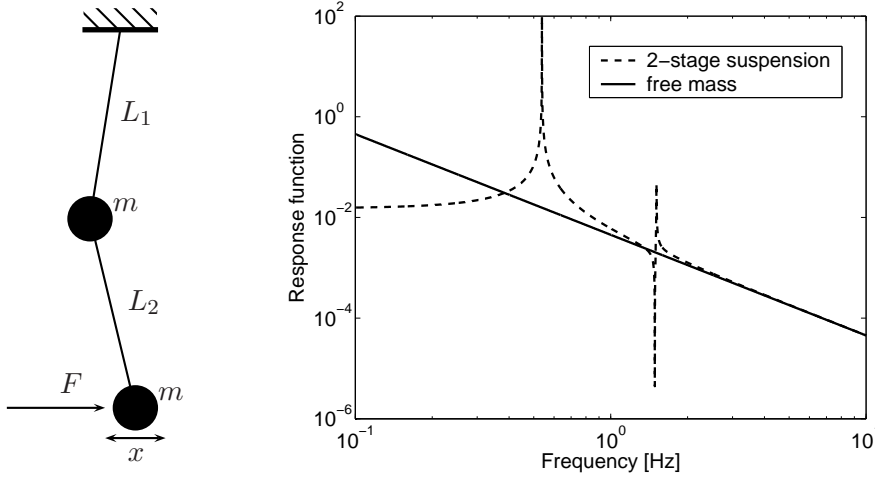


Figure 6.10: A two-stage mirror suspension exhibits two resonances. In the frequency domain, the response (susceptibility) of the coordinate x with respect to a force F which acts on the lower mass, asymptotically approaches the response of a free mass towards higher frequencies.

for the coordinate $x(\Omega)$ reads

$$x(\Omega) = \chi(\Omega) F(\Omega) \quad (6.22)$$

At higher frequencies, the susceptibility asymptotically approaches the free mass susceptibility

$$\chi(\Omega) \rightarrow -\frac{1}{m\Omega^2} \quad (6.23)$$

which means that a suspended mirror can be considered as freely moving along the optical axis if the relevant frequencies lie well above the resonance frequencies of the two-stage suspension. This conclusion holds for any multi-stage suspension. The radiation-pressure force is governed by the power of the incident beam

$$F(t) = 2\frac{P(t)}{c} \quad (6.24)$$

The factor 2 arises since, at this point, we consider the simple case where the mirror totally reflects the incident light. In terms of the field's quadrature amplitudes, the corresponding frequency-domain description is found to be

$$F(\Omega) = 2\frac{\hbar\omega_0}{c} \left(\frac{\Lambda^2}{2} \delta(\Omega) + \Lambda \cdot \hat{a}_1(\Omega) + \mathcal{O}(\hat{a}_{1;2}^2) \right) \quad (6.25)$$

where $\Lambda = \sqrt{P/(\hbar\omega_0)}$ is a strong classical excitation of the amplitude quadrature (i.e. the carrier field) and \hat{a}_1 incorporates the amplitude quadrature fluctuations. In the following, the contribution at zero frequency of the carrier field will be omitted. We also assume that the sideband amplitudes are much weaker than the carrier amplitude which allows us to neglect the contribution quadratic in the quadrature amplitudes. The phase shift

experienced by amplitudes acting at frequency Ω is derived from a propagation along the displacement x of the mirror

$$\begin{aligned}\Delta\phi(\Omega) &= 2\frac{\omega_0 x(\Omega)}{c} \\ &= -\sqrt{\hbar\omega_0 P} \frac{4\omega_0}{mc^2\Omega^2} \cdot \hat{a}_1(\Omega)\end{aligned}\quad (6.26)$$

Defining the optomechanical coupling constant \mathcal{K} , the respective transformation of the quadrature amplitudes is derived from a propagation along a small displacement x

$$\bar{\mathbf{a}}_{\text{out}} = \begin{pmatrix} 1 & 0 \\ -\mathcal{K} & 1 \end{pmatrix} \cdot \bar{\mathbf{a}}_{\text{in}}, \text{ with } \mathcal{K} \equiv \frac{4P\omega_0}{mc^2\Omega^2}\quad (6.27)$$

A coherent field which is reflected by a suspended mirror acquires a correlation between its phase and its amplitude quadrature, which means that the reflected field has non-stationary noise (although the quadrature phases do have stationary noise). Its spectral density

$$S_{\text{vac in}} = \begin{pmatrix} 1 & -\mathcal{K} \\ -\mathcal{K} & 1 + \mathcal{K}^2 \end{pmatrix}\quad (6.28)$$

has eigenvalues $1/2 \cdot (2 + \mathcal{K}^2 \pm \mathcal{K}\sqrt{4 + \mathcal{K}^2})$ and unit determinant. In other words, the reflected field is ponderomotively squeezed (Vyatchanin and Matsko; 1993). The frequency-dependent squeezing factor $r(\Omega)$ is determined by

$$r(\Omega) = \cosh^{-1} \left(1 + \frac{1}{2}\mathcal{K}^2(\Omega) \right)\quad (6.29)$$

Although the phase noise is increased and the amplitude noise is unaltered, the two-photon formalism reveals straight away that the reflected field is still in a minimum-uncertainty state with squeezed quadratures.

In a more general context, the carrier field does not have to be the phase reference which determines the decomposition into the phase and amplitude quadrature phases. Then, an additional phase parameter ϕ_C enters the transformation of quadrature amplitudes. It can be shown that the reflected field is given by

$$\begin{aligned}\bar{\mathbf{a}}_{\text{out}} &= \left[\mathbb{I} - \frac{4\hbar\omega_0^2}{mc^2\Omega^2} \bar{\Lambda}^P \otimes \bar{\Lambda} \right] \cdot \bar{\mathbf{a}}_{\text{in}} \\ &= \left[\mathbb{I} - \frac{4\hbar\omega_0^2}{mc^2\Omega^2} \begin{pmatrix} -\Lambda_1\Lambda_2 & -\Lambda_2^2 \\ \Lambda_1^2 & \Lambda_1\Lambda_2 \end{pmatrix} \right] \cdot \bar{\mathbf{a}}_{\text{in}} \\ &= \left[\mathbb{I} - \mathcal{K} \cdot \underbrace{\begin{pmatrix} -\cos(\phi_C)\sin(\phi_C) & -\sin^2(\phi_C) \\ \cos^2(\phi_C) & \cos(\phi_C)\sin(\phi_C) \end{pmatrix}}_{\equiv C(\phi_C)} \right] \cdot \bar{\mathbf{a}}_{\text{in}}\end{aligned}\quad (6.30)$$

with $\bar{\Lambda}^P \equiv (-\Lambda_2; \Lambda_1)$ which is defined in terms of the amplitude quadrature Λ_1 and phase quadrature Λ_2 of the carrier. The notation introduced in Eq. (6.30) helps to formulate the coupling relations for a mirror with arbitrary reflectivity ρ and two incident beams, one on each side (see Figure 6.11). In order to derive the radiation-pressure force which acts on

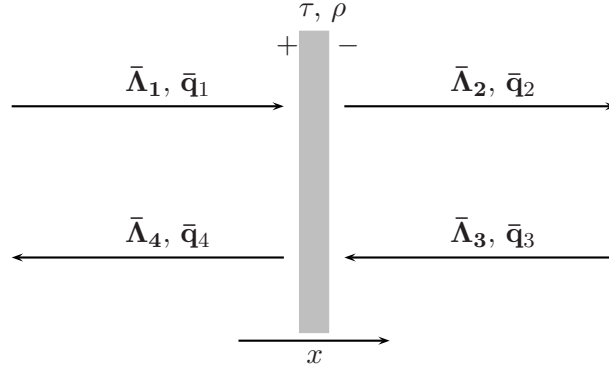


Figure 6.11: The displacement x of the mirror is governed by the conservation law of momentum of the mirror and the fields. The four carrier fields $\bar{\Lambda}_i$ interfere according to the standard mirror coupling equations. The displacement noise of the mirror contributes to the outgoing noise amplitudes \bar{q}_2, \bar{q}_4 .

the mirror, we have to take into account the interference of the fields. The displacement x of the mirror depends on the amplitude of the incident and outgoing beams:

$$x(\Omega) = -\frac{\hbar\omega_0}{mc\Omega^2}(\bar{\Lambda}_1 \cdot \bar{q}_1 + \bar{\Lambda}_4 \cdot \bar{q}_4 - \bar{\Lambda}_2 \cdot \bar{q}_2 - \bar{\Lambda}_3 \cdot \bar{q}_3) \quad (6.31)$$

The carrier amplitudes $\bar{\Lambda}_i$ couple according to Eq. (6.4). The quadrature amplitudes pick up displacement noise according to

$$\begin{aligned} \bar{q}_2 &= \tau\bar{q}_1 - \rho \left(\bar{q}_3 - 2\frac{\omega_0}{c}\bar{\Lambda}_3^P \cdot x(\Omega) \right) \\ \bar{q}_4 &= \tau\bar{q}_3 + \rho \left(\bar{q}_1 + 2\frac{\omega_0}{c}\bar{\Lambda}_1^P \cdot x(\Omega) \right) \end{aligned} \quad (6.32)$$

which is valid for small displacements $x \ll c/\omega_0 \sim 10^{-7}$ m. Substituting the right-hand side of Eq. (6.31) for the displacement and solving for the outgoing quadratures \bar{q}_2, \bar{q}_4 , one obtains the coupling relation with radiation pressure. The solution for a mirror with $\bar{\Lambda}_3 = 0$ reads

$$\begin{aligned} \bar{q}_2 &= \tau\bar{q}_1 - \rho\bar{q}_3 \\ \bar{q}_4 &= \left(\mathbb{I} - \rho^2 \frac{4\hbar\omega_0^2}{mc^2\Omega^2} \bar{\Lambda}_1^P \otimes \bar{\Lambda}_1 \right) \cdot (\tau\bar{q}_3 + \rho\bar{q}_1) \end{aligned} \quad (6.33)$$

The solution for the generic case is usually not applied algebraically. Complex optical systems with intricate radiation-pressure effects are calculated by setting up a system of equations which determines the field quadrature amplitudes at every optical element. Therefore, it is sufficient and time saving to implement Eq. (6.32) together with Eq. (6.31) instead of the solved coupling relations.

6.5 The Suspended Fabry-Pérot Cavity

The transfer functions of Fabry-Pérot cavities characterize the performance of all operating interferometric gravitational-wave detectors and also of the currently planned next-generation interferometers like advanced LIGO. Cavities are implemented as arm cavities or recycling cavities for the signal or the carrier field. In this section, we are going to consider cavities with suspended mirrors. Radiation pressure is taken into account as well as modulation sidebands due to a periodic displacement of the mirrors. Fields are represented in the two-photon formalism. The cavity is parametrized as shown in Figure 6.12. At first, we calculate the reflection of the input field $\bar{\mathbf{i}}$. The cavity is pumped through \mathcal{M}_1

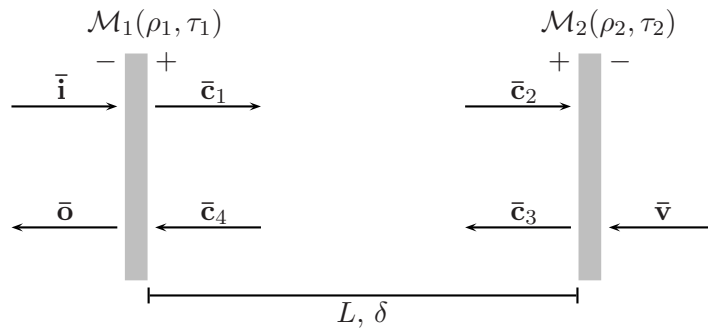


Figure 6.12: The two mirrors of the Fabry-Pérot cavity have amplitude transmissivities τ_1, τ_2 and reflectivities ρ_1, ρ_2 . The cavity has length L and is detuned by ϕ . The field $\bar{\mathbf{o}}$ is measured with a homodyne detector. Both mirrors have the same mass m .

and so the reflection of $\bar{\mathbf{c}}_2$ at \mathcal{M}_2 is governed by Eq. (6.33). It follows that in the absence of other forces acting on the mirrors (except radiation pressure) the amplitudes on the right side of \mathcal{M}_1 are related by

$$\bar{\mathbf{c}}_4 = \mathbf{P}_{L,\delta} \cdot (\mathbb{I} - \rho_2^2 \mathcal{K} \cdot C(\phi_{C2})) \cdot (\rho_2 \mathbf{P}_{L,\delta} \cdot \bar{\mathbf{c}}_1 + \tau_2 \bar{\mathbf{v}}) \quad (6.34)$$

where the propagation $\mathbf{P}_{L,\delta}$ along the cavity is governed by Eq. (6.3), ϕ_{C2} denotes the phase of the carrier field at mirror \mathcal{M}_2 and \mathcal{K} is determined by the power P inside the cavity. One can verify that

$$\begin{aligned} \mathbf{R} &\equiv \rho_2 \mathbf{P}_{L,\delta} \cdot (\mathbb{I} - \rho_2^2 \mathcal{K} \cdot C(\phi_{C2})) \cdot \mathbf{P}_{L,\delta} \\ &= \rho_2 \mathbf{P}_{2L,2\delta} \cdot (\mathbb{I} - \rho_2^2 \mathcal{K} \cdot C(\phi_{C2} - \delta)) \\ &= \rho_2 \mathbf{P}_{2L,2\delta} \cdot (\mathbb{I} - \rho_2^2 \mathcal{K} \cdot C(\phi_{C1})) \end{aligned} \quad (6.35)$$

The carrier phase ϕ_{C1} on the right side of \mathcal{M}_1 is arbitrary since the input phase of the carrier field is indeterminate. Setting $\phi_{C1} = 0$, the round-trip transfer matrix is cast into the form

$$\mathbf{R} = \mathbf{P}_{2L,2\delta} \cdot \begin{pmatrix} 1 & 0 \\ -\rho_2^2 \mathcal{K} & 1 \end{pmatrix} \quad (6.36)$$

In the following, we reason why in most cases it is possible to simplify the coupling relations of \mathcal{M}_1 even though there are carrier fields impinging on both sides of the mirror. Exceptions exist which are discussed in [Chapter 8](#). The power P_0 of the input carrier field furnished by a laser is usually too small to give rise to significant radiation-pressure forces. Since we do consider a cavity with significant radiation pressure, the power must be built up by the cavity itself. This entails that the power P inside the cavity is much greater than the input power P_0 . In that case, the displacement of \mathcal{M}_1 is governed predominantly by radiation pressure due to fields inside the cavity. Consequently, the coupling relations of \mathcal{M}_1 are well approximated by Eq. (6.33). Concerning the round-trip transfer, this means that the RP noise amplitudes for each mirror are summed up to yield the total noise amplitude: $\rho_2^2 \mathcal{K} \rightarrow (\rho_1^2 + \rho_2^2) \mathcal{K}$ in Eq. (6.36).

The output field $\bar{\mathbf{o}}$ is composed of the reflected input field $\bar{\mathbf{i}}$, the transmitted vacuum field $\bar{\mathbf{v}}$ and quadrature fields $\bar{\mathbf{q}}_i$ created inside the cavity by other forces acting on the mirrors (e.g. a gravitational wave, displacement noise). The contribution of the reflected field reads

$$\bar{\mathbf{o}}_{\text{ref}} = \frac{\mathbf{R} - \rho_1 \cdot \mathbb{I}}{\mathbb{I} - \rho_1 \mathbf{R}} \cdot \bar{\mathbf{i}} \quad (6.37)$$

where the round-trip transfer \mathbf{R} is adjusted according to the preceding discussion. From Eq. (5.20) one obtains the spectral density matrix $S(\bar{\mathbf{o}}_{\text{ref}})$ and using Eq. (5.21), we find the spectral density for a specific quadrature of the field. In all of the following figures

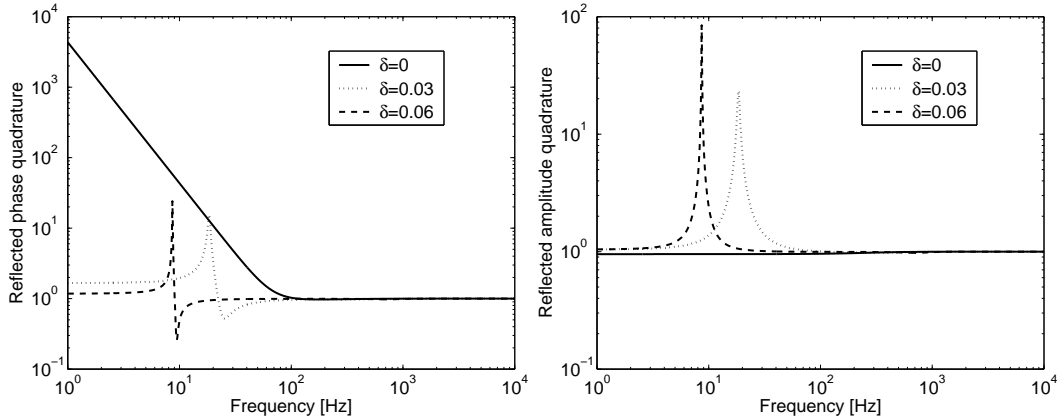


Figure 6.13: The figure shows the amplitude and phase quadratures of a vacuum field reflected from a cavity governed by Eq. (6.37). The detuning δ varies for each curve. The reflected amplitude quadrature for a tuned cavity $\delta = 0$ has a white noise spectrum as the input field $\bar{\mathbf{i}}$. In contrast, the phase quadrature collects all the radiation-pressure noise which increases with Ω^{-2} towards lower frequencies. A detuned cavity exhibits an optomechanical resonance which gives rise to a partly increased and partly decreased (i.e. ponderomotively squeezed) noise spectral density of the output field.

one has to keep in mind that with fixed input power P_{in} , the intracavity power P depends on δ according to

$$P = \frac{\tau_1^2}{1 + \rho_1^2 \rho_2^2 - 2\rho_1 \rho_2 \cos(2\delta)} P_{\text{in}} \quad (6.38)$$

Figure 6.13 shows the square root of the spectral density for the amplitude and phase quadrature of $\bar{\mathbf{o}}_{\text{ref}}$ with varying detuning of the cavity. The input field is a coherent vacuum field with spectral density matrix $S(\bar{\mathbf{i}}) = \mathbb{I}$. Obviously, there is a fundamental difference between tuned and detuned cavities. One might expect that the phase-quadrature noise at low frequencies always exhibits a radiation-pressure branch which falls with Ω^{-2} . The result shows that this is not the case for detuned cavities. However, as we will see soon, this property does not entail that detuned cavities have a better sensitivity at low frequencies with respect to a measurement of forces which act on the mirrors.

The transmission of the vacuum field $\bar{\mathbf{v}}$ reads

$$\bar{\mathbf{o}}_{\text{trans}} = \mathbf{P}_{L,\delta} \cdot \begin{pmatrix} 1 & 0 \\ -\rho_2^2 \mathcal{K} & 1 \end{pmatrix} \cdot \frac{\tau_1 \tau_2}{\mathbb{I} - \rho_1 \rho_2 \mathbf{R}} \cdot \bar{\mathbf{v}} \quad (6.39)$$

The transmitted noise shown in Figure 6.14 has to be compared with the reflected noise. Certainly, as long as the cavity is not impedance matched (i.e. for a lossless cavity: $\rho_1 = \rho_2$), the quantum noise of the output field is dominated by $\bar{\mathbf{o}}_{\text{ref}}$. Arm cavities in gravitational-wave detectors are strongly overcoupled. Therefore, one usually neglects the contribution of the field $\bar{\mathbf{o}}_{\text{trans}}$ to the total noise spectral density. Here, the spectral

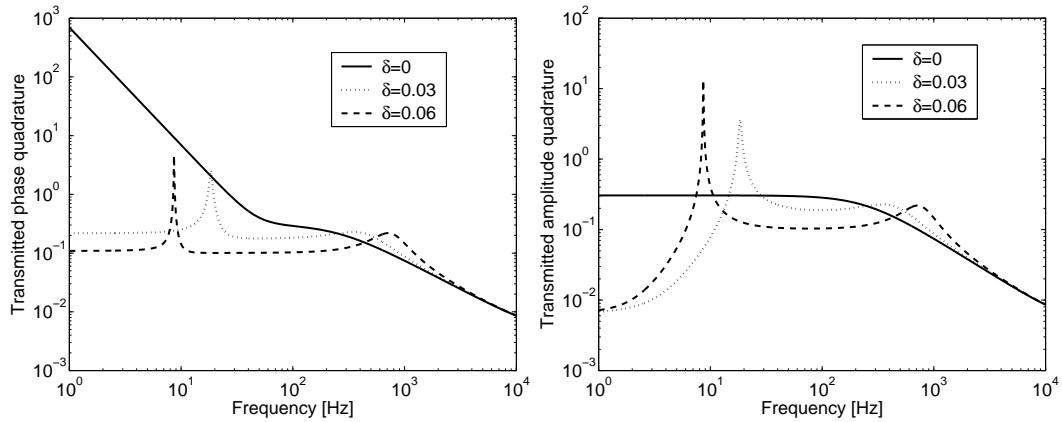


Figure 6.14: The transmitted noise spectral density is nearly an order of magnitude lower than the spectral density of the reflected noise. Beyond the half-bandwidth $\gamma \approx 125$ Hz of the cavity, the transfer function drops with Ω^{-1} (and rises again after one free spectral range). The detuned cavities show two resonances: The optical resonance at $\Omega_{r1} = \delta c/L$ and the optomechanical resonance.

densities are evaluated for an overcoupled cavity with $\rho_1 = 0.96$, $\rho_2 = 0.999$, and the plots show that indeed the transmitted noise is almost an order of magnitude less than the reflected noise.

Another important transfer function of the cavity governs the displacement noise in the output field due to a classical random force acting on the mirrors. The same transfer function describes the response of the cavity to gravitational waves. Assuming that a force

leads to a displacement $x(\Omega)$ of \mathcal{M}_2 , the contribution to the output field is found to be

$$\bar{\mathbf{o}}_{\text{disp}} = \mathbf{P}_{L,\delta} \cdot \frac{\tau_1}{\mathbb{I} - \rho_1 \rho_2 \mathbf{R}} \cdot \begin{pmatrix} 0 \\ \sqrt{\frac{P}{\hbar\omega_0}} \frac{2\omega_0}{c} x(\Omega) \end{pmatrix} \quad (6.40)$$

If the force is random then $x(\Omega)$ denotes the square root of the displacement noise spectral density. The displacement noise $\sqrt{S(\bar{\mathbf{o}}_{\text{disp}})}$ is shown in [Figure 6.15](#) where we impose the normalization $\sqrt{P/(\hbar\omega_0)} \cdot 2\omega_0/c \cdot x(\Omega) = 1$. If the cavity is detuned, the response drops

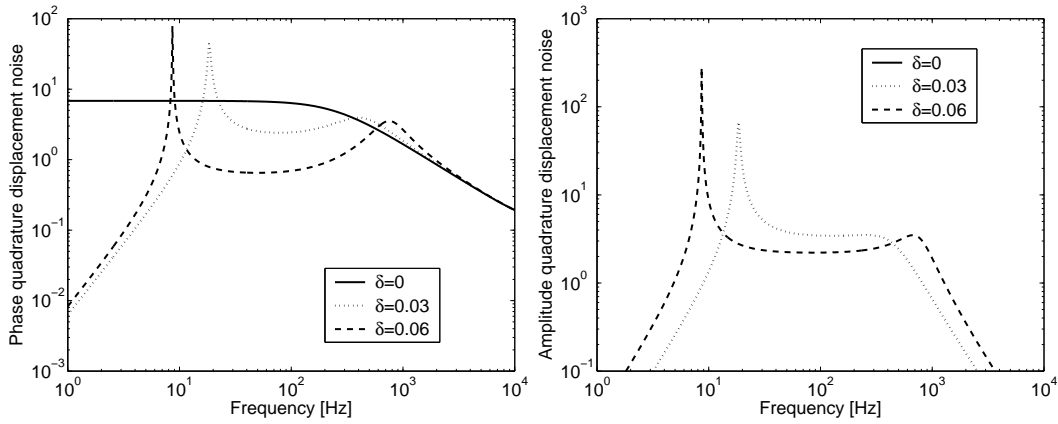


Figure 6.15: The plots show the displacement noise in the output field according to Eq. (6.40). If the cavity is tuned ($\delta = 0$), then the amplitude quadrature does not contain any displacement noise. As for the transmitted field (see [Figure 6.14](#)), the displacement noise of a detuned cavity is resonantly amplified at frequencies corresponding to the optical and optomechanical resonance.

to zero towards smaller frequencies. Consequently, although the reflected and transmitted noise is devoid of radiation-pressure fluctuations, the signal-to-noise ratio of the output field decreases for low frequencies. A more detailed sensitivity analysis for similar optical systems is found in [Chapter 8](#).

6.6 Third-Order Nonlinear Transformations

In this section, we investigate the Kerr medium inside the arm cavities of a Michelson interferometer and present signal and noise transfer functions. The results can be applied as a building block to evaluate the noise spectral density of a Kerr-enhanced Michelson interferometer with resonant sideband extraction (RSE) ([Mizuno et al.; 1993](#)) or even more complex optical systems with multiple mirrors at the dark port ([Rehbein et al.; 2005](#)). Our formalism is based on linearized transformations of the quadrature fields within two-photon quantum optics ([Caves and Schumaker; 1985](#)) which has previously been used to describe ponderomotive squeezing ([Kimble et al.; 2001](#)) and the optical spring effect ([Buonanno and Chen; 2002](#)). It is well-known that cavities containing a $\chi^{(3)}$ nonlinear

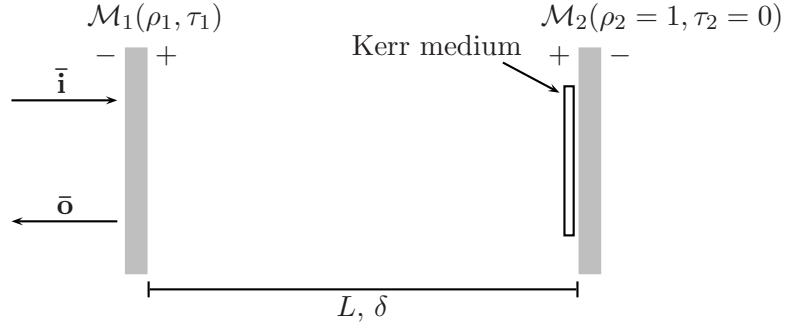


Figure 6.16: The Kerr medium is placed at the surface of \mathcal{M}_2 (e.g. a Kerr coating layer). The cavity is detuned by δ which adds to the power-dependent phase shift θP generated by the Kerr medium. Mirror \mathcal{M}_2 is assumed to be totally reflective.

crystal can provide an improved response to phase signals and quantum noise can become (Kerr) squeezed (Kitagawa and Yamamoto; 1986). Furthermore, there exist regions inside the parameter space where the cavity is multistable (Drummond and Walls; 1980). The nonlinear relation between the input power P_{in} and the intracavity power P reads

$$P = \frac{\tau_1^2}{1 + \rho_1^2 \rho_2^2 - 2\rho_1 \rho_2 \cos(2\delta + 2\theta P)} P_{\text{in}}. \quad (6.41)$$

where θ depends linearly on the $\chi^{(3)}$ nonlinearity; for $\theta = 0$ we obtain the intracavity power of a linear cavity. Figure 6.16 shows a sketch of the system considered here. We envision a cavity where a Kerr medium is placed at the surface of the second mirror \mathcal{M}_2 . High third-order nonlinearities have been reported (Miller et al.; 1983) suggesting that already a thin coating layer may exert the necessary transformation for our purposes. The nonlinear refractive index has to be of the order $n_2 \sim 10^{-8} \text{ m}^2/\text{W}$ if the layer has a thickness of a micron. In Figure 6.17, the phase shifts of light reflected from a Kerr cavity and the intra cavity powers are shown as a function of the cavity detuning. There is a critical choice of parameters where the phase response to a small change of the cavity detuning is infinite for one specific value of the detuning and where the cavity does not assume a multistable state. We consider this *critical state* to be the most promising one in view of enhancing the sensitivity for detecting signals induced by a cavity length change. It turns out that this is indeed the case.

For a rigorous treatment we start from the system's Kerr Hamiltonian in the interaction picture (see subsection 5.1.2)

$$\hat{H}_{\text{Kerr}} = \frac{\hbar}{2} \chi (\hat{a}^\dagger)^2 \hat{a}^2, \quad (6.42)$$

where \hat{a} is the field annihilation operator acting at a particular frequency and so does the Hamilton operator just involve one frequency. The quantity χ is proportional to the nonlinear susceptibility of the Kerr medium used. Denoting the interaction time by τ , the

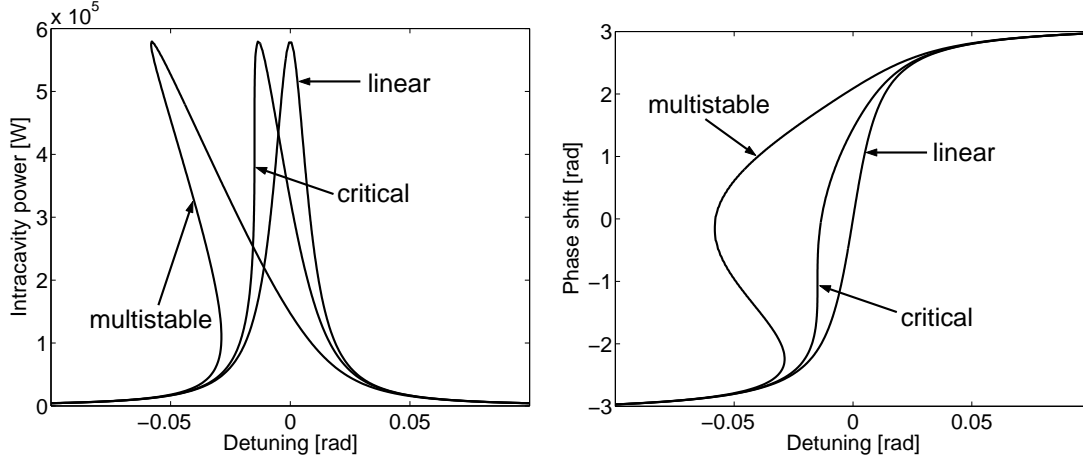


Figure 6.17: a) Intra cavity powers and b) phase shifts of reflected light for three cavities of different values for the nonlinear susceptibility of the Kerr medium. The critical state is characterized by possessing infinite slope at some value for the detuning.

equation of motion becomes

$$\frac{d\hat{a}}{d\tau} = -i\chi\hat{a}^\dagger\hat{a} \cdot \hat{a} \equiv -i\chi\hat{n} \cdot \hat{a}. \quad (6.43)$$

which is solved easily by making use of the fact that the photon number is conserved during the interaction with the Kerr medium ($[\hat{H}_{\text{Kerr}}, \hat{n}] = 0$):

$$\hat{a}(\tau) = e^{-i\chi\tau\hat{n}(0)} \cdot \hat{a}(0). \quad (6.44)$$

At first, we procure the usual linearized transformation rule that applies for intense optical fields weakly interacting with a Kerr medium. Therefore, the annihilation operator is decomposed into its (real) expectation value and a noise amplitude operator $\hat{a}(\tau) = \Lambda + \hat{v}(\tau)$. Keeping just first order terms of \hat{v} we obtain from Eq. (6.44)

$$\hat{v}(\tau) = e^{-i\chi\tau\Lambda^2} \left[\hat{v} - i\chi\tau\Lambda^2 \cdot (\hat{v} + \hat{v}^\dagger) \right]. \quad (6.45)$$

The linearized solution has to be evaluated for two sideband frequencies $\omega_0 \pm \Omega$ in order to obtain a field representation in terms of the quadrature amplitudes $\hat{v}_{1,2}(\tau)$ of the two-photon formalism (Caves and Schumaker; 1985). In this formalism the transfer functions map quadrature amplitudes which act at modulation frequencies Ω . The noise power spectral density of a phase sensitive photo detection (Harms et al.; 2003; Buonanno, Chen and Mavalvala; 2003) can be derived from the variances and covariances of the amplitude and phase quadrature amplitudes of the light field. To ease notation, we define the quadrature amplitude vector for small modulation frequencies $\Omega \ll \omega_0$

$$\bar{\mathbf{a}} = \begin{pmatrix} \hat{a}_1(\Omega) \\ \hat{a}_2(\Omega) \end{pmatrix} = \sqrt{\frac{1}{2}} \begin{pmatrix} \hat{a}(\omega_0 + \Omega) + \hat{a}^\dagger(\omega_0 - \Omega) \\ -i\hat{a}(\omega_0 + \Omega) + i\hat{a}^\dagger(\omega_0 - \Omega) \end{pmatrix}. \quad (6.46)$$

In the above quadrature notation the effect of a Kerr medium is easily described by introducing a so-called Kerr coupling constant \mathcal{K}_{op} which correlates amplitude quadrature fluctuations with phase quadrature fluctuations. In case of a Kerr nonlinear crystal (electro-optical Kerr effect) the coupling constant is frequency independent over a broad spectrum and reads

$$\mathcal{K}_{\text{op}} \equiv 2\chi\tau\Lambda^2 = 2\frac{n_2\omega_0 L_{\text{opt}} P}{\mathcal{A}c} \equiv \theta P, \quad (6.47)$$

where $n_2 \propto \chi \propto \chi^{(3)}$ is the nonlinear refractive index with units m^2/W , L_{opt} is the length of the Kerr medium and P/\mathcal{A} denotes the light intensity inside the Kerr medium. The factor 2 in Eq. (6.47) already anticipates the fact that the Kerr medium is placed inside a cavity and consequently the intensity is a sum of the intensities of two counter-propagating beams.

There are several effects in quantum optics experiments that show a light intensity dependent phase shift, similar to the electro-optical Kerr effect. It has been pointed out by (Loudon; 1981) that radiation pressure also results in intensity dependent phase shift and the same is true for light absorption in optics due to thermal expansion or temperature dependent refractive index. In analogy to Eq. (6.47) these effects may be described by appropriate coupling parameters \mathcal{K}_{rp} and \mathcal{K}_{th} , respectively. The radiation pressure effect was studied in great detail in (Kimble et al.; 2001; Buonanno and Chen; 2002) where, in analogy, the optomechanical coupling constant \mathcal{K}_{rp} was introduced. Note that radiation pressure and photo-thermally induced nonlinear phase shifts generally decrease with increasing frequency on scales which are smaller than the detection bandwidth.

Using the Kerr coupling constant, the respective linearized transformation of the quadrature noise fields assumes the form

$$\begin{pmatrix} \hat{v}_1(\tau) \\ \hat{v}_2(\tau) \end{pmatrix} = \begin{pmatrix} \cos(\mathcal{K}_{\text{op}}/2) & -\sin(\mathcal{K}_{\text{op}}/2) \\ \sin(\mathcal{K}_{\text{op}}/2) & \cos(\mathcal{K}_{\text{op}}/2) \end{pmatrix} \times \underbrace{\begin{pmatrix} 1 & 0 \\ -\mathcal{K}_{\text{op}} & 1 \end{pmatrix}}_{\equiv \mathbf{K}} \begin{pmatrix} \hat{v}_1 \\ \hat{v}_2 \end{pmatrix}. \quad (6.48)$$

One sees that the linearized Kerr transformation consists of a rotation in addition to a conversion of amplitude quadrature fluctuations into phase quadrature fluctuations. A rigorous statement concerning the conditions under which the linearization is valid can be made if we compare the spectral density matrix (i.e. Fourier transform of the correlation matrix) of the linearized theory with the exact spectral density matrix which one obtains from the expectation values $\langle \hat{a}(\tau)^2 \rangle$, $\langle \hat{a}(\tau) \rangle$ and their complex conjugates (see Appendix B). For instance, the variance of the amplitude-quadrature amplitude reads

$$S(\hat{v}_1) = 1 + 2\Lambda^2 \left[e^{\Lambda^2(\cos(2\chi\tau)-1)} \cos(\Lambda^2 \sin(2\chi\tau) + \chi\tau) - e^{2\Lambda^2(\cos(\chi\tau)-1)} (1 + \cos(2\Lambda^2 \sin(\chi\tau))) + 1 \right] \quad (6.49)$$

Expanding the right-hand sides with respect to $\chi\tau$, one finds that if terms of order $\mathcal{O}[(\chi\tau)^3]$ and $\mathcal{O}[(\Lambda\chi\tau)^2]$ are being neglected, then for coherent fields the spectral density matrix is indeed identical to the matrix $\mathbf{K}\mathbf{K}^T$. The system studied here has $\chi\tau \sim 10^{-24}$ and $\Lambda \sim 10^{12}$ so that both conditions are satisfied.

We will now derive the signal and quantum noise transfer functions of the Kerr nonlinear cavity. According to Figure 6.16 a (detuned) cavity of macroscopic length L is pumped by a coherent input field of frequency ω_0 through mirror \mathcal{M}_1 , the input noise being denoted by $\bar{\mathbf{i}}$. Propagation of the field from one to the other mirror is performed by the transfer matrix

$$\mathbf{P}_L \equiv e^{i\Phi} \begin{pmatrix} \cos(\phi) & -\sin(\phi) \\ \sin(\phi) & \cos(\phi) \end{pmatrix} \quad (6.50)$$

To take the sidebands into account, the (complex) phase with $\Phi = \Omega L/c$ is required. The transformation is applied to quadrature vectors such as Eq. (6.46). The rotation angle ϕ corresponds to the phase shift of the carrier light. Here, two different contributions have to be considered:

$$\phi = \delta + \frac{\mathcal{K}_{\text{op}}}{2} \quad (6.51)$$

where δ denotes the detuning of the cavity and $\mathcal{K}_{\text{op}}/2$ is the phase-shift of the carrier field due to the Kerr medium.

We choose to place the Kerr medium close to \mathcal{M}_2 . After propagating the field to the right mirror \mathcal{M}_2 we use the transfer matrix \mathbf{K} from Eq. (6.48) which embodies the transition from amplitude modulations to phase modulations. Using the matrix \mathbf{K} requires that the carrier of the electromagnetic field is found in the amplitude quadrature (then Λ is real). By choosing the phase of the incoming beam appropriately, the carrier field impinging on the right mirror is rotated into the amplitude quadrature of our reference system. Therefore the round trip matrix for the whole cavity reads:

$$\mathbf{R} \equiv \mathbf{P}_L \cdot \mathbf{K} \cdot \mathbf{P}_L. \quad (6.52)$$

We obtain the reflection transfer matrix \mathbf{C} for the (detuned) nonlinear cavity which represents the noise transfer function.

$$\mathbf{C} \equiv \frac{1}{\mathbb{I} - \rho_1 \mathbf{R}} \cdot [\mathbf{R} - \rho_1 \cdot \mathbb{I}]. \quad (6.53)$$

We now assume that a classical signal acts on mirror \mathcal{M}_2 inducing a motion which gives rise to a phase modulation of reflected fields. The quadrature vector corresponding to the signal sidebands is transferred from \mathcal{M}_2 to the output port via a matrix \mathbf{S}

$$\mathbf{S} \equiv \frac{\tau_1}{\mathbb{I} - \rho_1 \mathbf{R}} \cdot \mathbf{P}_L. \quad (6.54)$$

Vacuum fields attributed to losses inside the cavity will give a third contribution to the overall cavity output field. In that case, a vacuum field $\bar{\mathbf{n}}$ mixes with the intracavity field (see Eq. (6.7)). The loss transfer to the output port is governed by the same matrix \mathbf{S} .

Eventually, the input-output relation for a lossless cavity can be cast into the following form:

$$\bar{\mathbf{o}} = \mathbf{C} \cdot \bar{\mathbf{i}} + \mathbf{S} \cdot \left(\sqrt{\frac{P}{\hbar\omega_0}} \frac{\omega_0}{c} \begin{pmatrix} 0 \\ 2x(\Omega) \end{pmatrix} \right). \quad (6.55)$$

where $x(\Omega)$ is the amplitude of relative displacements between the two cavity mirrors.

We may now analyze the performance of interferometers that contain Kerr nonlinear cavities described by Eq. (6.55). If two such cavities are arranged within a Michelson interferometer, its antisymmetric signal mode is described by the signal transfer matrix given above multiplied with a factor $\sqrt{2}$ to each of its components. The transfer matrix \mathbf{C} and the adjusted signal transfer-function $\bar{\mathbf{s}}$ directly translate into the spectral noise density and sensitivity of the interferometer for a measured quadrature $\hat{o}_\zeta = \hat{o}_1 \cos \zeta + \hat{o}_2 \sin \zeta$, where ζ is the homodyne angle (see Eq. (5.21)). One finds that the optimal signal-to-noise

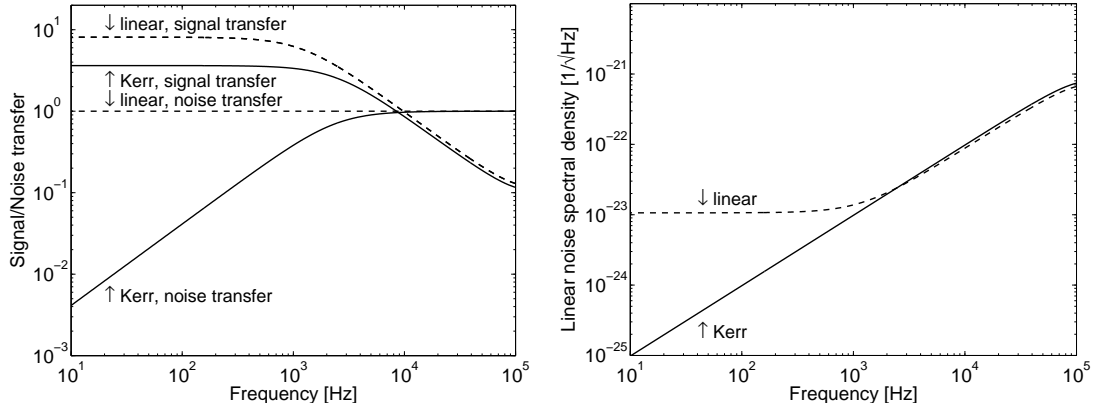


Figure 6.18: The left graph shows the signal and noise transfer functions for a Fabry-Pérot cavity which contains an optical Kerr medium. In comparison with the linear cavity, Kerr squeezing of the fields gives rise to a noise cancellation within the linewidth of the cavity. In parallel, the transfer function for displacement signals of the end mirror is decreased by a modest factor. Combining the two function, one obtains the strain sensitivity of the cavity (i.e. strain is equal to twice the displacement divided by the cavity length) which is shown in the right graph. The sensitivity is improved for low frequencies.

ratio is obtained by choosing a homodyne angle ζ such that the amplitude quadrature referred to the reflected carrier, i.e. to be distinguished from \hat{o}_1 , of the output field is measured. The results are presented in Figure 6.18. Obviously, the optimal parameter settings minimize the noise transfer function (Kerr squeezing) within the cavity linewidth. The signal transfer is decreased by a modest factor. The corresponding strain sensitivity is improved at low frequencies. The calculation does not take radiation pressure into account which would gravely degrade the low frequency improvement of the sensitivity. However, (Rehbein et al.; 2005) investigate a similar system with additional optics in the output port which exhibit the noise cancellation due to Kerr squeezing at much higher frequencies. Thereby, these schemes may become a promising candidate for an upgrade of next generation gravitational wave detectors.

CHAPTER 7

The Michelson Interferometer

The Michelson interferometer plays a prominent role in gravitational physics. More than 100 years ago, the first experiment with a Michelson interferometer falsified the aether theory ([Michelson and Morley; 1887](#)) for the propagation of light which might well be one of the many new discoveries in that time which 20 years later led Einstein to formulate the theory of relativity. The Michelson interferometer measures relative phase shifts of two coherent light trains which travelled along two different arms of the interferometer. This sounds remarkably simple, but the crux of the matter lies in the fact that Michelson interferometers are usually high precision instruments exploring fundamental limits of all kinds. Nowadays, interferometric gravitational wave detectors exist which generate a measurable phase shift of light if the length of one arm changes by 10^{-18} m and less. Luckily, a random thermal motion of the surface atoms is averaged out to some degree due to the fact that the beam has a cross section of the order 10 cm when it is reflected ([Levin; 1998a](#)), ([Liu and Thorne; 2000](#)), ([Braginsky and Vyatchanin; 2003](#)). In this chapter, we investigate Michelson interferometers without additional optics in the output port (the signal recycling technique is presented in [Chapter 8](#)). We start to develop a generic approach in [section 7.1](#) and introduce radiation pressure effects in [section 7.2](#). The performance of gravitational wave detectors, especially of the next generation, also depends on the photon detection scheme at the output port which is discussed in [section 7.3](#).

7.1 Input-Output Relations without Radiation Pressure

We want to address the question whether there exists a simple equation which completely characterizes a Michelson interferometer without specification of the different noise sources or details of the build-up. The answer is a conditional "yes". The conditions are that

- the interferometer is in a stationary state, i.e. constant power of the carrier field everywhere
- the transfer of signal or noise sidebands from one point of the interferometer to

another is linear

The respective equation is called the input-output relation of the interferometer which constitutes a linear function \mathbf{T} of all input fields onto the output field $\bar{\mathbf{o}}$. Figure 7.1 shows in which way a Michelson interferometer is abstracted. The only specification we choose to make is that there is a 50/50 beam splitter which couples the fields according to Eq. (6.6). Fields which propagate away from the beam splitter experience a back-transfer described by the linear functions $\mathbf{W}, \mathbf{N}, \mathbf{E}$ assigned to the bright port, the north arm and the east arm respectively (e.g. due to arm end mirrors or a power-recycling mirror in the bright port). Noise or signal sidebands emerge in each of these ports in addition to the dark port

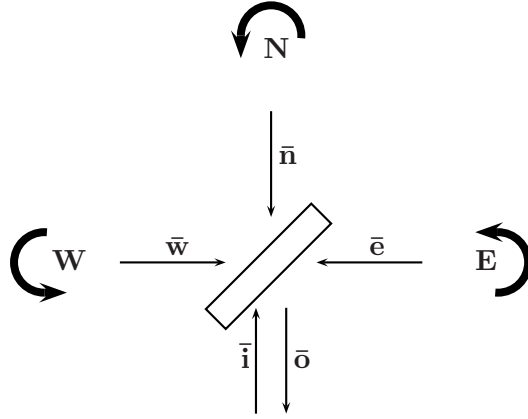


Figure 7.1: Consider a 50/50 beam splitter within a Michelson topology. The fields which are generated inside the four ports (e.g. displacement noise, technical laser noise, gravitational wave signals, vacuum noise etc.) are designated by $\bar{\mathbf{e}}, \bar{\mathbf{n}}, \bar{\mathbf{w}}$ and $\bar{\mathbf{i}}$. The transfer functions \mathbf{E}, \mathbf{N} and \mathbf{W} describe round trips inside each port (i.e. there might be a mirror which reflects the outgoing light back towards the beam splitter). The input-output relation is the linear function $\mathbf{T}(\bar{\mathbf{e}}, \bar{\mathbf{n}}, \bar{\mathbf{w}}, \bar{\mathbf{i}})$ which maps all these fields to the dark port represented by the output field $\bar{\mathbf{o}}$.

vacuum field $\bar{\mathbf{i}}$. These sidebands superpose linearly forming the fields $\bar{\mathbf{w}}, \bar{\mathbf{n}}, \bar{\mathbf{e}}$ in each port. Solving the beam splitter coupling relations Eq. (6.6) for the output field, we obtain

$$\bar{\mathbf{o}} = \frac{1}{2 - \mathbf{WE} - \mathbf{NW}} \left[(\mathbf{E} + \mathbf{N} - 2\mathbf{NEW})\bar{\mathbf{i}} + (\mathbf{N} - \mathbf{E})\bar{\mathbf{w}} + \sqrt{2}(1 - \mathbf{EW})\bar{\mathbf{n}} - \sqrt{2}(1 - \mathbf{NW})\bar{\mathbf{e}} \right] \quad (7.1)$$

Many well-known properties of Michelson interferometers can be derived from this equation

- The dark fringe condition is satisfied if the bright port fields $\bar{\mathbf{w}}$ do not contribute to the output $\bar{\mathbf{o}}$. Obviously, this is true if $\mathbf{E} = \mathbf{N}$ which entails that the arms must have equal lengths.

- If the interferometer operates at dark fringe, then the output field contains a component which is proportional to the difference $\bar{\mathbf{n}} - \bar{\mathbf{e}}$ which also means that the interferometer is exclusively sensitive to antisymmetric changes of the arm lengths.
- Due to the fraction in front of the square brackets, the input-output relation under generic conditions will exhibit an oscillatory form whose period is determined by the smallest free spectral range defined by any part of the interferometer (which requires the implementation of cavities, e.g. a power recycling cavity).

Imposing the dark-fringe condition $\mathbf{N} = \mathbf{E}$ and denoting the common arm transfer function by \mathbf{A} , the input-output relation simplifies to

$$\bar{\mathbf{o}} = \mathbf{A} \cdot \bar{\mathbf{i}} + \frac{1}{\sqrt{2}}(\bar{\mathbf{n}} - \bar{\mathbf{e}}) \quad (7.2)$$

The simplicity of the dark-fringe input-output relation is astonishing. Just one transfer function \mathbf{A} has to be specified to determine the output field and as mentioned before the bright-port field $\bar{\mathbf{w}}$ does not contribute to the output. Unfortunately, all currently operating detectors do not operate at dark fringe due to technical reasons (see [section 7.3](#)). Just the carrier field interferes destructively towards the dark port. However, although the arm transfer functions are not identical they become almost identical for low sideband frequencies. Therefore, the low frequency regime which includes the detection band of the interferometer is approximately governed by Eq. (7.2).

Let us explore a more generic case by considering a power-recycled interferometer with unequal arm lengths. A power recycling mirror with reflectivity ρ_w reflects light back which leaves the beam splitter towards the bright port (i.e. $\mathbf{W} \neq 0$). Its distance to the beam splitter is L_w . A power recycling cavity is formed by the power recycling mirror and the arm end mirrors which is tuned to the carrier frequency providing maximum power build-up. Therefore, the transfer functions \mathbf{WE}, \mathbf{WN} do not change the phase of the carrier field. Each arm (\mathbf{N}, \mathbf{E}) may well be detuned by an angle δ (i.e. inducing a phase shift δ of the carrier) which is compensated by an equal detuning with opposite sign of the bright-port transfer \mathbf{W} . Later we will discover that although δ appears in the input-output relations, it affects them in a way that one may choose to set it equal to zero. The sidebands sense a macroscopical length difference ΔL between the two arms which typically amounts to some centimeters for current detectors. The east arm has length L and the north arm length $L + \Delta L$. For simplicity, the arm end mirrors are totally reflective $\rho_n = 1, \rho_e = 1$. Altogether, one obtains the following set of transfer functions as functions of the sideband frequency Ω

$$\begin{aligned} \mathbf{W} &= \rho_w \mathbf{D}(-2\delta) e^{2i\Omega L_w/c} \\ \mathbf{N} &= \mathbf{D}(2\delta) e^{2i\Omega(L+\Delta L)/c} \\ \mathbf{E} &= \mathbf{D}(2\delta) e^{2i\Omega L/c} \end{aligned} \quad (7.3)$$

The form of the function $\mathbf{D}(\delta)$ depends on whether we choose to work in the one- or two-photon formalism (Eqs. (6.2)&(6.3) with $\Omega = 0$). In the latter case, Ω is the (positive)

modulation frequency instead of a (positive or negative) sideband frequency. Insertion of the transfer functions into Eq. (7.1) yields

$$\begin{aligned} \bar{\mathbf{o}} = & \frac{1}{1 - \rho_w e^{i\Omega(2L+2L_w+\Delta L)/c} \cos(\Omega\Delta L/c)} \cdot \\ & \left[\mathbf{D}(2\delta) \left(e^{i\Omega(2L+\Delta L)/c} \cos(\Omega\Delta L/c) - \rho_w e^{2i\Omega(2L+L_w+\Delta L)/c} \right) \bar{\mathbf{i}} \right. \\ & + \mathbf{D}(2\delta) i e^{i\Omega(2L+\Delta L)/c} \sin(\Omega\Delta L/c) \bar{\mathbf{w}} \\ & + \frac{1}{\sqrt{2}} (1 - \rho_w e^{2i\Omega(L+L_w)/c}) \bar{\mathbf{n}} \\ & \left. - \frac{1}{\sqrt{2}} (1 - \rho_w e^{2i\Omega(L+L_w+\Delta L)/c}) \bar{\mathbf{e}} \right] \end{aligned} \quad (7.4)$$

In the language of the one-photon formalism, the function $D(2\delta)$ describes a frequency independent phase shift 2δ . Signal amplitudes are generated at the end mirrors and have to be propagated to the beam splitter. Therefore, $\bar{\mathbf{n}}$, $\bar{\mathbf{e}}$ contain a factor $D(\delta)$. Propagating the field injected at the power-recycling mirror to the beam splitter yields the amplitude $\bar{\mathbf{w}}$ which, on that account, contains a factor $D(-\delta)$. Consequently, the term $D(\delta)$ can be factored out from the input-output relation, thereby becoming physically irrelevant. Henceforth, we set $D(\delta) = 1$.

The sidebands incorporated into the fields $\bar{\mathbf{n}}$, $\bar{\mathbf{e}}$ due to seismic or thermal noise and the gravitational wave signal occur at much smaller sideband frequencies than the free spectral range $\text{fsr}_{\text{pr}} = c/(2L + 2L_w + \Delta L)$ of a typical power-recycling cavity. So one may evaluate the respective transfer functions in the low frequency limit $\Delta L \rightarrow 0, L_w \rightarrow 0$. As outlined in subsection 7.3.2, the bright-port field $\bar{\mathbf{w}}$ of current interferometers contains so-called Schnupp modulation fields at higher sideband frequencies and for that reason, we focus on an investigation of the bright-port dark-port transfer. We consider an interferometer with

	Symbol	Value
Distance between PRM and BS	L_w	1.145 m
Length of east arm	L	1195.5 m
Arm length difference	ΔL	0.069 m
Reflectivity of PRM	ρ_w	0.9

Table 7.1: Parameters for an interferometer with bright-port dark-port transfer.

parameter values according to Table 7.1. The power-recycling cavity has a free spectral range of $\text{fsr}_{\text{pr}} \approx 1.24 \cdot 10^5$ Hz which is roughly two orders of magnitudes greater than the highest frequencies of the signal detection band. The amplitude of the transfer function to the dark port for fields which enter the interferometer at the power-recycling mirror is

given by

$$|\mathbf{T}_w| = \frac{\sqrt{1 - \rho_w^2} |\sin(\Omega \Delta L / c)|}{\sqrt{1 + \rho_w^2 \cos^2(\Omega \Delta L / c) - 2\rho_w \cos(\Omega \Delta L / c) \cos(\Omega(2L + 2L_w + \Delta L) / c)}} \quad (7.5)$$

The function is plotted in [Figure 7.2](#). The envelope of the fast oscillations which are characterized by the frequency fsr_{pr} has a first maximum at

$$f_{\text{max}} = \frac{c}{2\pi \Delta L} \arccos(\rho_w) \approx 2.2 \cdot 10^8 \text{ Hz} \quad (7.6)$$

As [Eq. \(7.5\)](#) shows, the amplitude of the transfer function is symmetric with respect to the sideband frequency Ω and consequently two sidebands at $+\Omega$ and $-\Omega$ which enter the interferometer with equal amplitude leave the interferometer at the dark port with equal amplitude. Since we have not yet introduced radiation pressure effects, it is useless

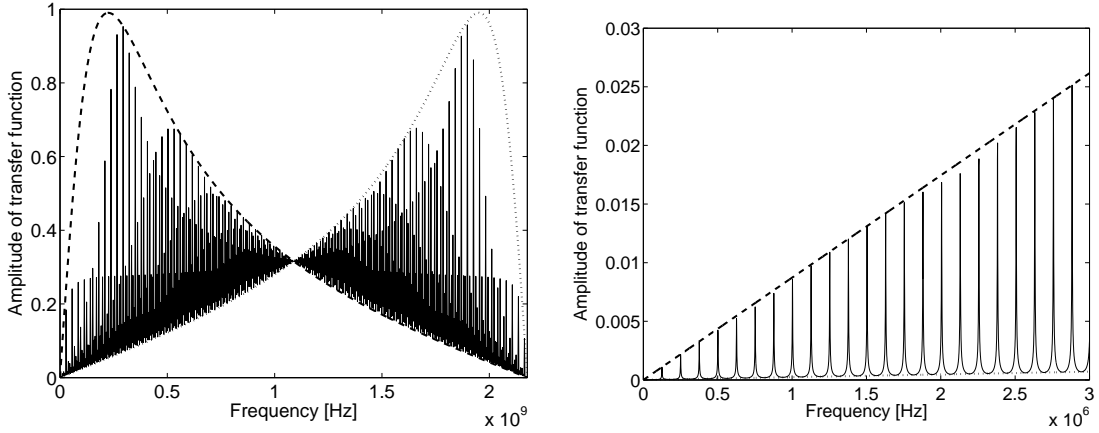


Figure 7.2: The amplitude of the bright-port dark-port transfer oscillates with the free spectral range of the power-recycling cavity. The upper and lower envelope touch at $f = c/(4\Delta L)$ where the amplitude is equal to the transmissivity of the power-recycling mirror.

to discuss in detail the sensitivity of detectors governed by [Eq. \(7.1\)](#). In fact, the whole story can be told in a few sentences. The quantum phase noise spectrum is the frequency independent relative photon-counting noise $1/\sqrt{N}$ and the phase shift of the light due to a gravitational wave can be evaluated in the long-wavelength limit [Eq. \(2.70\)](#). It follows that the sensitivity (i.e. noise to signal ratio) is given by

$$\sqrt{S_h} = \frac{c}{\omega_0 L} \sqrt{\frac{\hbar \omega_0}{P}} \quad (7.7)$$

where ω_0 is the carrier frequency and P is the power inside the power-recycling cavity. With $L = 1200 \text{ m}$, $\omega_0 = 1.77 \cdot 10^{15} \text{ s}^{-1}$ and $P = 10 \text{ kW}$ one obtains $\sqrt{S_h} \approx 6.1 \cdot 10^{-22} \text{ Hz}^{-1/2}$. [Eq. \(7.7\)](#) obtains for gravitational waves whose direction of propagation is perpendicular to the detector plane. We also assumed that the field $\bar{\mathbf{i}}$ which determines the quantum noise at the output of a lossless interferometer is a coherent vacuum field. Squeezed

vacuum fields for example, exhibit different photon statistics. The long-wavelength limit is well established since Earth bound detectors typically measure gravitational waves around 100 Hz which corresponds to a wavelength of 3000 km. In contrast, a detector's arm length does not exceed a few kilometers. More detail will be added in the following section and [Chapter 8](#).

7.2 Input-Output Relations with Radiation Pressure

The sensitivity of realistic interferometers suffers from many vacuum fields emerging at different input ports, and other noise sources further increase the noise spectral density of the photocurrent. Therefore, we develop a formalism which allows to gradually implement these sources by altering the equations at the beginning in a clear and systematic way. However, most loss related effects can be read off directly from the results.

In [subsection 7.2.1](#), we discuss some general properties of beam splitters and present the coupling equations of the fields. The solution is presented in [subsection 7.2.2](#) for a rather specific configuration, the power-recycled interferometer with equal Michelson arms and a 50-50 beam splitter operating at dark fringe. Here, "equal" refers to the transfer function of a light field which enters one arm through the beam splitter and follows a round trip back to the beam splitter. This notion depends on the coupling relations at the beam splitter. The Michelson interferometer with a symmetric beam splitter does not hold the dark fringe condition if the two arms are equal. In the last section, we present the noise spectral density for the current set-up of the (lossless) dual-recycled GEO 600 interferometer. We conclude that the corresponding dark port noise spectral density at low frequencies is dominated by technical bright port fluctuations. A comparison between the LIGO and GEO 600 configuration shows that the contribution of the bright port noise to the output spectral density of LIGO is smaller by 6 orders of magnitude.

7.2.1 The Coupling Equations

Usually, one describes quantum fields by means of their annihilation and creation operators. The two-photon formalism developed in ([Caves and Schumaker; 1985](#)) turns out to be a more suitable formalism for measurements with heterodyne or homodyne detectors. These two classes of detectors measure the quadrature fields of the light whose amplitudes annihilate quanta of modulations. Correlations between the two sidebands find a natural representation in that formalism and the spectral densities of the two quadratures' quantum noise is given by orthogonal sections through the so called noise ellipse. Modern publications discussing high-power interferometry show that one can derive simple and easy-to-interpret expressions for the quadrature transfer functions of various Michelson-based configurations ([Kimble et al.; 2001](#)), ([Buonanno and Chen; 2001](#)), ([Buonanno and Chen; 2002](#)), ([Harms et al.; 2003](#)). Therefore, we present all equations in the two-photon formalism benefiting from algebraic properties of the quadrature fields concerning radiation-pressure effects. The two quadratures \hat{a}_1, \hat{a}_2 merge into one single object which we call the quadra-

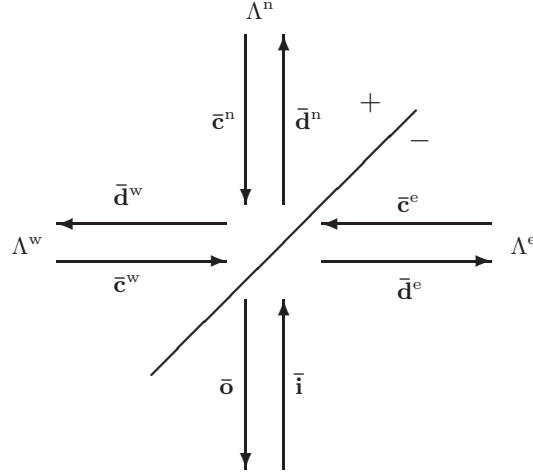


Figure 7.3: The noise density of the output field \bar{o} determines the noise of the gravitational-wave detection. All \bar{c}^i and the input field \bar{i} are propagating towards the beam splitter. The fields \bar{d}^i , \bar{o} propagate away from it. The asymmetric beam splitter reflects with a minus sign on the side where it is indicated in the picture. The Λ^i denote the classical amplitudes of the carrier in each direction. The south port does not contain any carrier field at dark fringe.

ture vector:

$$\bar{\mathbf{a}} = \begin{pmatrix} \hat{a}_1 \\ \hat{a}_2 \end{pmatrix} \quad (7.8)$$

Many important physical transformations acting on $\bar{\mathbf{a}}$ can be interpreted geometrically as rotations and scalings of vectors in the space spanned by the two quadrature fields (i.e. the quadrature space). A more detailed treatment is given in (Harms; 2002). Our notational conventions are introduced in Figure 7.3. We assume that the expectation values of both components of all quadrature vectors are much smaller than the carrier amplitudes Λ^i . We treat these amplitudes as fixed and they enter our calculations whenever they influence the quantum noise. In all other equations, we do not take account of them explicitly. The amplitudes couple at the beam splitter according to the following relations:

$$\begin{aligned} \bar{o} &= \tau \bar{c}^n - \rho \mathbf{P}_x \bar{c}^e \\ \bar{d}^e &= \tau \bar{c}^w - \rho \mathbf{P}_x \bar{i} \\ \bar{d}^n &= \tau \bar{i} + \rho \mathbf{P}_{-x} \bar{c}^w \\ \bar{d}^w &= \tau \bar{c}^e + \rho \mathbf{P}_{-x} \bar{c}^n \end{aligned} \quad (7.9)$$

The beam splitter deviates from its equilibrium position by an amount \hat{x} which is governed by the equation of motion and which is much smaller than the wavelength of the carrier light (typically $\langle \hat{x} \rangle \ll 1\mu\text{m}$). We just need one variable to determine the position of the beam splitter since, concerning the phase shift of the reflected fields, a motion downwards of the beam splitter is completely analogous to a motion to the right. Periodic forces

acting on the beam splitter yield a periodic motion and the propagations \mathbf{P}_x generate modulation fields each time when light is reflected. In principle, the equation of motion for \hat{x} may contain classical components if a signal acts on the beam splitter. Here, we do not consider classical contributions to \mathbf{P}_x . In that case, the modulation fields are completely determined by the radiation-pressure fluctuations of the light, i.e. by the fluctuations of the amplitude quadratures \hat{a}_1 of all the fields. The beam splitter has to compensate the momentum which is effectively carried out of the region by the light. Therefore, we make the following ansatz in terms of the modulation Fourier components neglecting higher orders of the vacuum amplitudes

$$\hat{x} \propto \Lambda^w(\hat{c}_1^w + \hat{d}_1^w) - \Lambda^e(\hat{c}_1^e + \hat{d}_1^e) + \Lambda^n(\hat{c}_1^n + \hat{d}_1^n). \quad (7.10)$$

The minus sign in front of the second bracket means that the momentum assigned to the east fields is carried in the opposite direction with respect to the momentum carried by the west fields, whereas the plus sign in front of the last bracket means that a motion of the mirror downwards is equivalent to a motion towards the east concerning phase shifts of the reflected light. An explicit expression for the propagation \mathbf{P}_x is developed in the next section, when the power-recycled Michelson interferometer is discussed. At this point, it suffices to mention that the propagation becomes the unity matrix if the field on which it acts is not accompanied by a high-power carrier amplitude. In other words, the position fluctuations of the beam splitter does not create any sidebands, because there is no carrier on which sidebands with significant amplitude could be modulated. For interferometers operating at dark fringe one obtains

$$\begin{aligned} \mathbf{P}_x \bar{\mathbf{i}} &= \bar{\mathbf{i}} \\ \mathbf{P}_x \bar{\mathbf{c}}^j &= \bar{\mathbf{c}}^j - \Lambda^j \cdot \bar{\kappa}(\bar{\mathbf{c}}^i, \bar{\mathbf{d}}^i) \end{aligned} \quad (7.11)$$

The vector $\bar{\kappa}$ depends on the displacement \hat{x} and consequently, it depends on all the fields which enter into the equation of motion.

Now, we are going to add three more equations to our system of coupling relations Eq. (7.9). The idea is to assign round trip transfer functions \mathbf{E} , \mathbf{N} , \mathbf{W} and independent fields $\bar{\mathbf{e}}$, $\bar{\mathbf{n}}$, $\bar{\mathbf{w}}$ to three of the four ports. The new fields comprise a sum of all fields originating in the corresponding port, e.g. vacuum fields due to losses or classical signal fields due to a gravitational wave. One may understand this step as some sort of closure of the ports by means of mirrors which reflect the outgoing light back to the beam splitter.

$$\begin{aligned} \bar{\mathbf{c}}^e &= \mathbf{E}\bar{\mathbf{d}}^e + \bar{\mathbf{e}} \\ \bar{\mathbf{c}}^n &= \mathbf{N}\bar{\mathbf{d}}^n + \bar{\mathbf{n}} \\ \bar{\mathbf{c}}^w &= \mathbf{W}\bar{\mathbf{d}}^w + \bar{\mathbf{w}} \end{aligned} \quad (7.12)$$

The latter equations are the most general, linear equations which govern the round trip of the light. In the two-photon formalism, the transfer functions \mathbf{E} , \mathbf{N} , \mathbf{W} are transfer matrices acting on quadrature vectors.

7.2.2 The Input-Output Relation

The input-output relations of an optical system comprise all contributions to the output field, i.e. the field which is detected by the photodiode. It is obtained by solving the

coupling equations Eq. (7.9) and Eq. (7.12):

$$\bar{\mathbf{o}} = \mathbf{IO}(\bar{\mathbf{i}}, \bar{\mathbf{w}}, \bar{\mathbf{n}}, \bar{\mathbf{e}}) \quad (7.13)$$

We present the solution for a power-recycled interferometer with equal arms and a 50-50

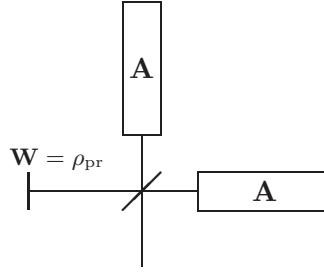


Figure 7.4: Power-recycled interferometer. Both arms are described by the same transfer matrix \mathbf{A} . The west port contains a power-recycling mirror with amplitude reflectivity ρ_{pr} . It forms the power-recycling cavity with the end mirrors of the Michelson interferometer. The mirror's distance to the beam splitter is set to be an integer multiple of the carrier wavelength. The same holds for the lengths of the two interferometer arms.

beam splitter as shown in Figure 7.4:

$$\begin{aligned} \rho = \tau &= \frac{1}{\sqrt{2}} && \text{50-50} \\ \mathbf{A} \equiv \mathbf{E} = \mathbf{N} &&& \text{equal arms} \\ \mathbf{W} &= \rho_{\text{pr}} && \text{power recycled} \\ \Lambda \equiv \Lambda^w &= \sqrt{2}\Lambda^e = \sqrt{2}\Lambda^n && \end{aligned} \quad (7.14)$$

The radiation-pressure induced noise sidebands are derived from the matrix for small propagations and from the equation of motion of the beam splitter. Small propagations \mathbf{P}_x lead to the following transformation of the quadrature vectors (Harms; 2002):

$$\begin{pmatrix} 1 & -\frac{\omega_0}{c}\hat{x} \\ \frac{\omega_0}{c}\hat{x} & 1 \end{pmatrix} \bar{\mathbf{c}}^j \approx \bar{\mathbf{c}}^j + \frac{\omega_0\Lambda^j}{c} \begin{pmatrix} 0 \\ \hat{x}(\bar{\mathbf{c}}^i, \bar{\mathbf{d}}^i) \end{pmatrix} \quad (7.15)$$

The second term on the right-hand side corresponds to the sidebands which are created by the oscillating beam splitter through phase modulations. The carrier frequency ω_0 is much bigger than the modulation frequency which, henceforth, is denoted by Ω . The equation of motion for \hat{x} is governed by Newton's law

$$\hat{x} = -\frac{\delta P(\bar{\mathbf{c}}^i, \bar{\mathbf{d}}^i)}{mc\Omega^2} \quad (7.16)$$

The fluctuating part δP of the radiation pressure is proportional to the right-hand side of Eq. (7.10)

$$\delta P = \hbar\omega_0 \cdot \left[\Lambda^w(\hat{c}_1^w + \hat{d}_1^w) - \Lambda^e(\hat{c}_1^e + \hat{d}_1^e) + \Lambda^n(\hat{c}_1^n + \hat{d}_1^n) \right] \quad (7.17)$$

Taking everything together, we cast Eq. (7.15) into the form

$$\mathbf{P}_x \bar{\mathbf{c}}^j \approx \bar{\mathbf{c}}^j - \frac{\hbar\omega_0^2 \Lambda \Lambda^j}{mc^2 \Omega^2} \begin{pmatrix} 0 & 0 \\ 1 & 0 \end{pmatrix} \cdot \left[(\bar{\mathbf{c}}^w + \bar{\mathbf{d}}^w) - \frac{1}{\sqrt{2}}(\bar{\mathbf{c}}^e + \bar{\mathbf{d}}^e) + \frac{1}{\sqrt{2}}(\bar{\mathbf{c}}^n + \bar{\mathbf{d}}^n) \right] \quad (7.18)$$

Before we write down the input-output relation, we introduce the abbreviation

$$K = \begin{pmatrix} 0 & 0 \\ -K_B & 0 \end{pmatrix}, \quad K_B \equiv \frac{\hbar\omega_0^2 \Lambda^2}{mc^2 \Omega^2} \quad (7.19)$$

Inserting Eq. (7.18) into the coupling equations and subsequently solving the system of linear equations for the output field, one obtains

$$\bar{\mathbf{o}} = \frac{1}{2(1 - \mathbf{A}\rho_{\text{pr}}) - (2 + (1 - \mathbf{A})\rho_{\text{pr}})(1 + \mathbf{A})K} \left[\begin{aligned} & (2\mathbf{A}(1 - \mathbf{A}\rho_{\text{pr}}) + (1 - (1 + 2\rho_{\text{pr}})\mathbf{A})(1 + \mathbf{A})K) \bar{\mathbf{i}} \\ & + \sqrt{2}(1 - \mathbf{A}\rho_{\text{pr}}) \bar{\mathbf{n}} \\ & - \sqrt{2}((1 - \mathbf{A}\rho_{\text{pr}}) - (1 + \rho_{\text{pr}})(1 + \mathbf{A})K) \bar{\mathbf{e}} \\ & + (1 + \mathbf{A})^2 K \bar{\mathbf{w}} \end{aligned} \right] \quad (7.20)$$

If the radiation-pressure fluctuations are negligible, then the matrix K becomes zero and the input-output relations reduce to a well-known form. The most interesting aspect of this result is probably contained in the last term within the square brackets. It says that whenever there are radiation-pressure fluctuations acting on the beam splitter, then all fluctuations from the west port (also known as the bright port) couple to the output port. This contribution is proportional to the non-zero component of the matrix K . This might turn out to be a problem for all high-power interferometers, since the laser field suffers from high technical noise at low sideband frequencies, which couples into the field $\bar{\mathbf{w}}$. The technical noise at low frequencies can be several orders higher compared to pure vacuum fluctuations. In the next section, we apply our solution to a specific configuration, namely the dual recycled interferometer GEO 600.

7.2.3 The Noise Spectral Density

The spectral density corresponding to the input-output relation Eq. (7.20) is obtained under the following assumptions. The state of the input field $\bar{\mathbf{i}}$ at the south port is a coherent vacuum field and $\bar{\mathbf{w}}$ is the fraction of the laser field which transmits into the power-recycling cavity. Expressed in terms of single-sided spectral density matrices these properties assume the form

$$\mathbf{S}(\bar{\mathbf{i}}) = \mathbf{1}, \quad \mathbf{S}(\bar{\mathbf{w}}) = \tau_{\text{pr}}^2 \cdot \mathbf{S}_{\text{tech}}(\Omega) \quad (7.21)$$

The matrix \mathbf{S}_{tech} is diagonal which means that the treatment does not account for correlations between the two quadratures built up inside the laser. The amount of technical noise which is brought into the interferometer by $\bar{\mathbf{w}}$ is estimated from measurements performed on the GEO 600 laser. Optical losses occurring in real interferometers at the end mirrors or at the beam splitter are not included in the sense that we do not mix the fields inside the interferometer with loss related vacuum fields. The value of the classical amplitude of the carrier light at different points of the interferometer is taken from real measurements. The

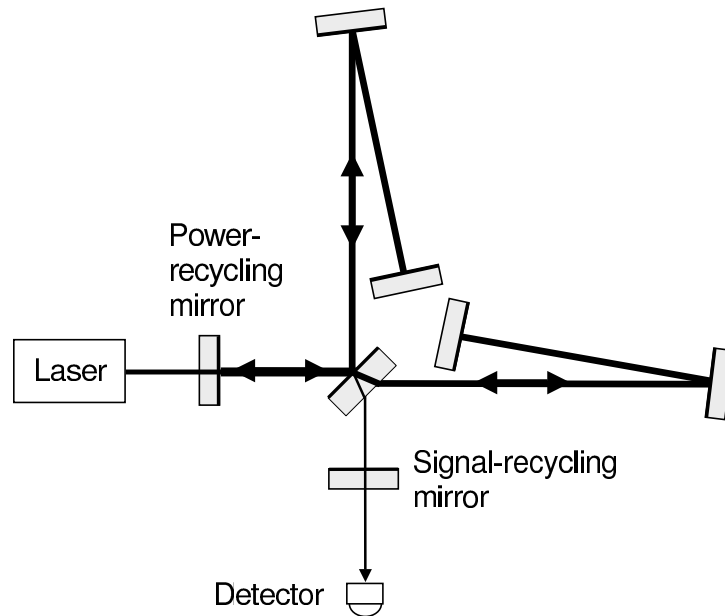


Figure 7.5: GEO 600 is a dual-recycled Michelson interferometer with a power-recycling mirror in the bright port that enhances the light power within the Michelson arms and a signal-recycling mirror in the dark port that can be tuned on a specific signal frequency. Since the arms are folded once, the effective arm length is doubled to 1200 m. The distance between the beam splitter and the so called far mirrors of the Michelson arms is 600 m, whereas the so called near mirrors which form the end of the arms are placed very close to the beam splitter.

equations of motion of all optical components are determined by the light pressure and the action of a gravitational wave. The latter one couples to the fields $\bar{\mathbf{n}}$ and $\bar{\mathbf{e}}$. No significant signal is found in the field $\bar{\mathbf{w}}$ since the distance of the power-recycling mirror to the origin of our reference frame (i. e the beam splitter) is small compared to the lengths of the two Michelson arms. A transfer matrix A for the arms was first presented in (Kimble et al.; 2001) and was derived in (Harms; 2002) for the GEO 600 configuration applying the same formalism:

$$\mathbf{A} = e^{2i\frac{\Omega L}{c}} \begin{pmatrix} 1 & 0 \\ -K_A & 1 \end{pmatrix} \quad (7.22)$$

The optomechanical coupling constant K_A of the Michelson arms is defined similarly to the beam splitter coupling constant K_B in Eq. (7.19) with the amplitude Λ substituted by the amplitude of the light inside the arms and the beam splitter mass m substituted by the reduced mass for the two end mirrors (each having mass m_M) which form the folded arms of GEO 600 (see Figure 7.5):

$$K_A \equiv 4 \cdot \frac{\hbar\omega_0^2(\Lambda^2/2)}{(m_M/5)c^2\Omega^2} \quad (7.23)$$

By folding the arms, the effective arm length L becomes twice the distance between the far mirror and the beam splitter. A gravitational wave h creates signal sidebands in both arms which possess equal amplitudes but different signs

$$\bar{\mathbf{n}} = -\bar{\mathbf{e}} = e^{i\frac{\Omega L}{c}} \frac{\sqrt{K_A}}{h_{\text{SQL}}} \begin{pmatrix} 0 \\ h \end{pmatrix}, \quad h_{\text{SQL}} = \frac{5\hbar}{m_M\Omega^2 L^2} \quad (7.24)$$

The quantity h_{SQL} is the standard quantum limit of GEO 600 with an infinite mass beam splitter. The "true" quantum limit for GEO 600 also depends on the dynamics of the beam splitter. We refrain from redefining h_{SQL} in that manner, since here we want to discuss the beam splitter dynamics explicitly and we do not want to find the reduced mass motion of the system. The problem to calculate the phase and coupling constant of a folded arm transfer function is related to the calculation of the same quantities for a delay line. A nice treatment of delay lines in our formalism can be found in the appendix of (Chen; 2003). For this particular set of matrices [Eqs. (7.22)&(7.24)], the input-output relation Eq. (7.20) is given by

$$\bar{\mathbf{o}} = e^{2i\frac{\Omega L}{c}} \begin{pmatrix} 1 & 0 \\ -K_1 & 1 \end{pmatrix} \bar{\mathbf{i}} + e^{2i\frac{\Omega L}{c}} \begin{pmatrix} 0 & 0 \\ -K_2 & 0 \end{pmatrix} \bar{\mathbf{b}} + \sqrt{2}\bar{\mathbf{n}} \quad (7.25)$$

We substituted the field $\bar{\mathbf{w}}$ by the transmitted bright port input field $\bar{\mathbf{w}} = \tau_{\text{pr}}\bar{\mathbf{b}}$. The two constants K_1 and K_2 depend on the arm and beam splitter coupling constants

$$\begin{aligned} K_1 &= K_A + 2\cos^2\left(\frac{\Omega L}{c}\right) \cdot K_B, \\ K_2 &= 2\cos^2\left(\frac{\Omega L}{c}\right) \frac{\tau_{\text{pr}}}{1 - \rho_{\text{pr}}e^{2i\frac{\Omega L}{c}}} \cdot K_B \end{aligned} \quad (7.26)$$

The coupling constant K_2 is a product of $2\cos^2(\frac{\Omega L}{c}) \approx 2$ and the amplification factor for modulation fields inside the power-recycling cavity. We should emphasize that K_2 is independent of the arm coupling constant K_A and thus independent of the arm topology (i. e. whether it is a Michelson interferometer without arm cavities or with arm cavities). However, the quantity K_2 decreases if the arm length L is increased. From Eq. (7.25) one derives the input-output relation of the signal-recycled interferometer in the usual manner. Propagating fields from the beam splitter to the signal-recycling mirror is accomplished by a rotation matrix $D(\phi)$ acting in quadrature space which lacks the additional phase shift

of the modulation fields since the wavelength $\lambda = (2\pi c)/\Omega$ of the sidebands within the detection band (i. e. 10 Hz-1000 Hz) is much longer than the length of the signal-recycling cavity (Buonanno and Chen; 2001)

$$\mathbf{D}(\phi) \equiv \begin{pmatrix} \cos(\phi) & -\sin(\phi) \\ \sin(\phi) & \cos(\phi) \end{pmatrix} \quad (7.27)$$

The angle ϕ is the detuning parameter of the signal-recycling cavity which is formed by the signal-recycling mirror and the Michelson interferometer. In Eq. (7.25), giving names \mathbf{T}_i and \mathbf{T}_b to the transfer matrices of the fields $\bar{\mathbf{i}}$ and $\bar{\mathbf{b}}$ respectively, the input-output relation for the signal-recycled interferometer reads

$$\bar{\mathbf{o}}_{\text{sr}} = \frac{1}{1 - \rho_{\text{sr}} \cdot \mathbf{D}(\phi) \mathbf{T}_i \mathbf{D}(\phi)} \left[\left(\mathbf{D}(\phi) \mathbf{T}_i \mathbf{D}(\phi) - \rho_{\text{sr}} \right) \bar{\mathbf{i}}_{\text{sr}} + \tau_{\text{sr}} \mathbf{D}(\phi) \cdot \left(\mathbf{T}_b \bar{\mathbf{b}} + \sqrt{2} \bar{\mathbf{n}} \right) \right] \quad (7.28)$$

The input-output relation determines the noise spectral density of the output field. It is convenient to normalize the spectral densities of the amplitude and phase quadratures of $\bar{\mathbf{o}}_{\text{sr}}$ such that the spectral density refers to the amplitude h of the gravitational wave. The way how to do this normalization in matrix notation is shown in subsection 8.1.1. The evaluation of the spectral density is based on the parameter values according to Table 7.2.3. A detuning $\phi = 0.015$ means that the sideband which lies 600 Hz above the carrier is

	Symbol	Value
Light power at BS	P	300 W
Transmissivity PRM	τ_{pr}^2	1.35%
Transmissivity SRM	τ_{sr}^2	2%
beam splitter mass	m	9.3 kg
Mirror mass	m_{M}	5.6 kg
Arm length	L	1200 m
Frequency of laser	ω_0	$1.77 \cdot 10^{15}$ rad/s
Detuning of SR cavity	ϕ	0.015 rad

Table 7.2: Parameters of the current GEO 600 configuration. The detuning ϕ of the signal-recycling cavity is the only quantity which can be varied with comparatively low efforts. The input light power at the power-recycling mirror is a little higher than 1 W.

resonantly amplified within the signal-recycling cavity. Adjusting the phase of the local

oscillator in a homodyne detection scheme (corresponding to the electronic demodulation phase in heterodyne detection schemes), one can choose the direction in quadrature space along which the measurement is carried out. In that manner, the phase quadrature, the amplitude quadrature or some intermediate linear combination of these two can be measured. We restrict to measurements of the phase quadrature. The single-sided noise spectral density of the phase quadrature of the output field is shown in Figure 7.6. The overall noise density is a sum of the two densities for the input field $\bar{\mathbf{i}}_{\text{sr}}$ and $\bar{\mathbf{w}}$. The latter one is the technical noise transferred from the bright port, the former one is the vacuum noise transferred from the dark port. The bright port noise at low frequencies

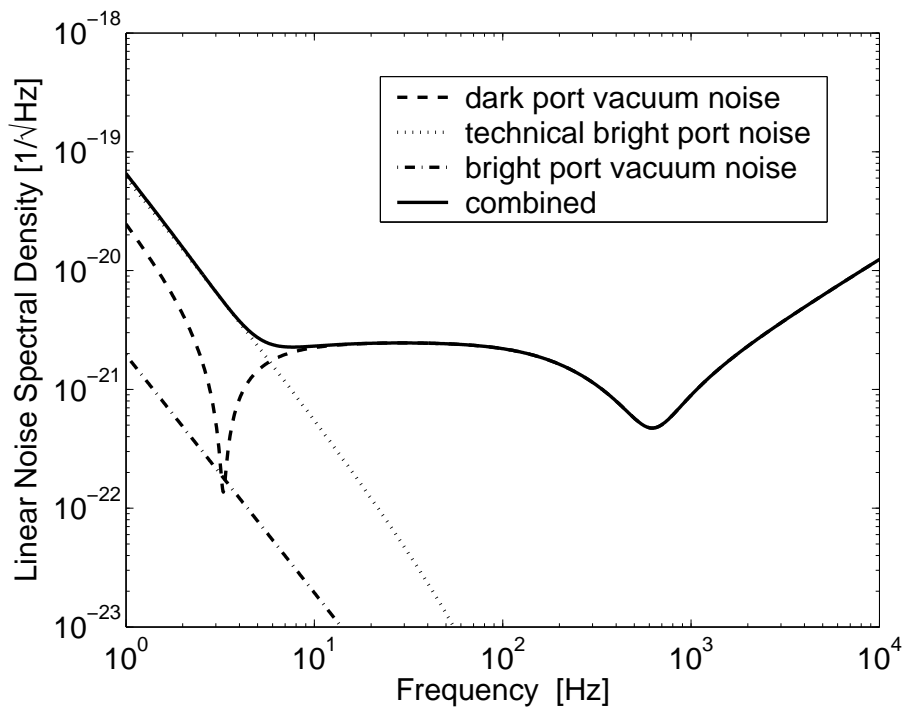


Figure 7.6: Single-sided spectral density of the optical noise with $P = 300$ W at beam splitter. The spectral density of the bright port vacuum field is lying below the dark port noise spectral density throughout the entire detection band. However, the technical noise from the bright port is dominating the spectral density up to 10 Hz where it is two orders of magnitude higher than the vacuum noise density. The technical noise corresponds to a 1.5 W input laser field.

causes the optomechanical resonance to disappear from the noise spectral density. On the one hand, this effect is merely of theoretical interest as the currently measured noise density at low frequencies is dominated by seismic noise which couples to the optical fields through the mirror suspension. On the other hand, the result suggests that one has to investigate the role of bright port fluctuations for future interferometers. The coupling constant K_B is proportional to the light power at the beam splitter. Therefore, one might expect that the transferred bright port noise might become even more significant for high power interferometers of the next generation. The corresponding noise spectral density

for GEO 600 with increased power $P = 10$ kW and adjusted detuning $\phi = 0.003$ is shown in [Figure 7.7](#) assuming the same relative technical noise than before. Indeed, according

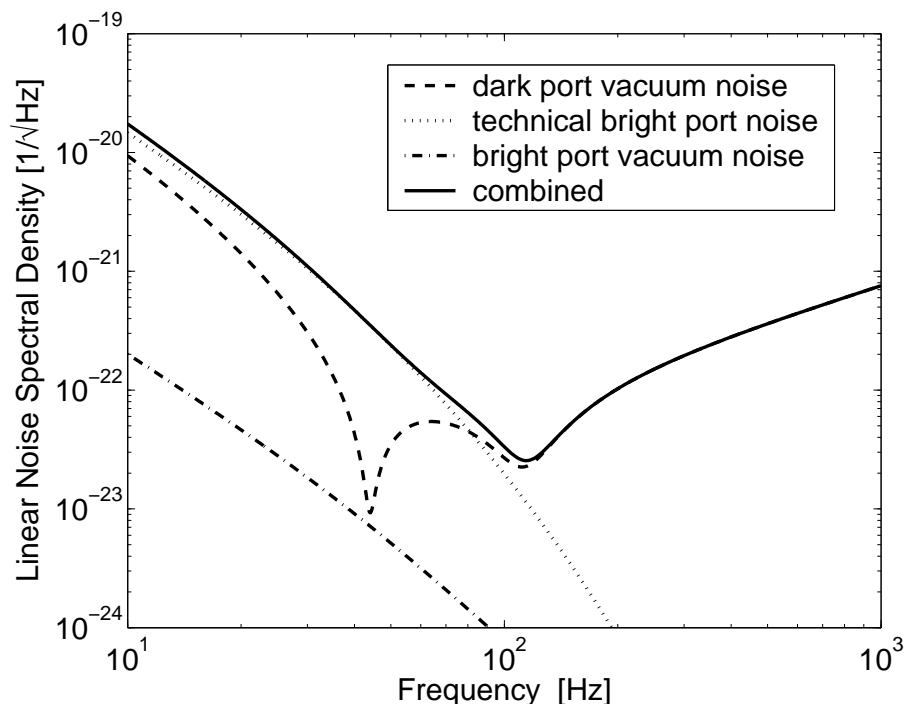


Figure 7.7: Single-sided spectral density of the optical noise with $P = 10$ kW at beam splitter. The technical noise does not correspond to a laser for interferometers of the next generation. Instead, we took the same relative technical noise here than for the low power interferometer [Figure 7.6](#). The power of the input laser field is 10 W.

to [Figure 7.7](#) the bright port noise is increased compared to the 300 W configuration and the optomechanical resonance does not appear in the combined noise spectral density of the output field.

We conclude this section with an order of magnitude estimation of the bright-port dark-port coupling for a different interferometer topology, namely the LIGO topology with arm cavities. Assuming for a moment that the bright port input field $\bar{\mathbf{b}}$ is in a coherent vacuum state, a very accurate estimation can be achieved by comparing the components of the transfer matrices in [Eq. \(7.26\)](#) of the GEO 600 and the LIGO topology. Therefore, in the case of GEO 600, we do not take into account the influence of the signal-recycling mirror. At low frequencies (i. e. around 10 Hz) it suffices to compare the values of the coupling constants K_1 and K_2 . Their ratio $|K_1|/|K_2|$ tells us which field mainly determines the fluctuations in the output field $\bar{\mathbf{o}}$. If the ratio is bigger than one, then the dark port field $\bar{\mathbf{i}}$ dominates. If the ratio is less than one, then the bright port field $\bar{\mathbf{w}}$ dominates. For GEO 600 one obtains the following expression:

$$\frac{|K_1|}{|K_2|} \approx \frac{\tau_{\text{pr}}}{2} \left(\frac{K_A}{2K_B} + 1 \right) = \frac{\tau_{\text{pr}}}{2} \cdot \frac{m + m_M/5}{m_M/5} \approx 0.5 \quad (7.29)$$

Comparing our results with the noise spectral density in [Figure 7.6](#), we see that due to the signal-recycling mirror the bright port fluctuations become less important. The reason is that we approximate at frequencies which are less than the (half-)bandwidth of the signal-recycling cavity $\gamma_{\text{sr}} = 200$ Hz. For $\Omega < 2\pi \cdot \gamma_{\text{sr}}$, the fluctuations from the dark port are amplified by the cavity.

Let us turn to the LIGO configuration. Due to the increased power in the arm cavities, LIGO's coupling constant K_{A} is much greater than K_{B} . The phase shift $\Omega L/c$ which appears in [Eq. \(7.26\)](#) has to be substituted by the expression $\arctan(\Omega/\gamma)$, where $\gamma = c\tau_{\text{itm}}^2/4L$ is the (half-)bandwidth of the arm cavities. For the power transmissivity of the inner test mirror we choose $\tau_{\text{itm}}^2 = 0.033$ in accordance with the value given in ([Kimble et al.; 2001](#)), ([Buonanno and Chen; 2001](#)). The coupling constant K_{A} for LIGO at low frequencies in terms of the power P at the beam splitter can be approximated by

$$K_{\text{A}} = \frac{4\omega_0 P}{mc^2 \Omega^2} \left(\frac{4}{\tau_{\text{itm}}^2} \right)^2 \quad (7.30)$$

Evaluating the ratio of the two matrix components at some low modulation frequency $\Omega \sim 2\pi \cdot 10 \text{ s}^{-1}$ yields

$$\frac{|K_1|}{|K_2|} \approx \frac{2\Omega}{\tau_{\text{pr}}\gamma} \left(\frac{K_{\text{A}}}{2K_{\text{B}}} + 1 \right) \approx \frac{4\Omega}{\tau_{\text{pr}}\gamma} \left(\frac{4}{\tau_{\text{itm}}^2} \right)^2 \approx 4 \cdot 10^5. \quad (7.31)$$

The result shows that the coupling of the bright port fluctuations to the dark port referred to the contribution of the dark port fluctuations is six orders of magnitude weaker at LIGO than at GEO 600. Even if the technical fluctuations of the input light are three or four orders of magnitude stronger than pure vacuum fluctuations, there will be no noticeable contribution to the spectral density of the output field.

We have shown that the coupling of technical bright port fluctuations towards the dark port is the major contribution to the optical output noise spectral density at low frequencies for interferometer topologies without arm cavities. From an estimation of orders of magnitude we concluded that the LIGO topology does not suffer from this problem. That is true even for a comparatively high level of technical laser noise. There are a couple of strategies to reduce these fluctuations at the dark port. One option is to decrease the transmissivity of the power-recycling mirror. The proposition seems to be in contradiction to [Eq. \(7.29\)](#) which states that the relative bright-port fluctuations increase with decreasing τ_{pr} . The reason why it works is that the factor $\tau_{\text{pr}}/2$ in front of the brackets has to be replaced by $\Omega L/(\tau_{\text{pr}}c)$ if the following condition holds: $\tau_{\text{pr}}^2 \ll \Omega L/c$. The required amplitude transmissivity had to be around 10ppm. The most obvious option is to increase the mass of the beam splitter. From [Eq. \(7.29\)](#) one can see that the beam splitter mass has to be increased by two orders of magnitude depending on the technical noise. Combined with efforts to lower the technical laser noise, this approach could be considered.

7.3 Phase Sensitive Photo Detection

Imagine a photo detection scheme measuring the output field $S(t)$ of an interferometer which operates at dark fringe for low sideband frequencies. The output is determined by

Eq. (7.2). A photo detector measures the power of the incoming light beam and so the photocurrent is proportional to the square of the output field $S(t)$. Squaring a field is a nonlinear operation which entails that amplitudes of the measured field at frequency Ω contribute to several frequencies of the photocurrent spectrum. In that case, the spectrum of the photocurrent furnishes no direct information of the signal spectrum unless there exists only one monochromatic signal. In addition, the signal is usually very weak and it would not excite any analyzable photocurrent. These two problems are solved with one simple trick. Before the light reaches the photo detector, it is superposed with another high-power light field, i.e. the local oscillator $L(t)$. It turns out that the main contribution of the total field to frequencies of the photocurrent spectrum which correspond to frequencies of the gravitational waves depends linearly on the signal field and furthermore, that the signal field is amplified by the amplitude of the local oscillator. In other words, the spectral density of the photocurrent is proportional to the spectral density of the output field. If the output field carries a signal, then, assuming ideal photo detection, the noise-to-signal ratio is unaltered during detection and thereby, it is a property of the interferometer itself independent of the photo detection process. However, the last conclusions are strictly true only for so-called homodyne detection schemes [subsection 7.3.1](#) which use a local oscillator whose frequency coincides with the carrier frequency inside the interferometer. As pointed out in (Buonanno, Chen and Mavalvala; 2003), the photocurrent spectrum has to be constructed in a more complicated way, if the frequency of the local oscillator is different from the carrier frequency. These heterodyne detection schemes are applied in all currently operating detectors for reasons which are discussed in [subsection 7.3.2](#).

7.3.1 The Homodyne Detection

In gravitational wave detectors, one could imagine two different possibilities to superpose the output $S(t)$ with a local oscillator whose frequency is identical with the carrier frequency. Either one abandons the dark fringe condition for the carrier allowing some of its power to leave the output port, or the local oscillator is superposed with the output field right in front of the photo detector by means of a beam splitter. We are going to illustrate that the first proposition is somewhat problematic. The noise spectral density of the carrier field (and thereby of the local oscillator $L(t)$) at low frequencies is dominated by technical noise which is many orders of magnitude greater than the quantum noise or the signal spectrum. If we denote the fluctuating part of the local oscillator by $L_{\text{fluct}}(t)$ and its expectation value by $L \equiv \langle L(t) \rangle$, then the photocurrent I_{PD} is proportional to

$$I_{\text{PD}} \propto L^2 + 2L \cdot (L_{\text{fluct}}(t) + S(t)) + (L_{\text{fluct}}(t) + S(t))^2 \quad (7.32)$$

The first term on the right-hand side which is time independent (the photo detector averages over fast oscillations at frequency ω_0 and $2\omega_0$) appears at zero frequency of the photocurrent spectrum and the last term is negligible if $L \gg L_{\text{fluct}}(t), S(t)$. Therefore, the spectrum is determined by the spectral density of $2L \cdot (L_{\text{fluct}}(t) + S(t))$. As we said, the spectral density of technical fluctuations $L_{\text{fluct}}(t)$ is much greater than the spectral density of the output field $S(t)$. Consequently, we are unable to measure gravitational waves in

that way as long as nobody comes up with a laser design revolution which furnishes low noise laser beams, i.e. a laser which is quantum noise limited at low sideband frequencies.

More promising is the second idea to superpose the local oscillator with the output field in front of the photo detector. **Figure 7.8** shows a balanced homodyne scheme which detects two beams coming from the beam splitter. The two detected fields are not identical. One field is equal to the sum $1/\sqrt{2}(L(t) + S(t))$, the other field is equal to the difference $1/\sqrt{2}(L(t) - S(t))$. The respective photocurrents are

$$\begin{aligned} I_{\text{PD1}} &\propto L^2 + 2L \cdot (L_{\text{fluct}}(t) + S(t)) + (L_{\text{fluct}}(t) + S(t))^2 \\ I_{\text{PD2}} &\propto L^2 + 2L \cdot (L_{\text{fluct}}(t) - S(t)) + (L_{\text{fluct}}(t) - S(t))^2 \end{aligned} \quad (7.33)$$

The balanced homodyne detector subtracts the two currents from each other and the difference current is recorded. The sign of the output field $S(t)$ is opposite in the two

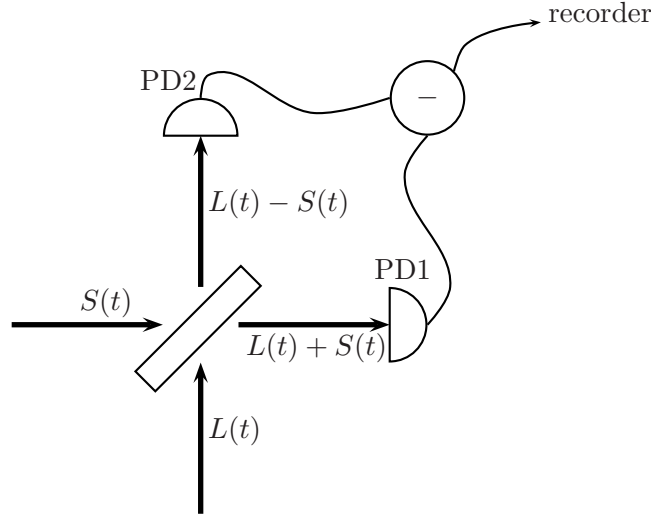


Figure 7.8: The balanced homodyne detector measures both output fields of a beam splitter which superposes the local oscillator $L(t)$ with the signal field $S(t)$. The two photocurrents are subtracted from each other which cancels the local oscillator noise from the data stream.

currents and therefore, the difference current is governed by

$$I_{\text{PD1}} - I_{\text{PD2}} \propto 2L \cdot S(t) + S(t) \cdot L_{\text{fluct}}(t) \quad (7.34)$$

Again, the second term of the right-hand side is negligible compared to the first term if $L \gg L_{\text{fluct}}(t)$. In conclusion, the balanced homodyne detector produces a signal which is proportional to the output field $S(t)$ amplified by the time independent expectation value of the local oscillator. The signal is devoid of technical noise $L_{\text{fluct}}(t)$. Signal-to-noise ratios and detection sensitivities are derivable from the spectral density of $S(t)$. In the language of the two-photon formalism, it becomes obvious why homodyning belongs to

the class of phase sensitive detection schemes. The product $L \cdot S(t)$ yields photocurrent amplitudes proportional to

$$i_{\text{PD}}(\Omega) \propto |L| e^{i\phi_{\text{LO}}} s(\Omega) \quad (7.35)$$

where $s(\Omega)$ denotes the amplitude of the field $S(t)$. By definition, the corresponding quadrature amplitude assumes the form

$$i_{\text{PD}}(\Omega) \propto |L| \left[s_1(\Omega) \sin\left(\frac{\pi}{2} + \phi_{\text{LO}}\right) + s_2(\Omega) \cos\left(\frac{\pi}{2} + \phi_{\text{LO}}\right) \right] \quad (7.36)$$

If $\phi_{\text{LO}} = 0$ ($\pi/2$), then the amplitude (phase) quadrature of the output field is measured, i.e. adjusting the phase of the local oscillator allows us to measure any of the signal quadratures.

7.3.2 The Heterodyne Detection

The heterodyne detection scheme is the prevalent method to measure the output field of gravitational wave detectors. The local oscillator is provided by a (Schnupp) modulation of the laser field before it enters the interferometer at the bright port. As we saw in [section 7.1](#), modulation sidebands at MHz frequencies are transferred to the dark port if the two interferometer arms have different lengths. The noise which is transferred together with the Schnupp sidebands is pure quantum noise since the laser is quantum noise limited at Mhz frequencies. This is the basic motivation why heterodyne detection schemes are used.

In general, it is not true that two sidebands at $\pm\omega_m$ which have equal amplitudes at the bright port still have equal amplitudes at the dark port. All signal-recycled interferometers for example exhibit asymmetric transfers. The two sidebands will also be subject to different phase shifts and therefore we are going to describe each sideband at the dark port by a complex amplitude. Adopting the notation of ([Buonanno, Chen and Mavalvala; 2003](#)), D_+ signifies the complex amplitude of the local oscillator sideband at $+\omega_m$ and D_- the amplitude at $-\omega_m$. [Figure 7.9](#) shows a representation of the total output field $E_{\text{out}}(t) = L(t) + S(t)$ in the frequency domain. The signal sidebands gather around the carrier frequency ω_0 . Certainly, the Schnupp sidebands also interact with the gravitational wave, but their amplitudes are much smaller than the carrier amplitude giving rise to negligible signal sidebands around frequencies $\omega_0 \pm \omega_m$. A photo detector which measures the field $E_{\text{out}}(t)$ generates a photocurrent according to [Eq. \(7.32\)](#). However, the local oscillator is offset from the carrier frequency by several MHz and calculating the square of $E_{\text{out}}(t)$, we find that the local oscillator beats with several frequencies of the noise and signal fields to generate a photocurrent which oscillates at $\pm\omega_m$ (contributions from $L(t)^2$, $S(t)^2$ and oscillations at higher harmonics of ω_m are irrelevant). More specifically, from [Figure 7.9](#) one can deduce that the amplitudes of the photocurrent are given by

$$\begin{aligned} 2D_+ \cdot v(\omega_0 + 2\omega_m + \Omega) + 2D_- \cdot s(\omega_0 + \Omega) & \quad \text{at } +\omega_m + \Omega \\ 2D_+ \cdot s(\omega_0 + \Omega) + 2D_- \cdot v(\omega_0 - 2\omega_m + \Omega) & \quad \text{at } -\omega_m + \Omega \end{aligned} \quad (7.37)$$

where Ω denotes the gravitational wave sideband frequency. The photocurrent is demodulated by multiplication with $\cos(\omega_m t + \phi_{\text{dem}})$ which converts amplitudes acting at $\pm\omega_m \pm \Omega$

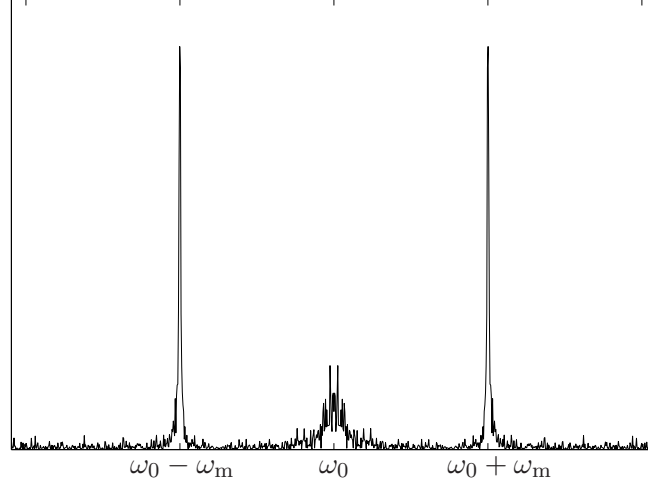


Figure 7.9: The plot sketches a typical spectrum of the dark-port field of interferometers which implement a heterodyne detection scheme. Vacuum noise amplitudes $v(\omega)$ contribute uniformly to all frequencies. The signal sidebands $s(\omega)$ are found near $\omega = \omega_0$. Two Schnupp sidebands (not necessarily with equal amplitudes) generate two peaks at $\omega = \omega_0 \pm \omega_m$.

to frequencies $\pm\Omega$. Higher frequencies are filtered out of the current by means of a low-pass filter as shown in [Figure 7.10](#). The amplitude at frequency Ω of the finally recorded current consists of three independent contributions determined by signal and vacuum noise amplitudes at frequencies $\omega_0 + \Omega$ and $\omega_0 \pm \omega_m + \Omega$ ([Buonanno, Chen and Mavalvala; 2003](#))

$$\begin{aligned}
 i_{\text{PD}}(\Omega) \propto & (D_+ e^{-i\phi_{\text{dem}}} + D_- e^{i\phi_{\text{dem}}}) \cdot s(\omega_0 + \Omega) \\
 & + D_+ e^{i\phi_{\text{dem}}} \cdot v(\omega_0 + 2\omega_m + \Omega) \\
 & + D_- e^{-i\phi_{\text{dem}}} \cdot v(\omega_0 - 2\omega_m + \Omega)
 \end{aligned} \tag{7.38}$$

Let us evaluate the heterodyne detection scheme for a power-recycled interferometer with a Schnupp phase modulation of the bright port field. The phase modulation generates two sidebands with equal imaginary amplitudes iD . According to [Eq. \(7.4\)](#), the bright-port dark-port transfer function $\mathbf{T}_w(\omega)$ satisfies

$$\mathbf{T}_w^*(\omega_m) = -\mathbf{T}_w(-\omega_m) \tag{7.39}$$

and thereby, the Schnupp phase modulation is converted into an amplitude modulation at the dark port

$$D_+ = D_-^* = iD \cdot \mathbf{T}_w(\omega_m) \quad \text{with } |D_+| = |D_-| \tag{7.40}$$

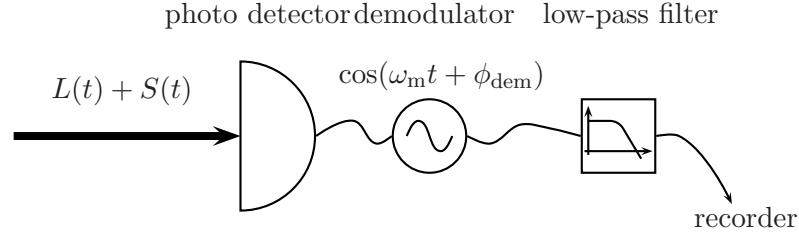


Figure 7.10: The figure shows the different operations which take place starting from the photo detection to the final record of the time series. The photocurrent is demodulated with the Schnupp heterodyning frequency ω_m . Frequencies beyond the detection band are filtered out by a subsequent low-pass filter.

Applying these relations, Eq. (7.38) simplifies to

$$\begin{aligned}
 i_{\text{PD}}^{\text{PR}}(\Omega) &\propto 2|D_+| \cos(\arg(D_+) - \phi_{\text{dem}}) \cdot s(\omega_0 + \Omega) \\
 &\quad + |D_+| e^{i(\arg(D_+) + \phi_{\text{dem}})} \cdot v(\omega_0 + 2\omega_m + \Omega) \\
 &\quad + |D_+| e^{-i(\arg(D_+) + \phi_{\text{dem}})} \cdot v(\omega_0 - 2\omega_m + \Omega)
 \end{aligned} \tag{7.41}$$

The first noteworthy property of our result is that the factor in front of the signal amplitude $s(\omega_0 + \Omega)$ is real. Consequently, translating Eq. (7.41) into the two-photon formalism, we recognize that the heterodyne scheme automatically measures the amplitude quadrature of the signal field for all demodulation phases. In fact, as shown by (Buonanno, Chen and Mavalvala; 2003), all balanced heterodyne schemes (i.e. $|D_+| = |D_-|$) measure one signal quadrature determined by the Schnupp modulation phase. A Schnupp amplitude modulation for example yields a heterodyne scheme which measures the signal phase quadrature.

The noise amplitudes $v(\omega_0 \pm 2\omega_m + \Omega)$ describe coherent vacuum noise which partly originates from the bright port and partly from the dark port. The respective phase shifts which are multiplied to the vacuum amplitudes in Eq. (7.41) are irrelevant. Normalizing the signal amplitude, one finally obtains

$$\begin{aligned}
 i_{\text{PD}}^{\text{PR}}(\Omega) &\propto s(\omega_0 + \Omega) \\
 &\quad + \frac{1}{2 \cos(\arg(D_+) - \phi_{\text{dem}})} \cdot v(\omega_0 + 2\omega_m + \Omega) \\
 &\quad + \frac{1}{2 \cos(\arg(D_+) - \phi_{\text{dem}})} \cdot v(\omega_0 - 2\omega_m + \Omega)
 \end{aligned} \tag{7.42}$$

The demodulation phase can be used to minimize the vacuum noise contribution. The optimal phase is given by

$$\phi_{\text{dem}} = \arg(D_+) + N\pi \quad N = 0, \pm 1, \dots \tag{7.43}$$

In the case of implementing a Schnupp amplitude modulation, one has to add $\pi/2$ to the latter equation. The optimized spectral density derived from Eq. (7.42) assumes the form

$$S_{\text{opt}}(\Omega) = S_{\text{homo}}(\Omega) + \frac{1}{2}S_{\text{vac}} \quad (7.44)$$

The first term signifies the homodyne spectral density. Additional vacuum noise adds to the homodyne spectrum. This is a generic feature of all heterodyne schemes since the modulation-demodulation process picks up vacuum fields at $\omega_0 \pm 2\omega_m \pm \Omega$. For any balanced heterodyne scheme, the minimal additional vacuum noise is $1/2 \cdot S_{\text{vac}}$. However, this does not mean that the power spectral density of the heterodyne shot noise has to be greater than the homodyne shot noise. In fact, the shot noise can be smaller in the former case. It is the sensitivity (i.e. shot noise normalized by signal transfer function) which degrades necessarily when switching to a heterodyne detection scheme.

The homodyne detection is more favorable for next generation interferometers which are designed with squeezed input optics (section 8.1). Although the additional vacuum noise which originates from the dark port could in principle be squeezed too, there remains unsqueezed vacuum noise from the bright port which limits the improvement of squeezed input schemes. However, a more detailed analysis of heterodyning has to be carried out. The transmission of bright port vacuum fields to the dark port at frequencies $\omega_0 \pm 2\omega_m \pm \Omega$ may be small enough to allow us neglecting it.

CHAPTER 8

Advanced Interferometer Topologies

8.1 Filtered Light for SR Interferometers

Gravitational waves (GW) have long been predicted by Albert Einstein using the theory of general relativity, but so far have not been directly observed ([Hawking and Israel; 1996](#)). Currently, an international array of first-generation, kilometer-scale laser interferometric gravitational-wave detectors, consisting of GEO 600 ([Willke et al.; 2002](#)), LIGO ([Abramovici et al.; 1992](#)), TAMA 300 ([Ando et al.; 2001](#)) and VIRGO ([Caron et al.; 1997](#)), targeted at gravitational-waves in the acoustic band from 10 Hz to 10 kHz, is going into operation. These first-generation detectors are all Michelson interferometers with suspended mirrors. Injecting a strong carrier light from the bright port, the anti-symmetric mode of arm-lengths oscillations (e.g. excited by a gravitational wave) yields a sideband modulation field in the anti-symmetric (optical) mode which is detected at the dark output port. To yield a high sensitivity to gravitational waves, long arm lengths of 300 m up to 4 km and circulating laser power in the order of 10 kW are going to be realized in 2003 with the help of the technique of *power recycling* proposed by Drever et. al. in ([Meystre and Scully; 1983](#)).

GEO 600 is the only first-generation detector that not only uses power recycling, but also includes the more advanced technique of *signal recycling* ([Meers; 1988](#)). The idea of signal recycling is to retro-reflect part of the signal light at the dark port back into the interferometer, establishing an additional cavity which can be set to resonate at a desired gravitational-wave frequency. Signal recycling leads to a well known (optical) resonance structure in the interferometer's sensitivity curve. This resonance can already beat the standard quantum limit (SQL) ([Buonanno and Chen; 2001](#)), which is the upper bound for the sensitivity of conventional interferometers without signal recycling and with conventional input and output optics. A further benefit of signal recycling is the reduced optical loss due to imperfect mode matching from the *mode healing effect* ([Strain and Meers; 1991](#)). The next-generation detectors currently being planned are likely to use this technique, for example the *Advanced LIGO*.

Buonanno and Chen also predict a second, optomechanical resonance in signal-recycled interferometers, around which the interferometer gains sensitivity, and can also beat the standard quantum limit (Buonanno and Chen; 2001, 2002, 2003). Their work has been limited to signal-recycled interferometers with arm cavities, or interferometers with one single end mirror in each arm, and with infinitely heavy beam splitters. In all cases considered, coherent vacuum was entering the interferometer's dark port, i.e. no additional input and output optics were investigated. On the other hand, Kimble *et al.* investigated these additional input and output optics for the conventional LIGO detector topology without signal-recycling (Kimble *et al.*; 2001) building on earlier work on squeezed-input interferometers (Caves; 1980; Meystre and Scully; 1983; Gea-Banacloche and Leuchs; 1987; Jaekel and Reynaud; 1990; Pace *et al.*; 1993) and variational-output interferometers (Vyatchanin and Matsko; 1993; Vyatchanin and Zubova; 1995; Vyatchanin and Matsko; 1996a,b; Vyatchanin; 1998).

In this section, we investigate the benefit of squeezed light with frequency-dependent squeezing angle injected into the interferometer's dark port and also the benefit of frequency-dependent (variational) homodyne readout, using the two-photon input-output formalism of quantum optics (Caves and Schumaker; 1985). In subsection 8.1.2 and subsection 8.1.3, we derive analytical expressions for the optimized frequency dependencies of squeezing angle and homodyning angle for optical-spring signal-recycled interferometers, respectively. For definiteness, our results are presented using the Michelson topology of GEO 600. Unlike the LIGO, VIRGO and TAMA 300 interferometers, GEO 600 has folded arms and no arm cavities (Figure 8.1). We plot and compare the spectral densities of the quantum noise of the GEO 600 topology without and with additional input and output optics. Using the coupling parameter of Advanced LIGO, the results are readily applicable to the proposed LIGO topology.

8.1.1 Signal Recycling

By placing a mirror in the dark port of an interferometer a cavity between this so-called signal-recycling mirror and the two end mirrors of the interferometer is formed. The length of this cavity can be tuned independently and can be made resonant at some signal frequency Ω . Thus the signal is recycled and amplified due to an increased interaction time. The original idea of the signal-recycling (SR) topology, i.e. a mirror in the dark port, was due to Meers (Meers; 1988), who proposed its use for *dual-recycling*, which is the combination of power- and signal-recycling. Later, (Mizuno *et al.*; 1993; Mizuno; 1995) and (Heinzel; 1999; Heinzel *et al.*; 1996) proposed the scheme of *resonant sideband extraction*, which uses a detuned signal-recycling mirror to extract the signal from high-finesse arm cavities. Both schemes of tuned and detuned signal-recycling cavities have been experimentally demonstrated by (Heinzel *et al.*; 1998) and (Freise *et al.*; 2000) with the 30 m laser interferometer in Garching near Munich. Recently the GEO 600 interferometer in Ruthe near Hannover has been completed by the implementation of the signal-recycling mirror. Since GEO 600 has no Fabry-Pérot cavities (Figure 8.1) the SR-mirror will be operated at or close to resonance. Relevant technical parameters of GEO 600 are summarized in Table 8.1.

Whereas it was well known that signal-recycled interferometers exhibit an optical res-

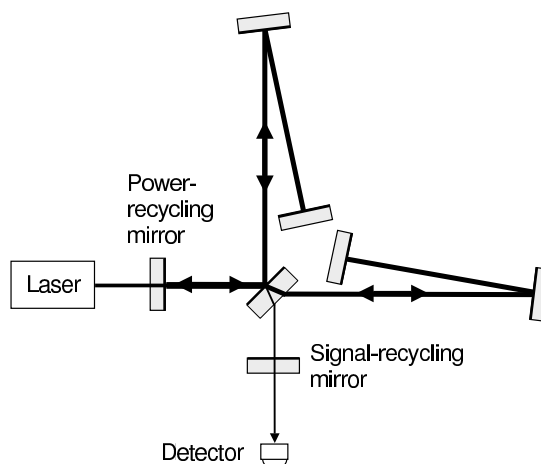


Figure 8.1: GEO 600 is a dual-recycled Michelson interferometer implementing a power-recycling mirror in order to enhance the light power within the Michelson arms and a signal-recycling mirror in the dark port which is tuned on a specific signal frequency. Since the arms are folded once, then the effective armlength is doubled to 1200 m.

symbol	physical meaning	numerical value
m	mirror mass (each)	5.6 kg
L	effective arm length	1200 m
P	circulating light power	10 kW
ω_0	angular frequency of carrier light	$1.77 \cdot 10^{15} \text{ s}^{-1}$
ρ	power reflectivity of SRM	0.99
ϕ	SR-cavity detuning	0.0055 rad

Table 8.1: Technical data and parameter values of GEO 600 which were used to calculate the spectral noise densities in Figures 8.2–8.4.

onance, Buonanno and Chen (Buonanno and Chen; 2001) have recently shown that SR-interferometers exhibit a second resonance, which is optomechanical. This resonance stems from the classical optomechanical coupling of the light field with the anti-symmetric mode of the otherwise free mirrors (Buonanno and Chen; 2002): in detuned signal-recycling schemes, the phase-modulation sidebands induced by a gravitational wave are partly converted into amplitude modulations, which beat with the carrier field, producing a motion-dependent force and acting back on the test masses. This classical back-action force can be thought of as generated by an *optical spring*. The optical spring makes the test masses no longer free, and can shift their resonant frequencies upwards into the detection band. The

interferometer gains sensitivity on and around this resonance, and can beat the standard quantum limit (Buonanno and Chen; 2001, 2002). Whereas the optical resonance is primarily determined by the detuning of the SR-cavity with respect to the carrier-frequency ω_0 (Fig. 5.8 in (Harms; 2002)), the optomechanical resonance appears at a specific side-band frequency of the carrier light which depends on the interferometer’s topology, the mirror masses m , the light-power P inside the interferometer and the detuning ϕ of the SR cavity from its resonance. The optomechanical coupling of the light field with the anti-symmetric mode of the interferometer also leads to the phenomenon of ponderomotive squeezing (Braginsky and Manukin; 1967), i.e. the amplitude and phase quantum noise become correlated. This quantum effect is automatically considered by the formalism revealing the optical-spring behavior. However, as pointed out in (Buonanno and Chen; 2001), in SR interferometers the ponderomotive squeezing only seems to be a secondary factor that enables the interferometer to beat the SQL, whereas the *classical* resonant amplification of the signal provides the main factor.

The investigations led by Buonanno and Chen focused on the topology of the proposed *Advanced* LIGO configuration, which consists of a dual-recycled Michelson-interferometer with a Fabry-Pérot cavity in each arm. Due to the weak laser power at the beam splitter, the optomechanical coupling of the light with the beam splitters free oscillation was neglected. In contrast, GEO 600 is a dual-recycled interferometer that builds up a high intensity field by means of a power-recycling (PR) mirror in the bright port of the interferometer. Therefore, the motion of the beam splitter (BS) in GEO 600 is affected by power fluctuations of fields impinging from different directions. Nevertheless, assuming that the laser is shot-noise limited, the optomechanical coupling at the beam splitter exerts only minor changes on the noise spectrum of the output. It can intuitively be understood that the quantum back-action noises associated with the arm mirrors, which have a reduced mass of 1/5 the actual mirror mass due to folding the arms, clearly dominates the beam splitter of $m_{\text{BS}} = 9.3 \text{ kg}$. In the following sections, we do not consider the effect of radiation-pressure noise on the beam splitter. This problem is treated in section 7.2. Henceforth the term “ideal GEO 600” refers to the interferometer with optomechanical coupling of the beam splitter neglected.

The optical noise in an interferometer can be expressed in terms of the (single-sided) noise spectral density S_h of the output field normalized by the transfer function of the signal. The noise spectral density is obtained from the *input-output relation*, which maps the numerous input fields $\bar{\mathbf{i}}_n$ and the gravitational-wave signal $h = \Delta L/L$ onto the detected output field $\bar{\mathbf{o}}$. Here we note that no additional noise due to the quantization of the test masses has to be considered. The sole forms of quantum noise affecting the output noise in interferometric gravitational wave detectors are the shot noise and the radiation pressure noise (Braginsky et al.; 2003).

The following calculations are most easily accomplished in the Caves-Schumaker two-photon formalism (Caves and Schumaker; 1985), where the optical fields are decomposed into amplitude and phase quadratures, which can then be put together into a vector, e.g.,

for the output field of the interferometer

$$\bar{\mathbf{o}} = \begin{pmatrix} \hat{o}_1 \\ \hat{o}_2 \end{pmatrix}, \quad (8.1)$$

where $\hat{o}_{1,2}$ are the output amplitude and phase quadratures. The input-output relation for a lossless SR interferometer can be cast into the following form:

$$\bar{\mathbf{o}} = \frac{1}{M} [\mathbf{T}\bar{\mathbf{i}} + \bar{\mathbf{s}}h]. \quad (8.2)$$

Here, \mathbf{T} designates a 2×2 -matrix. Its four components are (Harms; 2002):

$$\begin{aligned} T_{11,22} &= e^{2i\Phi} \left[(1 + \rho^2) \left(\cos(2\phi) + \frac{\mathcal{K}}{2} \sin(2\phi) \right) - 2\rho \cos(2\Phi) \right], \\ T_{12} &= -e^{2i\Phi} \tau^2 \left(\sin(2\phi) + \mathcal{K} \sin^2(\phi) \right), \\ T_{21} &= e^{2i\Phi} \tau^2 \left(\sin(2\phi) - \mathcal{K} \cos^2(\phi) \right), \end{aligned} \quad (8.3)$$

and M is given by

$$M = 1 + \rho^2 e^{4i\Phi} - 2\rho e^{2i\Phi} \left(\cos(2\phi) + \frac{\mathcal{K}}{2} \sin(2\phi) \right). \quad (8.4)$$

Thus, \mathbf{T} contains an overall phase factor $e^{2i\Phi}$. ρ and τ denote the amplitude reflectivity and transmissivity of the SR mirror. The signal transfer functions $\bar{\mathbf{s}}$ for the two quadratures are given by:

$$\begin{aligned} \hat{s}_1 &= -\frac{\sqrt{2\mathcal{K}}}{h_{\text{SQL}}} \tau \left(1 + \rho e^{2i\Phi} \right) \sin(\phi), \\ \hat{s}_2 &= -\frac{\sqrt{2\mathcal{K}}}{h_{\text{SQL}}} \tau \left(-1 + \rho e^{2i\Phi} \right) \cos(\phi). \end{aligned} \quad (8.5)$$

Remarkably, the input-output relations are formally identical for both configurations, *Advanced LIGO* and ideal *GEO600*. Their distinguishing properties lie in the definition of the optomechanical coupling-constant \mathcal{K} , the standard quantum-limit h_{SQL} and the phase-angle Φ which are also functions of the modulation-frequency Ω .

A phase-sensitive measurement (i.e. homodyne or heterodyne) yields a photocurrent which depends linearly on a certain combination of the two output quadrature-fields:

$$\hat{o}_\zeta = \hat{o}_1 \cos \zeta + \hat{o}_2 \sin \zeta, \quad (8.6)$$

where ζ is the homodyne angle (i.e. the angle of homodyne detection). The radiation-pressure forces acting on the mirrors are proportional to the amplitude quadrature and the

symbol	GEO 600	Advanced LIGO
\mathcal{K}	$\frac{20P\omega_0}{mc^2\Omega^2}$	$\frac{8P\omega_0}{mL^2\Omega^2(\Omega^2 + \gamma_{\text{arm}}^2)}$
h_{SQL}	$\frac{20\hbar}{m\Omega^2L^2}$	$\frac{8\hbar}{m\Omega^2L^2}$
Φ	$\frac{\Omega L}{c}$	$\arctan\left[\frac{\Omega}{\gamma_{\text{arm}}}\right]$

Table 8.2: Definitions of \mathcal{K} , h_{SQL} and Φ for GEO 600 and Advanced LIGO topologies. Here m is the individual mirror mass, L the Michelson arm length, P the input power at the beam splitter, ω_0 the laser angular frequency, $\gamma_{\text{arm}} = \tau_{\text{arm}}^2 c / (4L)$ the half linewidth of the Advanced LIGO arm cavity (τ_{arm} the input test-mass mirror amplitude transmissivity), and Ω the GW sideband angular frequency. Values for Advanced LIGO are kept to the leading order of τ_{arm}^2 , as in Refs. (Buonanno and Chen; 2001, 2002).

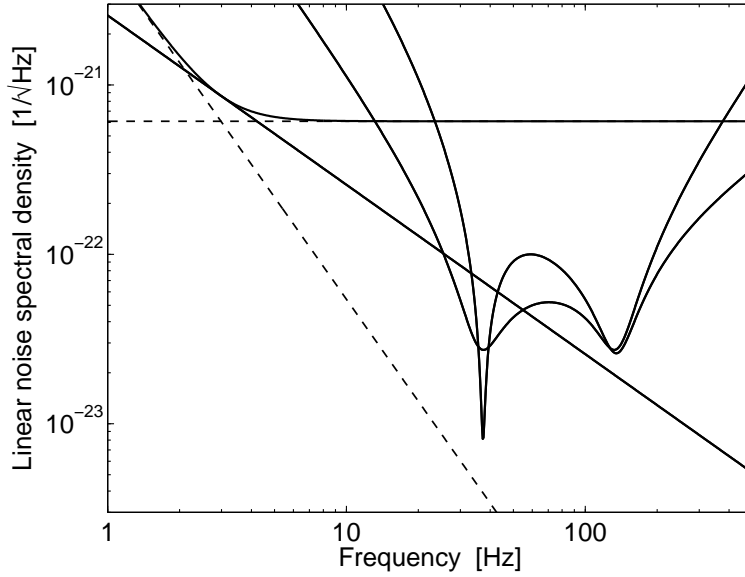


Figure 8.2: The dashed lines represent the uncorrelated white shot noise and the radiation-pressure noise ($\propto f^{-2}$). The sum of these shot and radiation-pressure noises yields the noise spectral density of a simple Michelson without arm cavities, here using GEO 600 parameters and $\rho = 0$. In comparison, the noise spectral densities of both orthogonal quadratures of the signal-recycled GEO 600 output-field exhibit a doubly resonant structure which beats the standard quantum limit.

motion-induced sideband fields are excitations of the light's phase quadrature. The noise

spectral density when detecting the quadrature \hat{o}_ζ is determined by the transfer matrix \mathbf{T} and the signal transfer-functions $\bar{\mathbf{s}}$. It assumes the form [see, e.g., Ref. (Buonanno and Chen; 2001)],

$$S_h = \frac{\begin{pmatrix} \cos \zeta & \sin \zeta \end{pmatrix} \mathbf{T} \mathbf{T}^\dagger \begin{pmatrix} \cos \zeta \\ \sin \zeta \end{pmatrix}}{\begin{pmatrix} \cos \zeta & \sin \zeta \end{pmatrix} \bar{\mathbf{s}} \bar{\mathbf{s}}^\dagger \begin{pmatrix} \cos \zeta \\ \sin \zeta \end{pmatrix}}, \quad (8.7)$$

provided that the input field $\bar{\mathbf{i}}$ entering from the dark port is a coherent vacuum field. Since $\bar{\mathbf{s}}$ is a complex vector, the product $\bar{\mathbf{s}} \bar{\mathbf{s}}^\dagger$ represents a symmetrized product

$$\langle \bar{\mathbf{s}} \bar{\mathbf{s}}^\dagger \rangle_{\text{sym}} = \frac{1}{2} (\bar{\mathbf{s}} \bar{\mathbf{s}}^\dagger + \bar{\mathbf{s}}^* \bar{\mathbf{s}}^T). \quad (8.8)$$

The same holds for the matrix product $\mathbf{T} \mathbf{T}^\dagger$ in the nominator. Its symmetrization becomes necessary, if a more general interferometer topology is considered with complex coupling constant \mathcal{K} . The expression in Eq. (8.7) for the noise spectral density is valid for any optical system whose transfer function can be given the form of Eq. (8.2).

Using Eq. (8.7) and the parameters and definitions in Table 8.1 and Table 8.1.1 we are now able to plot the linear noise spectral density of the ideal GEO 600 topology for output quadrature fields of arbitrary values of the angle ζ . Figure 8.2 shows the two spectral densities $S_h(\zeta = 0)$ and $S_h(\zeta = \frac{\pi}{2})$ compared with the SQL (straight solid line). It can be seen that for both quadrature angles the SQL is beaten at frequencies around 30 Hz. This noise minimum is due to the optomechanical resonance (i.e. the optical-spring effect). The second minimum at around 200 Hz corresponds to the optical resonance of the SR cavity. This resonance can also beat the SQL when higher reflectivities of the SR mirror ρ are used. For further comparison, the quantum noise limit of a conventional GEO 600 without signal-recycling is also given (solid line in the upper part of Figure 8.2. The dashed lines represent the two contributions to this (conventional) limit, the uncorrelated white shot noise and the radiation-pressure noise ($\propto f^{-2}$). The limit given here is calculated for a circulating light power of $P = 10$ kW that reaches the SQL at 3 Hz and of course can never beat the SQL. It is interesting to note that light powers of around 1 MW are needed to shift the conventional limit downwards to get standard quantum noise limited sensitivity at around 100 Hz (not shown in Figure 8.2).

In the next two sections we investigate how the sub-SQL spectral noise densities of signal-recycled gravitational wave detectors can be further improved by squeezed light injected into the dark port of the interferometer and by a frequency dependent read-out scheme.

8.1.2 Squeezed Light Input

As first proposed in (Caves; 1980), squeezed light can be employed to reduce the high power requirements in GW interferometers. Later Unruh in (Meystre and Scully; 1983) and

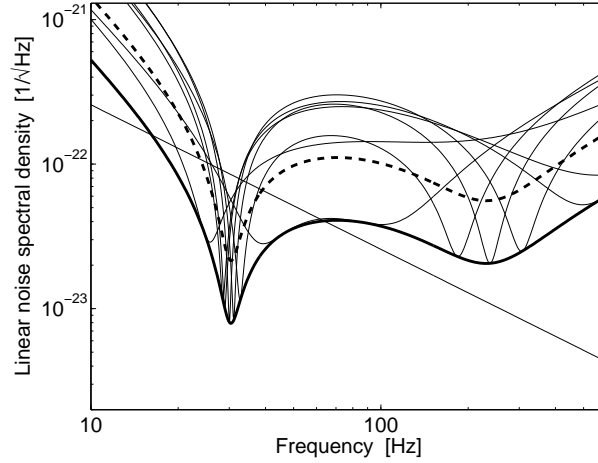


Figure 8.3: The bold dashed curve shows the phase-quadrature noise spectral density of a SR-interferometer with unsqueezed (coherent) vacuum input. The array of thin black curves evolves from the dashed curve, if the input vacuum-field at the dark port is squeezed with squeezing parameter $r = 1$ and the squeezing angle λ is varied in a frequency independent manner. The array is bounded from below by the lower bold black curve. Alternatively, one obtains the lower boundary, if the conventional SR noise spectral density is simply shifted downwards by a factor of e^{-r} . The same holds for the amplitude quadrature. The straight line represents the standard quantum-limit.

others (Gea-Banacloche and Leuchs; 1987; Jaekel and Reynaud; 1990; Pace et al.; 1993; Kimble et al.; 2001) have found and proven in different ways that squeezed light with a frequency dependent orientation of the squeezing ellipse can reduce the quantum noise down to values beyond the standard quantum limit. This research was done on interferometer topologies without signal-recycling. Chickarmane *et al.* (Chickarmane and Dhurandar; 1996; Chickarmane et al.; 1998) investigated the squeezed-input signal-recycled interferometer at low laser powers, i.e. the shot-noise limited case. In this section we consider the squeezed-input signal-recycled interferometer at high laser powers including the effect of back-action noise.

As discussed in Sec. IVB of Ref. (Kimble et al.; 2001), squeezed vacuum is related to the ordinary coherent vacuum state by an unitary operator

$$|\text{in}\rangle = \hat{S}(r, \lambda)|0\rangle, \quad (8.9)$$

where r is the squeezing parameter, and λ the squeezing angle (for an introduction to squeezed light see for example (Walls and Milburn; 1995)). Alternatively, we can transform the input state back to the vacuum state, by

$$|\text{in}\rangle \rightarrow \hat{S}^\dagger(r, \lambda)|\text{in}\rangle = |0\rangle, \quad (8.10)$$

and at the same time transform the input quadrature operators accordingly [Eq. (A8) of

Ref. (Kimble et al.; 2001)],

$$\begin{aligned}\bar{\mathbf{i}} &\rightarrow \hat{S}^\dagger(r, \lambda) \bar{\mathbf{i}} \hat{S}(r, \lambda) \\ &= \mathbf{D}(-\lambda) \mathbf{S}(r) \mathbf{D}(\lambda) \bar{\mathbf{i}},\end{aligned}\quad (8.11)$$

where

$$\mathbf{D}(\lambda) \equiv \begin{pmatrix} \cos \lambda & \sin \lambda \\ -\sin \lambda & \cos \lambda \end{pmatrix}, \quad \mathbf{S}(r) \equiv \begin{pmatrix} e^r & 0 \\ 0 & e^{-r} \end{pmatrix}. \quad (8.12)$$

From Eq. (8.11), we also see that a squeezed vacuum with squeezing angle λ can be obtained from a second-quadrature squeezing by applying a rotation of $\mathbf{D}(-\lambda)$ (note the minus sign). Any further rotation of quadratures will also add (with a minus sign) to the squeezing angle.

The input-output relation of the lossless interferometer with fixed beam splitter becomes

$$\bar{\mathbf{o}} = \frac{1}{M} [\mathbf{T} \mathbf{D}(-\lambda) \mathbf{S}(r) \mathbf{D}(\lambda) \bar{\mathbf{i}} + \bar{\mathbf{s}} h], \quad (8.13)$$

implying a noise spectral density of

$$S_h = \frac{\begin{pmatrix} \cos \zeta & \sin \zeta \end{pmatrix} \mathbf{T} \mathbf{D}(-\lambda) \mathbf{S}(2r) \mathbf{D}(\lambda) \mathbf{T}^\dagger \begin{pmatrix} \cos \zeta \\ \sin \zeta \end{pmatrix}}{\begin{pmatrix} \cos \zeta & \sin \zeta \end{pmatrix} \bar{\mathbf{s}} \bar{\mathbf{s}}^\dagger \begin{pmatrix} \cos \zeta \\ \sin \zeta \end{pmatrix}} \quad (8.14)$$

Note that here \mathbf{T} is a real matrix with an overall phase factor in front (cf. Eq. (8.3)). Figure 8.3 shows an array consisting of 7 curves (thin lines) where the quadrature angle $\zeta = \pi/2$ is constant and the frequency independent squeezing angle λ is varied. In all cases the squeezing parameter r has been set to unity. Interestingly a variation of the frequency-independent squeezing angle causes a frequency shift of both resonances. For comparison, the standard quantum limit (straight line) and the spectral noise density in the quadrature at $\zeta = \pi/2$ without squeezed input is also given (dashed line). As we can see, each individual frequency-independent value for λ can be advantageous to the case without squeezing only in a certain frequency band. Obviously, the envelope of the minima of the squeezed input array, as also drawn in the graph (lower bold line), is physically meaningful since it can in principle be realized by applying squeezed light with a squeezing angle optimized for each side-band frequency. Such light is called frequency-dependent squeezed light and yields a broad-band improvement in the quantum noise limited sensitivity. In the final paragraphs of this section we now derive an analytical expression for the optimized spectral noise density. Suppose now the squeezing angle λ can be an arbitrary function of frequency, and r is always positive, then as we can tell

from Eq. (8.14), the optimal $\lambda(\Omega)$ should make

$$\mathbf{D}(\lambda(\Omega))\mathbf{T}^\dagger \begin{pmatrix} \cos \zeta \\ \sin \zeta \end{pmatrix} \propto \begin{pmatrix} 0 \\ 1 \end{pmatrix}, \quad (8.15)$$

or

$$\tan \lambda(\Omega) = -\frac{T_{11} \cos \zeta + T_{21} \sin \zeta}{T_{12} \cos \zeta + T_{22} \sin \zeta}; \quad (8.16)$$

yielding an optimal noise spectrum of

$$S_h^{\text{SI}} = e^{-2r} \frac{\begin{pmatrix} \cos \zeta & \sin \zeta \end{pmatrix} \mathbf{T} \mathbf{T}^\dagger \begin{pmatrix} \cos \zeta \\ \sin \zeta \end{pmatrix}}{\begin{pmatrix} \cos \zeta & \sin \zeta \end{pmatrix} \bar{\mathbf{s}} \bar{\mathbf{s}}^\dagger \begin{pmatrix} \cos \zeta \\ \sin \zeta \end{pmatrix}}. \quad (8.17)$$

This expression turns out to be identical to the noise spectral density without squeezing in Eq. (8.7) being suppressed by a factor of e^{-2r} . This result can be understood intuitively as follows. The input quadrature field is going to be rotated (and possibly ponderomotively squeezed) by the matrix \mathbf{T} before being detected. The minimal noise quadrature of the squeezed state should therefore be rotated conversely before being injected into the interferometer, such that the detector always “sees” the minimal noise.

Squeezed vacuum can be generated with a variable but frequency-independent squeezing angle λ (see for example (Breitenbach et al.; 1998)). A frequency-dependent squeezing angle can be obtained subsequently by filtering the initial squeezed light through detuned Fabry-Pérot (FP) cavities, as proposed by (Kimble et al.; 2001), which can rotate the quadratures in a frequency dependent way. For small frequencies ($\Omega \ll c/L_{\text{FP}}$), a detuned FP cavity of length L_{FP} rotates the reflected quadrature in the following way:

$$\bar{\mathbf{a}}^{\text{out}} = e^{i\alpha_m} \mathbf{D}(-\alpha_p) \bar{\mathbf{a}}^{\text{in}} \quad (8.18)$$

with

$$\alpha_{p,m} = \frac{1}{2}(\alpha_+ \pm \alpha_-) \quad (8.19)$$

and

$$\alpha_\pm = 2 \arctan(\xi \pm \Omega/\delta). \quad (8.20)$$

where ξ is defined by the resonant frequency ω_{FP} and by δ which is the half-linewidth of the cavity: $\omega_{\text{FP}} = \omega_0 - \xi\delta$. As further shown in Appendix A of Ref. (Purdue and Chen; 2002), several such Fabry-Pérot filter cavities can be combined to give a broad category of frequency dependent rotation angles. Adopting their formulas [cf. Eqs. (A.8)—(A.14)] into our context, we found that, in order to realize an *additional* squeezing angle $\lambda(\Omega)$ with the form of

$$\tan \lambda(\Omega) = \frac{\sum_{k=0}^n B_k \Omega^{2k}}{\sum_{k=0}^n A_k \Omega^{2k}}, \quad |A_n + i B_n| > 0. \quad (8.21)$$

we first need to obtain an initial frequency independent squeezed state with

$$\lambda_0 = \arg(A_n - i B_n), \quad (8.22)$$

and then filter this squeezed light with n filters whose complex resonant frequencies differ from ω_0 by $\Omega_J^{\text{res}} \equiv -\delta_J \xi_J - i \delta_J$, $J = 1, 2, \dots, n$, with $\{\pm \Omega_J^{\text{res}}\}$ being the $2n$ roots of the characteristic equation:

$$\sum_{k=0}^n (A_k - i B_k) \Omega^{2k} = 0. \quad (8.23)$$

[Note that $\{\Omega_J^{\text{res}}\}$ are the n roots with the appropriate sign of imaginary part, in our case negative.]

Suppose the readout quadrature ζ is frequency independent, from the ideal input-output relation of GEO 600, we see that the desired λ from Eq. (8.16) is indeed of the form of Eq. (8.21) when $\Omega L/c$ is expanded to the leading order*. Two filter cavities are necessary for the generic case. However, as we look at the low-power limit, only one such filter is necessary. In this case, the input-output relation rotates the input quadratures into the output quadratures following the same law as a detuned cavity. Naturally, as we go through Eq. (8.22) and Eq. (8.23), we find that the required initial additional squeezing angle is

$$\lambda_0 = \zeta - \pi/2, \quad (8.24)$$

which puts the minor axis of the noise ellipse onto the ζ quadrature, while the required cavity has resonant frequency

$$\Omega^{\text{filter res}} = \frac{\phi_{\text{FPC}}}{L_{\text{FP}}} - i \frac{c\tau_{\text{FP}}^2}{4L_{\text{FP}}}, \quad (8.25)$$

which is just ‘‘opposite’’ to the signal-recycling resonant frequency,

$$\Omega^{\text{SR res}} \equiv \omega^{\text{SR}} - i \gamma^{\text{SR}} = -\frac{\phi c}{L} - i \frac{c\tau^2}{4L}, \quad (8.26)$$

and cancels the rotation induced by signal-recycling. For full-power GEO 600 interferometers, the initial additional squeezing angle is still given by Eq. (8.24), while the frequency-dependent part requires two cavities determined by the following characteristic equation:

$$\Omega^2(\Omega + \omega^{\text{SR}} + i \gamma^{\text{SR}})(\Omega - \omega^{\text{SR}} - i \gamma^{\text{SR}}) - \frac{10P\omega_0}{m_{\text{M}}Lc}(\omega^{\text{SR}} + 2e^{i\zeta} \sin(\zeta)\gamma^{\text{SR}}) = 0. \quad (8.27)$$

It is straightforward to solve for the four roots (in two pairs) of the characteristic equations. The corresponding transmissivity τ of the input mirror and the detuning ϕ of the filter cavity can be derived from these roots by virtue of Eq. (8.25).

*Note that, one has to take $\Omega L/c \sim T_{\text{SR}} \sim \phi \sim \mathcal{K}$ in order to get a meaningful expansion.

8.1.3 Squeezed-Variational Schemes

As shown in (Kimble et al.; 2001), the quantum noise spectral density of a conventional interferometer without signal-recycling can benefit simultaneously from both, frequency-dependent squeezed light input and frequency-dependent homodyne read-out. In this section we investigate the optical-spring signal-recycled interferometer with corresponding additional input and output optics. We start from the result of the previous section and vary the angle ζ of homodyne detection.

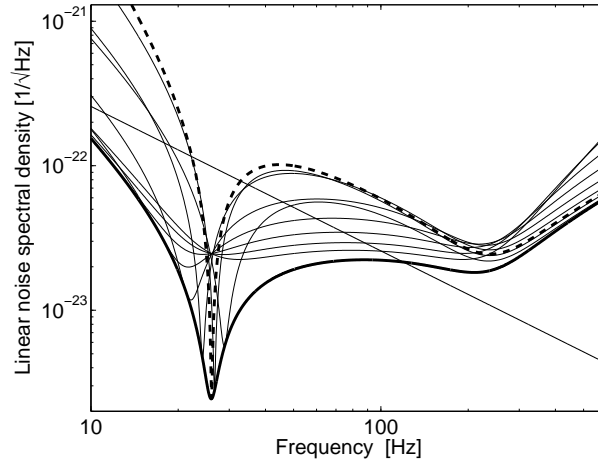


Figure 8.4: Another improvement of the SR-densities is achieved, if the detection angle is optimized for each signal frequency. Since the shot noise and radiation-pressure noise are highly correlated especially in the detection band, the effect is less beneficial than the optimization of the input squeezing angle. However, comparing the boundary curve with the dashed curve which corresponds to an arbitrary but fixed detection angle, the bandwidth of the noise minima is enhanced and a noise reduction by a factor of 10 can be achieved at some frequencies.

Figure 8.4 shows an array of noise spectral densities of the output quadrature with varying detection angle ζ which is here still frequency independent. The input vacuum at the dark port is optimally squeezed with squeezing parameter $r = 1$. Obviously, the array is bounded from below. This boundary corresponds to the optimized quantum noise spectral density of the signal-recycled interferometer. One member of the array is highlighted by a bold dashed line. Comparing the dashed curve with the optimized noise spectral density, one can see that the variational output provides a further improvement of the interferometer's performance which is mainly an increased bandwidth of the sub-SQL sensitivity. At some frequencies the noise is reduced by a factor of 10. We emphasize that the optimized noise spectrum presented can not be further improved for this interferometer topology without increasing the squeezing parameter r of the input vacuum. Obviously, our results are also significant without any squeezing of the input vacuum. The plots in Figure 8.4 are not altered except for a shift upwards by a factor of e^r .

In the final part of this section we give an analytical expression of the lower boundary starting from Eq. (8.17). S_h^{SI} has to be minimized with respect to the detection angle ζ .

One method to find the minimum noise is to determine analytically the minimum of the function $S_h^{\text{SI}}(\zeta)$. Then, a lengthy but straightforward calculation leads to a conditional equation for the optimized detection angle ζ_{opt} of the following form [†]:

$$\begin{pmatrix} \cos \zeta_{\text{opt}} & \sin \zeta_{\text{opt}} \end{pmatrix} \begin{pmatrix} Q_{11} & Q_{12} \\ Q_{12} & Q_{22} \end{pmatrix} \begin{pmatrix} \cos \zeta_{\text{opt}} \\ \sin \zeta_{\text{opt}} \end{pmatrix} = 0. \quad (8.28)$$

Representing a general SR interferometer, the coefficients of the symmetric quadric \mathbf{Q}

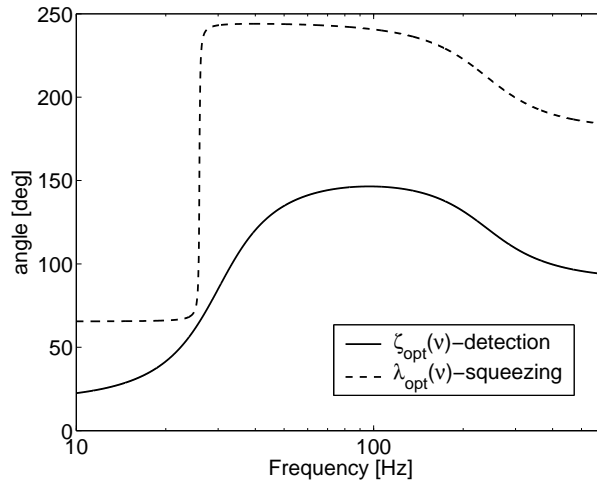


Figure 8.5: The optimized detection angle ζ_{opt} is determined by Eq. (8.30). The optimized squeezing angle λ_{opt} of the input field depends on ζ_{opt} by virtue of Eq. (8.16).

are complex (and complex-valued) functions of the interferometers' parameters (\mathcal{K}, Φ, \dots) which determine the input-output relation Eq. (8.2). It is more convenient to express them in terms of the elements of the two symmetrized matrices $\mathcal{S} = \langle \bar{\mathbf{s}} \bar{\mathbf{s}}^\dagger \rangle_{\text{sym}}$, $\mathcal{T} = \langle \mathbf{T} \mathbf{T}^\dagger \rangle_{\text{sym}}$:

$$\begin{aligned} Q_{11} &= \mathcal{S}_{11}(\mathcal{T}_{12} + \mathcal{T}_{21}) - \mathcal{T}_{11}(\mathcal{S}_{12} + \mathcal{S}_{21}), \\ Q_{12} &= \mathcal{S}_{11}\mathcal{T}_{22} - \mathcal{T}_{11}\mathcal{S}_{22}, \\ Q_{22} &= \mathcal{T}_{22}(\mathcal{S}_{12} + \mathcal{S}_{21}) - \mathcal{S}_{22}(\mathcal{T}_{12} + \mathcal{T}_{21}). \end{aligned} \quad (8.29)$$

In general, Eq. (8.28) has two solutions corresponding to a local minimum and a local maximum of the noise density:

$$\zeta_{\pm} = -\text{arccot} \left[\frac{1}{Q_{11}} \left(\pm \sqrt{-\det \mathbf{Q}} + Q_{12} \right) \right]. \quad (8.30)$$

[†]A similar analytic expression has also been obtained independently by Buonanno and Chen, but remained unpublished.

The minimum of the noise spectral density is given by inserting $\zeta_{\text{opt}} = \zeta_-$ into Eq. (8.17). The optimized detection angle ζ_{opt} is shown in Figure 8.5 together with the optimized squeezing angle λ_{opt} of the input field which depends on ζ_{opt} according to Eq. (8.16). The form of both curves suggests that the filtering of the input and output light is accomplishable. Due to the frequency dependence of the squeezing and detection angle, one has to investigate first if an expansion in the form of Eq. (8.21) yields an expression which represents a manageable number of filter cavities. Furthermore, both spectra in Figure 8.5 are sensitive to small changes of the parameters. Therefore, we do not propose a specific number of filter cavities needed to realize the frequency dependence.

8.2 Dual Resonators

Dual resonators were proposed as QND measuring devices of an external force which acts on the mirrors. The two simplest schemes are known as optical bar and speed meter. Interestingly, in contrast to the ostensible similarity of the two schemes, the signal read-out and mirror dynamics differ significantly. In fact, apart from fine tunings of the mirror

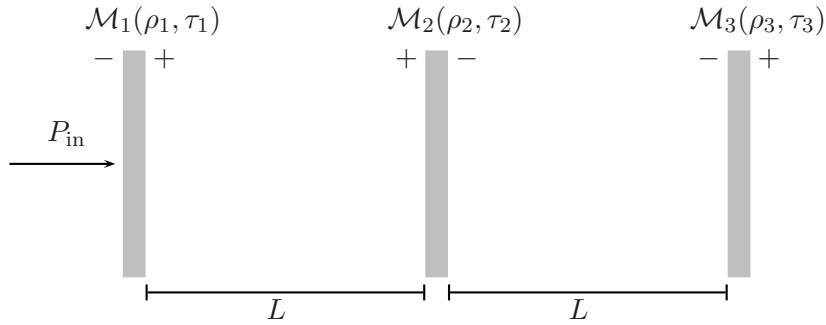


Figure 8.6: The dual resonator is formed by three mirrors. The system is pumped through mirror \mathcal{M}_1 . The two resonators are weakly coupled via an internal mirror \mathcal{M}_2 . The length L of both cavities are identical.

reflectivity, the proper difference lies in the chosen frequency of the laser which pumps one of the two resonators. The pump frequency is measured against the doublets of resonant frequencies of the dual resonator

$$\omega_{\text{res}} = \frac{c}{2L} \cdot (2\pi n \pm \arcsin(\tau_2)), \quad n \in \mathbb{N} \quad (8.31)$$

The frequency splitting is determined by the transmissivity of the inner mirror \mathcal{M}_2 . The linewidths of the resonances depend on the transmissivities τ_1, τ_3 (see Figure 8.6) and on further intracavity losses. If $\tau_1, \tau_3 \ll \tau_2$ then the resonances appear as two distinguished peaks in the power spectrum of the dual cavity which is the typical choice for optical bar detectors. Otherwise, the power spectrum exhibits a single broad peak typical for

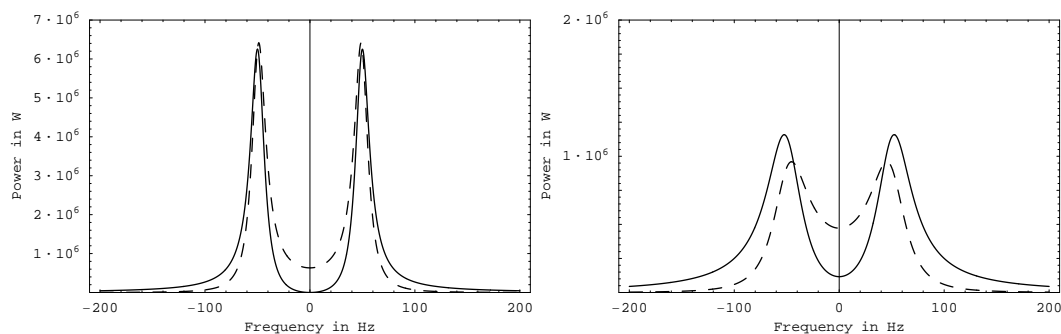


Figure 8.7: The figure shows the power inside a dual resonator as a function of the pumping frequency. Both graphs are drawn with the same values for the pumping power and pumping efficiency. The left figure displays a typical optical bar spectrum with lossless second cavity $[\mathcal{M}_2, \mathcal{M}_3]$ (except for its coupling to the first cavity $[\mathcal{M}_1, \mathcal{M}_2]$). The right figure displays a typical speed meter spectrum with further losses in the second cavity which count for a realistic signal extraction efficiency. The transmissivity of the inner mirror is chosen such that the two resonances are separated by 100 Hz which corresponds to a typical detection frequency of Earth-bound gravitational-wave detectors. The solid line displays the power of the directly pumped cavity, the dashed line the power of the second cavity.

speed meters. The spectra shown in [Figure 8.7](#) approximately represent each of the two operation modes.

This section summarizes the main methods and results obtain for several QND schemes of the dual resonator. In [subsection 8.2.1](#), we discuss the optical bar and its five mirror variant known as the optical lever. The optical bar translates the motion of end mirrors to a local test mass whereas the optical lever even amplifies the amplitude of the transfer. In [subsection 8.2.2](#), it is shown how to operate a dual resonator which is sensitive to the speed of the end masses. Finally, in [subsection 8.2.3](#), a more sophisticated topology is investigated which however bears some analogy to the optical bar scheme.

We mention that the dynamics of the optical dual resonator including its response to external forces possess a helpful mechanical analogue: the coupled pendulum. The most basic conventions and quantities which also appear in the following subsections are introduced in [Appendix E](#). There, the unperturbed coupled pendulum is treated and the calculation of its energy sloshing frequency is outlined.

8.2.1 Optical Bars

In ([Braginsky et al.; 1997](#)), optical bars where first proposed as gravitational wave antennas envisioning two different topologies (see [Figure 8.8](#)): The L-topology and the X-topology. The essential feature is that the extracavity measurement of the signal field is substituted by an intracavity readout which senses the motion of an internal mirror. The idea is that, at low frequencies, the motion of the internal mirror D is optomechanically coupled to the motion of the end mirrors A, B . Thereby, a gravitational-wave force which acts on the end mirrors is transferred to the internal mirror. The motion of mirror D may

then be measured by means of a small cavity. The frequency ω_0 of the pump is tuned

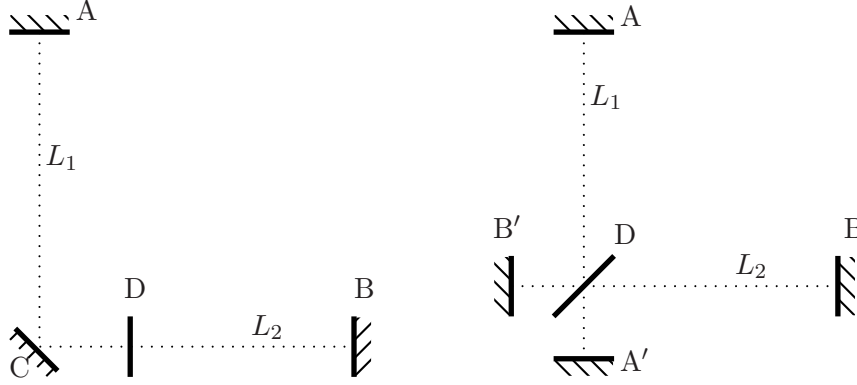


Figure 8.8: The L and X topology of an optical bar. The local mirror D is subject to a radiation pressure force which is driven by the gravitational wave. The spectrum of the optical bar contains resonance doublets. The difference of the two frequencies is a product of the transmissivity of the local mirror and the free spectral range of the cavities (which are approximately of the same length).

to the upper resonance frequency of the dual resonator whose linewidth is assumed to be much smaller than the doublet splitting $\frac{c}{L} \arcsin(\tau_D)$ (which is also the bar's sloshing frequency). According to [Figure 8.7](#), the two cavities of a typical optical bar scheme store approximately the same power. A gravitational wave gives rise to slight changes of the distances between the mirrors and a corresponding energy difference $\delta\mathcal{E}^h(t)$ between the two cavities. Accordingly, the wave generates a radiation-pressure force which acts on D :

$$\delta F^h(t) = -\frac{\delta\mathcal{E}^h(t)}{c} \quad (8.32)$$

In order to calculate $\delta\mathcal{E}^h(t)$, we get a little help from our mechanical analogue: the coupled pendulum. The equation of motion of the field amplitudes in each cavity is formally identical to the equation of motion for the coordinates of the coupled pendulum

$$\begin{aligned} \ddot{a}^{C1}(t) + \omega_1^2(t)a^{C1}(t) + \Omega_0\omega_0a^{C2}(t) &= 0 \\ \ddot{a}^{C2}(t) + \omega_2^2(t)a^{C2}(t) + \Omega_0\omega_0a^{C1}(t) &= 0 \end{aligned} \quad (8.33)$$

where the resonance frequencies of each cavity $\omega_{1,2}(t) = \omega_0(1 \mp h(t)/2)$ depend on the amplitude $h(t)$ of the gravitational wave and Ω_0 denotes the sloshing frequency. The solution up to first order in h expressed in terms of the normal coordinates $a_{\pm}(t) \equiv$

$1/\sqrt{2}(a^{C1}(t) \pm a^{C2}(t))$ reads

$$\begin{aligned} a_+(t) &= a_0 \cos(\omega_+ t) \\ a_-(t) &= \omega_0 a_0 \int_{-\infty}^t dt' \sin(\omega_-(t-t')) \cos(\omega_+ t') h(t') \end{aligned} \quad (8.34)$$

where ω_{\pm} denote the upper and lower resonance frequency of the doublet. The initial condition $a_-(0) = 0$ as well as the equations of motion represent an ideal bar completely devoid of losses. As we know, the realistic bar must have minimal losses determined by the pumping efficiency. The fractional energy difference averaged over several cycles of the fast oscillation ω_0 is given by

$$\begin{aligned} \frac{\delta \mathcal{E}^h(t)}{\mathcal{E}} &= \frac{2a_+(t)a_-(t)}{a_+^2(t) + a_-^2(t)} \simeq \frac{2a_-(t)}{a_+(t)} \\ &= \omega_0 \int_{-\infty}^t dt' \sin(\Omega_0(t-t')) h(t') \end{aligned} \quad (8.35)$$

where \mathcal{E} is the total energy of both cavities. The optical bar is a QND device since the intracavity readout scheme measures an energy $\delta \mathcal{E}^h(t)$ without disturbing the energy distribution between the two cavities (the readout is performed with a comparatively low power beam). As shown in (Braginsky et al.; 1997), the standard-quantum limit associated with a free mass can be beaten for gravitational-wave frequencies close to $\Omega = \Omega_0/\sqrt{2}$.

A slightly different topology, the optical lever, was considered by (Khalili; 2002). The optical lever has additional arm cavities (see Figure 8.9) which are tuned to the upper resonance of the doublet. The cavities $A' - C$ and $B' - C$ are tuned on antiresonance to that frequency. The arm cavities are weakly coupled via a small transmissivity τ_C of the local internal mirror C. Again, the resonance peaks are separated by Ω_0 . The arm cavity finesse is expected to amplify the local mirror displacement by their finesse \mathcal{F} compared to the optical bar scheme. The equations of motion for the optical lever in the frequency domain read

$$\begin{aligned} [-2m_x \Omega^2 + \chi_{xx}(\Omega)] x(\Omega) &= \chi_{xy} y(\Omega) + F_{\text{grav}}(\Omega) \\ [-m_y \Omega^2 + \chi_{yy}(\Omega)] y(\Omega) &= \chi_{xy} x(\Omega) + F_{\text{fluct}}(\Omega) \end{aligned} \quad (8.36)$$

where m_x is the mass of mirrors A, B and m_y the mass of the local mirror C . The gravitational wave and radiation pressure fluctuations appear as external forces acting on the end mirrors and local mirror respectively (radiation pressure acting on mirrors A, B is negligible if one chooses $m_x \gg m_y$). The susceptibilities χ_{ij} assume a rather complicated form. However, for signal frequencies well below the free spectral range of the arm cavities, there exists a simple relation between them

$$\chi_{xx} \propto \mathcal{F} \chi_{xy} \propto \mathcal{F}^2 \chi_{yy} \quad (8.37)$$

The latter equation together with Eq. (8.36) also describes the motion of mechanical levers. Therefore, the configuration is called an optical lever. The optical bar sensitivity is maximally increased by $\mathcal{F} \sim \Delta \nu_{\text{fsr}}/\Omega_0$.

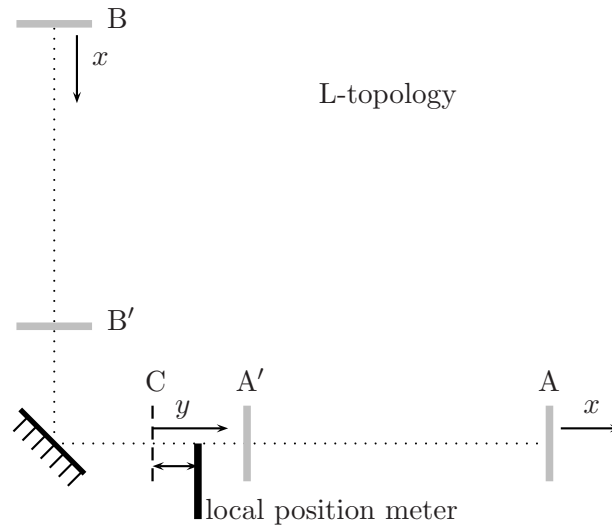


Figure 8.9: The figure displays the L-topology of an optical lever. A redistribution of energy between the two arms causes mirror C to move. Its motion also depends on the finesse \mathcal{F} of the arm cavities which constitutes an amplification factor of the coupling between the motion of the local mirror and the end mirrors.

8.2.2 Speed Meters

Operating the dual resonator as speed meter and thereby profiting from its QND properties was first investigated in detail by (Braginsky, Gorodetsky, Khalili and Thorne; 2000). As we already know from Figure 8.7, pumping one resonator on its resonance – which corresponds to frequency 0 Hz in that figure – causes the other lossless resonator to be excited. This choice of pumping frequency underlies the speed meter mode of the dual resonator whose QND properties can be explained as follows. A signal which changes the distance between the mirrors of the excited resonator creates a signal modulation field. This field sloshes between the two resonators and after each sloshing period returns with its sign being reversed. If the signal frequency Ω is much smaller than the sloshing frequency Ω_0 then the signal field in the excited resonator is proportional to the speed \dot{x} of distance changes. Speed (momentum) is a QND observable and we expect to beat the SQL for the coordinate measurement of a free mass for frequencies $\Omega \ll \Omega_0$.

The remaining problem is to extract the signal from the excited cavity. This issue is not trivial. So far we have assumed that the resonator is lossless ($\tau_3 = 0$). Obviously, we have to give up that condition when asking for a certain nonzero signal extraction efficiency τ_3 . By consequence, the pumped cavity starts to store part of the pumped energy (see right graph of Figure 8.7). The realistic speed meter becomes suboptimal and partly loses its QND character. The here investigated dual resonator design of a speed meter has another important flaw. The resonators could store much more energy (e.g. 10 times or more) if the frequency of the pump corresponded to one of the eigenfrequencies of the dual resonator. Meanwhile, these disadvantages are circumvented by means of innovative

speed meter designs which effectively separate the pump and signal channels (e.g. see (Purdue and Chen; 2002)). There, the signal extraction efficiency does not influence the distribution of energy between the two cavities and the QND character of the instrument is preserved.

Despite the many vetoes to this design, we give a brief summary of quantitative results for the optical speed meter according to (Purdue; 2002). Before we start to analyze the performance, we just have to introduce one small variation of the standard design. In order to restore the zero power condition of the pumped cavity for some given signal extraction efficiency τ_3 , it was suggested to pump the excited cavity such that the two pumps interfere destructively within the cavity $[\mathcal{M}_1, \mathcal{M}_2]$. The power of the additional pump is determined by

$$P_2 = \frac{P_1}{4} \frac{\tau_1 \tau_3}{\tau_2} \quad (8.38)$$

where P_1 denotes the power of the pump in the standard design. A simple argument leads to the following series of conditions

$$\tau_3 \gg \tau_2 \gg \tau_1 \quad (8.39)$$

If the pumping efficiency τ_1 were greater than the coupling τ_2 , then too much power would be lost within one sloshing period and the low-frequency signal inside the excited cavity would not be proportional to the speed \dot{x} . The other inequality is found by demanding that the signal extraction rate $\delta = c\tau_3^2/(4L)$ is similar to the sloshing frequency $\Omega_0 = c\tau_2/L$. For simplicity we also assume that all three mirrors have the same mass m . Then the SQL of a distance measurement between mirrors \mathcal{M}_2 and \mathcal{M}_3 is given by

$$h_{\text{SQL}} = \sqrt{\frac{16\hbar}{m\Omega^2 L^2}} \quad (8.40)$$

As we have already mentioned, we expect to beat this SQL which is described by a frequency-dependent factor ξ . The corresponding (single-sided) spectral density can be cast into the form

$$S^{\text{sm}}(\Omega) = h_{\text{SQL}}^2(\Omega) \cdot \xi^2(\Omega) \quad (8.41)$$

It turns out that the all-optimized minimum of $\xi(\Omega)$ is located at $\Omega_{\text{opt}} = \sqrt{\Omega_0^2 - \delta^2}/2$ including an adjustment of the homodyne detection angle. In contrast to position meters the optimized homodyne angle of the speed meter is frequency independent. The minimum $\xi_{\text{min}}(\Omega_{\text{opt}})$ can be written

$$\xi_{\text{min}}(\Omega_{\text{opt}}) = \frac{\delta \sqrt{\Omega_{\text{opt}}^2 + \delta^2/4}}{\sqrt{2}\Lambda^2} \quad (8.42)$$

in terms of the power dependent parameter

$$\Lambda^2 \equiv \sqrt{\frac{\hbar}{2m}} \frac{\tau_1 \tau_3}{\tau_2} \omega_0 P_1 \quad (8.43)$$

The complete function optimized with respect to the homodyne angle and a signal frequency at $\Omega_{\text{opt}} = 2\pi \cdot 100 \text{ s}^{-1}$ is displayed in Figure 8.10 for two different pumping powers.

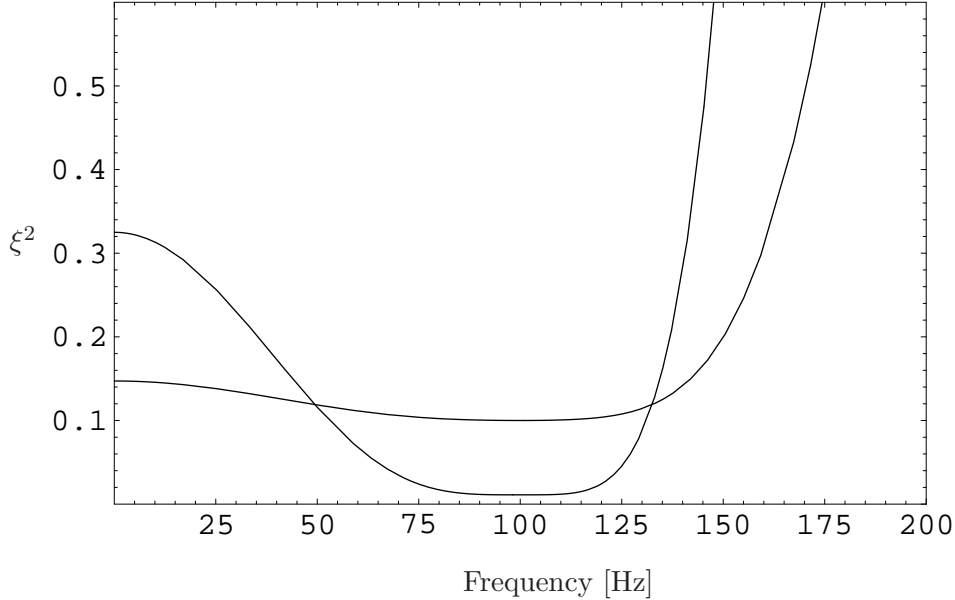


Figure 8.10: The graph shows the fractional sensitivity improvement ξ of a speed meter. The signal extraction rate and the sloshing frequency have the same values for both curves. The pumping power of the more narrow curve is 3 times greater than the pumping power of the other curve.

It was pointed out that the feasibility of that scheme is doubtful since it requires a pumping power of $P_1 \gtrsim 300$ MW in order to achieve satisfactory improvement compared with a position meter (which also means that more than half a megawatt leaks out of the resonator together with the signal). However, a similar analysis can be carried out for the speed meter topology presented in (Purdue and Chen; 2002). There, the respective numbers look much more promising.

8.2.3 Symphotonic States

In (Braginsky et al.; 1998) an interesting variant of a QND dual resonator appeared. The authors show how to measure the phase difference $\delta\phi$ between two linearly decoupled optical resonators. By linearly decoupled we mean that the fields do not transmit through mirrors from one resonator to the other as opposed to the optical bar scheme. However, the two resonators can communicate via radiation pressure on an intermediate test mass. The topology of that system is shown in Figure 8.11. The radiation-pressure force F acting on mirror D is proportional to the difference of the amplitude squares on each of its sides

$$F \propto |a + ib|^2 - |b + ia|^2 \quad (8.44)$$

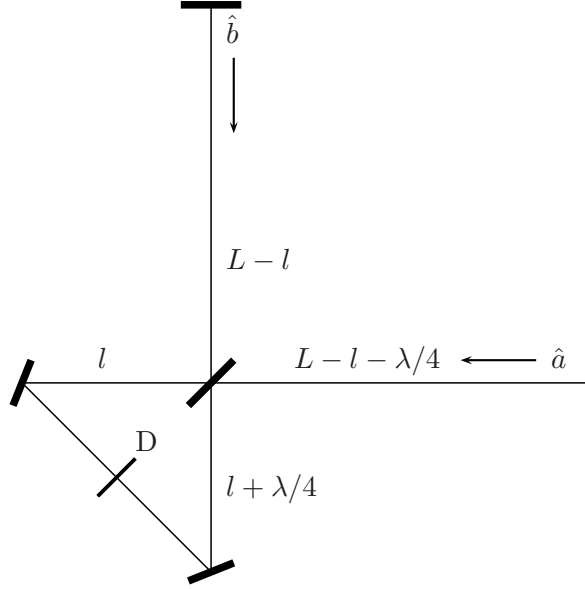


Figure 8.11: Modes are coupled by a third order nonlinearity at D due to the ponderomotive force. A local meter measures the position or speed of D . The field operator which determines the force is a QND observable of the system.

A simple calculation shows that the right-hand side is equal to $4|a||b|\sin(\delta\phi)$ where $\delta\phi$ is the phase difference of the two modes. Quantum mechanically, the force is determined by the operator

$$\hat{X}_{\pi/2} \equiv i(\hat{a}^\dagger \hat{b} - \hat{b}^\dagger \hat{a}) \quad (8.45)$$

which is a QND observable of the detector since it commutes with the free Hamiltonian of the system

$$[\hat{X}_{\pi/2}, \hbar\omega(\hat{a}^\dagger \hat{a} + \hat{b}^\dagger \hat{b})] = 0 \quad (8.46)$$

The eigenstates $|N, n\rangle$ of the cross-quadrature operator $\hat{X}_{\pi/2}$ are called symphotonic states.

$$|N, n\rangle = \frac{1}{\sqrt{2^N n!(N-n)!}} (\hat{a}^\dagger - i\hat{b}^\dagger)^n (\hat{a} + i\hat{b})^{N-n} |0\rangle \quad (8.47)$$

Here, N denotes the total number of photons in both modes which in the ideal case is conserved and n is an integer between 0 and N . The states have been named symphotonic because the amplitudes of n quanta are orthogonal to the other $N - n$ quanta. It has been shown that a small phase shift changes the number n with a probability close to one, provided that $\delta\phi \sim \sqrt{8}/N$ together with $n \sim N/2$. In other words, the phase shift is measurable under these conditions.

The force F is measured by means of a local meter which shall exert negligible back action on the test mass (a detailed investigation is carried out in (Braginsky et al.; 1998)). Then, denoting the classical carrier amplitude common to both arms by Λ and the carrier

frequency by ω_0 , the equations of motion for the fields of the ideal system read

$$\begin{aligned}\dot{\hat{a}}(t) &= \omega_0 \Lambda \left(\frac{i \hat{x}_a(t) - \hat{x}(t)}{L} + \frac{1}{2} i h(t) \right) \\ \dot{\hat{b}}(t) &= \omega_0 \Lambda \left(\frac{i \hat{x}_b(t) - \hat{x}(t)}{L} - \frac{1}{2} i h(t) \right)\end{aligned}\tag{8.48}$$

whereas the equations for the positions \hat{x}_a , \hat{x}_b of the two end mirrors and the position \hat{x} of the local mirror are given by

$$\begin{aligned}m \ddot{\hat{x}}(t) &= \frac{i \hbar \omega_0 \Lambda}{L} \left(\hat{a}^\dagger(t) - \hat{a}(t) + \hat{b}(t) - \hat{b}^\dagger(t) \right) \\ M \ddot{\hat{x}}_a(t) &= \frac{\hbar \omega_0 \Lambda}{L} \left(\hat{a}(t) + \hat{a}^\dagger(t) \right) \\ M \ddot{\hat{x}}_b(t) &= \frac{\hbar \omega_0 \Lambda}{L} \left(\hat{b}(t) + \hat{b}^\dagger(t) \right)\end{aligned}\tag{8.49}$$

Therefrom, an elaborate calculation leads to the ultimate sensitivity of the detector to gravitational waves. It is proportional the standard quantum limit of the mass M of the end mirrors which perhaps is not very surprising. For example, the strong pumping mode of the symphotonic detector must share properties of an optical bar. There, the local test mass ($m \ll M$) moves rigidly connected to the end masses and one should assume that it has to be the SQL of the end masses which characterizes the sensitivity of the optical bar mode.

CHAPTER 9

Space-Borne Interferometers

9.1 Time-Delay Interferometry

As pointed out in previous chapters, the frequency noise from the laser at ground-based interferometric gravitational wave detectors is automatically cancelled due to destructive interference of the light towards the output port of the interferometer. It is virtually impossible and unpractical to follow the same prescription with space-borne interferometers. One problem is that the light travels over long distances and just a tiny fraction of the emitted light reaches the next spacecraft. If one tried to reflect the light back to its origin, then one would have great difficulties to detect it. Therefore, space-borne interferometers work exclusively with one-way light trains and one has to devise a different scheme for the cancellation of the all dominating laser frequency noise. The space interferometer

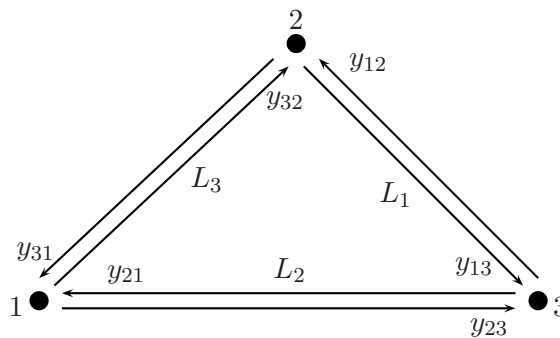


Figure 9.1: Doppler time series recorded by LISA. Assuming perfect phase locking between the two lasers of one spacecraft, there are six monitored time series which determine the sensitivity of the detector. These time series correspond to the six measurements of Doppler shifts.

LISA for example consists of three spacecrafts which ideally form an equilateral triangle (LISA study teams; 2000). The spacecrafts are separated by $5 \cdot 10^6$ km. Two lasers on each spacecraft send their light to the two neighbors where it is detected. Each spacecraft records two Doppler signals sensitive to gravitational waves which are denoted by y_{ij} as shown in Figure 9.1 where the first index signifies the path and the second index the receiving spacecraft. In addition to the Doppler signals y_{ij} , two more Doppler signals z_{ij} are recorded by each spacecraft. However, these signals are insensitive to gravitational waves, but merely communicate intra-spacecraft information with high SNR (Estabrook et al.; 2000). It is possible to combine the various signals such that the laser frequency noise is

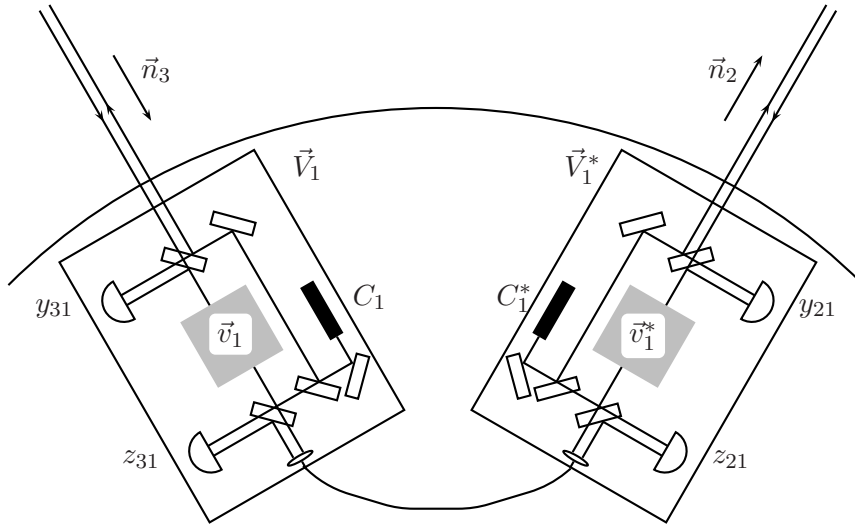


Figure 9.2: The picture shows a sketch of LISA spacecraft 1. The optical benches move with random velocities \vec{V}_1, \vec{V}_1^* and the test masses with velocities \vec{v}_1, \vec{v}_1^* giving rise to noise contributions to the Doppler signals. The laser frequency noise is denoted by C_1, C_1^* . Data combinations exist which cancel the laser frequency noise and the Doppler noise due to the optical bench motion.

removed from the data (Tinto and Armstrong; 1999). A data combination is composed of Doppler signals $y_{ij} \equiv y_{ij}(t), z_{ij} \equiv z_{ij}(t)$ at time t and signals delayed by light travel times, e.g. $y_{23,2} \equiv y_{23}(t - L_2/c), z_{23,13} \equiv z_{23}(t - L_1/c - L_3/c), \dots$ where we adopt the short notation introduced by (Armstrong et al.; 1999). Delaying the time series by light travel times requires knowledge of the arm lengths (Estabrook et al.; 2000). Complete expressions for the fields which are measured by the photo detectors can be derived from Figure 9.2 which shows the (simplified) optical build-up of spacecraft 1. It records four

Doppler signals

$$y_{21} = C_{3,2} - \frac{1}{c} \left(\vec{n}_2 \cdot \vec{V}_{3,2} - 2\vec{n}_2 \cdot \vec{v}_1^* + \vec{n}_2 \cdot \vec{V}_1^* \right) - C_1^* + y_{21}^{\text{shot}} + y_{21}^{\text{gw}} \quad (9.1)$$

$$y_{31} = C_{2,3}^* + \frac{1}{c} \left(\vec{n}_3 \cdot \vec{V}_{2,3}^* - 2\vec{n}_3 \cdot \vec{v}_1 + \vec{n}_3 \cdot \vec{V}_1 \right) - C_1 + y_{31}^{\text{shot}} + y_{31}^{\text{gw}} \quad (9.2)$$

$$z_{21} = C_1 + \frac{2}{c} \vec{n}_3 \cdot (\vec{v}_1 - \vec{V}_1) - C_1^* \quad (9.3)$$

$$z_{31} = C_1^* - \frac{2}{c} \vec{n}_2 \cdot (\vec{v}_1^* - \vec{V}_1^*) - C_1 \quad (9.4)$$

The intra spacecraft links z_{ij} are devoid of Doppler signals from gravitational waves and the shot noise is supposed to be insignificant, since the light is transmitted from the one to the other bench with much larger power than the signal bearing Doppler links between the spacecrafts. In the following subsections, we present two data combinations devoid of laser frequency noise C_i, C_i^* and optical bench noise \vec{V}_i, \vec{V}_i^* and calculate for each case the transfer functions for the test mass noise and the laser shot noise.

9.1.1 Unequal Arm Length Interferometric Combination

At first, we introduce the nominal configuration of LISA, the unequal-arm length Michelson interferometer. The laser frequency noise and the optical bench noise cancels. This mode is also known as the X -mode ([Tinto et al.; 2002a](#))

$$\begin{aligned} X &\equiv y_{32,322} - y_{23,233} + y_{31,22} - y_{21,33} + y_{23,2} - y_{32,3} + y_{21} - y_{31} \\ &\quad + \frac{1}{2}(-z_{21,2233} + z_{21,33} + z_{21,22} - z_{21}) \\ &\quad + \frac{1}{2}(z_{31,2233} - z_{31,33} - z_{31,22} + z_{31}) \end{aligned} \quad (9.5)$$

Exemplarily, we outline the calculation which leads to the noise spectral density of X under the assumption that all three arms have the same length L . Furthermore, the test mass noise spectral densities $S(\vec{v}_i), S(\vec{v}_i^*)$ are identical for all test masses as well as the shot noise spectral densities $S(y_{ij}^{\text{shot}})$ of each power measurement of light coming from a neighboring spacecraft. The first step is to apply a Fourier transformation to Eq. (9.5)

$$\begin{aligned} \tilde{X} &= e^{i\Omega L/c} \left(e^{2i\Omega L/c-1} - 1 \right) (\tilde{y}_{32} - \tilde{y}_{23}) + \left(e^{2i\Omega L/c-1} - 1 \right) (\tilde{y}_{31} - \tilde{y}_{21}) \\ &\quad + \frac{1}{2} \left(2e^{2i\Omega L/c-1} - e^{4i\Omega L/c-1} - 1 \right) (\tilde{z}_{21} - \tilde{z}_{31}) \end{aligned} \quad (9.6)$$

The shot noise which appears in each of the y_{ij} is uncorrelated. Therefore, we can readily write down the shot noise spectral density for the X -mode by summing up the absolute squares of the shot noise amplitudes

$$S_{\text{shot}}^X(\Omega) = 16 \sin^2(\Omega L/c) S_{\text{shot}}(\Omega) \quad (9.7)$$

where $S_{\text{shot}}(\Omega)$ denotes the common shot noise $S(y_{ij}^{\text{shot}})$. In order to calculate the test mass noise we have to bear in mind that the test mass noise of \tilde{z}_{21} and \tilde{y}_{31} and of \tilde{z}_{31} and \tilde{z}_{21}

is correlated. More specifically, the noise is identical with opposite sign. Subtracting the coefficients in front of the respective amplitudes and subsequently calculating the absolute square, one obtains

$$S_{\text{tm}}^{\text{X}}(\Omega) = [8 \sin^2(2\Omega L/c) + 32 \sin^2(\Omega L/c)] S_{\text{tm}}(\Omega) \quad (9.8)$$

Besides the X -mode, one also defines a Y or Z mode which are obtained from Eq. (9.5) by cyclic permutation of the indices.

The Doppler noise can be transformed into phase noise or strain noise by inserting the corresponding spectral densities for $S_{\text{tm}}(\Omega)$, $S_{\text{shot}}(\Omega)$. The transfer functions which relate these quantities with $S_{\text{tm}}^{\text{X}}(\Omega)$, $S_{\text{shot}}^{\text{X}}(\Omega)$ are the same in each case. The respective transformations are discussed in [subsection 9.1.3](#).

9.1.2 Fully Symmetric Sagnac Mode

In addition to the nominal X -mode configuration of LISA, we present the fully symmetric Sagnac mode. The reason is that the Sagnac mode is less sensitive to gravitational waves at low frequencies than the Michelson combination (see [section 9.2](#)). Thereby, it may be used to estimate the low-frequency instrumental noise by comparing the outputs of the X - and Sagnac modes ([Tinto et al.; 2000](#)). Consequently, one achieves higher sensitivities with respect to gravitational waves at low frequencies ([Hogan and Bender; 2001](#)). The Sagnac mode corresponds to the data combination

$$\begin{aligned} \zeta \equiv & y_{32,2} - y_{23,3} + y_{13,3} - y_{31,1} + y_{21,1} - y_{12,2} \\ & + \frac{1}{2}(-z_{13,21} + z_{23,12} - z_{21,23} + z_{31,23} - z_{32,13} + z_{12,13}) \\ & + \frac{1}{2}(-z_{32,2} + z_{12,2} - z_{13,3} + z_{23,3} - z_{21,1} + z_{31,1}) \end{aligned} \quad (9.9)$$

Repeating the calculation outlined in [subsection 9.1.1](#), we find the equal-arm shot noise spectral density of the ζ -mode

$$S_{\text{shot}}^{\zeta}(\Omega) = 6S_{\text{shot}}(\Omega) \quad (9.10)$$

and its test mass noise spectral density

$$S_{\text{tm}}^{\zeta}(\Omega) = 24 \sin^2(\Omega L/(2c)) S_{\text{tm}}(\Omega) \quad (9.11)$$

Three additional laser frequency noise free Sagnac configurations α, β, γ can be found ([Tinto and Armstrong; 1999](#)). In the following, Sagnac mode is used synonymously to fully symmetric Sagnac mode.

9.1.3 Noise Curves

The total instrumental noise of LISA or technically kindred space missions (e.g. LISA's potential follow-up mission BBO) is composed of test mass noise and shot noise. As mentioned in the previous subsections, all other noise sources cancel identically even for

unequal arm lengths if the Doppler signals are combined appropriately. In order to calculate the instrumental noise spectral density of the X -mode or ζ -mode, we need the spectral densities $S_{\text{tm}}(\Omega)$ and $S_{\text{shot}}(\Omega)$ derived from the noise amplitudes of $\vec{n}_i \cdot \vec{v}_j$, $\vec{n}_i \cdot \vec{v}_j^*$ and y_{ij}^{shot} . A detailed calculation of these spectral densities can be found in (Larson et al.; 2000). However, the authors of that publication adhere to slightly different conventions than we do in here and they do not work with noise transfer functions of them from Eq. (9.7) and Eq. (9.8). We base our calculations on parameter values given in (LISA study teams; 2000) which are specified in Table 9.1. In gravitational wave physics, noise spectral densities are

	Symbol	Value
Transmitted light power	P_t	1 W
Received light power	P_r	$6.5 \cdot 10^{-11}$ W
Diameter of transmitter optics	D	0.3 m
Efficiency of transmitter optics	ϵ	0.3
Arm length	L	$5 \cdot 10^9$ m
Frequency of laser	ω_0	$1.77 \cdot 10^{15}$ rad/s
Acceleration noise	S_{acc}	$9 \cdot 10^{-30}$ m ² /s ⁴ /Hz

Table 9.1: LISA parameters.

evaluated as phase noise S^ϕ , strain noise S^h or Doppler noise S^y . All these quantities are related by

$$S^\phi = \left(\frac{\omega_0}{\Omega}\right)^2 \cdot S^y = \left(\frac{\omega_0 L}{c}\right)^2 \cdot S^h \quad (9.12)$$

The shot noise is directly expressible as phase noise which is flat (i.e. frequency independent) and inversely proportional to the received light power P_r

$$S_{\text{shot}}^\phi = \frac{\hbar\omega_0}{P_r} \quad (9.13)$$

The received power is governed by the product of the directional gain of the transmitter optics, a power propagation over a distance L and the effective cross sectional area of the receiving optics (Larson et al.; 2000)

$$P_r = \epsilon_{\text{tot}} \cdot P \cdot \frac{\omega_0^2 D^2}{4c^2} \cdot \frac{1}{4\pi L^2} \cdot \pi \left(\frac{D}{2}\right)^2 \quad (9.14)$$

The optical train is characterized by an overall optical efficiency ϵ_{tot} and D denotes the diameter of the (receiving and emitting) antennae. The test mass noise is proportional to

the acceleration noise of a test mass. The acceleration noise is assumed to be flat over the relevant range of frequencies. Expressed as Doppler noise, one obtains

$$S_{\text{tm}}^y(\Omega) = \left(\frac{2\Omega}{c}\right)^2 \cdot S_x(\Omega) = \left(\frac{2}{\Omega c}\right)^2 \cdot S_{\text{acc}} \quad (9.15)$$

Note that the factor 2 which appears in the last equation is already included in the fundamental definition of the Doppler signal Eq. (9.1) - Eq. (9.4). Therefore, it has to be omitted when inserting S_{tm}^y into Eq. (9.8) or Eq. (9.11). The total instrumental noise

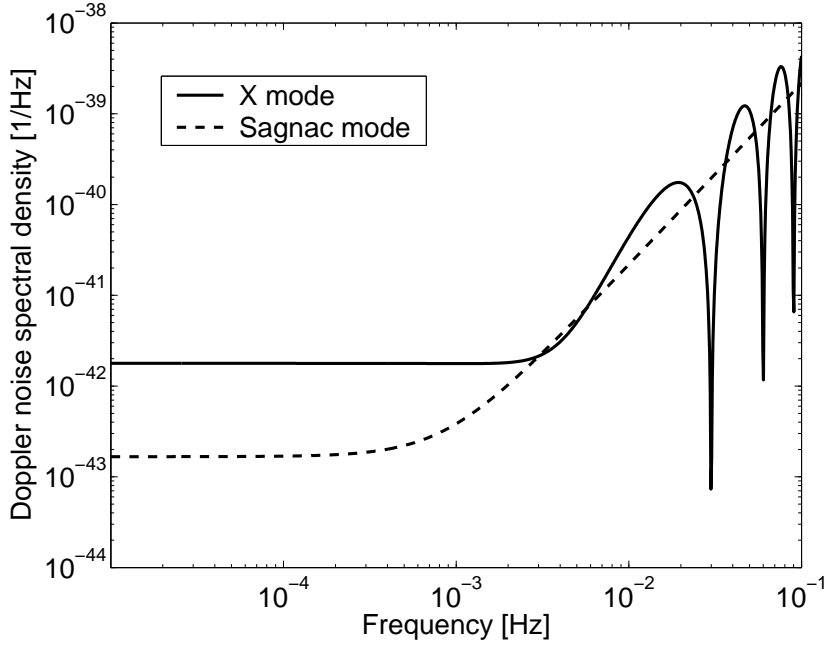


Figure 9.3: The plot shows the instrumental Doppler noise spectral densities for the X -mode and the fully symmetric Sagnac mode. The notches which appear at higher frequencies go down to zero. The low-frequency regime is dominated by test-mass noise, the high-frequency regime by shot noise.

spectral densities $S_{\text{inst}}^y = S_{\text{tm}}^{\{X,\zeta\}} + S_{\text{shot}}^{\{X,\zeta\}}$ of the X -mode and ζ -mode Doppler variables are displayed in Figure 9.3. The shot noise S_{shot}^y is calculated using Eq. (9.13) together with Eq. (9.12). At low frequencies, the Sagnac noise spectral density is smaller by a factor $32/3$ than the Michelson noise spectral density.

9.2 Doppler Signals from Gravitational Waves

In this section, we derive the one way Doppler signals for each link of a three spacecraft detector. Calculating the response of a detector to gravitational waves requires the introduction of two orthonormal coordinate systems. The first one $\{\vec{e}_i, \vec{e}_j, \vec{e}_k\}$ is assigned to the gravitational wave and the second one $\{\vec{e}_u, \vec{e}_v, \vec{e}_w\}$ to the detector (Wahlquist; 1987). We need to express the basis of the gravitational wave frame in terms of the basis of the

detector frame. The angular coordinates of a source on the celestial sphere are the right ascension ϕ and the declination θ . The latter one measures the angle between the detector plane and the direction to the source. The axes of the gravitational wave frame are oriented as follows (see [Figure 9.4](#)). The direction of propagation of the wave coincides with the direction of $-\vec{e}_k$ and the basis vectors \vec{e}_i, \vec{e}_j point along positive going ϕ, θ . The detec-

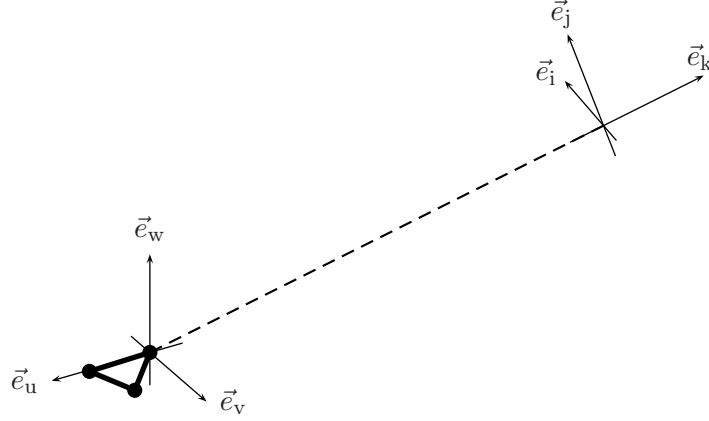


Figure 9.4: The detector plane is spanned by the unit vectors \vec{e}_u, \vec{e}_v . The gravitational-wave source lies in the direction of \vec{e}_k and the transversal coordinates of the wave's propagation frame point along \vec{e}_i, \vec{e}_j .

tor plane is spanned by \vec{e}_u, \vec{e}_v . Taking everything together, the basis for the propagation frame reads

$$\begin{aligned}\vec{e}_i &= -\cos(\phi)\sin(\theta)\vec{e}_u - \sin(\phi)\sin(\theta)\vec{e}_v + \cos(\theta)\vec{e}_w \\ \vec{e}_j &= -\sin(\phi)\vec{e}_u + \cos(\phi)\vec{e}_v \\ \vec{e}_k &= -\cos(\phi)\cos(\theta)\vec{e}_u - \sin(\phi)\cos(\theta)\vec{e}_v - \sin(\theta)\vec{e}_w\end{aligned}\tag{9.16}$$

As shown in [Figure 9.5](#), we lay the origin of the detector frame equidistant to each spacecraft which entails that at time t the metric perturbation is $\mathbf{h}(t)$ at the origin. The vectors $\{\vec{e}_1, \vec{e}_2, \vec{e}_3\}$ point from the origin to the respective spacecraft. For this choice of coordinates, Eq. (2.66) leads to the following gravitational wave Doppler signals ([Armstrong et al.; 1999](#))

$$\begin{aligned}y_{31}^{\text{gw}}(t) &= \left[1 + \frac{l}{L_3}(\mu_1 - \mu_2)\right] \left\{ \Psi_3\left(t - \frac{\mu_2 l + L_3}{c}\right) - \Psi_3\left(t - \frac{\mu_1 l}{c}\right) \right\} \\ y_{21}^{\text{gw}}(t) &= \left[1 + \frac{l}{L_2}(\mu_3 - \mu_1)\right] \left\{ \Psi_2\left(t - \frac{\mu_3 l + L_2}{c}\right) - \Psi_2\left(t - \frac{\mu_1 l}{c}\right) \right\}\end{aligned}\tag{9.17}$$

with $\mu_{\{1;2;3\}} = \vec{e}_k \cdot \vec{e}_{\{1;2;3\}}$ and l being the distance between the origin and a spacecraft. Again, the other four Doppler series are obtained from cyclic permutation of the indices. The coordinate independent projection of the metric perturbation onto the Doppler signal

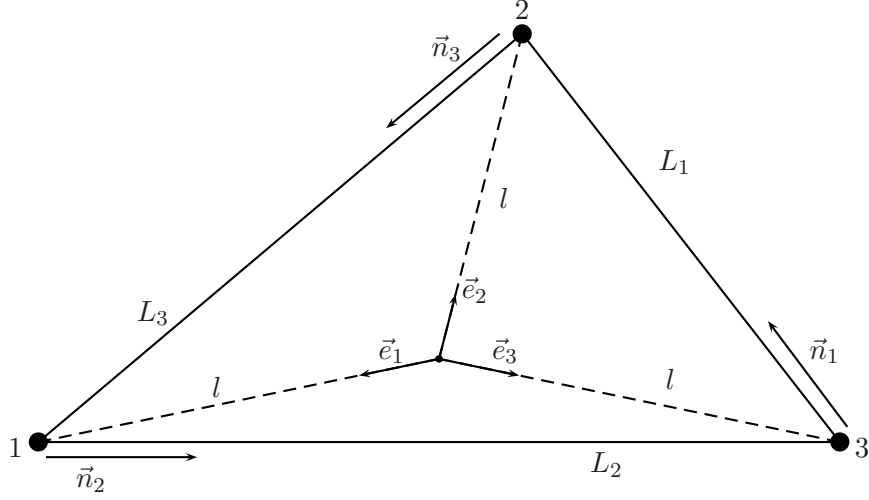


Figure 9.5: The origin of the detector frame is equidistant to each spacecraft. The unit vectors $\vec{e}_{\{1,2,3\}}$ point from the origin towards the spacecraft. The direction of each inter-spacecraft link is describes by the unit vectors \vec{n}_i .

assumes the form (Wahlquist; 1987)

$$\Psi_i(t) = \frac{1}{2} \frac{\vec{n}_i \cdot \mathbf{h}(t) \cdot \vec{n}_i}{1 - (\vec{e}_k \cdot \vec{n}_i)^2}, \quad i = 1, 2, 3 \quad (9.18)$$

The unit vectors \vec{n}_i are linear combinations of the two basis vectors \vec{e}_u, \vec{e}_v

$$\vec{n}_i = \cos(\alpha_i) \vec{e}_u + \sin(\alpha_i) \vec{e}_v \quad (9.19)$$

and the scalar products $\{\vec{e}_i, \vec{e}_j, \vec{e}_k\} \cdot \vec{n}_i$ can be written

$$\begin{aligned} \vec{n} \cdot \vec{e}_i &= -\sin(\theta) \cos(\alpha - \phi) \\ \vec{n} \cdot \vec{e}_j &= \sin(\alpha - \phi) \\ \vec{n} \cdot \vec{e}_k &= -\cos(\theta) \cos(\alpha - \phi) \end{aligned} \quad (9.20)$$

Here, we omitted the indices on \vec{n}_i, α_i in order to avoid confusion with the indexing of the basis vectors. The metric perturbation in TT-gauge is decomposed into its \times - and $+$ -polarisation with polarisation tensors $\mathbf{e}_+ \equiv \vec{e}_i \otimes \vec{e}_i - \vec{e}_j \otimes \vec{e}_j$ and $\mathbf{e}_\times \equiv \vec{e}_i \otimes \vec{e}_j + \vec{e}_j \otimes \vec{e}_i$

$$\mathbf{h}(t) \equiv h_+(t) \mathbf{e}_+ + h_\times(t) \mathbf{e}_\times \quad (9.21)$$

and finally we can evaluate the projections $\vec{n}_i \cdot \mathbf{h}(t) \cdot \vec{n}_i$ of the metric perturbation

$$\begin{aligned} \vec{n}_i \cdot \mathbf{e}_+ \cdot \vec{n}_i &= \sin^2(\theta) \cos^2(\alpha_i - \phi) - \sin^2(\alpha_i - \phi) \\ \vec{n}_i \cdot \mathbf{e}_\times \cdot \vec{n}_i &= -2 \sin(\alpha_i - \phi) \cos(\alpha_i - \phi) \sin(\theta) \end{aligned} \quad (9.22)$$

In section 9.3, we are going to evaluate our results for the equal-arm X -mode and plot its corresponding sensitivity curves.

9.3 Sensitivity Plots

The response of a detector is usually evaluated as a sky-averaged expression. Analytically, one had to integrate the response over all source positions θ , ϕ and wave polarizations. One finds different approaches in the literature to evaluate the average. (Larson et al.; 2000) developed a formalism which facilitates an explicit treatment of the polarization angles and sky directions and which allows to reduce the dimensionality of the integration, thereby accelerating the analytic calculation considerably. However, in the formalism which was expounded in the last sections, explicit parameter dependencies are difficult to expose and so it was proposed, e.g. in (Armstrong et al.; 1999), to carry out a Monte Carlo averaging of the response over arbitrary, elliptically polarized waves

$$h_+(t) = H \sin \Gamma \sin(\omega t + \Phi), \quad h_\times(t) = H \cos \Gamma \sin(\omega t) \quad (9.23)$$

The ellipticity and phase of the waves are characterized by two angles (Γ, Φ) corresponding to the coordinates on a Poincaré sphere for spin-2 waves. The strain sensitivity $h_{\text{sens}}(\Omega)$ of LISA's X combination sky-averaged over $N = 1000$ sources is displayed in Figure 9.3. It is

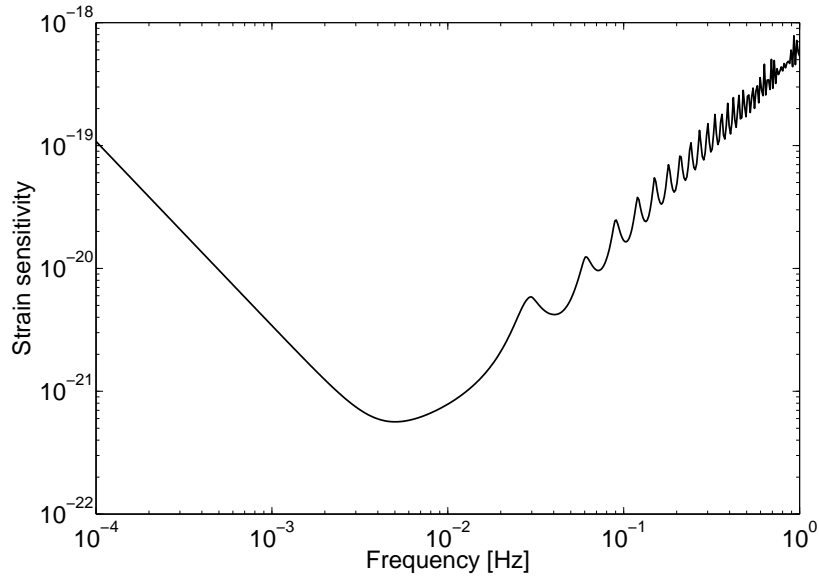


Figure 9.6: The plot shows the strain sensitivity of the LISA detector averaged over 1000 sources with arbitrary directions θ , ϕ and elliptical polarizations Γ , Φ .

determined by the ratio of the instrumental noise and the signal transfer function $|\tilde{X}|_{H=1}$. Furthermore, we adopt the convention to represent the interferometer's sensitivity in its integrated (multiplying by f) and single-sided (multiplying by 2) form. Since the transfer function has been calculated for the Doppler signal (Eq. (9.6)), one has to divide the Doppler instrumental noise spectral density

$$h_{\text{sens}}(\Omega, \theta, \phi, \Gamma, \Phi) \equiv \frac{\sqrt{2f S_{\text{inst}}^y(\Omega)}}{|\tilde{X}(\Omega, \theta, \phi, \Gamma, \Phi)|_{H=1}} \quad (9.24)$$

The integrated strain sensitivity is a dimensionless quantity. Its Monte Carlo sky-average is calculated according to

$$h_{\text{sens}}^{\text{s.a.}}(\Omega) \equiv \frac{1}{N} \sum_{i=1}^N h_{\text{sens}}(\Omega, \theta_i, \phi_i, \Gamma_i, \Phi_i) \quad (9.25)$$

The sensitivity curve marks the borderline between detectable and undetectable signals provided that data analysis manages with $\text{SNR} = 1$. Some data analysts prefer to impose a $\text{SNR} = 5$ criterion for manageable analysis. In that case, one simply has to multiply the sensitivity curve by that number.

Although the X Michelson mode constitutes the nominal operation mode of LISA, it is not the optimal combination with respect to its sensitivity. In (Prince et al.; 2002), the authors derive the optimum essentially showing that LISA behaves like two independent Michelson interferometers at low frequencies and roughly like three interferometers at high frequencies. They extract the independent channels and subsequently combine their output to form the most sensitive combination.

CHAPTER 10

Codes and Computations

10.1 MATLAB

10.1.1 The Michelson interferometer

The Michelson interferometer is the most simple interferometric device which can be simulated as gravitational-wave detector. Most interferometer simulations in the last chapters have been carried out with MATLAB. The following code calculates the transfer functions for the dark port vacuum field and the signal quadratures towards the output port (i.e. the photo detector). In the end, the power spectral density matrix (nd) of the dark port vacuum is divided by the power spectral density matrix (sd) of the signal. The ratio corresponds to the sensitivity of the detector provided that the signal is normalized appropriately.

```
1  %The Michelson interferometer
2
3  clear;
4
5  set(0,'DefaultAxesFontSize',18);
6  set(0,'DefaultTextFontSize',18);
7  set(gcf,'DefaultLineMarkerSize',18);
8
9  %Speed of light
10 c=299792458;
11 %Planck constant
12 hbar=1.054e-34;
13 %Mass of mirror
14 m=5.6;
15 %Arm length
16 L=1200;
17 %Power of the light inside arm cavities
18 Parm=5e3;
19 %Frequency of laser
20 o=1.77e15;
21 %Homodyning angle
```

```

22 zeta = pi/3;
23
24 %Initialize the data vector
25 data=[];
26 %Modulation-frequencies 10-1000 Hz
27 range=logspace(1,3,1000);
28
29 for x=range
30
31     %Relative phase shift of the sidebands with respect to
32     %the carrier along the distance L between the beam
33     %splitter and the end mirror.
34     f=(2*pi*x)*(L/c);
35
36     %Standard quantum limit.
37     h=sqrt(20*hbar/(m*L^2*(2*pi*x)^2));
38
39     %Optomechanical coupling (with reduced mass m/5 due to
40     %folded arms.
41     K=4*Parm*o/(m/5)/c^2/(2*pi*x)^2;
42
43     %Round trip transfer matrix of a field through an arm.
44     %Corresponds to the transfer matrix of fields
45     %reflected from the beam splitter if no further optics
46     %are placed in the dark port.
47     R1=exp(2*i*f)*[1 0; -K 1];
48
49     %sqrt(2)*(signal transfer function of one arm).
50     %The sqrt(2) originates from the constructive
51     %interference of the two signal fields towards the
52     %dark port.
53     R2=exp(i*f)*sqrt(2*K)/h*[0; 1];
54
55     %Spectral density matrices (FT of covariance matrices).
56     NM=1/2*(R1*transpose(conj(R1))+conj(R1)*transpose(R1));
57     SM=1/2*(R2*transpose(conj(R2))+conj(R2)*transpose(R2));
58
59
60     nd = [cos(zeta) sin(zeta)]*NM*[cos(zeta); sin(zeta)];
61     sd = [cos(zeta) sin(zeta)]*SM*[cos(zeta); sin(zeta)];
62     noisetosignal = sqrt(nd/sd);
63
64     %Construction of the data vector.
65     data=[data; [h noisetosignal]];
66
67 end
68 loglog(range,data(:,1),range,data(:,2))
69 xlabel('Frequency [Hz]')
70 ylabel('Strain Noise Spectrum [1/\surd Hz]')
71 legend('h_{sql}','\pi/3-quadrature')

```

10.1.2 The Signal-Recycled Interferometer

A modular extension of the simple Michelson interferometer simulation code furnishes the simulation of the signal-recycled interferometer. The code picks up the result for the transfer matrices of the simple Michelson and transforms them in order to obtain the overall transfer matrices of the build-up with SR mirror. The results are evaluated just like in the former case.

```

1  %Dual-recycled GEO600 interferometer
2
3  clear;
4
5  set(0,'DefaultAxesFontSize',18);
6  set(0,'DefaultTextFontSize',18);
7  set(gcf,'DefaultLineMarkerSize',18);
8
9  %Speed of light
10 c=299792458;
11 %Planck constant
12 hbar=1.054e-34;
13 %Mass of mirrors
14 m=5.6;
15 %Length of arm
16 L=1200;
17 %Power of light before entering the PR cavity
18 Pin=12;
19 %Frequency of light
20 o=1.77e15;
21 %Amplitude reflectivity of PRM
22 rPR=0.999;
23 %Amplitude reflectivity of SRM
24 rSR=0.999;
25 %Detuning of the SR cavity
26 phi=0.0035;
27 %Homodyne angle
28 zeta = pi/2;
29
30 %Range of frequencies (powers of 10)
31 min=1;
32 max=3;
33
34 Ein=[1 0; 0 1];
35 %Power inside arms valid for small transmissivities.
36 P=2*Pin/(1-rPR^2);
37 %Quadrature rotation by detuned cavity
38 PR0=[cos(phi) -sin(phi); sin(phi) cos(phi)];
39
40 data=[];
41
42 %Modulation frequencies 10-1000 Hz
43 x_range=logspace(min,max,1000);
44
45 for x=x_range
46
47     %Relative phase shift of the sidebands with respect to

```

```

48     %the carrier along the distance L between the beam
49     %splitter and the end mirror.
50     f=(2*pi*x)*(L/c);
51
52     %Standard quantum limit
53     h=sqrt(20*hbar/m/L^2/(2*pi*x)^2);
54
55     %Optomechanical coupling
56     K=4*P*o/(m/5)/c^2/(2*pi*x)^2;
57
58     %Round-trip transfer matrix of a field through an arm.
59     %Corresponds to the transfer matrix of fields
60     %reflected from the beam splitter.
61     ARM=exp(2*i*f)*[1 0; -K 1];
62
63     %sqrt(2)*(signal transfer function of one arm).
64     %The sqrt(2) originates from the constructive
65     %interference of the two signal fields towards the
66     %dark port.
67     S1=exp(i*f)*sqrt(2*K)/h*[0; 1];
68
69     %Transfer of the fields from BS to SRM
70     R1SR=PRO*ARM*PRO;
71     R2SR=PRO*S1;
72
73     %Transfer through SRM
74     IO=inv(Ein-rSR*R1SR)*(R1SR-Ein*rSR);
75     S=inv(Ein-rSR*R1SR)*sqrt(1-rSR^2)*R2SR;
76
77     %Spectral density matrices (FT of covariance matrices).
78     NM=1/2*(IO*transpose(conj(IO))+conj(IO)*transpose(IO));
79     SM=1/2*(S*transpose(conj(S))+conj(S)*transpose(S));
80
81     nd = [cos(zeta) sin(zeta)]*NM*[cos(zeta); sin(zeta)];
82     sd = [cos(zeta) sin(zeta)]*SM*[cos(zeta); sin(zeta)];
83     noisetosignal = sqrt(nd/sd);
84
85     %Construction of data vector
86     data=[data; [h noisetosignal]];
87
88 end
89
90 loglog (x_range,data(:,1),'b',x_range,data(:,2),'r')
91 xlabel('Frequenz [Hz]');
92 ylabel('Strain Noise Spectrum [1/\surdHz]');
93 save('\store\GEOSR.dat','data','-ascii')

```

10.2 Mathematica

10.2.1 Signal Transfer Functions

A gravitational wave modulates the distance between mirrors of an interferometric detector. In theory, this can be simulated in two different ways. Either, the light which reflects

off a mirror is phase modulated due to a motion of the mirror (LL system), or the light is phase modulated on its way from one to the other mirror (TT system). The latter method gives valid results for all GW frequencies whereas the former method is valid for small GW frequencies only (see [section 2.3](#)). The following Mathematica code calculates the signal transfer functions of a three mirror cavity using both methods and compares the two results. We artificially impose the long wavelength condition on the TT calculation in order to be able to compare all frequencies and to ascertain whether the interferometer simulation really does not distinguish TT from LL.

```

1      mirror A                mirror B                mirror C
2      - +                    + -                    - +
3      AOL | AIR                BOL | BIR                COL |
4  <-----|<-----          <-----|<-----          <-----|
5      |                        |                        |
6      | AOR                    BIL | BOR                CIL |
7      |----->              ----->|----->          ----->|
8      |                        |                        |
9      rA,tA                    rB,tB                    rC,tC
10
11  Off[General::spell,General::spell1]
12  <<Graphics'Graphics'
13
14  w0 = 1.77*10^15;
15  Amp0 = Sqrt[62.5];
16  c = 299792458;
17  L = 2000;
18  rA = Sqrt[0.995];
19  tA = Sqrt[1 - rA^2];
20  rB = Sqrt[0.99984];
21  tB = Sqrt[1 - rB^2];
22  rC = Sqrt[0.99995];
23  tC = Sqrt[1 - rC^2];
24  p1 = 0.0062875;
25  p2 = 0.0062875;
26
27  Rot[a_] := {{Cos[a], -Sin[a]}, {Sin[a], Cos[a]}};
28
29  (*-----*)
30  (*PART 1: Calculation of the carrier amplitudes*)
31  (*-----*)
32
33  (*The complex amplitudes of the carrier field are needed since signal
    is generated at various places inside the multiple mirror cavity
    with different amplitudes and phases depending on the amplitude
    and phase of the carrier field. The carrier amplitudes could
    equally well be calculated in the one-photon formalism.*)
34
35  (*Defining symbols for carrier quadrature amplitude vectors.*)
36
37  cAIL={{Amp0},{0}}; cAOL={{cAOL1},{cAOL2}};
38  cAIR={{cAIR1},{cAIR2}}; cAOR={{cAOR1},{cAOR2}};
39  cBIL={{cBIL1},{cBIL2}}; cBOL={{cBOL1},{cBOL2}};
40  cBIR={{cBIR1},{cBIR2}}; cBOR={{cBOR1},{cBOR2}};
41  cCIL={{cCIL1},{cCIL2}}; cCOL={{cCOL1},{cCOL2}};

```

```

42
43 carrierBGK =
44     Simplify[Solve[{-rA cAIL + tA cAIR - cAOL == 0,
45                 rA cAIR + tA cAIL - cAOR == 0,
46                 Rot[p1] . cAOR - cBIL == 0,
47                 Rot[p1] . cBOL - cAIR == 0,
48                 rB cBIL + tB cBIR - cBOL == 0,
49                 -rB cBIR + tB cBIL - cBOR == 0,
50                 Rot[p2] . cBOR - cCIL == 0,
51                 Rot[p2] . cCOL - cBIR == 0,
52                 -rC cCIL - cCOL == 0}], {cAOL1, cAOL2, cAIR1,
53                 cAIR2, cAOR1, cAOR2, cBOL1, cBOL2, cBIL1,
54                 cBIL2, cBOR1, cBOR2, cBIR1, cBIR2, cCOL1,
55                 cCOL2, cCIL1, cCIL2}], {rA^2 + tA^2 == 1,
56                 rB^2 + tB^2 == 1, rC^2 + tC^2 == 1}];
57
58 (*Assignment of the solution to quadrature variables.*)
59
60 carrAIR=cAIR/.carrierBGK[[1]];
61 carrBIL=cBIL/.carrierBGK[[1]];
62 carrBIR=cBIR/.carrierBGK[[1]];
63 carrCIL=cCIL/.carrierBGK[[1]];
64
65 (*Calculation of carrier phases and amplitudes at all points of the
66     cavity where signal is generated in the simulation.*)
67
68 phAIR = ArcTan[carrAIR[[1]], carrAIR[[2]]][[1]];
69 phBIL = ArcTan[carrBIL[[1]], carrBIL[[2]]][[1]];
70 phBIR = ArcTan[carrBIR[[1]], carrBIR[[2]]][[1]];
71 phCIL = ArcTan[carrCIL[[1]], carrCIL[[2]]][[1]];
72
73 powAIR = (carrAIR[[1]]^2 + carrAIR[[2]]^2)[[1]];
74 powBIL = (carrBIL[[1]]^2 + carrBIL[[2]]^2)[[1]];
75 powBIR = (carrBIR[[1]]^2 + carrBIR[[2]]^2)[[1]];
76 powCIL = (carrCIL[[1]]^2 + carrCIL[[2]]^2)[[1]];
77
78 (*-----*)
79 (*PART 2: Calculation of signal output in TT gauge*)
80 (*-----*)
81
82 (*Defining symbols for the signal quadrature amplitude vectors.*)
83
84 quAOL={{quAOL1},{quAOL2}};
85 quAIR={{quAIR1},{quAIR2}};
86 quAOR={{quAOR1},{quAOR2}};
87 quBIL={{quBIL1},{quBIL2}};
88 quBOL={{quBOL1},{quBOL2}};
89 quBIR={{quBIR1},{quBIR2}};
90 quBOR={{quBOR1},{quBOR2}};
91 quCIL={{quCIL1},{quCIL2}};
92 quCOL={{quCOL1},{quCOL2}};
93 sig={{0},{1}};
94
95 coup={tA quAIR-quAOL,rA quAIR-quAOR==0,
96       rB quBIL+tB quBIR-quBOL,-rB quBIR+tB quBIL-quBOR==0,

```

```

96     -rC quCIL-quCOL==0};
97 prop1={ Exp[ I W L/c] Rot[p1].quAOR+powBIL Exp[ I W L/c] Rot[phBIL].
      sig- quBIL==0,
98     Exp[ I W L/c] Rot[p1].quBOL+powAIR Exp[ I W L/c] Rot[phAIR].
      sig- quAIR==0};
99 prop2={ Exp[ I W L/c] Rot[p2].quBOR+powCIL Exp[ I W L/c] Rot[phCIL].
      sig- quCIL==0,
100     Exp[ I W L/c] Rot[p2].quCOL+powBIR Exp[ I W L/c] Rot[phBIR].
      sig- quBIR==0};
101 eqs=Join[coup,prop1,prop2];
102
103 solnBGK=Solve[
104     eqs,{quAOL1,quAOL2,quAIR1,quAIR2,quAOR1,quAOR2,quBIL1,quBIL2,
105     quBOL1,quBOL2,quBIR1,quBIR2,quBOR1,quBOR2,quCIL1,quCIL2,quCOL1
      ,
106     quCOL2}];
107
108 (*TT amplitude quadrature of the signal in the output port.*)
109
110 TTquadAOL=Transpose[quAOL/.solnBGK[[1]][[1]]/.W-> 2 Pi f;
111
112 (*The output quadrature is normalized in order to make the signal
      independent of the input power.*)
113
114 plotTT =
115     LogLogPlot[Evaluate[Abs[TTquadAOL[[1]]]/Amp0^2], {f, 10, 10000},
116     PlotPoints -> 500];
117
118 (*-----*)
119 (*PART 3: Calculation of signal output in LL frame*)
120 (*-----*)
121
122 coup={tA quAIR-quAOL,rA quAIR-quAOR==0,
123     rB quBIL+2 rB powBIL Rot[phBIL].sig+tB quBIR-quBOL==0,
124     -rB quBIR+2 rB powBIR Rot[phBIR].sig+tB quBIL-quBOR==0,
125     -rC quCIL-4 rC powCIL Rot[phCIL].sig-quCOL==0};
126 prop1={ Exp[ I W L/c] Rot[p1].quAOR- quBIL==0,
127     Exp[ I W L/c] Rot[p1].quBOL- quAIR==0};
128 prop2={ Exp[ I W L/c] Rot[p2].quBOR- quCIL==0,
129     Exp[ I W L/c] Rot[p2].quCOL- quBIR==0};
130 eqs=Join[coup,prop1,prop2];
131
132 solnBGK=Solve[
133     eqs,{quAOL1,quAOL2,quAIR1,quAIR2,quAOR1,quAOR2,quBIL1,quBIL2,
134     quBOL1,quBOL2,quBIR1,quBIR2,quBOR1,quBOR2,quCIL1,quCIL2,quCOL1
      ,
135     quCOL2}];
136
137 (*LL amplitude quadrature of the signal in the output port.*)
138
139 LLquadAOL=Transpose[quAOL/.solnBGK[[1]][[1]]/.W->2 Pi f;
140
141 (*The output quadrature is normalized in order to make the signal
      independent of the input power.*)
142

```

```

143 plotLL =
144     LogLogPlot[Evaluate[Abs[LLquadAOL[[1]]]/Amp0^2], {f, 10, 10000},
145     PlotPoints -> 500];
146
147 Show[{plotTT, plotLL}, Frame->True,
148     FrameLabel->{"Frequency [Hz]", "Signal"},
149     TextStyle->{FontFamily\[Rule]"Times", FontSize->12}]

```

10.2.2 Parametric Resonance

The following Mathematica code generates the two figures in [Appendix F](#). At first, it solves the Mathieu equation for two different initial conditions. These solutions govern the stability properties of the system (with arbitrary initial conditions). Finally, a contour plot is used to represent the stability landscape.

```

1  (*-----*)
2  (*Parametric Resonance*)
3  (*-----*)
4
5  Off[General::spell, General::spell1]
6
7  (*Two solutions A1,A2 with two different initial conditions. Both are
8     needed, in order to obtain information about the instable or
9     stable regime of the resonator.*)
10
11 xA1 = x[t] /. (DSolve[{x''[t] + g x'[t] + (2 Pi f)^2 (1 + h0 Cos[2
12     Pi F t]) x[t] == 0, x'[0] == 0, x[0] == 1}, x[t], t][[1, 1]]);
13 vA1 = D[xA1, t];
14 xA2 = x[t] /. (DSolve[{x''[t] + g x'[t] + (2 Pi f)^2 (1 + h0 Cos[2
15     Pi F t]) x[t] == 0, x'[0] == 1, x[0] == 0}, x[t], t][[1, 1]]);
16 vA2 = D[xA2, t];
17
18 (*Plot of a stable (plotSt) and an instable (plotIn) parametric
19     oscillation.*)
20
21 T=50;
22 paraSt={F->1, g->0, h0->0.08, f->0.52};
23 paraIn={F->1, g->0, h0->0.08, f->0.51};
24
25 plotSt=Plot[Evaluate[xA1/. paraSt], {t, 0, T}, Frame->True,
26     FrameLabel->{"Time", "Amplitude"}, TextStyle->{FontSize->10},
27     PlotPoints->500, PlotRange->{{0, T}, {-2, 2}}];
28
29 Export["\store\ResStable.eps", plotSt, "EPS"];
30
31 plotIn=Plot[Evaluate[xA1/. paraIn], {t, 0, T}, Frame->True,
32     FrameLabel->{"Time", "Amplitude"}, TextStyle->{FontSize->10},
33     PlotPoints->500, PlotRange->{{0, T}, {-7, 7}}];
34
35 Export["\store\ResInst.eps", plotIn, "EPS"];
36
37 (*Investigation of the instability regime for the undamped (g=0) and
38     damped (g=0.02) oscillator. The contour plot which shows the
39     stability landscape is evaluated in several steps. Each step

```


*focusses on one of the two evaluated orders of the parametric resonance and one value of g . Thereby, the algorithm is forced to elaborate exclusively on nontrivial sections of the plot (saving computation time). *)*

```

33
34 paraA={F->1,g->0};
35 paraB={F->1,g->0.02};
36
37 TrA = (xA1 + vA2) /. {t -> 1/F} /. paraA;
38 TrB = (xA1 + vA2) /. {t -> 1/F} /. paraB;
39
40 plot1=ContourPlot[Evaluate[Abs[TrA]-2],{f,0.4,0.65},{h0,0,0.8},
41   PlotPoints->100,
42   FrameLabel->{"Unperturbed frequency","Strain amplitude"},
43   TextStyle->{FontSize->10},Contours->{0},
44   AspectRatio->0.70,ContourShading->False];
45
46 plot2=ContourPlot[Evaluate[Abs[TrA]-2],{f,0.97,1.15},{h0,0,0.8},
47   PlotPoints->150,
48   FrameLabel->{"Unperturbed frequency","Strain amplitude"},
49   TextStyle->{FontSize->10},Contours->{0},
50   AspectRatio->0.70,ContourShading->False];
51
52 plot3=ContourPlot[Evaluate[Abs[TrB]-2],{f,0.4,0.65},{h0,0,0.8},
53   PlotPoints->40,
54   FrameLabel->{"Unperturbed frequency","Strain amplitude"},
55   TextStyle->{FontSize->10},Contours->{0},
56   AspectRatio->0.70,
57   ColorFunction->(If[#<0.0001,GrayLevel[1],GrayLevel[0.8]]&)];
58
59 plot4=ContourPlot[Evaluate[Abs[TrB]-2],{f,0.97,1.15},{h0,0,0.8},
60   PlotPoints->40,
61   FrameLabel->{"Unperturbed frequency","Strain amplitude"},
62   TextStyle->{FontSize->10},Contours->{0},
63   AspectRatio->0.70,
64   ColorFunction->(If[#<0.0001,GrayLevel[1],GrayLevel[0.8]]&)];
65
66 plotT=Show[{plot3,plot4,plot1,plot2},PlotRange
67   ->{{0,1.5},{-0.01,0.81}}]
68 Export["\store\ParaRes.eps",plotT,"EPS"];

```

APPENDIX A

The Bivariate Normal Distribution

We expose to some detail the basic properties of bivariate normal distributions due to their frequent appearance when considering linearized transformations on quantum vacuum noise. Consider two normal random variables X_1, X_2 with zero mean. Their bivariate distribution can be written

$$p(\vec{x}) = \frac{1}{2\pi\sigma_1\sigma_2\sqrt{1-\rho^2}} \cdot \exp\left[-\frac{1}{2}\vec{x}^T \cdot \Sigma^{-1} \cdot \vec{x}\right] \quad (\text{A.1})$$

where Σ^{-1} is the inverse of the covariance matrix between X_1 and X_2

$$\Sigma^{-1} = \frac{1}{\sigma_1^2\sigma_2^2(1-\rho^2)} \begin{pmatrix} \sigma_2^2 & -\rho\sigma_1\sigma_2 \\ -\rho\sigma_1\sigma_2 & \sigma_1^2 \end{pmatrix} \quad (\text{A.2})$$

given in terms of the variances $\text{var}(X_1) = \sigma_1^2$, $\text{var}(X_2) = \sigma_2^2$ and covariance $\text{cov}(X_1, X_2) = \rho\sigma_1\sigma_2$. We are particularly interested in the case, where the variances are equal. Then it is easy to show that the eigenvalues of the covariance matrix are given by

$$\sigma_{\pm}^2 = \sigma^2(1 \pm \rho) \quad (\text{A.3})$$

This means that there exists a linear transformation (a rotation) into a new coordinate system with quantities \vec{x}' and Σ'^{-1} which represent a probability distribution of two uncorrelated normal random variables X_+, X_- with variances σ_{\pm} . Normal distributions possess a simple and useful graphical representation which helps clarifying the analytic calculations. The expression $\vec{x}^T \cdot \Sigma^{-1} \cdot \vec{x} = 1$ determines an ellipse in the coordinate system x_1, x_2 . The left hand side appears in the exponent of Eq. (A.1). Therefore, the ellipse comprises all points \vec{x}_{ell} with $p(\vec{x}_{\text{ell}})/p(\vec{0}) = e^{-1/2} \approx 0.6$ and corresponds to a contour level of the bivariate probability distribution $p(\vec{x})$ (see [Figure A.1](#)). One feature of normal random variables is that if they are uncorrelated ($\rho = 0$), then they are also independent ($p(\vec{x}) = g(x_1) \cdot h(x_2)$). Statistical independence means, that if one measures a pair of

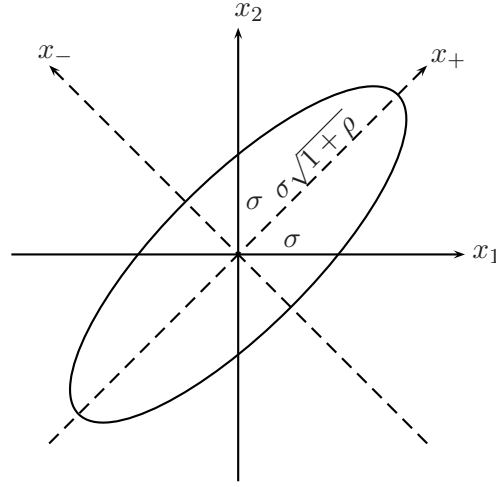


Figure A.1: The bivariate normal distribution. The eigenvalues of the covariance matrix determine the lengths of the semi axes of a noise ellipse. The area of the ellipse is $\mathcal{A} = \pi\sigma^2\sqrt{1-\rho^2}$.

independent variables simultaneously, then the outcome of the X_1 measurement does not allow you to infer anything about the outcome of the X_2 measurement.

At next, we calculate the *marginal* distribution $p_1(x_1)$ which tells you how likely the value x_1 is if you don't look on the value x_2 . The marginal distribution is defined as

$$\begin{aligned} p_1(x_1) &= \int dx_2 p(\vec{x}) \\ &= \frac{1}{\sqrt{2\pi\sigma_1^2}} \cdot \exp\left[-\frac{x_1^2}{2\sigma_1^2}\right] \end{aligned} \quad (\text{A.4})$$

The result should not be very surprising. It is perhaps noteworthy that the marginal distribution is independent of the correlation between the two variables. Exchanging the indices $1 \leftrightarrow 2$ provides you with $p_2(x_2)$. Finally, we write down the *conditional* distribution $p_{X_2|X_1=x_1}(x_2)$ that is the likelihood of the value x_2 under the condition that we have $X_1 = x_1$

$$\begin{aligned} p_{X_2|X_1=x_1}(x_2) &= \frac{p(\vec{x})}{p_1(x_1)} \\ &= \frac{1}{\sqrt{2\pi\sigma_2^2(1-\rho^2)}} \cdot \exp\left[-\frac{(x_2 - \rho\sigma_2/\sigma_1 \cdot x_1)^2}{2\sigma_2^2(1-\rho^2)}\right] \end{aligned} \quad (\text{A.5})$$

The latter equation states that for high correlation (ρ close to 1), the conditional (normal) distribution is centered approximately around $\sigma_2/\sigma_1 \cdot x_1$ with a very small variance. In this case, you may infer the value of an unmeasured random variable with high confidence provided that you measured its correlated partner. Correlations of this kind are exploited in experiments with two entangled light fields by means of highly squeezed quadratures.

APPENDIX B

A Normal Ordering Theorem

In [section 6.6](#), linearized transformations of third-order non-linearities are derived from the solution of the quantum mechanical equations of motion. The corresponding linearized transformation on the expectation value and the noise spectral density matrix was compared with the exact quantum mechanical expressions for coherent input fields $|\alpha\rangle$. Here, we will show how to obtain these exact quantities. The only problematic part of the derivation concerns the calculation of the expectation value

$$\langle \alpha | e^{-i\chi\tau\hat{a}^\dagger\hat{a}} \hat{a} | \alpha \rangle \quad (\text{B.1})$$

The key to solve the problem is to realize the equality between the exponential function and a normally ordered operator in the form

$$e^{\theta\hat{a}^\dagger\hat{a}} \equiv : e^{p(\theta)\hat{a}^\dagger\hat{a}} : \quad (\text{B.2})$$

and then to calculate the function $p(\theta)$ ([Barnett and Radmore; 1997](#)). A differentiation of both sides with respect to θ yields

$$\hat{a}^\dagger\hat{a} e^{\theta\hat{a}^\dagger\hat{a}} = p'(\theta)\hat{a}^\dagger : e^{p(\theta)\hat{a}^\dagger\hat{a}} : \hat{a} \quad (\text{B.3})$$

Using Eq. (B.2), we transform the right-hand side of the latter equation

$$\begin{aligned} p'(\theta)\hat{a}^\dagger : e^{p(\theta)\hat{a}^\dagger\hat{a}} : \hat{a} &= p'(\theta)\hat{a}^\dagger e^{\theta\hat{a}^\dagger\hat{a}} \hat{a} \\ &= p'(\theta)\hat{a}^\dagger e^{\theta\hat{a}^\dagger\hat{a}} \hat{a} e^{-\theta\hat{a}^\dagger\hat{a}} e^{\theta\hat{a}^\dagger\hat{a}} \\ &= p'(\theta) e^{-\theta} \hat{a}^\dagger \hat{a} e^{\theta\hat{a}^\dagger\hat{a}} \end{aligned} \quad (\text{B.4})$$

The last step involves the well-known operator series expansions of expressions like $e^{\hat{A}} \hat{B} e^{-\hat{A}}$. Comparing Eqs. (B.3)&(B.4), we find the following condition for the function $p(\theta)$

$$p'(\theta) e^{-\theta} = 1, \quad \text{with } p(0) = 0 \quad (\text{B.5})$$

which is solved by

$$p(\theta) = e^\theta - 1 \quad (\text{B.6})$$

Now, let us apply our result and write down the expectation value of the first equation

$$\langle \alpha | e^{-i\chi\tau\hat{a}^\dagger\hat{a}} \hat{a} | \alpha \rangle = \alpha \exp[(e^{-i\chi\tau} - 1) |\alpha|^2] \quad (\text{B.7})$$

For weak non-linearities and small interaction times $\chi\tau \ll 1$, we obtain the approximate result that the expectation value is phase shifted by $\exp(-i\chi\tau|\alpha|^2)$. A calculation of the noise spectral density of the output field involves additional expectation values which can all be easily related to the value of

$$\langle \alpha | e^{-i\chi\tau\hat{a}^\dagger\hat{a}} \hat{a} e^{-i\chi\tau\hat{a}^\dagger\hat{a}} \hat{a} | \alpha \rangle \quad (\text{B.8})$$

This expression is transformed such that the normal ordering theorem can be directly applied. One obtains

$$\begin{aligned} \langle \alpha | e^{-i\chi\tau\hat{a}^\dagger\hat{a}} \hat{a} e^{-i\chi\tau\hat{a}^\dagger\hat{a}} \hat{a} | \alpha \rangle &= \langle \alpha | e^{-i\chi\tau\hat{a}^\dagger\hat{a}} e^{-i\chi\tau\hat{a}^\dagger\hat{a}} e^{i\chi\tau\hat{a}^\dagger\hat{a}} \hat{a} e^{-i\chi\tau\hat{a}^\dagger\hat{a}} \hat{a} | \alpha \rangle \\ &= \alpha^2 e^{-i\chi\tau} \langle \alpha | e^{-2i\chi\tau\hat{a}^\dagger\hat{a}} | \alpha \rangle \\ &= \alpha^2 e^{-i\chi\tau} \exp[(e^{-2i\chi\tau} - 1) |\alpha|^2] \end{aligned} \quad (\text{B.9})$$

Finally, the noise spectral density (Eq. (6.49)) is found by applying these results to the expectation value and the variance of Eq. (6.44).

APPENDIX C

Signal Combinatorics

Consider N bins and k signals which distribute among these bins under the assumption that none of the bins is preferred among the others. One may wonder how many bins contain more than one signal. It is rather difficult to calculate an exact answer to that problem. Nevertheless, it is rather easy to find a lower boundary and then to conclude that the exact number has to be close to that boundary under certain conditions. The

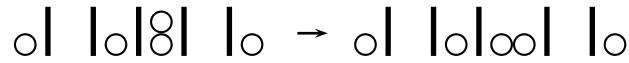


Figure C.1: Distributing k signals among N bins is equivalent to ordering $N - 1$ lines and k circles.

total number of combinations when k signals are distributed among N bins is equivalent to the number of combinations of $N - 1$ lines and k circles (see [Figure C.1](#)). Therefore, one obtains

$$N_{\text{tot}}(N, k) = \binom{N - 1 + k}{N - 1} = \binom{N - 1 + k}{k} \quad (\text{C.1})$$

This number also includes configurations where bins contain more than two signals. The next step is to restrict to configurations which do not contain bins with more than two signals. For that set of configurations, an expectation value of the number of bins with two signals can be calculated. The number of combinations with i doubly occupied bins (excluding configurations with higher occupation numbers per bin) is given by

$$N_{i,\text{dbl}} = \binom{N}{i} \binom{N - i}{k - 2i} \quad (\text{C.2})$$

The expression consists of a factor which counts the number of combinations of i doubly occupied bins distributed among N bins and a factor which counts the number of combinations of the remaining $k - 2i$ signals singly occupying $N - i$ available bins. Consequently, the expectation value for the number of signals in doubly occupied bins satisfies

$$S_{\text{dbl}} > \sum_{i=1}^{\lfloor k/2 \rfloor} 2i \cdot \frac{N_{i,\text{dbl}}}{N_{\text{tot}}} \quad (\text{C.3})$$

The excess number of signals in doubly occupied bins is due to combinations with higher occupation numbers which also contain doubly occupied bins. Therefore, the right-hand side of Eq. (C.3) yields an accurate estimate of S_{mult} – the number of signals in multiply occupied bins – whenever the probability for combinations with threefold, fourfold,... occupied bins is negligible. Intuitively, one might expect that this is true provided that $N \gg k$. In the following, we show that the sum of the probabilities

$$\begin{aligned} r(N, k) &= p_{\text{sng}}(N, k) + p_{\text{dbl}}(N, k) \\ &= \frac{1}{N_{\text{tot}}} (N_{\text{sng}} + N_{\text{dbl}}) \end{aligned} \quad (\text{C.4})$$

constitutes a measure for the accurateness of estimating S_{mult} by means of Eq. (C.3), where N_{sng} and N_{dbl} denote the number of combinations with exclusively singly or combinations with singly and doubly occupied bins respectively:

$$N_{\text{sng}} = \binom{N}{k}, \quad N_{\text{dbl}} = \sum_{i=1}^{\lfloor k/2 \rfloor} N_{i,\text{dbl}} \quad (\text{C.5})$$

The closer r is to 1, the better is our estimate of the number of signals in multiply occupied bins. As shown in Table C.1, the measure r is sufficiently close to 1 for $N/k \geq 100$.

$k \quad N$	10	10^2	10^3	10^4
10	0.097	0.94	1	1
10^2	0.00	0.00	0.47	0.99
10^3	0.00	0.00	0.00	0.00

Table C.1: The table shows the ratio r defined in Eq. (C.4) for various parameters N, k . Accordingly, the corresponding estimate of the number of signals in multiply occupied bins is sufficiently accurate for all shown values with $N/k \geq 100$.

However, one should be careful with attaching one's confidence to values of the ratio N/k . Keeping N/k constant, r is decreasing with increasing number of signals (see Figure C.2). This does not mean that the number of bins with higher occupation numbers increases. Instead, the probability for combinations which contain at least one bin with occupation

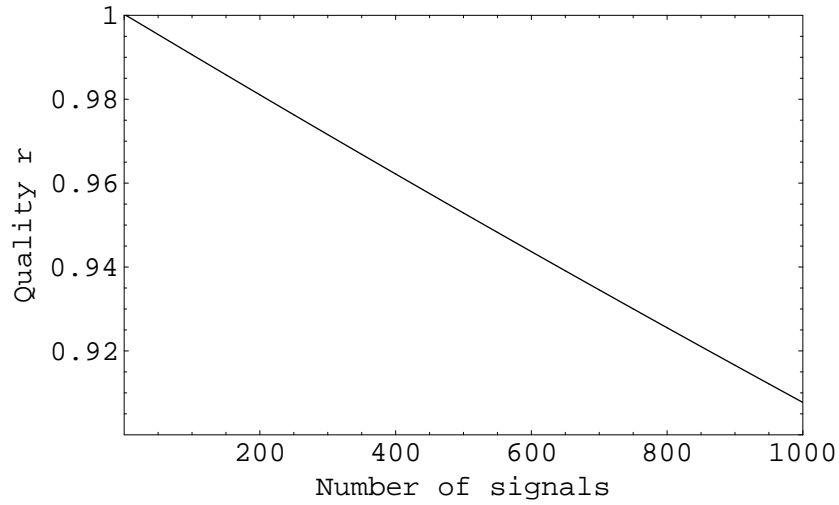


Figure C.2: The figure shows that while keeping N/k constant, the accuracy of the estimate of the number of signals in multiply occupied bins is decreasing with increasing number k of signals.

number greater than two increases. Finally, let us consider combinations with a very high number of bins $N = 10^7$ and a comparatively small number of signals $k = 10^4$. The corresponding quality ratio is $r = 0.99$. By virtue of Eq. (C.3), one obtains $S_{\text{mult}} = 19.74 \pm 6.27$ for the number of signals in multiply occupied bins. In the worst case, we had to assume an additional error of ± 100 (i.e. 1% of the total number of signals) since we do not know how many of the signals in neglected combinations reside in bins with higher occupation numbers. Anyway, we expect that in any combination with significant probability and $N \gg k$, the number of signals in multiply occupied bins is much smaller than the number of signals in singly occupied bins and that the additional error due to $r < 1$ is of the same order than the inherent error of our estimate.

APPENDIX D

Derivation of merger SNR

In this Appendix we derive Eq. (4.91). We begin by averaging over all angles, including $\mu \equiv \hat{L} \cdot \hat{N}$; we return to the μ -dependence near the end.

Consider first a single synthetic Michelson data stream from a single LISA-like detector. Let the waveform at the detector be $h_{ij}(t) = h_+(t)e_{ij}^+ + h_\times(t)e_{ij}^\times$, where e_{ij}^+ and e_{ij}^\times are “+” and “ \times ” polarization tensors, respectively. The average matched-filter SNR^2 for some source (where the average is over source-direction and polarization angle) is given by

$$\langle \text{SNR}^2 \rangle = 4 \int_0^\infty \frac{|\tilde{h}_+(f)|^2 + |\tilde{h}_\times(f)|^2 df}{S_h(f)} \quad (\text{D.1})$$

where, as throughout this paper, $S_h(f)$ is the “sky-averaged” noise spectral density. Parseval’s theorem states that

$$\int_0^\infty |\tilde{h}_+(f)|^2 df = \frac{1}{2} \int_{-\infty}^\infty h_+^2(t) dt, \quad (\text{D.2})$$

and similarly for h_\times so for a chirping signal with a slowly changing frequency $f(t)$, it is clear that

$$|\tilde{h}_+(f)|^2 + |\tilde{h}_\times(f)|^2 = \frac{1}{2} (\bar{h}_+^2(t) + \bar{h}_\times^2(t)) dt/df, \quad (\text{D.3})$$

where the overbar denotes time-averaging.

For now, consider some GW source at low redshift ($z \ll 1$). Then the rate at which the source loses energy due to GW emission is

$$\dot{E}(t) = 4\pi D^2 (\pi f^2/4) \langle \bar{h}_+^2(t) + \bar{h}_\times^2(t) \rangle \quad (\text{D.4})$$

where D is its distance, and where the averaging is over all directions from the source. Therefore we have

$$\langle |\tilde{h}_+(f)|^2 + |\tilde{h}_\times(f)|^2 \rangle = \frac{1}{2} \frac{\dot{E}}{\pi^2 D^2 f^2} dt/df. \quad (\text{D.5})$$

The product $\dot{E}(dt/df)$ equals $|dE/df|$. For a circular-orbit binary, the energy is approximately

$$E \approx -\frac{1}{2}\mu M/r \approx -\frac{1}{2}\mu(M\pi f)^{2/3} \quad (\text{D.6})$$

$$= -\frac{1}{2}\mathcal{M}^{5/3}(\pi f)^{2/3} \quad (\text{D.7})$$

from which we obtain

$$|dE/df| \approx \frac{1}{3}\mathcal{M}^{5/3}\pi^{2/3}f^{-1/3}. \quad (\text{D.8})$$

Using this result along with Eqs. (D.1) and (D.5), we arrive at

$$\langle \rho^2 \rangle = \frac{2\mathcal{M}^{5/3}}{3\pi^{4/3}D^2} \int_0^\infty \frac{f^{-7/3} df}{S_h(f)}. \quad (\text{D.9})$$

The generalization of Eq. (D.9) to arbitrary redshift is accomplished by the standard replacement (Marković; 1993) $\mathcal{M} \rightarrow \mathcal{M}(1+z)$ and $D \rightarrow D_L$, where D_L is the luminosity distance. The μ -dependence of the waveform's strength—i.e., the $f(\mu)$ factor in Eq. (4.91) – follows almost immediately from, e.g., Eqs.(2a-2b) of (Apostolatos et al.; 1994). Finally, to arrive at Eq. (4.91), we multiply the rhs of Eq. (D.9) by a factor of 8, to account for the fact that at low-to-mid frequencies BBO is approximately equivalent to 8 independent Michelson detectors, each with the same noise density $S_h(f)$.

APPENDIX E

The Coupled Pendulum

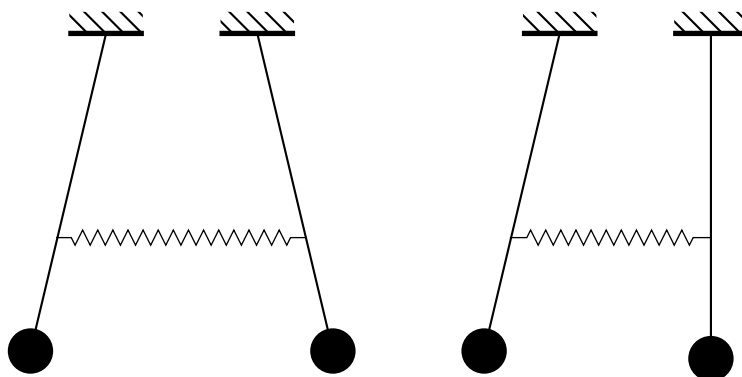


Figure E.1: A coupled pendulum has two eigenmodes. The system to the left oscillates in an eigenmode characterized by the upper resonance frequency. The system to the right must be described by a linear combination of both eigenmodes. Then, energy will slosh back and forth between the two pendulums.

Consider two pendulums in the gravitational field of the Earth which are coupled by a spring. The two pendulums have equal lengths and their coordinates are governed by

$$\begin{aligned}\ddot{x}_1 + \left(\frac{g}{l} + \frac{k}{m}\right)x_1 &= \frac{k}{m}x_2 \\ \ddot{x}_2 + \left(\frac{g}{l} + \frac{k}{m}\right)x_2 &= \frac{k}{m}x_1\end{aligned}\tag{E.1}$$

Introducing normal coordinates $u_{\pm} \equiv 1/\sqrt{2}(x_1 \pm x_2)$, the two equations decouple and one

finds the resonance frequencies

$$\omega_- = \sqrt{\frac{g}{l}}, \quad \omega_+ = \sqrt{\frac{g}{l} + 2\frac{k}{m}} \quad (\text{E.2})$$

Alternatively, these two frequencies can be characterized by model independent parameters, namely in terms of two frequencies

$$\begin{aligned} \omega_0^2 &\equiv \frac{g}{l} + \frac{k}{m} \\ \Omega_0 \cdot \omega_0 &\equiv \frac{k}{m} \end{aligned} \quad (\text{E.3})$$

In that way, the solution to the coupled pendulum does not depend any longer on its mechanical parameters g , l , k , m and the result can be transferred to arbitrary coupled resonators. Rewriting Eq. (E.1)

$$\begin{aligned} \ddot{x}_1 + \omega_0^2 x_1 &= \Omega_0 \omega_0 x_2 \\ \ddot{x}_2 + \omega_0^2 x_2 &= \Omega_0 \omega_0 x_1 \end{aligned} \quad (\text{E.4})$$

and evaluating the resonance frequencies in the weak coupling limit $\Omega_0 \ll \omega_0$, one obtains

$$\omega_- = \omega_0 - \frac{\Omega_0}{2}, \quad \omega_+ = \omega_0 + \frac{\Omega_0}{2} \quad (\text{E.5})$$

If initially only one pendulum is pulled to the side, then – evaluating explicitly the solutions for $x_1(t)$, $x_2(t)$ – one finds that energy will slosh back and forth between the two pendulums with frequency Ω_0 . In other words, in the weak coupling regime, the difference between the two natural frequencies is also the sloshing frequency which determines the rate of the energy transfer between the two pendulums.

In [section 8.2](#), the results derived in this appendix for the mechanical pendulum are applied to coupled optical resonators. The optical bar and the speed meter make use of the energy sloshing in the one or other way depending on the initial excitations of the two Fabry-Pérot resonators.

APPENDIX F

Parametric Resonance

Consider a Fabry-Pérot cavity which is oriented parallel to the wavefront of a gravitational wave with frequency Ω . A strain $h(t) = h_0 \cos(\Omega t)$ causes a resonance frequency ω_0 of the cavity to change according to

$$\omega(t)^2 = \omega_0^2(1 + h(t)) = \omega_0^2(1 + h_0 \cos(\Omega t)) \quad (\text{F.1})$$

The equation of motion for the light amplitudes then reads

$$\ddot{a}(t) + \gamma \dot{a}(t) + \omega_0^2(1 + h_0 \cos(\Omega t))a(t) = 0 \quad (\text{F.2})$$

This equation without damping term γ is known as the Mathieu equation. The usually constant frequency parameter ω_0 is now subject to a harmonic variation. Systems described by this equation are very often investigated with respect to their stability properties. The two parameters h_0 and ω_0 have to fulfill certain conditions in order to give rise to stable solutions $a(t)$ which remain bounded for all times. We are going to show that a system without dissipation has unstable solutions for arbitrarily small strain amplitudes h_0 provided that the unperturbed resonance frequency ω_0 lies close to $\omega_0 = \Omega \cdot k/2$ with $k \in \mathbb{Z}$. Accordingly, we say that first order parametric resonance occurs when the parameter frequency Ω is twice the resonance ω_0 of the unperturbed oscillator.

Here, we use the method presented in (Arnold; 1989) to identify unstable solutions of Eq. (F.2). Therefore, we need the state of the system after one period $T = 2\pi/\Omega$ of the strain perturbation for two sets of initial conditions

$$\begin{aligned} \text{system 1: } & a(0) = 1, \dot{a}(0) = 0 \\ \text{system 2: } & b(0) = 0, \dot{b}(0) = 1 \end{aligned} \quad (\text{F.3})$$

The stability condition is formulated in terms of the matrix A which acts in the phase space of the oscillator. It maps the initial state vectors of our two systems to the state vector $\{a(T), \dot{a}(T)\}$ after one period:

$$A = \begin{pmatrix} a(T) & b(T) \\ \dot{a}(T) & \dot{b}(T) \end{pmatrix} \quad (\text{F.4})$$

Now, a system is stable whenever it satisfies the stability condition $|\text{Tr}A| < 2$. This

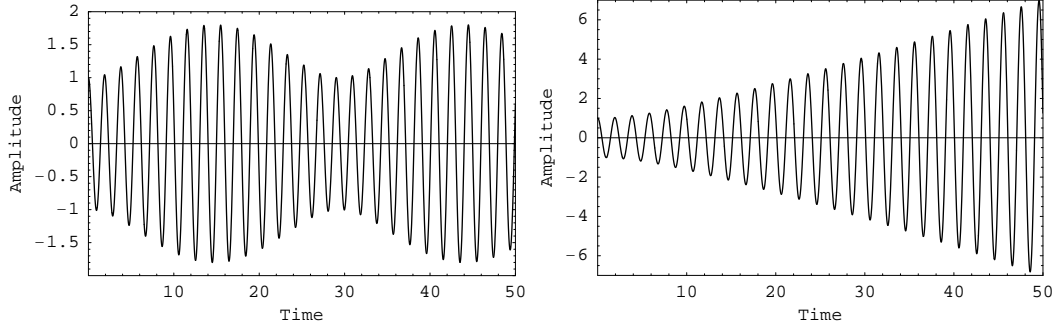


Figure F.1: Both graphs show oscillations of an undamped resonator with initial conditions $a(0) = 1$, $\dot{a}(0) = 0$. In both cases, the strain perturbation has frequency $\Omega = 2\pi$ and amplitude $h_0 = 0.08$. However, a small change of the frequency ω_0 is sufficient to drive a stable system into an unstable state. The stable system has $\omega_0 = 2\pi \cdot 0.52$ whereas the unstable system has $\omega_0 = 2\pi \cdot 0.51$.

inequality can be solved numerically. One elegant way of representing the solution is by drawing the contour plot of the function $|\text{Tr}A| - 2$ defining two different shading colors for positive and negative values (see [subsection 10.2.2](#)). The result can be seen in [Figure F.2](#).

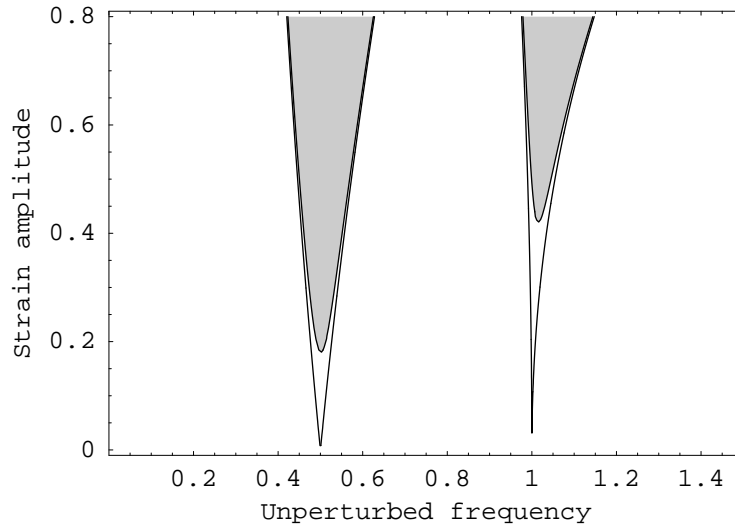


Figure F.2: The figure displays curves which enclose all points $\{\omega_0/(2\pi), h_0\}$ which lead to parametric resonance (parametric amplification) of a strain perturbation $h(t)$. The shaded regions represent unstable solutions of the damped oscillator with $\gamma = 0.02$, whereas the curves belong to the undamped oscillator. The strain frequency is kept constant: $\Omega/(2\pi) = 1$.

It shows the first two orders of parametric resonance for the undamped and a damped oscillator. The instability region shrinks when the damping γ is increased. Especially, in

the case of the damped oscillator, the strain perturbation has to exceed a certain threshold value in order to initiate parametric resonance.

The whole situation can be considered from another perspective. Let us assume that we want to amplify oscillations. For example, a Fabry-Pérot resonator is tuned to an optical frequency ω_{red} . Then, according to our theory, we could amplify the fields inside the cavity by harmonically perturbing the resonance of the cavity with a frequency $\omega_{\text{green}} = 2 \cdot \omega_{\text{red}}$. In practice, experiments are carried out where the cavity contains a nonlinear crystal whose index of refraction $n(t) = n_0 + n_1 E(t)$ depends on the current field amplitude $E(t)$ inside it. Then, a so-called pump beam is inserted into the cavity which induces an index modulation at frequency ω_{green} . This modulation is equivalently treated as a strain perturbation like in Eq. (F.2):

$$h(t) = 2 \frac{n_1}{n_0} E(t) \quad (\text{F.5})$$

Once the pump beam exceeds the instability threshold (certainly, the cavity has losses), the amplitude of the field ω_{red} experiences an amplification depending on the mean time which the light spends inside the cavity. The system is known as OPA (optical parametric amplifier). The OPA model can be reformulated in terms of the oscillator's quadratures $a_1(t)$, $a_2(t)$ which determine its amplitude according to $a(t) = a_1(t) \cos(\omega_0 t) + a_2(t) \sin(\omega_0 t)$. Inserting this expression into Eq. (F.2) and subsequently separating the quadratures again, one finds two coupled equations of motion for the two quadratures

$$\begin{aligned} \ddot{a}_1(t) + \omega_0^2 h(t) a_1(t) &= -2\omega_0 \dot{a}_2(t) \\ \ddot{a}_2(t) + \omega_0^2 h(t) a_2(t) &= 2\omega_0 \dot{a}_1(t) \end{aligned} \quad (\text{F.6})$$

which again can be solved numerically. The solution reveals that the OPA acts as amplifier for one quadrature, but in the same moment attenuates the orthogonal quadrature. This property is exploited to reshape the common noise distribution of the two quadratures and generate so-called squeezed states of the field.

BIBLIOGRAPHY

- Abramovici et al. (1992). LIGO: the Laser Interferometer Gravitational-Wave Observatory, *Science* **256**: 325.
- Allen, B. (1996). The stochastic gravity-wave background: sources and detection.
URL: *gr-qc/9604033*
- Allen, B. and Romano, J. D. (1999). Detecting a stochastic background of gravitational radiation: Signal processing strategies and sensitivities, *Phys. Rev. D* **59**: 102001.
- Andersson, N. (1998). A new class of unstable modes of rotating relativistic stars, *ApJ* **502**: 708.
- Ando et al. (2001). Stable Operation of a 300-m Laser Interferometer with Sufficient Sensitivity to Detect Gravitational-Wave Events within Our Galaxy, *Phys. Rev. Lett.* **86**: 3950.
- Apostolatos, T. A., Cutler, C., Sussman, G. J. and Thorne, K. S. (1994). Spin-induced orbital precession and its modulation of the gravitational waveforms from merging binaries, *Phys. Rev. D* **49**: 6274.
- Armstrong, J. W., Estabrook, F. B. and Tinto, M. (1999). Time-delay interferometry for spaced-based gravitational wave searches, *ApJ* **527**: 814.
- Arnold, V. I. (1989). *Mathematical Methods of Classical Mechanics*, Springer.
- Arthurs, E. and Goodman, M. S. (1988). Quantum correlations: A generalized Heisenberg uncertainty relation, *Phys. Rev. Lett.* **60**: 2447.
- Balasubramanian, R., Sathyaprakash, B. S. and Dhurandhar, S. V. (1996). Gravitational waves from coalescing binaries: Detection strategies and Monte Carlo estimation of parameters, *Phys. Rev. D* **53**: 3033.
- Barnett, S. M. and Radmore, P. M. (1997). *Methods in Theoretical Quantum Optics*, Oxford university press.

- Belczynski, K., Kalogera, V. and Bulik, T. (2002). A comprehensive study of binary compact objects as gravitational wave sources: Evolutionary channels, rates, and physical properties, *ApJ* **572**: 407.
- Black, E. D. (2000). An introduction to Pound-Drever-Hall laser stabilization, *Am. J. Phys.* **69**: 79.
- Bocko, M. F. and Onofrio, R. (1996). On the measurement of a weak classical force coupled to a quantum-mechanical oscillator: experimental progress, *Phys. Rev. Mod.* **68**: 755.
- Bose, S., Pai, A. and Dhurandhar, S. (2000). Detection of gravitational waves from inspiraling, compact binaries using a network of interferometric detectors, *Int. J. Mod. Phys. D* **9**: 325.
- Boyd, R. W. (2003). *Nonlinear Optics*, Academic Press.
- Brady, P. R. and Creighton, T. (2000). Searching for periodic sources with LIGO. II. hierarchical searches, *Phys. Rev. D* **61**: 082001.
- Brady, P. R., Creighton, T., Cutler, C. and Schutz, B. F. (1998). Searching for periodic sources with LIGO, *Phys. Rev. D* **57**: 2101.
- Braginsky, V. B., Gorodetsky, M. L. and Khalili, F. Y. (1997). Optical bars in gravitational wave antennas, *Phys. Lett. A* **232**: 340.
- Braginsky, V. B., Gorodetsky, M. L. and Khalili, F. Y. (1998). Quantum limits and symphotonic states in free-mass gravitational-wave antennae, *Phys. Lett. A* **246**: 485.
- Braginsky, V. B., Gorodetsky, M. L., Khalili, F. Y., Matsko, A. B., Thorne, K. S. and Vyatchanin, S. P. (2003). Noise in gravitational-wave detectors and other classical-force measurements is not influenced by test-mass quantization, *Phys. Rev. D* **67**: 082001.
- Braginsky, V. B., Gorodetsky, M. L., Khalili, F. Y. and Thorne, K. S. (2000). Dual-resonator speed meter for a free test mass, *Phys. Rev. D* **61**: 044002.
- Braginsky, V. B., Gorodetsky, M. L. and Vyatchanin, S. P. (1999). Thermodynamical fluctuations and photo-thermal shot noise in gravitational wave antennae, *Phys. Lett. A* **264**: 1.
- Braginsky, V. B., Gorodetsky, M. L. and Vyatchanin, S. P. (2000). Thermo-refractive noise in gravitational wave antennae, *Phys. Lett. A* **271**: 303.
- Braginsky, V. B. and Khalili, F. Y. (1996a). Nonlinear meter for the gravitational wave antenna, *Phys. Lett. A* **218**: 167.
- Braginsky, V. B. and Khalili, F. Y. (1996b). Quantum nondemolition measurements: the route from toys to tools, *Rev. Mod. Phys.* **68**: 1.
- Braginsky, V. B. and Khalili, F. Y. (1999a). Low noise rigidity in quantum measurements, *Phys. Lett. A* **257**: 241.

- Braginsky, V. B. and Khalili, F. Y. (1999b). *Quantum Measurement*, Cambridge University Press.
- Braginsky, V. B. and Manukin, A. B. (1967). Ponderomotive effects of electromagnetic radiation, *Sov. Phys. JETP* **25**: 653.
- Braginsky, V. B., Mitrofanov, V. P. and Vyatchanin, S. P. (1994). Isolation of test masses in the advanced laser interferometric gravitational-wave antenna, *Rev. Sci. Instrum.* **65**: 3771.
- Braginsky, V. B., Strigin, S. E. and Vyatchanin, S. P. (2001). Parametric oscillatory instability in Fabry-Pérot interferometer, *Phys. Lett. A* **287**: 331.
- Braginsky, V. B., Strigin, S. E. and Vyatchanin, S. P. (2002). Analysis of parametric oscillatory instability in power recycled LIGO interferometer, *Phys. Lett. A* **305**: 111.
- Braginsky, V. B. and Vyatchanin, S. P. (2002). Low quantum noise tranquilizer for Fabry-Pérot interferometer, *Phys. Lett. A* **293**: 228.
- Braginsky, V. B. and Vyatchanin, S. P. (2003). Thermodynamical fluctuations in optical mirror coatings, *Phys. Lett. A* **312**: 244.
- Braunstein, S. L. and Caves, C. M. (1990). Phase and homodyne statistics of generalized squeezed states, *Phys. Rev. A* **42**: 4115.
- Breitenbach, G., Illuminati, F., Schiller, S. and Mlynek, J. (1998). Broadband detection of squeezed vacuum: A spectrum of quantum states, *Europhys. Lett.* **44**: 192.
- Buonanno, A. and Chen, Y. (2001). Quantum noise in second generation, signal-recycled laser interferometric gravitational-wave detectors, *Phys. Rev. D* **64**: 042006.
- Buonanno, A. and Chen, Y. (2002). Signal recycled laser-interferometer gravitational-wave detectors as optical springs, *Phys. Rev. D* **65**: 042001.
- Buonanno, A. and Chen, Y. (2003). Scaling law in signal recycled laser-interferometer gravitational-wave detectors, *Phys. Rev. D* **67**: 062002.
- Buonanno, A. and Chen, Y. (2004). Improving the sensitivity to gravitational-wave sources by modifying the input-output optics of advanced interferometers, *Phys. Rev. D* **69**: 102004.
- Buonanno, A., Chen, Y. and Mavalvala, N. (2003). Quantum noise in laser-interferometric gravitational-wave detectors with a heterodyne readout scheme, *Phys. Rev. D* **67**: 122005.
- Buonanno, A., Chen, Y., Pan, Y. and Vallisneri, M. (2004). Quasiphysical family of gravity-wave templates for precessing binaries of spinning compact objects: Application to double-spin precessing binaries, *Phys. Rev. D* **70**: 104003.

- Buonanno, A., Chen, Y. and Vallisneri, M. (2003a). Detecting gravitational waves from precessing binaries of spinning compact objects: Adiabatic limit, *Phys. Rev. D* **67**: 104025.
- Buonanno, A., Chen, Y. and Vallisneri, M. (2003b). Detection template families for gravitational waves from the final stages of binary-black-hole inspirals: Nonspinning case, *Phys. Rev. D* **67**: 024016.
- Buonanno, A., Sigl, G., Raffelt, G. G., Janka, H.-T. and Müller, E. (2005). Stochastic Gravitational Wave Background from Cosmological Supernovae.
URL: *astro-ph/0412277*
- Caldwell, R. R. and Allen, B. (1992). Cosmological constraints on cosmic-string gravitational radiation, *Phys. Rev. D* **45**: 3447.
- Caldwell, R. R., Battye, R. A. and Shellard, E. P. S. (1996). Relic gravitational waves from cosmic strings: Updated constraints and opportunities for detection, *Phys. Rev. D* **54**: 7146.
- Callen, H. B. and Greene, R. F. (1952). On a Theorem of Irreversible Thermodynamics, *Phys. Rev.* **86**: 702.
- Callen, H. B. and Welton, T. A. (1951). Irreversibility and Generalized Noise, *Phys. Rev.* **83**: 34.
- Carmicheal, H. J. (1984). Self-oscillation in a detuned cavity, *Phil. Trans. R. Soc. Lond. A* **313**: 433.
- Caron et al. (1997). The Virgo interferometer, *Class. Quantum Grav.* **14**: 1461.
- Caves, C. M. (1980). Quantum-mechanical noise in an interferometer, *Phys. Rev. D* **23**: 1693.
- Caves, C. M. (1982). Quantum limits on noise in linear amplifiers, *Phys. Rev. D* **26**: 1817.
- Caves, C. M. (1986). Quantum theory of measurements distributed in time. A path-integral formulation, *Phys. Rev. D* **33**: 1643.
- Caves, C. M. and Schumaker, B. L. (1985). New formalism for two-photon quantum optics, *Phys. Rev. A* **31**: 3068 & 3093.
- Caves, C. M., Thorne, K. S., Drever, R. W., Sandberg, V. D. and Zimmermann, M. (1980). On the measurement of a weak classical force coupled to a quantum-mechanical oscillator: I. issues of principle, *Rev. Mod. Phys.* **52**: 341.
- Chen, Y. (2003). Sagnac interferometer as a speed-meter-type, quantum-nondemolition gravitational-wave detector, *Phys. Rev. D* **67**: 122004.
- Chiao, R. Y. and Speliotopoulos, A. D. (2004). Towards MIGO, the matter-wave interferometric gravitational-wave observatory, and the intersection of quantum mechanics with general relativity, *J. Mod. Opt.* **51**: 861.

- Chickarmane, V. and Dhurandar, S. V. (1996). Performance of a dual recycled interferometer with squeezed light, *Phys. Rev. A* **54**: 786.
- Chickarmane, V., Dhurandar, S. V., Ralph, T. C., Gray, M., Bachor, H.-A. and McClelland, D. E. (1998). Squeezed light in a frontal-phase-modulated signal-recycled interferometer, *Phys. Rev. A* **57**: 3898.
- Collett, M. J. and Gardiner, C. W. (1984). Squeezing of intracavity and traveling-wave light fields produced in parametric amplification, *Phys. Rev. A* **30**: 1386.
- Collett, M. J. and Walls, D. F. (1985). Squeezing spectra for nonlinear optical systems, *Phys. Rev. A* **32**: 2887.
- Cornish, N. J. and Crowder, J. (2005). LISA data analysis using Markov chain Monte Carlo methods, *Phys. Rev. D* **72**: 043005.
- Cornish, N. J. and Hellings, R. W. (2003). The effects of orbital motion on LISA time delay interferometry, *CQG* **20**: 4851.
- Cornish, N. J. and Larson, S. L. (2003). LISA data analysis: Source identification and subtraction, *Phys. Rev. D* **67**: 103001.
- Cornish, N. J. and Rubbo, L. J. (2003). LISA response function, *Phys. Rev. D* **67**: 022001.
- Courty, J. M., Heidmann, A. and Pinard, M. (2003). Back-action cancellation in interferometers by quantum locking, *Europhys. Lett.* **23**: 226.
- Courty, J. M. and Reynaud, S. (1992). Generalized linear input-output theory for quantum fluctuations, *Phys. Rev. A* **46**: 2766.
- Crowder, J. and Cornish, N. J. (2004). LISA Source Confusion.
URL: [gr-qc/0404129](https://arxiv.org/abs/gr-qc/0404129)
- Cutler, C., Finn, L. S., Poisson, E. and Sussman, G. J. (1993). Gravitational radiation from a particle in circular orbit around a black hole. II. Numerical results for the nonrotating case, *Phys. Rev. D* **47**: 1511.
- Cutler, C. and Flanagan, É. É. (1994). Gravitational waves from merging compact binaries: How accurately can one extract the binary's parameters from the inspiral waveform?, *Phys. Rev. D* **49**: 2658.
- Cutler, C., Gholami, I. and Krishnan, B. (2005). Improved stack-slide searches for gravitational-wave pulsars.
URL: [gr-qc/0505082](https://arxiv.org/abs/gr-qc/0505082)
- Cutler, C. and Harms, J. (2006). Big Bang Observer and the neutron-star-binary subtraction problem, *Phys. Rev. D* **73**: 042001.
- Cutler, C. and Schutz, B. F. (2005). Generalized F-statistic: Multiple detectors and multiple gravitational wave pulsars, *Phys. Rev. D* **72**: 63006.

- Cutler et al. (1993). The Last Three Minutes: Issues in Gravitational-Wave Measurements of Coalescing Compact Binaries, *Phys. Rev. Lett.* **70**: 2984.
- Davis, T. M., Lineweaver, C. H. and Webb, J. K. (2003). Solutions to the tethered galaxy problem in an expanding universe and the observation of receding blueshifted objects, *Am. J. Phys.* **71**: 358.
- Dhurandhar, S. V. and Sathyaprakash, B. S. (1994). Choice of filters for the detection of gravitational waves from coalescing binaries. II. Detection in colored noise, *Phys. Rev. D* **49**: 1707.
- Dorsel, A., McCullen, J. D., Meystre, P., Vignes, E. and Walther, H. (1983). Optical Bistability and Mirror Confinement Induced by Radiation Pressure, *Phys. Rev. Lett.* **51**: 1550.
- Dorsel, A., McCullen, J. D., Meystre, P., Walther, H. and Wright, E. (1984). Optical resonators driven by radiation pressure, *Phil. Trans. R. Soc. Lond. A* **313**: 341.
- Dorsel, A., McCullen, J. D., Meystre, P., Walther, H. and Wright, E. (1985). Light-Pressure Mirror Stabilization, *Act. Phys. Austr.* **57**: 133.
- Drever et al. (1983). Laser phase and frequency stabilization using an optical resonator, *Appl. Phys. B* **31**: 97.
- Drever, R. W. P. (1996). Concepts for extending the ultimate sensitivity of interferometric gravitational wave detectors using non-transmissive optics with diffractive or holographic coupling, *Proceedings of the 7th Marcel Grossmann Conference on General Relativity*.
- Drummond, P. D. and Walls, D. F. (1980). Quantum theory of optical bistability. I:nonlinear polarisability model, *J. Phys. A:Math. Gen.* **13**: 725.
- Estabrook, F. B., Tinto, M. and Armstrong, J. W. (2000). Time-delay analysis of LISA gravitational wave data: Elimination of spacecraft motion effects, *Phys. Rev. D* **62**: 042002.
- Estabrook, F. B. and Wahlquist, H. D. (1975). Response of Doppler spacecraft tracking to gravitational radiation, *Gen. Rel. Gravitation* **6**: 439.
- Finn, L. S. (1992). Detection, measurement, and gravitational radiation, *Phys. Rev. D* **46**: 5236.
- Flanagan, É. É. and Hughes, S. A. (2005). The basics of gravitational wave theory, *N. Jour. Phys.* **7**: 204.
- Freise et al. (2000). Demonstration of detuned dual recycling at the Garching 30m laser interferometer, *Phys. Lett. A* **277**: 135.
- Gea-Banacloche, J. and Leuchs, G. (1987). Squeezed states for interferometric gravitational-wave detectors, *J. Mod. Opt.* **34**: 793.

- Harms et al. (2003). Squeezed-input, optical-spring, signal-recycled gravitational-wave detectors, *Phys. Rev. D* **68**: 042001.
- Harms, J. (2002). *Quantum Noise in the Laser-Interferometric Gravitational-Wave Detector GEO600*, Master's thesis, Universität Hannover.
- Harms, J., Schnabel, R. and Danzmann, K. (2004). The finite mass beamsplitter in high power interferometers, *Phys. Rev. D* **70**: 102001.
- Harrison, E. (1993). The redshift-distance and velocity-distance laws, *ApJ* **403**: 28.
- Hartle, J. B. (2003). *Gravity*, Addison Wesley.
- Hawking, S. and Israel, W. (eds) (1996). *300 Years of Gravitation*, Cambridge University Press.
- Heinzel et al. (1998). Experimental Demonstration of a Suspended Dual Recycled Interferometer for Gravitational Wave Detection, *Phys. Rev. Lett.* **81**: 5493.
- Heinzel, G. (1999). *Advanced optical techniques for laser-interferometric gravitational-wave detectors*, PhD thesis, Universität Hannover and Max-Planck-Institut für Quantenoptik.
- Heinzel, G., Mizuno, J., Schilling, R., Winkler, W., Rüdiger, A. and Danzmann, K. (1996). An experimental demonstration of resonant sideband extraction for laser-interferometric gravitational wave detectors, *Phys. Lett. A* **217**: 305.
- Hildred, G. P., Hassan, S. S., Puri, R. R. and Bullough, R. K. (1984). Quantum statistical properties of a quantum theory of optical bistability, *Phil. Trans. R. Soc. Lond. A* **313**: 439.
- Hogan, C. J. and Bender, P. L. (2001). Estimating stochastic gravitational wave backgrounds with the sagnac calibration, *Phys. Rev. D* **64**: 062002.
- Hogg, D. W. (2000). Distance measures in cosmology.
URL: [astro-ph/9905116](https://arxiv.org/abs/astro-ph/9905116)
- Hong, C. K. and Mandel, L. (1985). Higher-order squeezing of a quantum field, *Phys. Rev. Lett.* **54**: 323.
- Hughes, S. A. and Thorne, K. S. (1998). Seismic gravity-gradient noise in interferometric gravitational-wave detectors, *Phys. Rev. D* **58**: 122002.
- Imoto, N., Haus, H. A. and Yamamoto, Y. (1985). Quantum nondemolition measurement of the photon number via the optical Kerr effect, *Phys. Rev. A* **32**: 2287.
- Isaacson, R. A. (1968a). Gravitational Radiation in the Limit of High Frequency. I. The Linear Approximation and Geometrical Optics, *Phys. Rev.* **166**: 1263.
- Isaacson, R. A. (1968b). Gravitational Radiation in the Limit of High Frequency. II. Nonlinear Terms and the Effective Stress Tensor, *Phys. Rev.* **166**: 1272.

- Jaekel, M. T. and Reynaud, S. (1990). Quantum Limits in Interferometric Measurements, *Europhys. Lett.* **13**: 301.
- Jaranowski, P., Królak, A. and Schutz, B. F. (1998). Data analysis of gravitational-wave signals from spinning neutron stars: The signal and its detection, *Phys. Rev. D* **58**: 063001.
- Kalogera, V., Narayan, R., Spergel, D. N. and Taylor, J. H. (2001). The coalescence rate of double neutron star systems, *ApJ* **556**: 340.
- Khalili, F. Y. (2001). Frequency-dependent rigidity in large-scale interferometric gravitational-wave detectors, *Phys. Lett. A* **288**: 251.
- Khalili, F. Y. (2002). The "optical lever" intracavity readout scheme for gravitational-wave antennae, *Phys. Lett. A* **298**: 308.
- Kheruntsyan, K. V. (1999). Wigner function for a driven anharmonic oscillator, *J. Opt. B* **1**: 225.
- Kidders, L. E. (1995). Coalescing binary systems of compact objects to (post)^{5/2}-newtonian order V. Spin effects, *Phys. Rev. D* **52**: 821.
- Kimble et al. (2001). Conversion of conventional gravitational-wave interferometers into quantum nondemolition interferometers by modifying their input and/or output optics, *Phys. Rev. D* **65**: 022002.
- Kitagawa, M. and Yamamoto, Y. (1986). Number-phase minimum-uncertainty state with reduced number uncertainty in a Kerr nonlinear interferometer, *Phys. Rev. A* **34**: 3974.
- Królak, A., Kokkotas, K. D. and Schäfer, G. (1995). Estimation of the post-Newtonian parameters in the gravitational-wave emission of a coalescing binary, *Phys. Rev. D* **52**: 2089.
- Królak, A., Tinto, M. and Vallisneri, M. (2004). Optimal filtering of the LISA data, *Phys. Rev. D* **70**: 022003.
- Landau, L. D. and Lifshitz, E. M. (1962). *The Classical Theory of Fields*, Addison-Wesley.
- Larson, S. L. (2005).
URL: www.srl.caltech.edu/shane/sensitivity/index.html
- Larson, S. L., Hiscock, W. A. and Hellings, R. W. (2000). Sensitivity curves for spaceborne gravitational wave interferometers, *Phys. Rev. D* **62**: 062001.
- Lattimer, J. M. and Schutz, B. F. (2004). Constraining the equation of state with moment of inertia measurements.
URL: astro-ph/0411470
- Levin, Y. (1998a). Internal thermal noise in the LIGO test masses: A direct approach, *Phys. Rev. D* **57**: 659.

- Levin, Y. (1998b). Quantum nondemolition and higher order effects for a nonlinear meter in an interferometric gravitational wave antenna, *Phys. Rev. D* **57**: 2069.
- LISA study teams (2000). *LISA-Final Technical Report*.
- Liu, Y. T. and Thorne, K. S. (2000). Thermoelastic noise and homogeneous thermal noise in finite sized gravitational-wave test masses, *Phys. Rev. D* **62**: 122002.
- Loudon, R. (1981). Quantum limit on the michelson interferometer used for gravitational-wave detection, *Phys. Rev. Lett.* **47**: 815.
- Mandel, L. and Wolf, E. (1995). *Optical Coherence and Quantum Optics*, Cambridge university press.
- Marković, D. (1993). Possibility of determining cosmological parameters from measurements of gravitational waves emitted by coalescing, compact binaries, *Phys. Rev. D* **48**: 4738.
- McKenzie, K., Shaddock, D. S., McClelland, D. E., Buchler, B. C. and Lam, P. K. (2002). Experimental Demonstration of a Squeezing-Enhanced Power-Recycled Michelson Interferometer for Gravitational Wave Detection, *Phys. Rev. Lett.* **88**: 231102.
- Meers, B. J. (1988). Recycling in laser-interferometric gravitational-wave detectors, *Phys. Rev. D* **38**: 2317.
- Meers, B. J. (1989). The frequency response of interferometric gravitational wave detectors, *Phys. Lett. A* **142**: 465.
- Meystre, P. and Scully, M. O. (eds) (1983). *Quantum Optics, Experimental Gravitation, and Measurement Theory*, Plenum.
- Meystre, P., Wright, E. M., McCullen, J. D. and Vignes, E. (1985). Theory of radiation-pressure-driven interferometers, *J. Opt. Soc. Am. B* **11**: 1830.
- Michelson, A. A. and Morley, E. W. (1887). On the relative motion of the Earth and the luminiferous ether, *Am. J. Sci.* **34**: 333.
- Milburn, G. J. (1987). Quantum measurement theory of optical heterodyne detection, *Phys. Rev. A* **36**: 5271.
- Miller et al. (1983). Degenerate four-wave mixing in room-temperature GaAs/GaAlAs multiple quantum well structures, *App. Phys. Lett.* **42**: 925.
- Misner, C. W., Thorne, K. S. and Wheeler, J. A. (1973). *Gravitation*, Freeman.
- Misra, B. and Sudarshan, E. C. G. (1977). The Zeno's paradox in quantum theory, *J. Math. Phys.* **18**: 756.
- Mizuno et al. (1993). Resonant sideband extraction: a new configuration for interferometric gravitational wave detectors, *Phys. Lett. A* **175**: 273.

- Mizuno, J. (1995). *Comparison of optical configurations for laser-interferometric gravitational-wave detectors*, PhD thesis, Universität Hannover and Max-Planck-Institut für Quantenoptik, Garching.
- Nissanke, S. and Blanchet, L. (2005). Gravitational radiation reaction in the equations of motion of compact binaries to 3.5 post-Newtonian order, *Class. Quant. Grav* **22**: 1007.
- Owen, B. J. (1996). Search templates for gravitational waves from inspiraling binaries: Choice of template spacing, *Phys. Rev. D* **53**: 6749.
- Owen et al. (1998). Gravitational waves from hot young rapidly rotating neutron stars, *Phys. Rev. D* **58**: 084020.
- Pace, A. F., Collett, M. J. and Walls, D. F. (1993). Quantum limits in interferometric detection of gravitational radiation, *Phys. Rev. A* **47**: 3173.
- Pan, Y., Buonanno, A., Chen, Y. and Vallisneri, M. (2004). Physical template family for gravitational waves from precessing binaries of spinning compact objects: Application to single-spin binaries, *Phys. Rev. D* **69**: 104017.
- Peters, P. C. (1964). Gravitational radiation and the motion of two point masses, *Phys. Rev.* **136**: B1224.
- Peters, P. C. and Mathews, J. (1963). Gravitational Radiation from Point Masses in a Keplerian orbit, *Phys. Rev.* **131**: 435.
- Pfenning, M. J. (2001). Quantum inequalities for the electromagnetic field, *Phys. Rev. D* **65**: 024009.
- Phinney, E. S. (1991). The rate of neutron star binary mergers in the universe: minimal predictions for gravity wave detectors, *ApJ* **380**: L17.
- Phinney, E. S. (2001). A practical theorem on gravitational wave backgrounds.
URL: [astro-ph/0108028](https://arxiv.org/abs/astro-ph/0108028)
- Phinney et al. (2003). The big bang observer: direct detection of gravitational waves from the birth of the universe to the present, *NASA Mission Concept Study* .
- Priestley, M. B. (2001). *Spectral Analysis and Time Series*, Academic Press.
- Prince, T. A., Tinto, M., Larson, S. L. and Armstrong, J. W. (2002). LISA optimal sensitivity, *Phys. Rev. D* **66**: 122002.
- Purdue, P. (2002). Analysis of a quantum nondemolition speed-meter interferometer, *Phys. Rev. D* **66**: 022001.
- Purdue, P. and Chen, Y. (2002). Practical speed meter designs for quantum nondemolition gravitational-wave interferometers, *Phys. Rev. D* **66**: 122004.
- Rehbein, H., Harms, J., Schnabel, R. and Danzmann, K. (2005). Optical transfer functions of Kerr nonlinear cavities and interferometers, *Phys. Rev. Lett.* **95**: 193001.

- Reid, M. D. (1988). Quantum theory of optical bistability without adiabatic elimination, *Phys. Rev. A* **37**: 4792.
- Robertson, N. A. (2000). Laser interferometric gravitational wave detectors, *CQG* **17**: R19.
- Roura et al. (2004). Gravitational wave detectors based on matter wave interferometers (MIGO) are no better than laser interferometers (LIGO).
URL: *gr-qc/0409002*
- Santamore, D. H. and Levin, Y. (2001). Eliminating thermal violin spikes from LIGO noise, *Phys. Rev. D* **64**: 042002.
- Sasaki, M. and Tagoshi, H. (2003). Analytic Black Hole Perturbation Approach to Gravitational Radiation, *Liv. Rev.* .
- Sathyaprakash, B. S. and Dhurandhar, S. V. (1991). Choice of filters for the detection of gravitational waves from coalescing binaries, *Phys. Rev. D* **44**: 3819.
- Schilling, R. (1997). Angular and frequency response of LISA, *CQG* **14**: 1513.
- Schnabel, R. et al. (2004). Squeezed light for the interferometric detection of high-frequency gravitational waves, *CQG* **21**: S1045.
- Schneider et al. (2001). Low-frequency gravitational waves from cosmological compact binaries, *MNRAS* **324**: 797.
- Schulz, H. (1993). *Physik mit Bleistift*, Springer.
- Schutz, B. F. (1991). *The detection of gravitational waves*, Cambridge Univ. Press.
- Shaddock, D. A., Ware, B., Spero, R. E. and Vallisneri, M. (2004). Post-processing time-delay interferometry for LISA, *unpublished* .
- Shapiro, H. S. and Silverman, R. A. (1960). Alias-Free Sampling of Random Noise, *J. SIAM* **8**: 225.
- Sheard, B. S., Gray, M. B., Mow-Lowry, C. M., McClelland, D. E. and Whitcomb, S. E. (2004). Observation and characterization of an optical spring, *Phys. Rev. A* **69**: 051801(R).
- Sintes, A. M. and Schutz, B. F. (2000). Removal of interference from external coherent signals, *AIP conference proceedings*, Vol. 456, p. 135.
- Sivasubramanian, S., Srivastava, Y. N. and Widom, A. (2003). Gravitational wave detection with Michelson interferometers.
URL: *gr-qc/0307085*
- Somiya, K. (2003). Photodetection method using unbalanced sidebands for squeezed quantum noise in a gravitational wave interferometer, *Phys. Rev. D* **67**: 122001.

- Speliotopoulos, A. D. and Chiao, R. Y. (2004). Coupling of linearized gravity to non-relativistic test particles: Dynamics in the general laboratory frame, *Phys. Rev. D* **69**: 084013.
- Stoler, D. (1970). Equivalence classes of minimum uncertainty packets, *Phys. Rev. D* **1**: 3217.
- Strain, K. A. and Meers, B. J. (1991). Experimental Demonstration of Dual Recycling for Interferometric Gravitational-Wave Detectors, *Phys. Rev. Lett.* **66**: 1392.
- Taylor, J. H., Fowler, L. A. and McCulloch, P. M. (1979). Measurements of general relativistic effects in the binary pulsar PSR1913+16, *Nature* **277**: 437.
- Teukolsky, S. A. (1973). Perturbation of a rotating black hole. I. Fundamental equations for gravitational, electromagnetic, and neutrino-field perturbations, *ApJ* **185**: 635.
- Thorne, K. S. (1980). Multipole expansions of gravitational radiation, *Rev. Mod. Phys.* **52**: 299.
- Thorne, K. S. (2005). *Lecture notes; Chapter 26*, Master's thesis, California Institute of Technology.
- Tinto, M. and Armstrong, J. W. (1999). Cancellation of laser noise in an unequal-arm interferometer detector of gravitational radiation, *Phys. Rev. D* **59**: 102003.
- Tinto, M., Armstrong, J. W. and Estabrook, F. B. (2000). Discriminating a gravitational wave background from instrumental noise in the LISA detector, *Phys. Rev. D* **63**: 021101(R).
- Tinto, M., Estabrook, F. B. and Armstrong, J. W. (2002a). Time-delay interferometry and LISA's sensitivity to sinusoidal gravitational waves, *unpublished*.
- Tinto, M., Estabrook, F. B. and Armstrong, J. W. (2002b). Time-delay interferometry for LISA, *Phys. Rev. D* **65**: 082003.
- Turner, M. S. (1997). Detectability of inflation-produced gravitational waves, *Phys. Rev. D* **55**: R435.
- Ungarelli, C., Corasaniti, P., Mercer, R. A. and Vecchio, A. (2005). Gravitational waves, inflation and the cosmic microwave background: towards testing the slow-roll paradigm, *CQG* **22**: S955.
- Ungarelli, C. and Vecchio, A. (2001). High energy physics and the very early universe with LISA, *Phys. Rev. D* **63**: 064030.
- Vachaspati, T. and Vilenkin, A. (1985). Gravitational radiation from cosmic strings, *Phys. Rev. D* **31**: 3052.
- Vecchio, A. (2004). LISA observations of rapidly spinning massive black hole binary systems, *Phys. Rev. D* **70**: 042001.

- Vecchio, A. and Wickham, E. D. L. (2004). LISA response function and parameter estimation, *CQG* **21**: S661.
- Voss, R. and Tauris, T. M. (2003). Galactic distribution of merging neutron stars and black holes - prospects for short gamma-ray burst progenitors and LIGO/VIRGO, *MNRAS* **342**: 1169.
- Vyatchanin, S. P. (1998). The estimation of signal force parameters in quantum variation measurement, *Phys. Lett. A* **239**: 201.
- Vyatchanin, S. P. and Matsko, A. B. (1993). Quantum limit on force measurements, *JETP* **77**: 218.
- Vyatchanin, S. P. and Matsko, A. B. (1996a). Quantum variational force measurement and the cancellation of nonlinear feedback, *JETP* **82**: 1007.
- Vyatchanin, S. P. and Matsko, A. B. (1996b). Quantum variational measurements of force and compensation of the nonlinear backaction in an interferometric displacement transducer, *JETP* **83**: 690.
- Vyatchanin, S. P. and Zubova, E. A. (1995). Quantum variation measurement of a force, *Phys. Lett. A* **201**: 269.
- Wahlquist, H. (1987). The Doppler response to gravitational waves from a binary star source, *Gen. Rel. Gravitation* **19**: 1101.
- Wainstein, L. A. and Zubakov, V. D. (1962). *Extraction of Signals from Noise*, Dover.
- Walls, D. F. and Milburn, G. J. (1995). *Quantum Optics*, Springer.
- Welch, P. D. (1967). The Use of Fast Fourier Transform for the Estimation of Power Spectra: A Method Based on Time Averaging Over Short, Modified Periodograms, *IEEE Transactions on Audio and Electroacoustics* **15**: 70.
- Wen, L. (2003). On the eccentricity distribution of coalescing black hole binaries driven by the Kozai mechanism in globular clusters, *ApJ* **598**: 419.
- Willke et al. (2002). The GEO 600 gravitational wave detector, *CQG* **19**: 1377.
- Yuen, H. P. (1976). Two-photon coherent states of the radiation field, *Phys. Rev. A* **13**: 2226.
- Zhang, W.-M., Feng, D. H. and Gilmore, R. (1990). Coherent states: Theory and some application, *Rev. Mod. Phys.* **62**: 867.

INDEX

A

acceleration noise, 161
Airy function, 97
autocovariance, 42

B

back action, 84
Bianchi identity, 14
bias, 40
Big Bang Observer, 49
Bose-Einstein statistics, 83
bright-port dark-port coupling, 127

C

celestial sphere, 162
chirp mass, 29
circularization of orbits, 30
confusion noise, 57
connection coefficient, 12
consistency, 40

D

dark fringe, 114
demodulation phase, 133
detuning, 89
Dirichlet kernel, 46
displacement noise, 102
displacement operator, 78
distance measures
—, angular diameter distance, 6
—, comoving distance, 5
—, luminosity distance, 7

distant wave zone, 28
Doppler signal, 163
doublet, frequency, 148

E

eccentricity, 30
efficiency, optical, 161
Einstein field equations, 13
energy density, 51
error signal, 96
error, mean square, 40

F

Fabry-Pérot cavity, 92, 103
false alarm, 63
filter cavity, 144
fineness of template grid, 64
finesse, 93
first-generation detector, 135
Fisher information, 55
Fourier transform, discrete, 43
free spectral range, 93
Friedmann equation, 2

G

geometric optics, 18

H

Heisenberg inequality, 81
heterodyne detection, 131
homodyne detection, 129
Hubble constant, 4
Hubble law, 4

-
- I
- impedance matched, [97](#)
 - inflation, slow-roll, [37](#)
 - inner product, [55](#)
 - input-output relation, [114](#), [122](#), [142](#)
 - interaction picture, [76](#)
 - intracavity readout, [149](#)
-
- K
- Kepler's third law, [29](#)
 - Kerr
 - , Hamilton operator, [107](#)
 - , medium, [106](#)
-
- L
- linewidth, [94](#)
 - local wave zone, [27](#)
 - low frequency limit, [116](#)
-
- M
- Möbius map, [96](#)
 - merger rate density, [51](#)
 - metric
 - , FRW, [3](#)
 - , Robertson-Walker, [2](#)
 - Michelson interferometer, [114](#)
 - mirror, [91](#)
 - modulation depth, [95](#)
 - modulation picture, [77](#)
 - momentum conservation, [119](#)
 - Moore's law, [65](#)
-
- N
- Newtonian waveform, [28](#)
-
- O
- optical
 - , bar, [149](#)
 - , lever, [151](#)
 - optomechanical coupling, [101](#)
 - overcoupled, [97](#)
 - overlap of binary tracks, [57](#)
-
- P
- periodogram, [43](#)
 - perturbation
 - , metric, [12](#)
 - , trace-reversed metric, [13](#)
 - phase-sensitive detection, [128](#)
 - polarization tensor, [16](#)
 - ponderomotive squeezing, [104](#)
 - post-Newtonian expansion, [30](#)
 - Pound-Drever-Hall scheme, [94](#)
 - power recycling, [115](#)
 - precession, [33](#)
 - primordial gravitational waves, [37](#)
 - probe, [84](#)
 - projection of errors, [62](#)
 - propagation, [89](#)
 - propagation frame, [163](#)
 - propagation vector, [18](#)
-
- Q
- quadrature phase, [77](#)
 - , amplitudes, [77](#)
 - , vector, [78](#)
 - quadrupole moment, [28](#)
 - quantum measurement, linear, [84](#)
 - quantum non demolition, [81](#)
-
- R
- radiation-pressure force, [83](#), [100](#)
 - random process
 - , Markov, [48](#)
 - , purely random, [44](#)
 - realization, [55](#)
 - received power, [161](#)
 - redshift, [4](#)
 - Ricci tensor, [13](#)
 - Riemann tensor, [12](#)
 - round-trip transfer, [103](#)
-
- S
- Schrödinger picture, [76](#)
 - shot noise, [75](#), [161](#)
 - signal recycling, [124](#), [136](#)
 - signal-to-noise ratio, [55](#)
 - simultaneous measurability, [85](#)
 - sky average, [164](#)
 - sloshing frequency, [152](#)
 - spectral density, [47](#), [139](#)
 - , single sided, [48](#)
 - speed meter, [152](#)

spin-orbit coupling, [34](#)
 spin-spin coupling, [34](#)
 splitting, frequency, [148](#)
 squeezed light
 —, frequency dependent, [144](#)
 —, input, [141](#)
 —, optimized angle, [146](#)
 squeezing
 —, factor, [79](#), [101](#)
 —, operator, [79](#)
 standard quantum limit, [81](#), [153](#)
 stationary noise, [54](#)
 storage time, [94](#)
 subtraction of signals, [67](#)
 sufficiency, [40](#)
 susceptibility, [85](#), [100](#)
 symphotonic states, [155](#)

T

test mass noise, [161](#)
 time-delay interferometry, [157](#)
 —, Michelson X combination, [159](#)
 —, Sagnac ζ combination, [160](#)
 traceless-transverse
 —, gauge, [15](#)
 —, projection, [15](#)
 two-lengthscale condition, [14](#)

U

undercoupled, [97](#)

W

wave equation, [14](#)
 Wiener-Khintchine theorem, [43](#)
 Wigner function, [86](#)
 window, [46](#)
 —, Bartlett, [47](#)

ACKNOWLEDGMENTS

Being part of a young and intelligent research team is very exciting. I was lucky that right in the beginning of my doctoral studies, a team of that kind formed in the Albert-Einstein-Institute which since has been growing and has contributed many important pieces of science. Therefore, I want to say my first thank you to Prof. Karsten Danzmann and Prof. Roman Schnabel who made all this come true and who enabled my participation.

I also thank Mr Danzmann who gave me the opportunity to gain experience in a foreign country. My time at Caltech was very stimulating and happy. Many persons there left a permanent impression and I thank my supervisor Prof. Kip Thorne for integrating me in his research team and for his inspiration.

Almost none of my research was accomplished by me alone. From the beginning of my studies until now I have worked together with Roman Schnabel, Yanbei Chen, Henning Rehbein, Gudrun Diederichs and Curt Cutler. Discussions with you were always fun and rewarding. I thank all of you and sincerely hope that we will have more common research in the future.

Many more colleagues have influenced this work or my understanding of certain research topics. I especially thank Andreas Freise and André Thüring for sharing their understanding of optics with me. Thanks to Simon Chelkowski, Boris Hage, Henning Vahlbruch and Alexander Franzen for showing me how interesting experimental physics can be.

My daily work in this institute did have its ups and downs. Thank you Nancy, Philippe and Gabi for supporting and encouraging me. I am proud to share all this with you.

CURRICULUM VITAE

Jan Harms
Lutherstraße 61
30171 Hannover

Born on August 17, 1976 in Lehrte, Germany

01.2004 – 04.2004	California Institute of Technology, Pasadena
11.2002 – to date	Doctoral studies in Physics, University of Hannover
10.2002	Physik-Diplom, University of Hannover
09.2000 – 12.2000	University of Lancaster, UK
10.1997 – 10.2002	Diploma studies in Physics, University of Hannover
09.1996 – 09.1997	Community service
06.1996	Abitur, Gymnasium Lehrte

PUBLICATIONS

- 2002 J. Harms: 'Quantum Noise in the Laser-Interferometric Gravitational-Wave Detector GEO 600', Diploma thesis, University of Hannover
- 2003 J. Harms et al.: 'Squeezed-input, optical-spring, signal-recycled gravitational-wave detectors', *Phys. Rev. D* **68**, 042001
- 2004 R. Schnabel et al.: 'Squeezed light for the interferometric detection of high-frequency gravitational waves', *CQG* **21**, S1045
- 2004 J. Harms, R. Schnabel, K. Danzmann: 'The finite mass beam splitter in high power interferometers', *Phys. Rev. D* **70**, 102001
- 2005 H. Rehbein et al., 'Optical transfer functions of Kerr nonlinear cavities and interferometers', *Phys. Rev. Lett.* **95**, 193001
- 2006 C. Cutler, J. Harms, 'Big Bang Observer and the neutron-star-binary subtraction problem', *Phys. Rev. D* **73**, 042001